

Building Nanostructures Toward Improved RO Membrane Performance

A thesis submitted for the degree of Doctor of Philosophy

Nasser Alotaibi

School of Chemical and Physical Sciences

Faculty of Science and Engineering

Flinders University



2016, May

Adelaide, South Australia



“BY THE NAME OF THE LOARD THE MOST GRACIOUS AND
THE MOST MERCIFUL”, I START MY WORK.

Table of Contents

Declaration	III
abstract	IV
Acknowledgments	VI
list of Figures	VII
List of tables	XV
List of abbreviations	XVI
Chapter I	1
1.1 Introduction	2
1.2 Reverse osmosis desalination (RO)	4
1.2.1 RO desalination mechanism	6
1.2.2 Thin Film Composite membranes (TFC)	9
1.2.3 RO membrane development	12
1.3 Nanotechnology and water desalination	15
1.4 Carbon nanotubes (CNTs)	20
1.4.1 Functionalisation of carbon nanotubes	23
1.4.2 Carbon nanotubes functionalisation and model reactions	25
1.5 Thesis objectives	28
1.6 Thesis outline	28
1.7 References	30
Chapter II	37
2.1 Materials	38
2.2 Instruments	39
2.2.1 Stirred cell	39
2.2.2 Scanning Electron Microscopy	42
2.2.3 Raman spectroscopy	43
2.2.4 Nuclear Magnetic Resonance (NMR) spectroscopy	45
2.2.5 Contact Angle (CA)	47
2.2.6 Fourier Transform Infra-Red (FT-IR) spectroscopy	48
2.2.7 Fluorescence	49
2.2.8 Thermogravimetric analysis (TGA)	50
2.2.9 Atomic Force Microscopy (AFM)	51
2.3 References	54
Chapter III	56
3.1 Introduction	57

3.2	Synthesis and characterisations	58
3.2.1	¹ H NMR	60
3.2.2	FT-IR	63
3.2.3	SEM	64
3.2.4	Self-assembly of other molecules	66
3.3	Self-assembly behaviour investigation	68
3.3.1	Fluorescence spectroscopy	69
3.3.2	FT-IR spectroscopy	78
3.3.3	SEM analysis	87
3.4	Conclusion	97
3.5	Experimental section	98
3.6	References	106
Chapter IV		113
4.1	Introduction	114
4.2	Synthesis and functionalisation	116
4.2.1	Synthesis of organic compounds	116
4.2.2	Functionalisation of single wall carbon nanotubes (SWNTs)	118
4.2.3	Thin layer of polyamide in TFC membrane	123
4.3	Uniformity and Repeatability	130
4.4	Surface and performance membranes characterisation	131
4.4.1	Modified membrane with SWNTs-2-BTA	131
4.4.2	Grafting with SWNTs-6-BTA	138
4.5	Control membranes	145
4.6	Chain length influence on SWNT distribution in the membrane	148
4.7	Conclusion	150
4.8	Experimental	151
4.5	References	160
Chapter V		166
5.1	Conclusion	167
5.1.1	Self-assembly	167
5.1.2	RO membrane	169
5.2	Future work	171
5.2.1	Self-assembly	171
5.2.2	RO membrane	176
5.3	References	180
Appendices		182

DECLARATION

'I certify that this thesis does not incorporate without acknowledgement any material previously submitted for a degree or diploma in any university; and that to the best of my knowledge and belief it does not contain any material previously published or written by another person except where due reference is made in the text.'

.....

(Nasser Alotaibi)

ABSTRACT

In this thesis, single wall carbon nanotubes (SWNTs) were embedded into the polyamide layer of RO membranes. Functionalisation of SWNTs was performed to improve their distribution in the polyamide layer. To study the functionalisation reactions of SWNTs, model reactions were undertaken. Anthracene-9-carboxylic acid was the model substrate of the SWNTs because of the similarity of its aromatic properties. The produced amine compounds from the model substrate reactions were explored for formation of supramolecular structures. Benzene-1,3,5-tricarboxylic acid chloride (TMC) was used to synthesise benzene-1,3,5-tricarboxamide (BTA) derivatives as supramolecular motifs.

Four BTA molecules, with varying aliphatic chain lengths, were synthesised and characterised. Supramolecular structures were formed through the self-assembly process in a chloroform solution. Due to the chain length differences between the molecules, different self-assembled shapes were observed. Thus, this self-assembly behaviour as a function of time was investigated for the shortest and longest aliphatic chain molecules. This self-assembly was investigated by monitoring the change in fluorescence, FT-IR and SEM as a function of time. It was found that the long-chain molecule showed faster self-assembly and with greater overlap between the aromatic rings, due to the flexibility of the long-chain molecule. Moreover, the molecule with the long chain showed higher fluorescence and longer fibre formation on a substrate.

After investigating the self-assembly behaviour and the influence of chain length on the model substrate, the functionalisation reaction progressed to the SWNTs in order to embed them into the polyamide layer of the RO membrane. The influence of chain length on the distribution of SWNTs into the polyamide layer was investigated as well. Two molecules with different aliphatic chain lengths were synthesised and separately grafted to SWNTs. Raman and FT-IR showed successful grafting of SWNTs with the synthesised molecules.

Synthesis of the polyamide layer was performed by the interfacial polymerisation method. TMC (0.1 wt%) in the organic phase was allowed to react with *m*-phenylenediamine (MPD) (2 wt%) in the aqueous phase on the top surface of the polysulfone (PSf) layer, forming a thin polyamide film. To modify the polyamide

layer, the two grafted SWNTs were dispersed separately in the organic phase prior to the polymerisation. Two modified polyamide layers, with a variety of mass loadings of grafted SWNTs, were synthesised. Characterisation of the modified polymers was obtained by Raman, FT-IR, AFM and SEM.

Membrane water flux and salt rejection were determined using 2000 ppm sodium chloride as the feed solution. The modified membranes showed an improvement in water flux, but there was a decrease in salt rejection. For example, an improvement in flux from 24 to 32 Lm⁻² h⁻¹ for SWNTs-free membrane and modified membrane with 5 wt% SWNTs respectively was observed, while for the same membranes the salt rejection decreased from 73% to 67%.

Further investigation of the chain-length influence was obtained by the model reaction. Anthracene-9-carboxylic acid was used to mimic the SWNTs and synthesise the model reaction molecules. The model membranes were synthesised using the model molecules as a mimic for grafted SWNTs. The flux and salt rejection of the model membranes were determined under the same conditions as the modified membranes.

ACKNOWLEDGMENTS

My journey to complete this thesis would never have been accomplished without the supportive contributions of some of the people around me. It is said that he who thanks not people, thanks not his Lord. Thus, I feel I must thank and appreciate the people who have helped me.

Personal thanks to my father, Fahad Al Otaibi, and my mother, Shema Al Sadeer, who have always given me the strength, support and motivation to reach this moment. Amsha Al Hamadi, my wife, has supported me, especially emotionally, along my journey to complete this work. Further support has been given by my extended family and my friends as well.

I would like to thank my respected supervisors, Professor Joe Shapter and Associate Professor Martin Johnston, for their significant contributions to this project. They gave me the freedom to choose my research direction, while still providing scientific guidance. Their patience and valuable information have been greatly appreciated.

Flinders University, for giving me this chance to do my PhD study, the staff in the Chemical and Physical Sciences School, and staff in the TSU Workshop, especially Bill, Bob and Chris, thank you all. For his training and answering all my technical questions, thanks go to David Vincent.

Without the financial support of my sponsor, Al Jouf University, it would be impossible to realise this opportunity. Their support is appreciated.

LIST OF FIGURES

Figure 1- 1. Relative amounts of Earth’s water resources, showing the majority of water is salty. [9].	2
Figure 1-2. Schematic diagram of major desalination technologies and their relative contributions to worldwide installed capacity for seawater and brackish water desalination. MSF accounts for 44.4%, RO 41.1%, MED and other thermal methods 8.4%, ED and other methods 6.1% [15].	3
Figure 1-3. Illustrates water movement across a selective membrane from lower salt concentration to higher salt concentration according to the osmosis phenomenon [18].	5
Figure 1-4. Molecular motion through membranes can be explained by solution-diffusion, or by a flow through permanent pores models [26].	7
Figure 1-5. Schematic representation shows the motion of a CO ₂ molecule between polymer chains through the appearance and disappearance of pores due to the thermal motion of polymer molecules [37].	8
Figure 1-6. Schematic representation shows the motion of a CO ₂ molecule between polymer chains through the appearance and disappearance of pores due to the thermal motion of polymer molecules [37].	10
Figure 1-7. SEM image for cross-section of PSf showing that upper side pores are smaller than the lower side pores [49].	11
Figure 1-8. Interfacial polymerisation for <i>m</i> -phenylenediamine (MPD) and trimesoyl chloride (TMC). Two structures may occur, crosslinked and linear structures, which have unreacted acid chloride groups that subsequently hydrolyse to carboxylic acid groups [11].	11
Figure 1-9. SEM images of (a) PA membrane, (b) magnified image of square outlined region in (a) showing the surface morphology of the PA membranes with ridge-and-valley structures[53].	12
Figure 1-10. Power usage in RO seawater plant with high consumption energy for the high pressure pumps [54].	13
Figure 1-11. Schematic representation of water molecule transportation through aquaporins (AQP) across the cell wall.	16
Figure 1-12. Multi wall carbon nanotube membrane (A); schematic target membrane	

structure with polystyrene embedded between MWNTs (B); the cleaved edge of the CNTs-PS membrane after exposure to H ₂ O ₂ plasma oxidation (C)[82].....	17
Figure 1- 13. Schematic of the fabrication process steps starting from the substrate step (1) to the last step (7), (B) SEM cross-section of the as-grown DWNTs, (C) SEM cross-section of the membrane, illustrating excellent gap filling by silicon nitride [85].	18
Figure 1-14. Schematic cross-section of CNTs embedded in TFC membrane [90]..	19
Figure 1-15. (left) Graphene sheet demonstrating how the chiral vector is described, (right) armchair, zigzag and helical carbon nanotube structures [96, 97].	22
Figure 1-16. (A) a single-wall carbon nanotube (SWNTs) and (B) a multi-wall carbon nanotube (MWNTs) [96].	22
Figure 1-17. Some possible wrapping arrangements of a polymer on CNTs - a double helix (top) and a triple helix (middle) and multiple parallel wrapping strands (bottom) [99]......	23
Figure 1- 18. Oxidation of CNTs and derivatisation reaction with amines or alcohols [105].....	24
Figure 1-19. ATRP ‘grafting from’ functionalisation approach of carbon nanotubes[105].....	25
Figure 1- 20. (A) Anthracene-9-carboxylic acid was used as a model substrate for the development of the labelling process, (B) The process of ¹⁴ C-labelled MWNTs showing radiology activity [113].....	26
Figure 1- 21. Schematic representing the amidation reaction for SWNTs and anthracene-9-carboxylic acid with amine group in the aliphatic molecules using HATU and DIPEA base in DMF solvent.	27
Figure 2- 1. Schematic of stirred cell showing the cell parts [2].	39
Figure 2- 2. Stirred cell water flux result of membrane embedded with SWNTs. The feed solution was 2000 ppm of NaCl. The flux was measured as a function of time.	40
Figure 2-3. Calibration curve for the conversion of NaCl conductivity to concentration.....	41
Figure 2-4. Schematic diagram of SEM parts and the electron beam path from gun to sample [6].....	42
Figure 2-5. (a) Different relaxation to lower energy of excited molecule as light	

scattering, (b) spectrum of CCl ₄ , using an Ar ⁺ laser at 488 nm showing Stokes, anti-Stokes and Rayleigh scattering [10, 11].	44
Figure 2-6. Raman spectrum at 532 nm laser of pristine SWNTs showing RBM, D and G bands.	45
Figure 2-7. Schematic diagram showing splitting of nuclei spin states in an external magnetic field [20].	46
Figure 2- 8. Partial ¹ H NMR (600 MHz) spectrum of <i>N</i> -(anthracene-9-carbonyl)hexandiamine (3c) showing the peaks shapes and descriptions; s = DMSO.	47
Figure 2- 9. Illustration of contact angles formed by liquid drops on smooth solid surface.	48
Figure 2-10. Jablonski diagram and luminescence process, figure adapted from [26].	49
Figure 2-11. TGA curve of the TFC membrane supporting layer; polysulfone coated on polyester layer. First degradation step (75%) is attributed to the polyester layer while the second degradation step (20%) is attributed to polysulfone layer.	50
Figure 2-12. Schematic of AFM showing the basic components of the instrument [28].	51
Figure 2- 13. AFM images (a) 2D and (a') 3D profile of TFC membrane.	52
Figure 2- 14. Representation of Rq roughness measurement based on the mean line [34].	53
Figure 3-1. Synthesis of anthracene amine derivatives starting with aliphatic diamines.	58
Figure 3- 2. Synthesis of BTA derivatives using amine compounds with TMC.	59
Figure 3- 3. Partial ¹ H NMR spectrum (600 MHz) of <i>N,N',N''</i> -[<i>N</i> -(anthracene-9-carbonyl)ethandiamine]benzene-1,3,5-tricarboxamide (9AC-2-BTA) in CDCl ₃ , (S = CHCl ₃).	61
Figure 3- 4. Partial ¹ H NMR spectrum (600 MHz) of 9AC-2-BTA in CDCl ₃ after standing in chloroform solution for five days at room temperature; (I= impurity).	62
Figure 3- 5. Partial ¹ H NMR spectra of 9AC-2-BTA after standing five days measured at different temperatures; (I= impurity).	63
Figure 3-6. ATR-FTIR spectra for <i>N</i> -(anthracene-9-carbonyl)ethandiamine and 9AC-	

2-BTA.	64
Figure 3- 7. SEM images showing fibres formed from self assembly after standing in chloroform solution for five days at room temperature.	65
Figure 3- 8. SEM images of synthesised fibres on a silicon surface after evaporation of chloroform, (a) 9AC-4-BTA, (b) 9AC-6-BTA, (c) 9AC-8-BTA.	67
Figure 3- 9. The compound structure shows three potential aggregation forces – π - π stacking between the core and anthracene moieties, hydrogen bonding between amide groups, and van der Waals between the aliphatic chains.	68
Figure 3- 10. π - π stacking geometries of anthracene (a) face-to-face, (b) edge-to-face, (c) end-to-face, figure was adapted from [33].	70
Figure 3- 11. Typical arrangements of H- and J-aggregates for a π -conjugated molecule (monomer) and corresponding effects in the fluorescence spectra [52]. ...	71
Figure 3- 12. Fluorescence emission spectra of 9AC-2-BTA in chloroform at various self-assembly times at room temperature with concentration (2 mg mL ⁻¹).	72
Figure 3- 13. Fluorescence spectrum shifted from 440 nm at 0 hours to 456 nm at 24 hours which indicates aggregation occurrence within 24 hours. To determine the red shift subtraction of the 24 hrs from the 0 hrs spectra was performed.	73
Figure 3- 14. Fluorescence emission spectra of 9AC-8-BTA in chloroform (2 mg mL ⁻¹) with various self-assembly times at room temperature.	74
Figure 3- 15. Red shift was not observed in fluorescence spectra in time up to 15 hr which was shown by subtractions of 0.25 hr, 0.75 hr and 15 hr spectra from 0 hr spectrum.	75
Figure 3- 16. Chemical structures of the investigated aggregation compounds showing the difference only in the aliphatic chain length.	76
Figure 3- 17. Scheme showing the effect of flexibility of the compounds on the overlapping area (a > b) between the anthracene moieties.	77
Figure 3-18. Hydrogen bonding interaction of BTA derivatives resulting in self-assembly of the derivatives.	78
Figure 3- 19. ATR-FTIR spectrum of freshly made solution of 9AC-2-BTA in chloroform at room temperature.	79
Figure 3- 20. ATR-FTIR spectra of 9AC-2-BTA as a function of time.	81
Figure 3- 21. ATR-FTIR spectra of 9AC-2-BTA N-H band at 3310 cm ⁻¹ showing a shift to high frequency.	82
Figure 3- 22. ATR- FTIR spectra of freshly made solution of 9AC-8-BTA in	

chloroform at room temperature.	83
Figure 3- 23. ATR-FTIR spectra changes of 9AC-8-BTA as a function of time.	85
Figure 3- 24. ATR-FTIR of 9AC-8-BTA at various aggregation times showing shift of N-H band at 3270 cm^{-1}	86
Figure 3- 25. Solute flow showing that differential evaporation rates at the edge and middle drive the solute to the edges, leading to the coffee-stain formation [95].	88
Figure 3- 26. SEM images of 9AC-2-BTA at the centre of the chloroform droplet for different aggregation times.	90
Figure 3- 27. The formation of linear fibres instead of a ring shape as a result of aggregation occurring in the chloroform solution.	91
Figure 3- 28. SEM images of 9AC-2-BTA at the edge of the chloroform droplet for different aggregation times.	92
Figure 3- 29. SEM images of 9AC-8-BTA at the centre of the chloroform droplet at different aggregation times.	94
Figure 3- 30. SEM images of 9AC-8-BTA at the edge of the chloroform droplet at different aggregation times.	95
Figure 3- 31. Aggregation comparison between synthesised compounds using quenching percentage as a function of time (Lines added to guide eye).	96
Figure 3- 32. The comparison between 9AC-2-BTA and 9AC-8-BTA to form fibres through hydrogen bonding by observing N-H stretching band shifting (Lines added to guide eye).	97
Figure 4- 1. Schematic structure showing the thin film composite (TFC) membrane, with the active polyamide layer on top, supported by polysulfone, and with polyester as the base layer[3].	114
Figure 4- 2. Synthetic route of organic compounds synthesis.	117
Figure 4- 3. Synthetic route of SWNT functionalisation.	119
Figure 4- 4. Raman spectra with 532 nm laser of pristine SWNTs (black line), oxidised SWNTs (red line) and functionalised SWNTs with synthesised compound (blue line).	120
Figure 4- 5. FT-IR spectra of pristine SWNTs, oxidised SWNTs (SWNTs-COOH), functionalised SWNTs (SWNTs-BTA ester) and SWNTs after hydrolysing (SWNTs-BTA acid).	122

Figure 4- 6. FT-IR spectra of SWNTs-BTA-acid, SWNTs-BTA-COCl in toluene, and pure toluene recorded using NaCl disks.....	123
Figure 4- 7. Polyamide membrane derived from <i>m</i> -phenylenediamine (MPD) in the aqueous phase and trimesoyl chloride (TMC) in the organic phase via interfacial polymerisation [3].....	124
Figure 4- 8. Schematic diagram of the membrane preparation process. The PSf layer was covered with the aqueous phase (2% MPD) for 5 minutes then after removal of the excess aqueous phase contact to organic layer (0.1% TMC) was allowed for 60s. In the modified polyamide layer, SWNTs were dispersed in the organic layer.	125
Figure 4- 9. FT-IR spectra of polyamide membrane (PA) and polyamide membrane with SWNTs (PA-2-50).	126
Figure 4- 10. Raman spectra of polyamide (PA), polyamide embedded with 50 wt% (PA-2-50), and 2.5 wt% (PA-2-2.5) at laser wavelength 532 nm.....	127
Figure 4- 11. TGA curves of all membranes, including the support layer (PSf). The scan rate was 20 °C/min in an air atmosphere.	128
Figure 4- 12. TGA curves in air of supporting layer (PSf), polyamide (PA), and modified polyamide membrane with 0.5 wt% SWNTs in the organic phase.	129
Figure 4- 13. Top surface SEM images for (a) polysulfone, (b) polyamide, (c) PA-2-0.5, (d) PA-2-1, (e) PA-2-2.5, (f) PA-2-5, (g) PA-2-10 and (h) PA-2-50.	132
Figure 4- 14. (2D, 3D) AFM surface images of (a ,a') polyamide layer, (b,b') PA-2-0.5, (c,c'), (d,d') PA-2-2.5 and (e,e') PA-2-50.	134
Figure 4- 15. Roughness parameters of polyamide membranes, Rq (red line) and SAD (blue line). (Lines added to guide the eye).	135
Figure 4- 16. Contact angle of polyamide (PA), PA-2-0.5, PA-2-1, PA-2-2.5, PA-2-5, PA-2-10 and PA-2-50 with SWNTs concentration 0, 0.5, 1, 2.5, 5, 10 and 50 wt% respectively. (Lines added to guide the eye).....	136
Figure 4- 17. Effect of loading of SWNTs-2-BTA in the polyamide membrane on flux and salt rejection performance. Feed solution was 2000 ppm and N ₂ pressure was 16 bar. (Lines added to guide the eye).....	137
Figure 4- 18. Top surface SEM images for (a) polysulfone (PSf), (b) plain polyamide (PA), (c) PA-6-0.5, (d)PA-6-1, (e) PA-6-2.5, (f) PA-6-5, (g) PA-6-10 and (h) PA-6-50.....	139
Figure 4- 19. (2D, 3D)AFM surface images for (a, a') polyamide layer (PA), (b, b') PA-6-0.5, (c, c') PA-6-2.5, (d, d') PA-6-50.....	141

Figure 4- 20. Roughness parameters of polyamide membranes, Rq (red line) and SAD (blue line). (Lines added to guide the eye).	142
Figure 4- 21. Contact angle for polyamide/SWNT membranes with SWNT-6-BTA concentration 0, 0.5, 1, 2.5, 5, 10 and 50 wt% in the organic phase. (Line added to guide the eye).....	143
Figure 4- 22. Effect of loading of SWNT-6-BTA in the polyamide membranes on flux and salt rejection performance. Feed solution was 2000 ppm and N ₂ pressure was 16 bar. (Lines added to guide the eye).....	144
Figure 4- 23. Synthetic route of model compounds containing anthracene in place of SWNTs.....	146
Figure 4- 24. Effect of loading 9AC-2-BTA in the polyamide membranes on flux and salt rejection performance. Feed solution was 2000 ppm NaCl and N ₂ pressure was 16 bar. (Lines added to guide the eye).....	147
Figure 4- 25. Effect of loading 9AC-6-BTA in the polyamide membranes on flux and salt rejection performance. Feed solution was 2000 ppm NaCl and N ₂ pressure was 16 bar. (Lines added to guide the eye).....	148
Figure 4- 26. Illustration of molecules grafted to SWNTs (a) short chain (b) long chain, showing the molecules folding over SWNTs as result of the higher flexibility of the long chain.....	149
 Figure 5-1. BTA derivative structure showing anthracene moieties as substituents coupled to the BTA core through amide bonds.	167
Figure 5- 2. SEM images of (A) short-chain molecule and (B) long-chain molecule on silicon surface after 96 hours of aggregation time in chloroform (presented in Chapter III). Note different scale sizes.	168
Figure 5- 3. Illustration of the functionalised SWNTs with the organic compounds.	169
Figure 5- 4. SEM images for the embedded polyamide layer with 50 wt% of (A) functionalised SWNTs with the short-chain compound, (B) with the long-chain compound.....	170
Figure 5- 5. SEM images of (10 mM) supramolecules prepared in 50% DMSO–H ₂ O (a), 50% DMF–H ₂ O (b), and 50% THF–H ₂ O (c and d). Transmission electron microscope (TEM) images of the spheres (e and f). The inset in (b) shows a vial	

containing gel, figure was adapted from [4].	172
Figure 5- 6. Optical (a) and fluorescence (b) microscope images of the Rhodamine B encapsulated spheres [4].	173
Figure 5- 7. Fluorescence spectra enhancement in the gel phase compared to the solution phase [9].	174
Figure 5- 8. Photodimerisation of anthracene upon UV light irradiation [11].	174
Figure 5- 9. Transparent organogel formation in THF after exposure to UV light [10].	175
Figure 5- 10. SEM images displaying E. coli bacteria at the surface of (A) control membrane and (C) SWNT-functionalised membrane (some cells with lost integrity are highlighted in orange). (D) Magnified view of the surface of a SWNT-TFC membrane with E. coli cells [18].	177
Figure 5- 11. Illustration of FO and RO schemes showing that the water flow is driven by the osmotic pressure in FO, while external pressure is applied in RO.	178
Figure 5- 12. Schematic illustration of embedded graphene oxide in the polyamide layer on top of the polysulfone layer [25].	179

LIST OF TABLES

Table 1-1. Feedwater characterisation by salt content [8]	6
Table 1-2. monomers that have been used to improve the active layer separation properties [60].	14
Table 3-1. Fluorescence intensity of the flexible compound (9AC-8-BTA) and the less flexible compound (9AC-2-BTA).	77
Table 3-2. ATR-FTIR peaks observed for 9AC-2-BTA compound.	80
Table 3-3. ATR-FTIR peaks observed for the 9AC-8-BTA compound.	84
Table 4-1. Raman spectra peak position using a 532 nm laser of pristine SWNTs (SWNTs), oxidised SWNTs and functionalised SWNTs with BTA-2-ester (SWNT-BTA ester).	121
Table 4-2. Polyamide membrane content of functionalised SWNTs with short-chain and long-chain compounds.	126
Table 4-3. Flux, salt rejection values and relative standard deviations (RSD) of polyamide/SWNT membrane. SWNT concentration in the organic phase was 1 wt%.	130
Table 4-4. Roughness parameters of polyamide membranes. Rq represents the root mean square roughness and SAD represents the percentage of difference between the image's three-dimensional surface area and two-dimensional surface area.	135
Table 4-5. Roughness parameters of polyamide/SWNT-6-BTA membranes. Rq represents the root mean square roughness and SAD represents the percentage of difference between the image's three-dimensional surface area and two-dimensional surface area.	142
Table 4-6. Control membranes performance results.	147

LIST OF ABBREVIATIONS

2D	Two dimensional
3D	Three dimensional
AFM	Atomic Force Microscopy
BTA	Benzene-1,3,5-tricarboxamide
CNTs	Carbon nanotubes
CSA	Camphor sulfonic acid
CVD	Chemical vapour deposition
DCM	Dichloromethane
DI	Deionised water
DIPEA	<i>N,N</i> -Diisopropylethylamine
DMF	<i>N,N</i> dimethylformamide
DWNTs	Double-wall carbon nanotubes
ED	Electrodialysis
FO	Forward osmosis
FT-IR	Fourier Transform Infra-Red
HATU	2-(1H-7-azabenzotriazol-1-yl)-1,1,3,3-tetramethyl uranium hexafluorophosphate methanaminium
IP	Isopropanol
J_w	Water flux
MED	Multi-effect distillation
MPD	<i>m</i> -phenylenediamine
MSF	Multi-stage flash
MWNTs	Multi-wall carbon nanotubes
NF	Nanofiltration
NMR	Nuclear Magnetic Resonance
OLEDs	Organic light-emitting diodes
PSf	Polysulfone
R	Salt rejection
RO	Reverse osmosis
Rq	Root mean square roughness
RSD	Relative standard deviation
SAD	Surface area difference
SDS	Sodium dodecyl sulphate
SEM	Scanning Electron Microscopy
SWNTs	Single-wall carbon nanotubes
TDS	Total dissolved solids
TEA	Triethyl amine
TEM	Transmission Electron Microscopy
TFA	Trifluoroacetic acid

TFC	Thin film composite
TFN	Thin film nanocomposite
TGA	Thermogravimetric analysis
TMA	Benzene-1,3,5-tricarboxylic acid
TMC	Benzene-1,3,5-tricarboxylic acid chloride
UF	Ultrafiltration
VCD	Vapour compression desalination

CHAPTER I

1.1 Introduction

Fresh water is being consumed in vast quantities by the world population. However, the increase in population around the world is not only the reason for the decline in fresh water resources. There are also other factors contributing to the rise in the global shortage of fresh water, such as pollution and climate change [1-3]. Despite that, there are 1.4 billion cubic kilometres of water in the world, with fresh water available as rivers, lakes and ground water being less than 2% of that, as shown in Figure 1-1 [4-6]. The polar ice caps have locked up 1.74% as fresh water, while the remaining 96.5% is salty water in the global oceans [7]. These resources are unequally distributed across the globe [8].

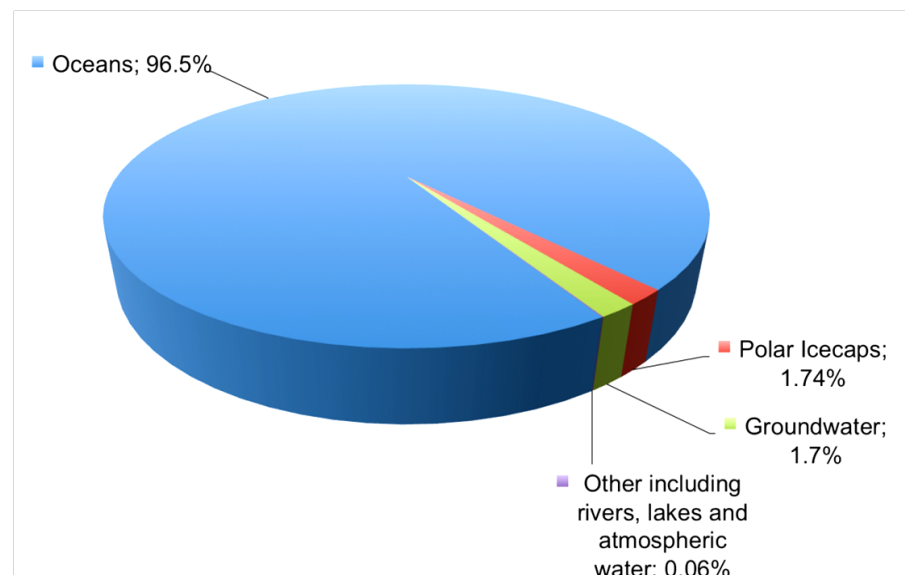


Figure 1-1. Relative amounts of Earth's water resources, showing the majority of water is salty. [9].

Approximately one billion people lack access to safe drinking water, and 26 countries do not have sufficient water resources to sustain agriculture and economic development. There are some regions with water scarcity, including a significant portion of the Middle East, North Africa, Australia, parts of Central and South Asia, and the southwestern areas of North America [6, 8]. In addition, it is expected that human population will increase by 40-50% over the next 50 years, with increases in industrialisation and urbanisation activities, which will increase the demand on fresh water resources [10]. Therefore, addressing this fresh water need requires a search for alternative sources. The shortage of fresh water has led to the invention of a number of technologies to provide reliable sources of purified water.

These technologies are divided into two types [11]. The first type is thermal process technology, which includes multi-stage flash (MSF), multi-effect distillation (MED) and vapour compression desalination (VCD). The second type is membrane-based processes, which involve electrodialysis (ED), reverse osmosis (RO) and nanofiltration (NF) [12-14]. Figure 1-2 presents schematic diagrams for the widespread desalination technologies across the world. As seen, RO, MSF and MED produce over 90% of the global desalinated water. RO plants capacities represent 41% of the total desalination capacity, and MSF plants represent 44%, have the largest capacities of water desalination technologies [6, 15].

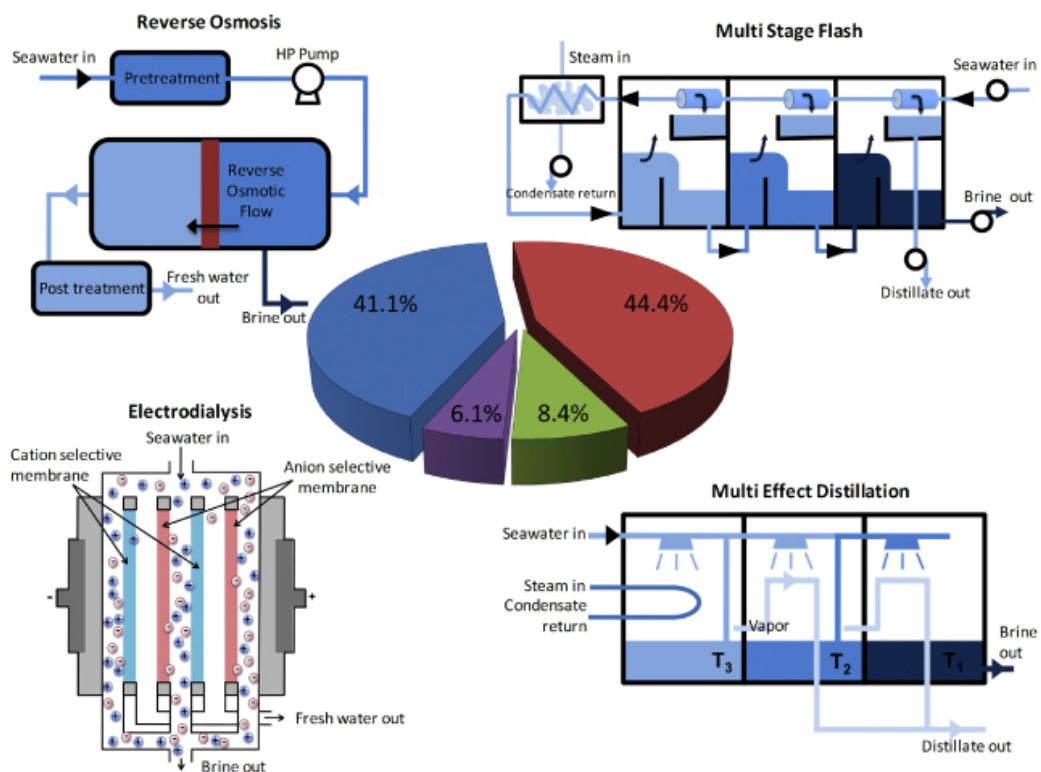


Figure 1-2. Schematic diagram of major desalination technologies and their relative contributions to worldwide installed capacity for seawater and brackish water desalination. MSF accounts for 44.4%, RO 41.1%, MED and other thermal methods 8.4%, ED and other methods 6.1% [15].

The main challenges to expanding desalination technologies are the costs of infrastructure and energy. Even though RO is competitive with MSF regarding the volumes of clean water that can be produced, RO technology costs less in energy than MSF. The energy costs range from 3.6-5.7 kWh m⁻² for RO, while MSF costs 23.9-96.0 kWh m⁻² [15]. The improvements in RO membranes during the last few

decades have led to a reduction in energy consumption and the widespread use of RO desalination across the world [16].

1.2 Reverse osmosis desalination (RO)

Reverse osmosis desalination depends on the osmosis phenomenon, which has been used by human beings since the early days of mankind [17]. The osmosis phenomenon has been used to preserve food for long periods by adding salt to it. According to the osmosis phenomenon, food dehydration would have occurred due to water molecules moving from the food, as the low concentration part, to the salt, as the high concentration part. As a result, the interior food environment would be converted to a saline environment, leading to the death or inactivity of any bacteria or organisms in the food [18].

In 1748, Abbe Nollet (French cleric) discovered the osmosis phenomenon and explained it in the first publications on osmosis [19, 20]. However, the attention of scientists was attracted by the ability of membranes to prevent salt molecules from permeating the membranes [21]. The experimental membranes, at that time, were animal membranes (bladders) and plant origin membranes (onions) [22].

Osmosis is a net movement of water molecules across a semipermeable membrane due to the difference in osmotic pressure across the membrane. Osmotic pressure is a result of concentration differences in the liquids on either side of the membrane sides [18]. As illustrated in Figure 1-3, the semipermeable membrane allows water molecules to pass through the membrane from fresh water to high salt concentration water [23-25]. When external pressure is applied to overcome the osmotic pressure it forces water molecules to pass the semipermeable membrane in the opposite direction to osmosis and this is the RO process [11, 26-28].

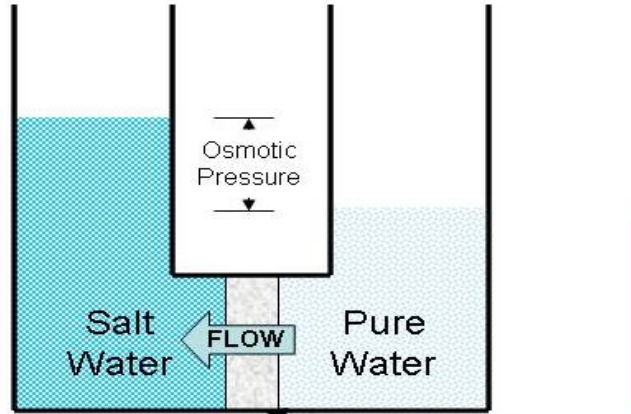


Figure 1-3. Illustrates water movement across a selective membrane from lower salt concentration to higher salt concentration according to the osmosis phenomenon [18].

The water flux, J_i , direction through the membrane is linked to the pressure and concentration gradients across the membrane by the equation:

$$J_i = A(\Delta p - \Delta\pi) \quad (1-1)$$

where Δp is the pressure difference across the membrane, $\Delta\pi$ is the osmotic pressure difference across the membrane, and A is a constant. The water flows by the osmosis phenomenon from the dilute to the concentrated salt solution side when $\Delta p < \Delta\pi$. The flow will not occur when $\Delta p = \Delta\pi$. In the opposite direction to the osmosis phenomenon, the water flows from the concentrated salt-solution side to the dilute side when $\Delta p > \Delta\pi$ through the application of an external pressure higher than the osmotic pressure [8, 26, 29, 30].

The osmotic pressure can be thermodynamically defined by the equation:

$$\pi = -\frac{R.T}{V_b} \ln(X_w) \quad (1-2)$$

where π is the osmotic pressure, V_b is the molar volume of water, X_w is the molar fraction of water, T is the operating temperature, and R is the ideal gas constant [8, 31].

In dilute solutions, the osmotic pressure can be estimated using van't Hoff's law, which is in the same form as the ideal gas law:

$$\pi = -\frac{n_s}{V}RT \quad \text{or} \quad \pi = CRT \quad (1-3)$$

When non-ideality and dissociation of the ions in solution are taken into account, van't Hoff's law [30] can be rewritten as:

$$\pi = i\phi CRT \quad (1-4)$$

where the dissociation parameter i , is equal to the number of ions and molecules per mole of solute produced by dissolution of the solute. The correction factor ϕ represents the non-ideality [8].

The osmotic pressure value depends on the salt concentration in the feedwater. Total dissolved solids (TDS) is used to define the feedwater. Water with TDS more than 15000 ppm (mg/L) is defined as seawater. Brackish water has TDS ranging from 1500 to 15000 ppm. Table 1-1 shows the TDS range for different feedwaters.

Table 1-1. Feedwater characterisation by salt content [8]

	Minimum TDS (ppm)	Maximum TDS (ppm)
Seawater	15000	50000
Brackish water	1500	15000
River water	500	1500
Pure water	0	500

For RO desalination to occur, the external applied pressure must exceed the osmotic pressure of the feedwater. To achieve reasonable fluxes ($> 12 \text{ m}^2 \text{ h}^{-1}$) for seawater and brackish water, the applied pressures are 55-65 bar and 10-30 bar respectively [16, 32].

1.2.1 RO desalination mechanism

From the nineteenth century, there have been attempts to understand the permeation behaviour of membranes. Due to the ability to separate undesirable species and control the rate of flux through the membranes, permeability is the most important property of membranes, with a number of mechanisms proposed [22, 26, 33]. Until the mid-1940s, there was one mechanism more popular than others, due to its closeness to normal physical experience. The pore-flow model attributes the permeability of membranes to the presence of tiny pores that are responsible for permeate movement through them by pressure-driven convective flow. The filtration occurs due to the exclusion of one

permeate by some pores, while the other permeates move through the membrane pores [26].

During the 1940s, the solution diffusion model emerged as an explanation for understanding the transportation of gases through polymeric films. In the 1960s to the early 1970s, there was a strong debate about the transporting mechanism in a reverse osmosis membrane. However, by 1980 the solution diffusion model had become widely accepted for understanding membrane permeation [25, 26, 33-35].

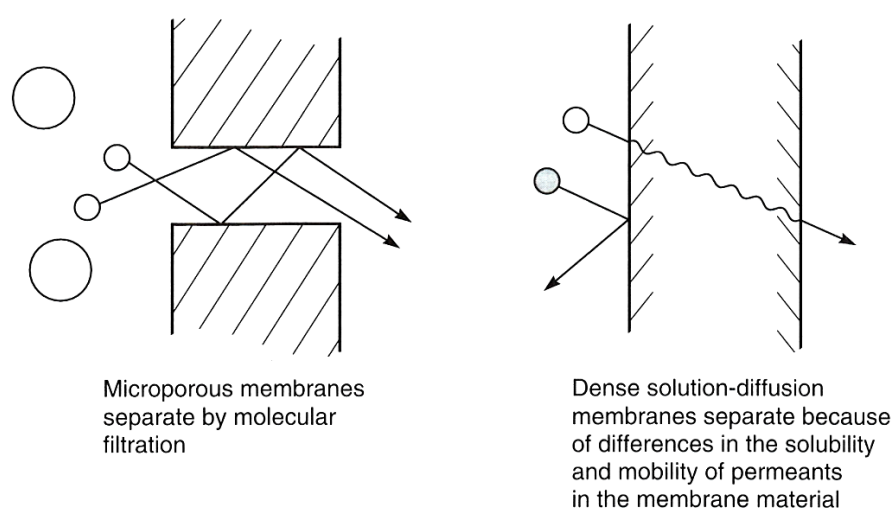


Figure 1-4. Molecular motion through membranes can be explained by solution-diffusion, or by a flow through permanent pores models [26].

The solution-diffusion process occurs when the water molecules dissolve into the water-swollen polymer matrix at the upstream surface of the membrane [36]. Subsequently, molecule diffusion from the concentrated side of the membrane to the less concentrated side will happen as a result of the concentration gradient or chemical potential. Figure 1-4 schematically illustrates molecular motion through membranes by solution-diffusion and flow through permanent pores [26, 36].

In spite of reverse osmosis membranes having a dense active polymer layer with no visible pores, the transfer of molecules through the membrane from concentrated to less concentrated sides occurs via the free-volume elements. Figure 1-5 schematically shows the motion through the polymer. Free-volume elements are tiny spaces between

the chains of polymer of around 2-5 Å in diameter. These pores appear and disappear due to the thermal motions of polymer molecules on about the same timescale as permeate motion while traversing the membrane [26].

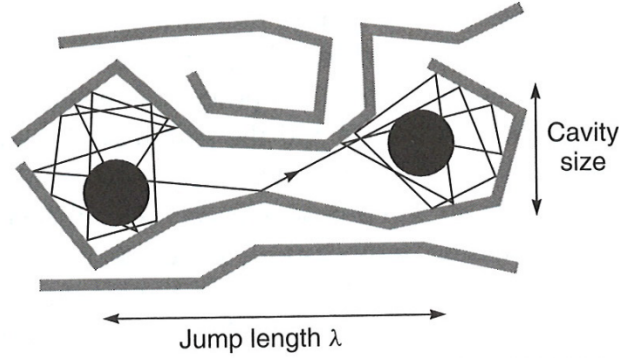


Figure 1-5. Schematic representation shows the motion of a CO₂ molecule between polymer chains through the appearance and disappearance of pores due to the thermal motion of polymer molecules [37].

Lonsdal et al. used the solution-diffusion mechanism to derive the water flux equation as follows [26, 33, 35]:

$$J_w = A(\Delta P - \Delta\pi) \quad (1-5)$$

$$A = \frac{D_w C_w \bar{V}_w}{R_g T t} \quad (1-6)$$

where J_w = water flux, D_w = diffusion coefficient of water in the membrane, C_w = concentration of dissolved water in the membrane, \bar{V}_w = partial molar volume of water in the external phase, R_g = the gas constant, T = absolute temperature, t = active layer thickness.

$\Delta P = P' - P''$ = the applied pressure difference across the membrane

$\Delta\pi = \pi' - \pi''$ = the osmotic pressure difference across the membrane

The salt flux is described by the equation following [26, 33, 35]:

$$J_s = \frac{D_s K_s}{t} \Delta C_s \quad (1-7)$$

D_s = the diffusion coefficient of salt in the membrane

K_s = the partition coefficient of salt between membrane and solution

$\Delta C_s = C'_s - C''_s$ = the salt concentration difference on the two sides of the membrane

The salt rejection (R) could be obtained from [26, 33, 35]:

$$R = 1 - \frac{C''_s}{C'_s} = 1 - \frac{D_s K_s R_s T}{D_w C_w \bar{V}_w} \times \frac{C''_s - C'_s}{C'_s} \times \frac{1}{\Delta P - \Delta \Pi} \quad (1-8)$$

There are some observations that can be made from water and salt flux equations. Firstly, water flux increases with an increase in the applied pressure, and an increase in the active layer thickness will lead to a decrease in water flux. On the other hand, there is no relationship between pressure drop and salt flux, while there is a strong negative influence on salt flux from an increase in the active layer thickness [33]. In the last equation, regardless the membrane thickness (t), the salt rejection (R) can be calculated by measuring the salt concentration on the two sides of the membrane [33].

1.2.2 Thin Film Composite membranes (TFC)

Reid and Berton synthesised cellulose acetate films as the first applicable membrane, which had good salt rejection of better than 98% in 1959. Improvement of the membrane by Loeb-Sourirajan led to the creation of an anisotropic cellulose acetate membrane, which had ten times better flux without sacrificing salt rejection. A few years later, the first RO plant was installed [26].

In the mid-1970s, John Cadotte had synthesised a thin film composite membrane (TFC) via the interfacial polymerisation method. As demonstrated in Figure 1-6, a composite membrane includes three layers. The first layer is a thin active layer that is prepared on a support substrate, which is stabilised on a non-woven layer. The layers are described under the following subheadings: support backing, porous support and thin active layer.

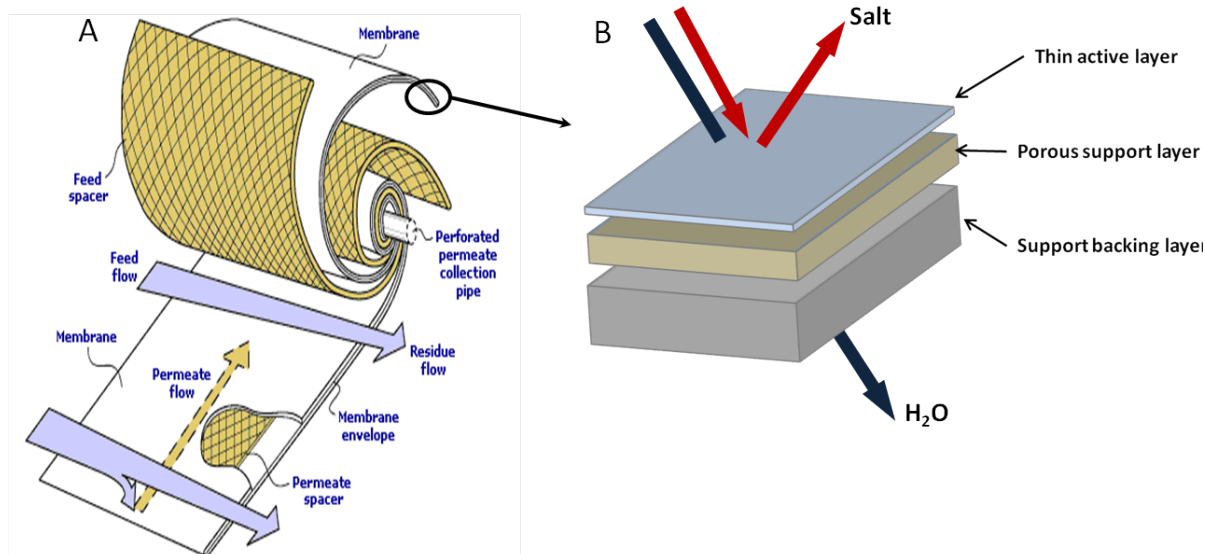


Figure 1-6. Schematic representation shows the motion of a CO₂ molecule between polymer chains through the appearance and disappearance of pores due to the thermal motion of polymer molecules [37].

1.2.2.1 Support backing

Non-woven polyester fabric is used as the support backing for the thin film composite membrane [38, 39]. The stability of polyester against harsh conditions, either chemical or physical, lead to the utilisation of polyester as the support backing of the TFC. Its tolerance to acids, oxidising agents and solvents makes polyester the preferred support backing in thin film composites [40-42]. The thickness of polyester layer ranges from 120 μm to 150 μm [43].

1.2.2.2 Porous support

The second layer is the porous layer, with a thickness of about 40 μm [35, 43]. There are several materials used as the porous support layer in TFC membranes, such as polypropylene, polyethersulfone, polycarbonate, polyphenylene oxides and others [44]. However, polysulfone (PSf) is widely used due to a number of advantages, such as low price, wide availability, and stable physiochemical properties. Moreover, the easy soaking of PSf in amine solution during the interfacial polymerisation process is one of the important features of PSf. Hydrophilicity is also a significant advantage of PSf [45-47]. Figure 1-7 shows the porosity of the PSf layer. The pore size of PSf ranges from 200 \AA to 40,000 \AA for the upper and lower sides respectively [48].

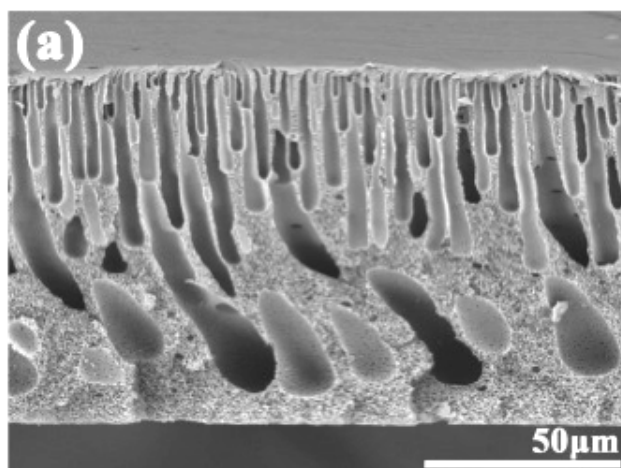


Figure 1-7. SEM image for cross-section of PSf showing that upper side pores are smaller than the lower side pores [49].

1.2.2.3 Thin active layer

The thin or active layer in TFC is a polyamide that is responsible for rejection of salt while still passing of water molecules. In the 1970s, Cadotte and his co-workers synthesised a polyamide layer on a porous substrate via an interfacial polymerisation process by reacting trimesoyl chloride (TMC) and meta-phenylenediamine (MPD) [22, 26, 50]. The reaction process is illustrated in Figure 1-8.

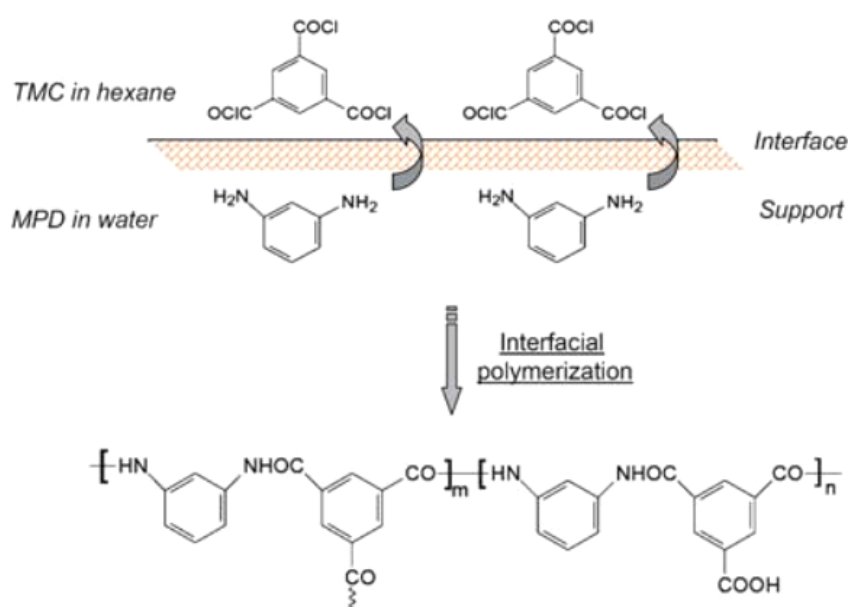


Figure 1-8. Interfacial polymerisation for *m*-phenylenediamine (MPD) and trimesoyl chloride (TMC). Two structures may occur, crosslinked and linear structures, which have unreacted acid chloride groups that subsequently hydrolyse to carboxylic acid groups [11].

Interfacial polymerisation is generally performed by reacting a polyfunctional amine

in aqueous solution on a porous layer with an organic solution containing polyfunctional acid chloride. It is widely believed that the interfacial polymerisation reaction takes place at the organic side of the interface due to the negligible solubility of acid chlorides in water and the fairly good solubility of amines in organic solvents [35, 51, 52]. Usually, the polymerisation is incomplete and a number of amine and carboxylic functional groups can be unreacted, as illustrated in Figure 1- 8 [35]. The surface of the synthesised thin active layer is described as a rough surface with ridges and valleys, as seen in Figure 1-9.

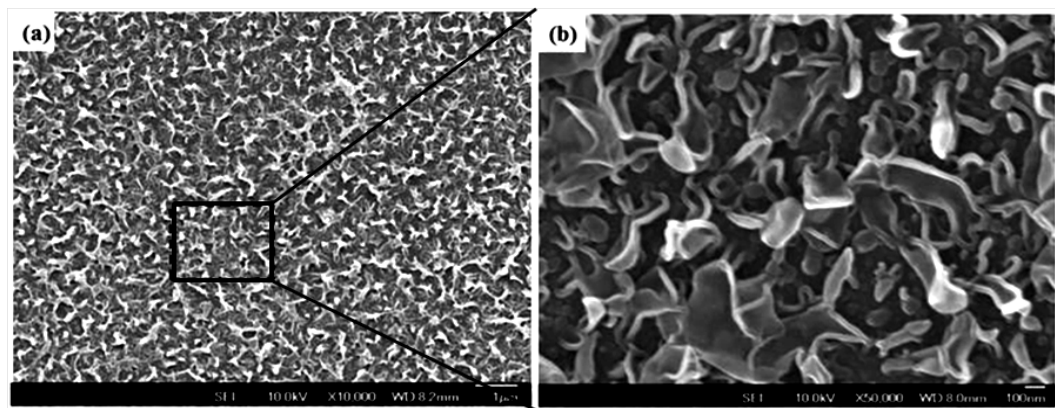


Figure 1-9. SEM images of (a) PA membrane, (b) magnified image of square outlined region in (a) showing the surface morphology of the PA membranes with ridge-and-valley structures[53].

The thin active layer exclusively determines the water permeability and solute rejection efficiency of the membrane. The support backing and porous support layers do not contribute to the separation process and their role is to provide mechanical support to the active layer.

1.2.3 RO membrane development

The performance and quality of the membrane affects the energy consumption of the desalination processes. As shown in Figure 1-10, more than 80% of the energy is consumed in applying high pressure to the RO membrane to overcome the osmotic pressure and obtain a reasonable water flux [54]. Reduction in energy consumption has been a significant driving factor in the development of desalination processes.

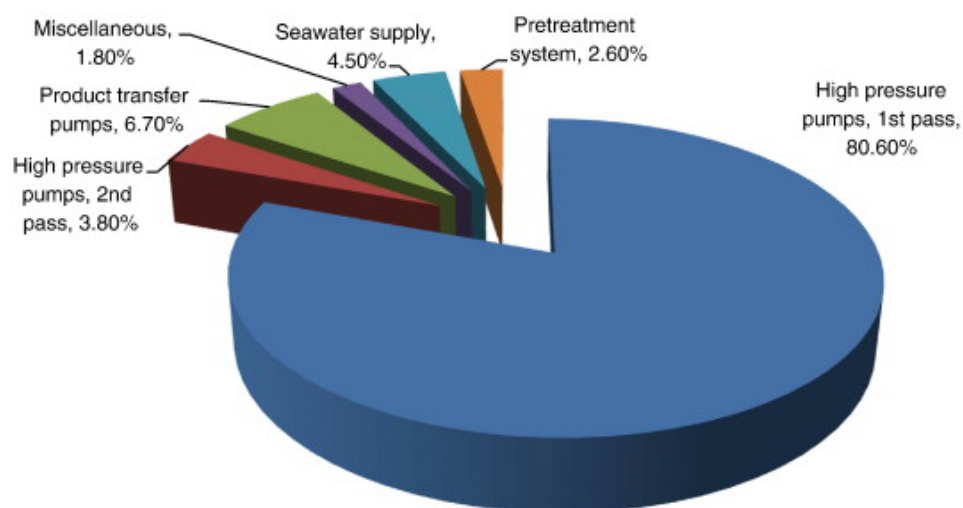


Figure 1-10. Power usage in RO seawater plant with high consumption energy for the high pressure pumps [54].

There are some technologies that have been suggested to reduce energy consumption, for example using renewable energy. Solar cells are one of the renewable sources that can be used to reduce the consumption of energy, and at the same time be friendly to the environment, with less pollution [55, 56]. However, this solution will not be discussed because it is beyond the scope of this thesis.

In addition, the membrane has been modified in order to discover new membrane generations with higher capabilities for rejecting impurities, high resistance to any possible fouling processes, high resistance towards chemical additives, and that can be operated at lower pressures without sacrificing the high flux rate. In order to obtain these properties, a number of monomers and additives have been used to promote RO membranes. These will now be briefly discussed.

1.2.3.1 Monomers

There are a number of monomers have been utilised to improve water separation properties through the active layer, as shown in Table 1-2. However, TMC and MPD are still commonly used in the synthesis of the polyamide active layer. MPD-derived polyamide has a higher salt rejection compared with polyamides made from other amines such as 1,2-phenylenediamine, 1,4-phenylenediamine and piperazine [57-59]. TMC is commonly used for polyamide layer fabrication among different acid chlorides due to its ability to form a three-dimensional cross-linked structure of polymers. It can also increase the hydrophilicity of the active layer polymers by hydrolysing the acid

chloride groups to carboxylic groups [11, 57, 58].

Table 1-2. Monomers that have been used to improve the active layer separation properties, adapted from [60].

Amine monomer (abbreviation)	Chemical structure	Acyl chloride monomer (abbreviation)	Chemical structure
Piperazine (PIP)		Trimesoyl chloride (TMC)	
M-Phenylenediamine (MPD)		Isophthaloyl chloride (IPC)	
P-Phenylenediamine (PPD)		5-isocyanato-isophthaloyl chloride (ICIC)	
Sulfonated cardo poly(arylene ether sulfone) (SPES-NH2)		mm-Biphenyl tetraacyl chloride (mm-BTEC)	
3,5-diamino-N-(4-aminophenyl)benzamide (DABA)		om-Biphenyl tetraacyl chloride (om-BTEC)-	
Triethanolamine (TEOA)		op- Biphenyl tetraacyl chloride (op-BTEC)	
Methyl-diethanolamine (MDEOA)		Cyclohexane-1,3,5-tricarbonyl chloride (HTC)	
1,3-cyclohexanebis(methylamine) (CHMA)		5-chloroformyloxy-isophthaloyl chloride (CFIC)	
m-phenylenediamine-4-methyl (MMPD)			
Hexafluoroalcohol-m-Phenylenediamine (HFA-MPD)			

It was proposed that the excessively tight cross-linking and low free volume of the polymer would reduce the permeability of the polyamide layer derived from MPD-TMC. To overcome this issue, incorporation of new amines with MPD during the interfacial polymerisation process was attempted. For instance, adding sulfonated cardo poly(arylene ether sulfone) into MPD solution led to a significant improvement of water flux of the polyamide membrane due to poly(arylene ether sulfone) improving

the hydrophilicity of the membrane. Salt rejection was also improved because of the high degree of cross-linking and the copolymer chain stiffness [61, 62].

1.2.3.2 Additives

Additives used during the interfacial polymerisation process can affect the structure of the membrane, such as the cross-linking density and porosity, and therefore the permeability properties.

The addition of surfactants such as sodium dodecyl sulphate (SDS) to the diamine aqueous solution improves the absorption of the diamine solution in the support layer. As it is widely believed that the polymerisation occurs on the organic side, the surfactants are able to help the diamine monomer to move from the aqueous phase into the organic phase, so efficiency of polymerisation can be improved [63].

In the interfacial polymerisation reaction, the pH of the solution decreases due to the formation of hydrochloric acid as a result of the reaction between the diamine and acid chloride monomers. The membrane structure and properties are negatively influenced by the pH. The removal of the hydrochloric acid produced is achieved by adding some acid acceptors, for example triethylamine. Camphor sulfonic acid (CSA) is used as an additive to maintain and overcome any pH change through hydrochloric acid production [64-66].

The water flux of the polyamide layer can be increased by adding alcohol molecules to the aqueous diamine solution [67]. Isopropyl alcohol (IPA) addition increased the water flux by two and a half times over the initial result, as reported by Qiu et al. [68]. The flux enhancement was attributed to the swelling effect of IPA, which expanded the distance between molecular chains of both support and top layers. The flux also corresponds to the change in the polarity, which enhances the interaction between the membrane and water molecules. Salt rejection was not significantly affected by adding alcohol molecules [68].

1.3 Nanotechnology and water desalination

Nanotechnology has produced new classes of functional materials, known as nanomaterials. Due to applications of nanomaterials in different areas, nanotechnology has garnered a great deal of public interest. For example, in membrane-based

desalination technology, nanomaterials have been used to improve mechanical, chemical and thermal stability, as well as to enhance the separation performance of the nanomaterial membranes developed, known as nanocomposite membranes. Nanoparticles of materials such as zeolite [69, 70], silica [71, 72], silver [73] and TiO_2 [74, 75] have been used as fillers in the polyamide when forming the nanocomposite membranes.

Increasing attention, however, has been paid to utilising carbon nanotubes (CNTs) in water filtration. This is due to the similarity between the fluid transport properties of CNTs and water transport through biological membrane channels [76]. Biologically, water passes through the cell membrane via special proteins called aquaporins (AQP). These nanoscale protein channels serve as water-filled pipes across the membrane, with a high water flux rate that effectively block everything else, even individual protons. Therefore, water molecules are transported freely through aquaporins, depending on the relative change of pressure inside and outside the cell membrane [77-81]. Figure 1-11 illustrates the transport of water through AQP.

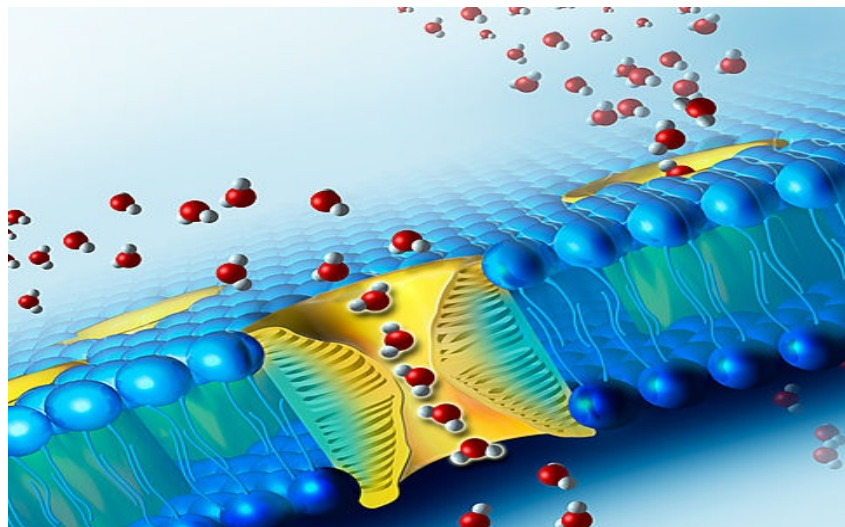


Figure 1-11. Schematic representation of water molecule transportation through aquaporins (AQP) across the cell wall.

The similarity between CNTs and AQP led to initiation of research into simulating biological transport of water through the membrane. As a result, in 2004, there was the first report on the investigation of fluid flow in a CNTs membrane [2, 82]. Multi-wall carbon nanotubes (MWNTs) were synthesised and well aligned by catalytic chemical vapour deposition (cCVD) on the surface of a quartz substrate. The MWNTs were spin

coated with polystyrene to seal the inter-tube gaps. Next, plasma etching was used to open the tips of the MWNTs, as demonstrated in Figure 1-12.

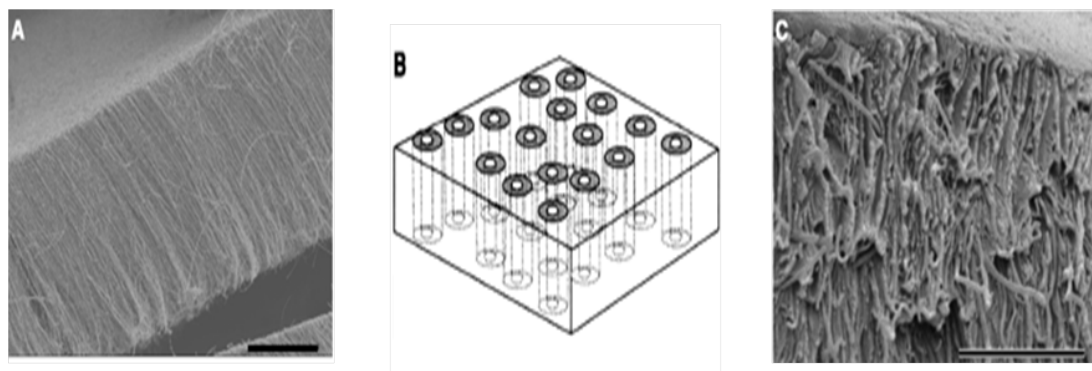


Figure 1-12. Multi wall carbon nanotube membrane (A); schematic target membrane structure with polystyrene embedded between MWNTs (B); the cleaved edge of the CNTs-PS membrane after exposure to H₂O₂ plasma oxidation (C) [82].

After this report, water transport in a solid polystyrene film membrane incorporating 7 nm diameter MWNTs was reported [83]. The flow velocity was four to five orders of magnitude higher than the expected value [84].

Another experiment on fluid used for construction with a CNTs membrane has been reported using nanofabrication techniques. In that membrane, double-wall carbon nanotubes (DWNTs) with sub-2 nm nanotube pore and silicon nitride were used instead of MWNTs and polystyrene, respectively. Figure 1- 13 illustrates the synthesis process. cCVD was used to grow a vertically aligned array of DWNTs, followed by encapsulation of the nanotubes by low pressure chemical vapour-deposition silicon nitride (Si₃N₄). The excess silicon nitride was removed by ion milling and the nanotubes were opened with reactive ion etching.

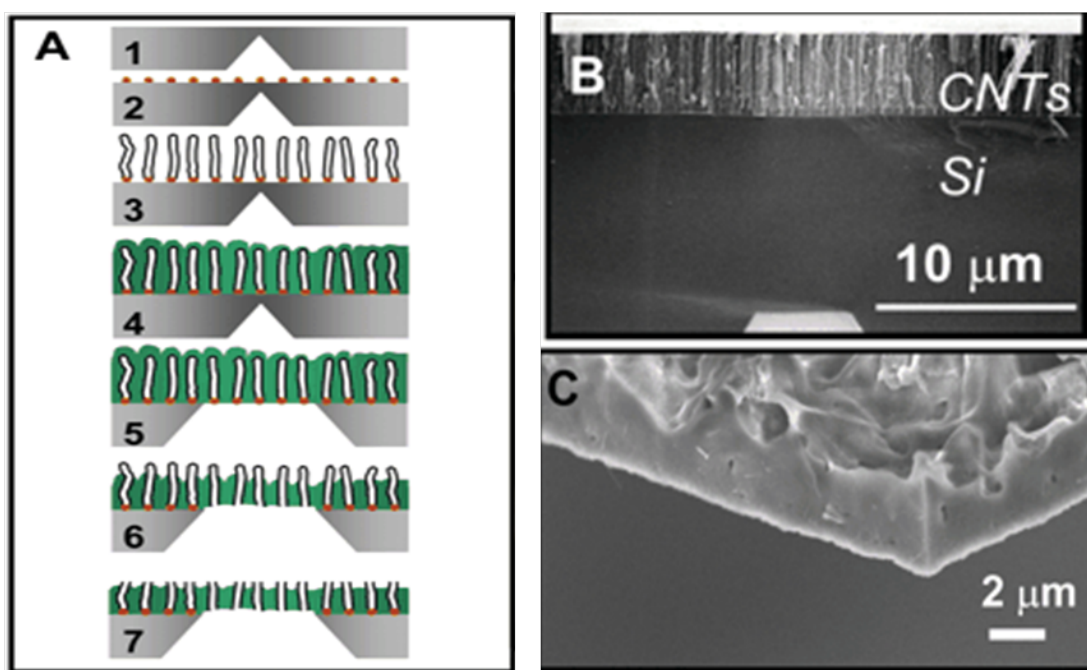


Figure 1- 13. Schematic of the fabrication process steps starting from the substrate step (1) to the last step (7), (B) SEM cross-section of the as-grown DWNTs, (C) SEM cross-section of the membrane, illustrating excellent gap filling by silicon nitride [85].

Testing of the membrane showed the flow to be three to four orders of magnitude higher than the theoretical calculation [85]. Ion rejection was studied via transport of ions of various valencies through negatively charged groups at the openings of the plasma treated carbon nanotubes. The ion exclusion was dominated by electrostatic interactions (Donnan exclusion) between fixed membrane charges and mobile ions, rather than steric effects. Unfortunately, the result showed insufficient ion rejection for desalination [86].

In 2008, water transport through template-grown carbon nanopipes about 44 nm in diameter assembled using a non-catalytic CVD process was reported. Structural imperfections such as branching, tortuosity and pore misalignment were avoided by the presence of the template. The flow factor enhancement over the predicted value was about 20 [2, 87].

Ion rejection for aligned carbon nanotubes was also investigated by Majumder's group. Two methods demonstrate the selectivity of different ion species, namely alteration of pore size by CNTs tip-functionalisation and voltage based gate control. These methods have demonstrated the potential of altering pore properties to enhance selectivity [88, 89].

The previous attempts to fabricate CNTs with polymers to obtain an effective desalination membrane included multiple complex steps, such as catalytic growth of CNTs onto expensive substrates, polymer filling of the inter-tube spaces, substrate removal and CNTs tip opening via etching. Moreover, the size distribution of CNTs diameters is still not small enough to complement the simulation studies performed [2]. To overcome these issues, in a patent, Ratto et al. disclosed the blending of CNTs into cross-linking agent solutions such as trimesoyl or isophthalic chlorides, to formulate a composite polymeric membrane. The CNTs need to be functionalised with octadecylamine to improve solubility in organic solvents. In this way, CNTs were effectively embedded into the active layer, which is formed on a micro-porous polyethersulfone support by conventional interfacial polymerisation, as illustrated in Figure 1-14 [90].

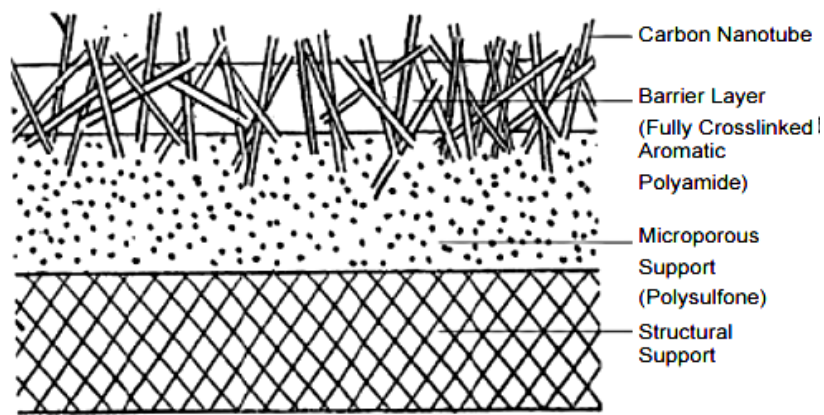


Figure 1-14. Schematic cross-section of CNTs embedded in TFC membrane [90].

This membrane can easily be adapted into current filtration and RO systems. Water filtration occurs through both the conventional polymeric layer and the embedded CNTs pathways. Test results showed enhancement of the properties of the fabricated membrane with embedded CNTs, compared with a non-fabricated CNTs embedded membrane. The water flux increased by nearly double, from $26 \text{ L m}^{-2} \text{ day}^{-1} \text{ bar}^{-1}$ to $44 \text{ L m}^{-2} \text{ day}^{-1} \text{ bar}^{-1}$, while salt rejection rose slightly from 96.19% to 97.69% [2, 90].

This patent presents a new approach applicable for fabricating the polyamide membrane with CNTs. Transport of CNTs and separation of the polyamide membrane were combined in a producible nanocomposite membrane.

Due to the potential importance of CNTs applications in water desalination, the structure and properties of CNTs will be addressed in the following section.

There are several challenges related to embedding of CNTs in polyamide membrane. These challenges lead to unfavourable results occurring when CNTs are included in interfacial polymerisation process. One of these challenges is the agglomeration which is attributed to the low dispersion of CNTs in solutions. The agglomeration of CNTs makes them unable to uniformly spread out through the membrane. Most of published research has preferred to disperse CNTs in aqueous phase due to the difficulties of dispersion in organic phase. However, the removal of excessive aqueous phase (during the membrane preparation) by applying a rubber roller on the support layer surface causes a removal of large amount of CNTs together with the amine solution (aqueous phases). Another challenge is the lack of chemical interaction between CNTs and the polyamide membrane causing a potential leaching out of the membrane during the filtration process.

In order to overcome these challenges, CNTs should be dispersed in the organic phase to avoid a removal of large amount of CNTs together with the excessive aqueous phase and chemically bonded to the polyamide membrane. Therefore, CNTs should be surface-modified in order to improve the dispersion quality in organic phase and create chemical bonding with polyamide membrane.

1.4 Carbon nanotubes (CNTs)

Carbon is one of the most significant applied elements, forming more compounds than any other element. In fact, the classification of carbon is non-metallic in the periodic table of elements, and it can bond in different ways to form four allotrope structures [91]. There were only two forms of carbon-crystalline materials known, graphite and diamond, until the late twentieth century [91].

Diamond crystals are formed under high temperature and pressure, and have a cubic crystal system. The isomer structures consist of a 'spatial network of tetrahedral, covalently-bonded carbon atoms'. These structures are linked by sp^3 -bonded (sp^3 hybridised) atoms. Co-ordination of the four valence electrons in carbon crystals is completely satisfied in all dimensions, making diamonds isotropically strong [92].

Graphite, which is formed under low pressure and temperature, has a structure consisting of planar sheets with hexagonal, honeycombed networks of carbon atoms. These atoms are sp^2 hybridised, and just three out of the four valence electrons are bonded covalently between neighbours in a planar sheet. The fourth electron is a mobile π -electron. The resulting material is conductive, with strong bonding in the plane and weak bonding between layers called ‘van der Waals bonds’ [92, 93]. Graphite, therefore, is weak between its planes, and is known to be a soft material because of its capability to slide along the basal planes [92].

The belief that there were only two carbon-crystalline allotropes was shattered in 1985. A group of scientists at Rice University discovered closed, cage-like carbon molecules – in other words closed-shell, all-carbon molecules subsequently called fullerenes, of which the football-shaped C_{60} is the most well-known [94]. After the discovery of fullerene, there was a deluge of research studies characterising different types of fullerenes produced through the electric-arc method, thus creating synthetic fullerenes.

Advances in Transmission Electron Microscopy (TEM) resulted in the recognition of different carbon cluster structures. In 1991, these experiments resulted in the discovery – totally by accident – of carbon nanotubes by Sumio Iijima. The carbon nanotubes were a by-product found at the cathode during electric-arc experiments to produce C_{60} molecules. The carbon nanotube structure can be imagined as an elongated fullerene molecule. The geometry of CNTs structures consists of 12 pentagons and millions of hexagons bound by two members of the fullerenes at the ends [95].

CNTs are frequently depicted as cylindrical sheets of graphene closed at either end with a hemisphere of fullerene, which shows that, at some point during the growth process, nucleation of pentagon rings occurs to initiate the closing mechanism [92, 95]. As seen in Figure 1-15, based on the direction of rolling up the graphene sheet relative to its diameter and helical geometry, the resultant carbon nanotubes can be either metallic or semiconducting, which can be distinguished depending on the difference in energy configuration.

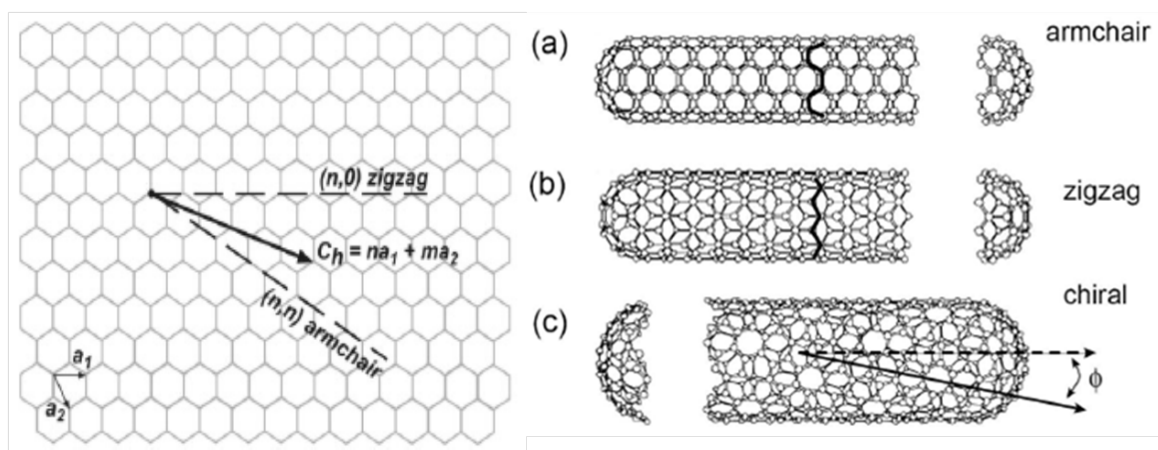


Figure 1-15. (left) Graphene sheet demonstrating how the chiral vector is described, (right) armchair, zigzag and helical carbon nanotube structures [96, 97].

CNTs can be present as either single isolated tubes, called Single Wall Carbon Nanotubes (SWNTs), or as a series of concentric nanotubes. The latter are known as either Double Wall Carbon Nanotubes for two concentric CNTs (DWNTs), or Multi-Wall Carbon Nanotubes (MWNTs) for nanotubes with greater numbers of concentric tubes, as seen in Figure 1-16 [92, 96, 98].

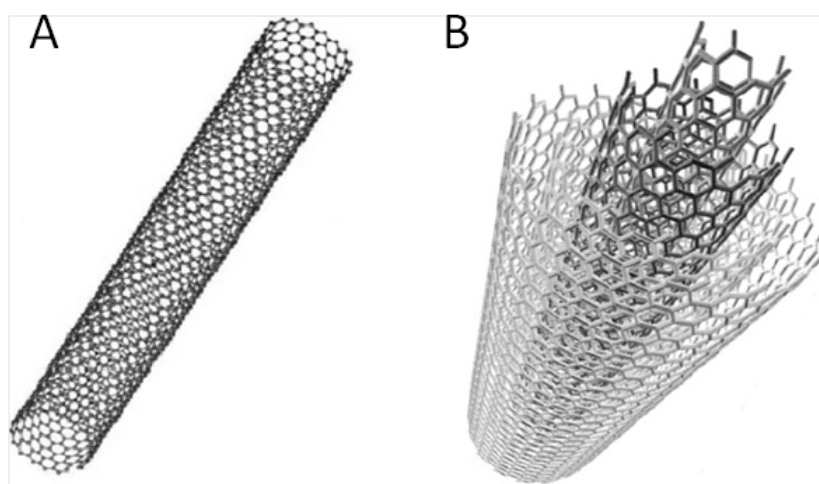


Figure 1-16. (A) a single-wall carbon nanotube (SWNTs) and (B) a multi-wall carbon nanotube (MWNTs) [96].

Carbon nanotube technology has been one of the most studied subjects since its 1991 discovery. In the field of nanotechnology, widespread research continues on utilising their exceptional – and unique – physical, optical, electrical and therapeutic properties for biomaterial substances [95].

1.4.1 Functionalisation of carbon nanotubes

Carbon nanotubes need to be functionalised to improve their distribution in the polymer used to construct the water purification membrane. This functionalisation can be divided into two main subdivisions depending on whether covalent or non-covalent bonding occurs between the CNTs and the polymer.

Non-covalent chemical bonding, the first functionalisation type, is a physical adsorption and/or wrapping of polymers to the surface of carbon nanotubes as illustrated in Figure 1-17 [99-103]. This adsorption is attributed to π -stacking interactions and van der Waals forces [104] with conjugated polymers, due to organic polymers containing heteroatoms with a free electron pair [105].

The main advantage of this kind of CNTs functionalisation is that the conjugated system of the CNTs side walls will be not destroyed [106]. Consequently, the final structure will have the same properties as the original material [104, 105].

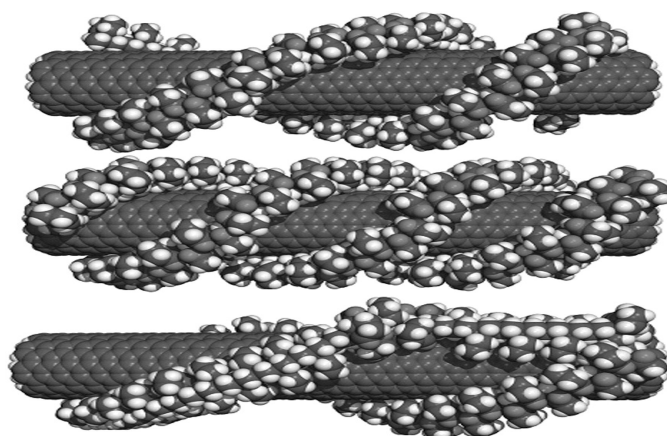


Figure 1-17. Some possible wrapping arrangements of a polymer on CNTs - a double helix (top) and a triple helix (middle) and multiple parallel wrapping strands (bottom) [99].

The second functionalisation is the covalent chemical bonding (grafting) of polymer chains to CNTs. A strong chemical bond between CNTs and polymers is established in this type of modification. In covalent functionalisation, there are two fundamental methodologies, depending on polymer chains attached on the carbon nanotube surface. The ‘grafting to’ approach is the first method that involves synthesis of a polymer with a specific molecular weight terminated with reactive groups or radical precursors. As a result, the attachment of polymer chains to the surface of nanotubes occurs through a substitution reaction. This method has encountered some issues, so polymer grafting

to the CNTs surface is not often used. The high steric hindrance, and relatively low reactivity of macromolecules are the main disadvantages of this method [104]. Figure 1-18 shows a schematic illustration of the ‘grafting to’ approach.

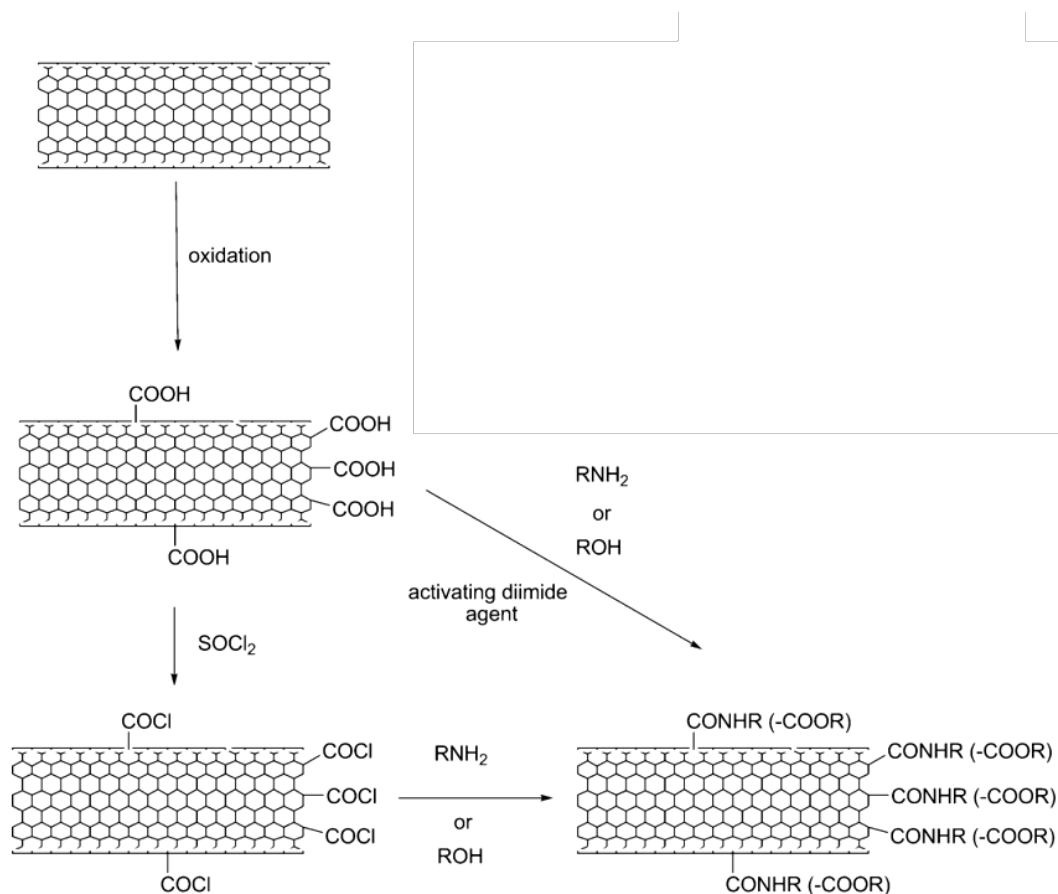


Figure 1-18. Oxidation of CNTs and derivatisation reaction with amines or alcohols [105].

‘Grafting from’ is the second method of covalent modification. In this approach, the polymer grows from the nanotube surface via *in situ* polymerisation of monomers that is initiated by chemical species immobilised on the sidewalls and the edges of CNTs. Figure 1-19 illustrates an example of this approach. This kind of polymerisation is called surface-initiated polymerisation. In comparison with the ‘grafting to’ approach, this method utilises the higher reactivity of monomers that makes efficient, controllable, designable, and tailored grafting feasible [104, 105].

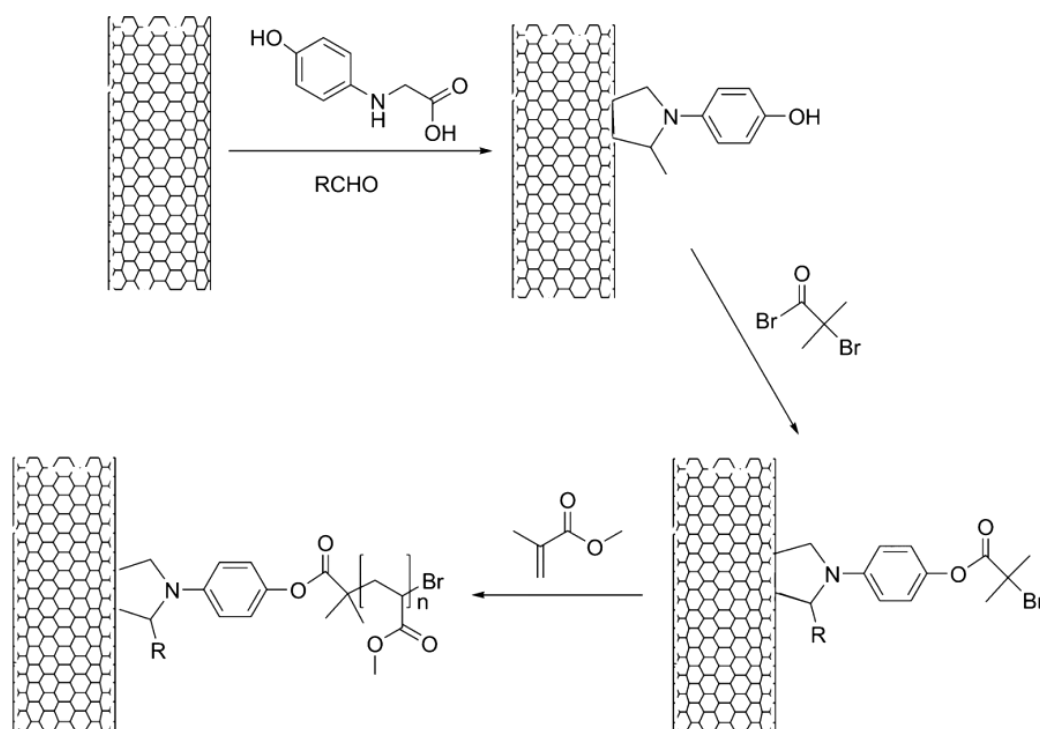


Figure 1-19. ATRP ‘grafting from’ functionalisation approach of carbon nanotubes[105].

1.4.2 Carbon nanotubes functionalisation and model reactions

Polyacene molecules such as anthracene, tetracene and pentacene can be used to mimic the side wall of CNTs, due to the similarity in their aromatic structure. CNTs are depicted as a cylindrical sheet of graphene [107, 108], which is a single layer of sp^2 carbon atoms densely packed in a honeycomb crystal lattice [109-112]. Georgin and his co-workers used anthracene-9-carboxylic acid as a model substrate to mimic the aromatic network of MWNTs [113]. For biological applications, the ^{14}C -labelling of MWNTs process and conditions were investigated by using anthracene-9-carboxylic acid as a model substrate, as seen in Figure 1- 20. They applied the same process and conditions to MWNTs, and ^{14}C -labelled MWNTs, as an active radiology material, were successfully obtained [113].

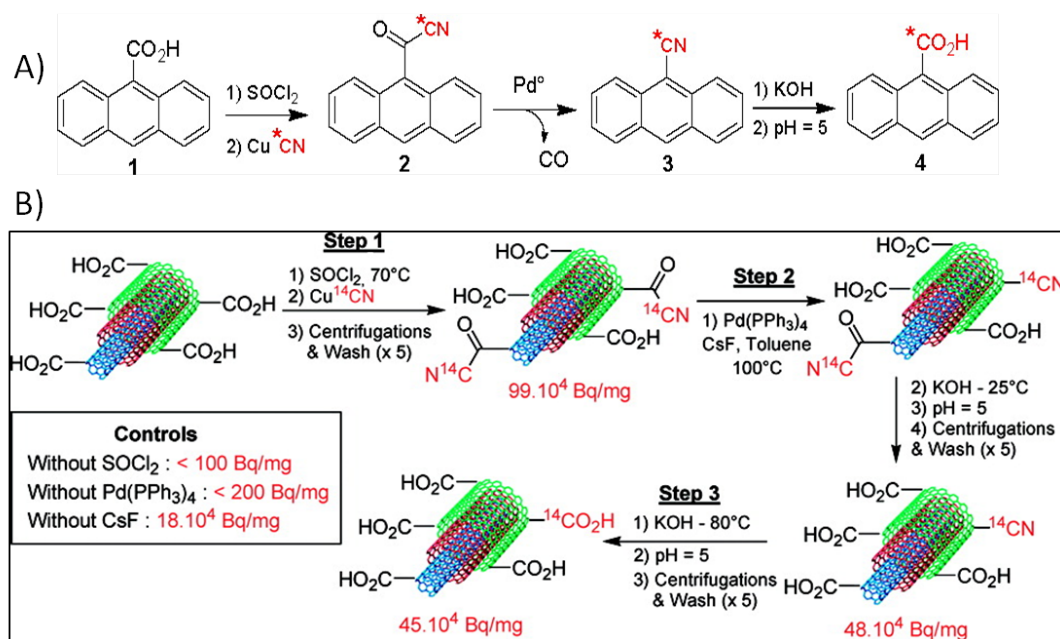


Figure 1- 20. (A) Anthracene-9-carboxylic acid was used as a model substrate for the development of the labelling process, (B) The process of ^{14}C -labelled MWNTs showing radiology activity [113].

In this project, in order to improve the distribution of SWNTs in the polyamide layer of a desalination membrane, SWNTs were functionalised with different aliphatic linear diamines. The aliphatic chain lengths of the diamines were two, four, six and eight carbon atoms. The length of the chain affected the reaction yield, which therefore affected the quantity of the molecules grafted to the SWNTs. As a consequence, the distribution of SWNTs in the polymer could be affected. A model reaction was used to investigate the chain length effect on the reaction, using anthracene-9-carboxylic acid as the mimicing substrate of the acid treated SWNTs. Figure 1- 21 illustrates the analogous amidation reaction process for both SWNTs and anthracene-9-carboxylic acid. The amine group in the aliphatic molecules and the carboxylic acid group were reacted through the amidation reaction. The reactions were performed by using HATU as the coupling reagent in the presence of DIPEA as a base, and the solvent was DMF.

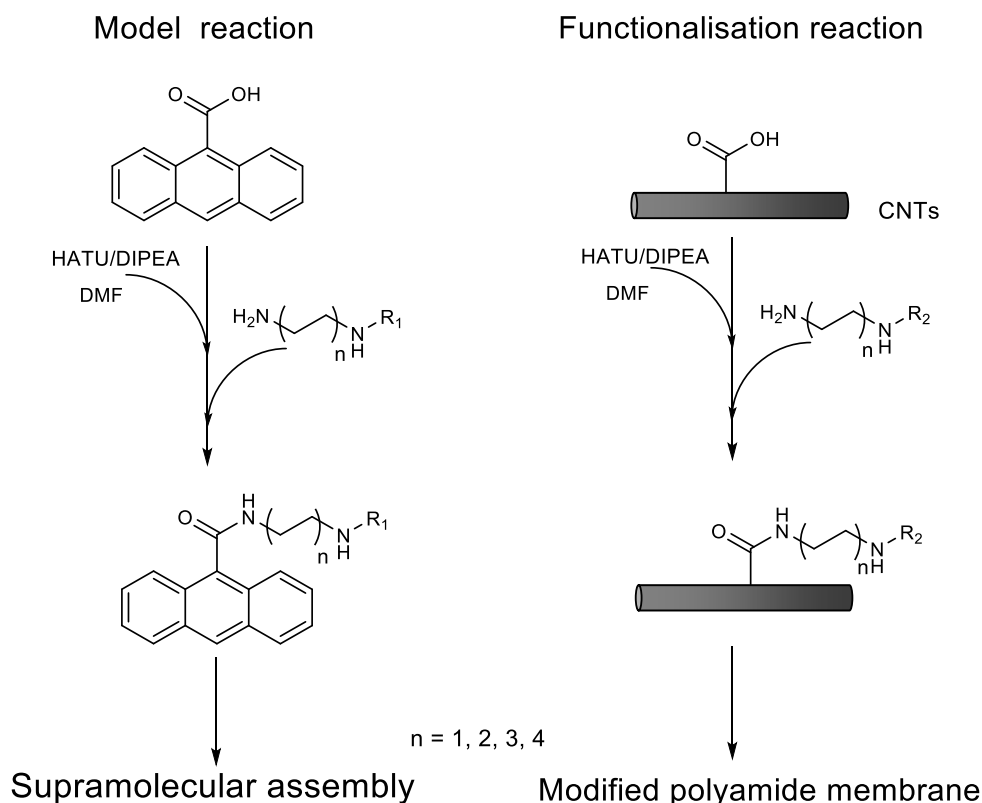


Figure 1- 21. Schematic representing the amidation reaction for SWNTs and anthracene-9-carboxylic acid with amine group in the aliphatic molecules using HATU and DIPEA base in DMF solvent.

Despite the model reactions being performed in identical conditions, the quantity yields were not equal. The yield of the short-chain molecule with two carbon atoms was 98%, while the other yields were 86%, 75% and 65% for molecules with four, six and eight carbon atom chain lengths respectively (see Chapter III, section 3.5). It was observed that the reactivity of the amine group decreases with chain length increase. This observation led to the expectation that the quantity of molecules grafted to the SWNTs will not be equal even under identical reaction conditions. Accordingly, the long-chain molecule will be grafted to SWNTs in lower quantities than the short-chain molecule. Therefore, the functionality of SWNTs will be lower with the long-chain molecule than the short-chain molecule, and distribution in the polyamide membrane could be reduced as well.

It was worth exploiting the model reaction products to form a supramolecular assembly. The synthesis of supramolecular assemblies was obtained by reacting model reaction amine products with benzene-1,3,5-tricarboxylic acid chloride (trimesoyl chloride, TMC) to produce BTA derivatives. Benzene-1,3,5-tricarboxamide (BTA)

derivatives as supramolecular motifs are capable of self-assembly through hydrogen bonding forming a supramolecular assembly.

1.5 Thesis objectives

- 1- Modified the polyamide membrane by adding SWNTs which will be dispersed in organic phase during the interfacial polymerisation process.
- 2- The functionalization reactions of SWNTs will be mimicked by using anthracene-9-carboxylic acid as a model of the aromatic wall of SWNTs.
- 3- The produced compounds from the model reactions will be exploited to prepare BTA compounds. The ability of BTA compounds to assemble themselves in chloroform and form supramolecule will be investigated.
- 4- The modified membrane will be characterised and investigate the imbedded of SWNTs in the polyamide membrane.
- 5- The membrane performance (flux and salt rejection) will be tested before and after loading the modified membrane with different amount of SWNTs.

1.6 Thesis outline

Water desalination is a promising source of fresh water for the future, especially with the high rate of water consumption. Thus, the thesis project was designed to contribute to the global effort to address the water shortage issue.

Reverse osmosis (RO) technology was chosen due to the low cost and ease of setup in comparison to other desalination technologies. In order to improve RO efficiency and reduce its energy consumption, the RO membrane was subjected to different changes to achieve this objective. Nanotechnology is a promising method of improving RO membranes through the synthesis of nanomaterials with unique and exceptional properties. Carbon nanotubes (CNTs) are amongst the nanomaterials possessing great ability for water transportation and promising separation capability.

In this project, an RO membrane was modified by embedding single wall carbon nanotubes (SWNTs) into the polyamide membrane. Functionalisation of SWNTs was needed to improve the distribution of SWNTs in the polyamide membrane. The model substrate was used to study the functionalisation reaction of SWNTs. The results of the model substrate reactions were invested into the formation of supramolecular

structures. The resultant amines were reacted with benzene-1,3,5-tricarboxylic acid chloride (TMC) to synthesise benzene-1,3,5-tricarboxamide (BTA) derivatives as supramolecular motifs.

The materials produced in this project were characterised by various instruments. The essential theory behind each instrument is briefly described in Chapter II. The starting materials and solvents are also described in this Chapter.

In Chapter III, the supramolecular structure synthesis and characterisation are presented. Four molecules were synthesised with differences in the aliphatic chain length. Interestingly, the supramolecular structures were formed through the self-assembly process with different self-assembled shapes, which was attributed to the chain length differences. Thus, the self-assembly process was investigated for the shortest and longest aliphatic chain molecules among the synthesised molecules. Their self-assembly was investigated by monitoring the change in fluorescence, FT-IR and SEM as a function of time.

Water desalination is presented in Chapter IV. Functionalisation of SWNTs was performed in order to improve the SWNTs distribution in the polyamide membrane. Interfacial polymerisation was the method used to synthesise the polyamide membrane. The functionalised SWNTs were dispersed in the organic phase prior to the polymerisation. SWNTs were functionalised with two molecules containing different aliphatic chain lengths to investigate the influence of the chain length on the distribution of the SWNTs in the membrane polymer which as consequence affect RO efficiency. Characterisation of functionalised SWNTs and the modified polymer was done using Raman, FT-IR, AFM and SEM. Membrane performance was tested by water flux and salt rejection measurements. Further investigation of the chain length influence was obtained through the model reaction. Anthracene-9-carboxylic acid was used as a model reaction molecule to mimic the SWNTs. The model membranes were synthesised by using the model reaction molecule derivatives. The flux and salt rejection of the model membranes were measured.

Chapter V summarises the findings from this project. As a result of these findings, future investigations are recommended. A number of projects are suggested based on the findings.

1.7 References

1. Seitz, J.L., *Globale Issues*. 2008.
2. Lee, K.P., T.C. Arnot, and D. Mattia, *A Review of Reverse Osmosis Membrane Materials for Desalination-Development to Date and Future Potential*. Journal of Membrane Science. **370**(1-2): p. 1-22.
3. Seitz, J.L., *Global issues: an introduction*. 2007: Wiley-Blackwell.
4. Löwenberg, J., J.A. Baum, Y.-S. Zimmermann, C. Groot, W. van den Broek, and T. Wintgens, *Comparison of Pre-treatment Technologies Towards Improving Reverse Osmosis Desalination of Cooling Tower Blow Down*. Desalination, 2015. **357**: p. 140-149.
5. El-Dessouky, H. and H. Ettouney, *Teaching Desalination-A Multidiscipline Engineering Science*. Heat Transfer Engineering, 2002. **23**(5): p. 1-3.
6. Miller, J.E., *Review of Water Resources and Desalination Technologies*. Sandia National Labs Unlimited Release Report SAND-2003-0800, 2003.
7. Shiklomanov, I.A. and J.C. Rodda, *World Water Resources at the Beginning of the Twenty-First Century*. 2004: Cambridge University Press.
8. Fritzmann, C., J. Löwenberg, T. Wintgens, and T. Melin, *State-of-the-art of Reverse Osmosis Desalination*. Desalination, 2007. **216**(1-3): p. 1-76.
9. Shiklomanov, I.A., *World Water Resources*. A new appraisal and assessment for the 21st century, 1998.
10. Shannon, M.A., P.W. Bohn, M. Elimelech, J.G. Georgiadis, B.J. Marinas, and A.M. Mayes, *Science and Technology for Water Purification in the Coming Decades*. Nature, 2008. **452**(7185): p. 301-310.
11. Li, D. and H. Wang, *Recent Developments in Reverse Osmosis Desalination Membranes*. Journal of Materials Chemistry. **20**(22): p. 4551-4566.
12. Darwish, M.A. and H. El-Dessouky, *The Heat Recovery Thermal Vapour-Compression Desalting System: A Comparison With Other Thermal Desalination Processes*. Applied Thermal Engineering, 1996. **16**(6): p. 523-537.
13. Almulla, A., A. Hamad, and M. Gadalla, *Integrating Hybrid Systems With Existing Thermal Desalinationplants*. Desalination, 2005. **174**(2): p. 171-192.
14. Van der Bruggen, B. and C. Vandecasteele, *Distillation vs. Membrane Filtration: Overview of Process Evolutions in Seawater Desalination*. Desalination, 2002. **143**(3): p. 207-218.
15. Humplik, T., J. Lee, S. O'hern, B. Fellman, M. Baig, S. Hassan, M. Atieh, F. Rahman, T. Laoui, and R. Karnik, *Nanostructured Materials for Water Desalination*. Nanotechnology, 2011. **22**(29): p. 292001.
16. Greenlee, L.F., D.F. Lawler, B.D. Freeman, B. Marrot, and P. Moulin, *Reverse Osmosis Desalination: Water Sources, Technology, and Today's Challenges*. Water Research, 2009. **43**(9): p. 2317-2348.
17. Qasim, M., N.A. Darwish, S. Sarp, and N. Hilal, *Water Desalination by Forward (direct) Osmosis Phenomenon: A Comprehensive Review*. Desalination, 2015. **374**: p. 47-69.
18. Cath, T.Y., A.E. Childress, and M. Elimelech, *Forward osmosis: Principles, Applications, and Recent Developments*. Journal of Membrane Science, 2006. **281**(1-2): p. 70-87.
19. Zhang, C., *Sub-nanometer Porous Membrane Based on Cyclic Peptide-Polymer Conjugate and Block Copolymer*. 2015.
20. Kucera, J., *Reverse Osmosis: Design, Processes, and Applications for Engineers*.

- 2015: John Wiley & Sons.
21. Voicu, S.I., *Pharmaceutical Applications of Polymeric Membranes*. Handbook of Polymers for Pharmaceutical Technologies: Processing and Applications, Volume 2, 2015: p. 173-194.
 22. Koltuniewicz, A. and E. Drioli, *Membranes in Clean Technologies*. 2008: WILEY-VCH.
 23. McCutcheon, J.R., R.L. McGinnis, and M. Elimelech, *Desalination by Ammonia-carbon Dioxide Forward Osmosis: Influence of Draw and Feed Solution Concentrations on Process Performance*. Journal of Membrane Science, 2006. **278**(1-2): p. 114-123.
 24. Xie, M., J. Lee, L.D. Nghiem, and M. Elimelech, *Role of Pressure in Organic Fouling in Forward Osmosis and Reverse Osmosis*. Journal of Membrane Science, 2015. **493**: p. 748-754.
 25. Duan, J., Y. Pan, F. Pacheco, E. Litwiller, Z. Lai, and I. Pinnau, *High-performance Polyamide Thin-Film-Nanocomposite Reverse Osmosis Membranes Containing Hydrophobic Zeolitic Imidazolate Framework-8*. Journal of Membrane Science, 2015. **476**: p. 303-310.
 26. Baker, R.W., *Membrane Technology and Applications*. Second Edition ed. 2004, England: McGraw-Hill.
 27. Yang, Y., J.J. Pignatello, J. Ma, and W.A. Mitch, *Effect of Matrix Components on UV/H₂O₂ and UV/S₂O₈²⁻ Advanced Oxidation Processes for Trace Organic Degradation in Reverse Osmosis Brines From Municipal Wastewater Reuse Facilities*. Water research, 2016. **89**: p. 192-200.
 28. Kazner, C., S. Jamil, S. Phuntsho, H. Shon, T. Wintgens, and S. Vigneswaran, *Forward Osmosis for the Treatment of Reverse Osmosis Concentrate from Water Reclamation: Process Performance and Fouling Control*. Water Science & Technology, 2014. **69**(12).
 29. Pappenheimer, J.R. and A. Soto-Rivera, *Effective Osmotic Pressure of the Plasma Proteins and Other Quantities Associated with the Capillary Circulation in the Hindlimbs of Cats and Dogs*. American Journal of Physiology--Legacy Content, 1948. **152**(3): p. 471-491.
 30. Fiscus, E.L., *The Interaction Between Osmotic and Pressure Induced Water Flow in Plant Roots*. Plant Physiology, 1975. **55**(5): p. 917-922.
 31. Alexander, S., P. Chaikin, P. Grant, G. Morales, P. Pincus, and D. Hone, *Charge Renormalization, Osmotic Pressure, and Bulk Modulus of Colloidal Crystals: Theory*. The Journal of chemical physics, 1984. **80**(11): p. 5776-5781.
 32. Soltanieh, M. and W.N. GILL', *Review of Reverse Osmosis Membranes and Transport Models*. Chemical Engineering Communications, 1981. **12**(4-6): p. 279-363.
 33. Roh, I.J., J.-J. Kim, and S.Y. Park, *Mechanical Properties and Reverse Osmosis Performance of Interfacially Polymerized Polyamide Thin Films*. Journal of Membrane Science, 2002. **197**(1-2): p. 199-210.
 34. Shen, J. and A. Schäfer, *Removal of Fluoride and Uranium by Nanofiltration and Reverse Osmosis: A review*. Chemosphere, 2014. **117**: p. 679-691.
 35. Fujioka, T., N. Oshima, R. Suzuki, W.E. Price, and L.D. Nghiem, *Probing the Internal Structure of Reverse Osmosis Membranes by Positron Annihilation Spectroscopy: Gaining More Insight into the Transport of Water and Small Solutes*. Journal of Membrane Science, 2015. **486**: p. 106-118.
 36. Sherwood, T.K., P.L.T. Brian, and R.E. Fisher, *Desalination by Revers Osmosis*. Ind. Eng. Chem. Fundamen, 1967. **6**(1): p. 2-12.

37. Smit, E., M.H.V. Mulder, C.A. Smolders, H. Karrebeld, J. Eerden van, and D. Feil, *Modelling of the Diffusion of Carbon Dioxide in Polyimide Matrices by Computer Simulation*. Journal of Membrane Science, 1992. **73**(2-3): p. 247-257.
38. Huang, S.-H., C.-J. Hsu, D.-J. Liaw, C.-C. Hu, K.-R. Lee, and J.-Y. Lai, *Effect of Chemical Structures of Amines on Physicochemical Properties of Active Layers and Dehydration of Isopropanol Through Interfacially Polymerized Thin-film Composite Membranes*. Journal of Membrane Science, 2008. **307**(1): p. 73-81.
39. Lee, H.S., S.J. Im, J.H. Kim, H.J. Kim, J.P. Kim, and B.R. Min, *Polyamide Thin-film Nanofiltration Membranes Containing TiO₂ Nanoparticles*. Desalination, 2008. **219**(1-3): p. 48-56.
40. Lohokare, H.R., Y.S. Bhole, and U.K. Kharul, *Effect of Support Material on Ultrafiltration Membrane Performance*. Journal of Applied Polymer Science, 2006. **99**(6): p. 3389-3395.
41. Benavente, J., M. Oleinikova, M. Muñoz, and M. Valiente, *Characterization of Novel Activated Composite Membranes by Impedance Spectroscopy*. Journal of electroanalytical chemistry, 1998. **451**(1-2): p. 173-180.
42. Kavon. *Holytex Nonwovens*. Available from: <http://www.kavonfilter.com/contact.html>.
43. Porter, M.C., *Handbook of Industrial Membrane Technology*. 1990: William Andrew Publishing.
44. Ghosh, A.K. and E.M.V. Hoek, *Impacts of Support Membrane Structure and Chemistry on Polyamide–Polysulfone Interfacial Composite Membranes*. Journal of Membrane Science, 2009. **336**(1-2): p. 140-148.
45. Kim, H.I. and S.S. Kim, *Fabrication of Reverse Osmosis Membrane via Low Temperature Plasma Polymerization*. Journal of Membrane Science, 2001. **190**(1): p. 21-33.
46. Prakash Rao, A., N.V. Desai, and R. Rangarajan, *Interfacially Synthesized Thin Film Composite RO Membranes for Seawater Desalination*. Journal of Membrane Science, 1997. **124**(2): p. 263-272.
47. Kim, H.I. and S.S. Kim, *Plasma Treatment of Polypropylene and Polysulfone Supports for Thin Film Composite Reverse Osmosis Membrane*. Journal of Membrane Science, 2006. **286**(1-2): p. 193-201.
48. Cadotte, J.E., R.J. Petersen, R.E. Larson, and E.E. Erickson, *A New Thin-Film Composite Seawater Reverse Osmosis Membrane*. Desalination, 1980. **32**(0): p. 25-31.
49. Xu, Z., S. Ye, G. Zhang, W. Li, C. Gao, C. Shen, and Q. Meng, *Antimicrobial Polysulfone Blended Ultrafiltration Membranes Prepared with Ag/Cu₂O Hybrid Nanowires*. Journal of Membrane Science, 2016. **509**: p. 83-93.
50. Takeshi, M., *Progress in Membrane Science and Technology for Seawater Desalination — A Review*. Desalination, 2001. **134**(1-3): p. 47-54.
51. Petersen, R.J., *Composite Reverse Osmosis and Nanofiltration Membranes*. Journal of Membrane Science, 1993. **83**(1): p. 81-150.
52. Cadotte, J.E., R.S. King, R.J. Majerle, and R.J. Petersen, *Interfacial Synthesis in the Preparation of Reverse Osmosis Membranes*. Journal of Macromolecular Science: Part A - Chemistry, 1981. **15**(5): p. 727-755.
53. Kim, H.J., Y. Baek, K. Choi, D.-G. Kim, H. Kang, Y.-S. Choi, J. Yoon, and J.-C. Lee, *The Improvement of Antibiofouling Properties of A Reverse Osmosis Membrane by Oxidized CNTs*. RSC Advances, 2014. **4**(62): p. 32802-32810.

54. Ang, W.L., A.W. Mohammad, N. Hilal, and C.P. Leo, *A Review on the Applicability of Integrated/Hybrid Membrane Processes in Water Treatment and Desalination Plants*. Desalination, 2015. **363**: p. 2-18.
55. Byrne, P., L. Fournaison, A. Delahaye, Y. Ait Oumeziane, L. Serres, P. Loulergue, A. Szymczyk, D. Mugnier, J.-L. Malaval, R. Bourdais, H. Gueguen, O. Sow, J. Orfi, and T. Mare, *A Review on the Coupling of Cooling, Desalination and Solar Photovoltaic Systems*. Renewable and Sustainable Energy Reviews, 2015. **47**: p. 703-717.
56. Kargari, A. and M.M.A. Shirazi, *Water desalination: Solar-Assisted Membrane Distillation*, in *Encyclopedia of Energy Engineering and Technology*. 2014, CRC Press.
57. Kim, J.H., E.J. Moon, and C.K. Kim, *Composite Membranes Prepared From Poly(m-animostyrene-co-vinyl alcohol) Copolymers for the Reverse Osmosis Process*. Journal of Membrane Science, 2003. **216**(1-2): p. 107-120.
58. Saha, N.K. and S.V. Joshi, *Performance Evaluation of Thin Film Composite Polyamide Nanofiltration Membrane with Variation in Monomer Type*. Journal of Membrane Science, 2009. **342**(1-2): p. 60-69.
59. Kim, C.K., J.H. Kim, I.J. Roh, and J.J. Kim, *The Changes of Membrane Performance with Polyamide Molecular Structure in the Reverse Osmosis Process*. Journal of Membrane Science, 2000. **165**(2): p. 189-199.
60. Lau, W.J., A.F. Ismail, N. Misdan, and M.A. Kassim, *A Recent Progress in Thin Film Composite Membrane: A Review*. Desalination. In Press, Corrected Proof.
61. Chen, G., S. Li, X. Zhang, and S. Zhang, *Novel Thin-film Composite Membranes with Improved Water Flux From Sulfonated Cardo Poly(arylene ether sulfone) Bearing Pendant Amino groups*. Journal of Membrane Science, 2008. **310**(1-2): p. 102-109.
62. Chen, G., S. Li, X. Zhang, and S. Zhang, *Novel Thin-film Composite Membranes with Improved Water Flux From Sulfonated Cardo Poly(arylene ether sulfone) Bearing Pendant Amino Groups*. Journal of Membrane Science, 2008. **310**(1-2): p. 102-109.
63. Duan, M., Z. Wang, J. Xu, J. Wang, and S. Wang, *Influence of Hexamethyl Phosphoramide on Polyamide Composite Reverse Osmosis Membrane Performance*. Separation and Purification Technology, 2010. **75**(2): p. 145-155.
64. Ghosh, A.K., B.-H. Jeong, X. Huang, and E.M.V. Hoek, *Impacts of Reaction and Curing Conditions on Polyamide Composite Reverse Osmosis Membrane Properties*. Journal of Membrane Science, 2008. **311**(1-2): p. 34-45.
65. Saha, N.K. and S.V. Joshi, *Performance Evaluation of Thin Film Composite Polyamide Nanofiltration Membrane with Variation in Monomer Type*. Journal of Membrane Science, 2009. **342**(1-2): p. 60-69.
66. Yang, F., S. Zhang, D. Yang, and X. Jian, *Preparation and Characterization of Polypiperazine Amide/PPESK Hollow Fiber Composite Nanofiltration Membrane*. Journal of Membrane Science, 2007. **301**(1-2): p. 85-92.
67. Liu, M., S. Yu, J. Tao, and C. Gao, *Preparation, Structure Characteristics and Separation Properties of Thin-Film Composite Polyamide-Urethane Seawater Reverse Osmosis Membrane*. Journal of Membrane Science, 2008. **325**(2): p. 947-956.
68. Qiu, S., L. Wu, L. Zhang, H. Chen, and C. Gao, *Preparation of Reverse Osmosis Composite Membrane with High Flux by Interfacial Polymerization of MPD and TMC*. Journal of Applied Polymer Science, 2009. **112**(4): p. 2066-2072.

69. Lind, M.L., A.K. Ghosh, A. Jawor, X. Huang, W. Hou, Y. Yang, and E.M. Hoek, *Influence of Zeolite Crystal Size on Zeolite-polyamide Thin Film Nanocomposite Membranes*. Langmuir, 2009. **25**(17): p. 10139-10145.
70. Lind, M.L., B.H. Jeong, A. Subramani, X. Huang, and E. Hoek, *Effect of Mobile Cation on Zeolite-polyamide Thin Film Nanocomposite Membranes*. Journal of Materials Research, 2009. **24**(05): p. 1624-1631.
71. Singh, P.S. and V.K. Aswal, *Characterization of Physical Structure of Silica Nanoparticles Encapsulated in Polymeric Structure of Polyamide Films*. Journal of Colloid and Interface Science, 2008. **326**(1): p. 176-185.
72. Jadav, G.L. and P.S. Singh, *Synthesis of Novel Silica-polyamide Nanocomposite Membrane with Enhanced Properties*. Journal of Membrane Science, 2009. **328**(1-2): p. 257-267.
73. Lee, S.Y., H.J. Kim, R. Patel, S.J. Im, J.H. Kim, and B.R. Min, *Silver Nanoparticles Immobilized on Thin Film Composite Polyamide Membrane: Characterization, Nanofiltration, Antifouling Properties*. Polymers for Advanced Technologies, 2007. **18**(7): p. 562-568.
74. Kim, S.H., S.-Y. Kwak, B.-H. Sohn, and T.H. Park, *Design of TiO₂ Nanoparticle Self-assembled Aromatic Polyamide Thin-film-composite (TFC) Membrane as an Approach to Solve Biofouling Problem*. Journal of Membrane Science, 2003. **211**(1): p. 157-165.
75. Kwak, S.-Y., S.H. Kim, and S.S. Kim, *Hybrid Organic/Inorganic Reverse Osmosis (RO) Membrane for Bactericidal Anti-Fouling. 1. Preparation and Characterization of TiO₂ Nanoparticle Self-Assembled Aromatic Polyamide Thin-Film-Composite (TFC) Membrane*. Environmental Science & Technology, 2001. **35**(11): p. 2388-2394.
76. Noy, A., H.G. Park, F. Fornasiero, J.K. Holt, C.P. Grigoropoulos, and O. Bakajin, *Nanofluidics in Carbon Nanotubes*. Nano Today, 2007. **2**(6): p. 22-29.
77. Berger, M. *Nanotechnology water pump imitating cell pores* 2007 [cited 2011 30Nov]; Available from: <http://www.nanowerk.com/spotlight/spotid=3246.php>.
78. Hampton, T. *Navigating the Body's Water Channels, Scientists Gain Insights Into Disease* 2004 [cited 2011 30Nov]; Available from: <http://jama.ama-assn.org/content/292/13/1537.full>.
79. Hummer, G., *Water, Proton, and Ion Transport: from Nanotubes to Proteins*. Molecular Physics, 2007. **105**(2-3): p. 201-207.
80. Sui, H., B.-G. Han, J.K. Lee, P. Walian, and B.K. Jap, *Structural Basis of Water-Specific Transport Through the AQP1 Water Channel*. Nature, 2001. **414**(6866): p. 872-878.
81. Kalra, A., S. Garde, and G. Hummer, *Osmotic Water Transport Through Carbon Nanotube Membranes*. Proceedings of the National Academy of Sciences, 2003. **100**(18): p. 10175.
82. Hinds, B.J., N. Chopra, T. Rantell, R. Andrews, V. Gavalas, and L.G. Bachas, *Aligned Multiwalled Carbon Nanotube Membranes*. Science, 2004. **303**(5654): p. 62-65.
83. Majumder, M., N. Chopra, R. Andrews, and B.J. Hinds, *Nanoscale Hydrodynamics: Enhanced Flow in Carbon Nanotubes*. Nature, 2005. **438**(7064): p. 44-44.
84. Suter, S.P. and R. Skalak, *The History of Poiseuille's law*. Annual Review of Fluid Mechanics, 1993. **25**(1): p. 1-20.
85. Holt, J.K., H.G. Park, Y. Wang, M. Stadermann, A.B. Artyukhin, C.P.

- Grigoropoulos, A. Noy, and O. Bakajin, *Fast Mass Transport Through Sub-2-Nanometer Carbon Nanotubes*. Science, 2006. **312**(5776): p. 1034-1037.
86. Fornasiero, F., H.G. Park, J.K. Holt, M. Stadermann, C.P. Grigoropoulos, A. Noy, and O. Bakajin, *Ion Exclusion by Sub-2-nm Carbon Nanotube Pores*. Proceedings of the National Academy of Sciences, 2008. **105**(45): p. 17250.
 87. Whitby, M., L. Cagnon, M. Thanou, and N. Quirke, *Enhanced Fluid Flow through Nanoscale Carbon Pipes*. Nano letters, 2008. **8**(9): p. 2632-2637.
 88. Majumder, M., N. Chopra, and B.J. Hinds, *Effect of Tip Functionalization on Transport through Vertically Oriented Carbon Nanotube Membranes*. Journal of the American Chemical Society, 2005. **127**(25): p. 9062-9070.
 89. Majumder, M., X. Zhan, R. Andrews, and B.J. Hinds, *Voltage Gated Carbon Nanotube Membranes*. Langmuir, 2007. **23**(16): p. 8624-8631.
 90. Ratto, T.V., J.K. Holt, and A.W. Szmodis, *Membranes with Embedded Nanotubes for Selective Permeability*. 2008, Google Patents.
 91. Ajayan, P., J.C. Charlier, and A. Rinzler, *Carbon nanotubes: From macromolecules to nanotechnology*. Proceedings of the National Academy of Sciences, 1999. **96**(25): p. 14199.
 92. Ajayan, P.M., *Nanotubes from Carbon*. Chemical Reviews, 1999. **99**(7): p. 1787-1800.
 93. Iijima, S., *Carbon Nanotubes: Past, Present, and Future*. Physica B: Condensed Matter, 2002. **323**(1-4): p. 1-5.
 94. H. W. Kroto, J.R.H., S. C. O'Brien, R. F. Curl, R. E. Smalley *Buckminsterfullerene*. Nature, 14 November 1985. **318**(6042): p. 162-163
 95. Iijima, S., *Helical Microtubules of Graphitic Carbon* Nature, 7 November 1991. **354**: p. 776-778
 96. Terranova, M.L., V. Sessa, and M. Rossi, *The World of Carbon Nanotubes: An Overview of CVD Growth Methodologies*. Chemical Vapor Deposition, 2006. **12**(6): p. 315-325.
 97. Baughman, R.H., A.A. Zakhidov, and W.A. de Heer, *Carbon Nanotubes-the Route Toward Applications*. Science, 2002. **297**(5582): p. 787-792.
 98. Qiu, J., Y. Li, Y. Wang, and W. Li, *Production of Carbon Nanotubes from Coal*. Fuel Processing Technology, 2004. **85**(15): p. 1663-1670.
 99. O'Connell, M.J., P. Boul, L.M. Ericson, C. Huffman, Y. Wang, E. Haroz, C. Kuper, J. Tour, K.D. Ausman, and R.E. Smalley, *Reversible Water-Solubilization of Single-Walled Carbon Nanotubes by Polymer Wrapping*. Chemical Physics Letters, 2001. **342**(3-4): p. 265-271.
 100. Chen, J., H. Liu, W.A. Weimer, M.D. Halls, D.H. Waldeck, and G.C. Walker, *Noncovalent Engineering of Carbon Nanotube Surfaces by Rigid, Functional Conjugated Polymers*. Journal of the American Chemical Society, 2002. **124**(31): p. 9034-9035.
 101. Star, A., J.F. Stoddart, D. Steuerman, M. Diehl, A. Boukai, E.W. Wong, X. Yang, S.-W. Chung, H. Choi, and J.R. Heath, *Preparation and Properties of Polymer-Wrapped Single-Walled Carbon Nanotubes*. Ange. Chem., 2001. **113**(9): p. 1771-1775.
 102. Kong, J. and H. Dai, *Full and Modulated Chemical Gating of Individual Carbon Nanotubes by Organic Amine Compounds*. The Journal of Physical Chemistry B, 2001. **105**(15): p. 2890-2893.
 103. Chen, R.J., Y. Zhang, D. Wang, and H. Dai, *Noncovalent Sidewall Functionalization of Single-Walled Carbon Nanotubes for Protein Immobilization*. Journal of the American Chemical Society, 2001. **123**(16): p.

- 3838-3839.
104. Tasis, D., N. Tagmatarchis, A. Bianco, and M. Prato, *Chemistry of Carbon Nanotubes*. Chemical Reviews, 2006. **106**(3): p. 1105-1136.
 105. Spitalsky, Z., D. Tasis, K. Papagelis, and C. Galiotis, *Carbon Nanotube–Polymer Composites: Chemistry, Processing, Mechanical and Electrical Properties*. Progress in Polymer Science, 2010. **35**(3): p. 357-401.
 106. Curran, S.A., P.M. Ajayan, W.J. Blau, D.L. Carroll, J.N. Coleman, A.B. Dalton, A.P. Davey, A. Drury, B. McCarthy, S. Maier, and A. Strevens, *A Composite from Poly(m-phenylenevinylene-co-2,5-diethoxy-p-phenylenevinylene) and Carbon Nanotubes: A Novel Material for Molecular Optoelectronics*. Advanced Materials, 1998. **10**(14): p. 1091-1093.
 107. Van Lier, G., C. Van Alsenoy, V. Van Doren, and P. Geerlings, *Ab initio Study of the Elastic Properties of Single-walled Carbon Nanotubes and Graphene*. Chemical Physics Letters, 2000. **326**(1–2): p. 181-185.
 108. Wilder, J.W.G., L.C. Venema, A.G. Rinzler, R.E. Smalley, and C. Dekker, *Electronic Structure of Atomically Resolved Carbon Nanotubes*. Nature, 1998. **391**(6662): p. 59-62.
 109. Popov, I.A., K.V. Bozhenko, and A.I. Boldyrev, *Is Graphene Aromatic?* Nano Research, 2012. **5**(2): p. 117-123.
 110. Li, X., X. Wang, L. Zhang, S. Lee, and H. Dai, *Chemically Derived, Ultrasmooth Graphene Nanoribbon Semiconductors*. Science, 2008. **319**(5867): p. 1229-1232.
 111. Zhang, Y., Y.-W. Tan, H.L. Stormer, and P. Kim, *Experimental Observation of the Quantum Hall Effect and Berry's Phase in Graphene*. Nature, 2005. **438**(7065): p. 201-204.
 112. Novoselov, K.S., A.K. Geim, S.V. Morozov, D. Jiang, Y. Zhang, S.V. Dubonos, I.V. Grigorieva, and A.A. Firsov, *Electric Field Effect in Atomically Thin Carbon Films*. Science, 2004. **306**(5696): p. 666-669.
 113. Georgin, D., B. Czarny, M. Botquin, M. Mayne-L'Hermite, M. Pinault, B. Bouchet-Fabre, M. Carriere, J.-L. Poncey, Q. Chau, and R. Maximilien, *Preparation of ¹⁴C-Labeled Multiwalled Carbon Nanotubes for Biodistribution Investigations*. Journal of the American Chemical Society, 2009. **131**(41): p. 14658-14659.

CHAPTER II

2.1 Materials

Sigma Aldrich supplied all diamines (1,2-diamine, 1,4-diamine, 1,6-diamine and 1,8-diamine), anthracene-9-carboxylic acid, di-*tert*-butyl dicarbonate, trifluoroacetic acid (TFA), triethyl amine (TEA), *N,N*-diisopropylethylamine (DIPEA), *N,N*-dimethylformamide (DMF), benzene-1,3,5-tricarboxylic acid (trimesic acid, TMA), and thionyl chloride. In addition, drying reagent MgSO_4 , sodium hydroxide (NaOH), sulfuric acid H_2SO_4 (98%) and nitric acid HNO_3 (70%) were purchased from Sigma-Aldrich.

Toluene (98%), benzene-1,3,5-tricarboxyl acid chloride (trimesoyl chloride, TMC) and *m*-phenylenediamine (MPD) were purchased from Sigma-Aldrich.

O-(7-Azabenzotriazol-1-yl)-*N,N,N',N'*-tetramethyluronium hexafluorophosphate (HATU) was purchased from GL Biochem (Shanghai) Ltd.(China). Carbon nanotubes (CNTs) were purchased as single-wall carbon nanotubes (SWNTs) from Carbon Solutions Inc. (USA) (AP-SWNT).

Polysulfone (PSf) membranes supported by polyester layer were purchased from GE. *n*-Hexane (96%) was purchased from Scharlau. Methanol was purchased from Merck. Sodium dodecyl sulphate (SDS) was purchased from BDH while Campor-10-sulfonic acid (CSA) was purchased from Fluka. Isopropanol (IP) was purchased from Vetec.

Dichloromethane (DCM) was distilled in presence of calcium sulphate as a drying reagent and in a dry nitrogen atmosphere [1].

All chemicals were used as received without further purification.

2.2 Instruments

2.2.1 Stirred cell

Salt rejection and water flux were measured by using a Sterlitech HP4750 unit. This stirred cell, as illustrated in Figure 2- 1, is made from stainless steel with high chemical resistance for aqueous and non-aqueous solutions. The maximum pressure that this stirred cell is able to withstand is 69 bar (1000 psi) which makes it suitable for reverse osmosis filtration.

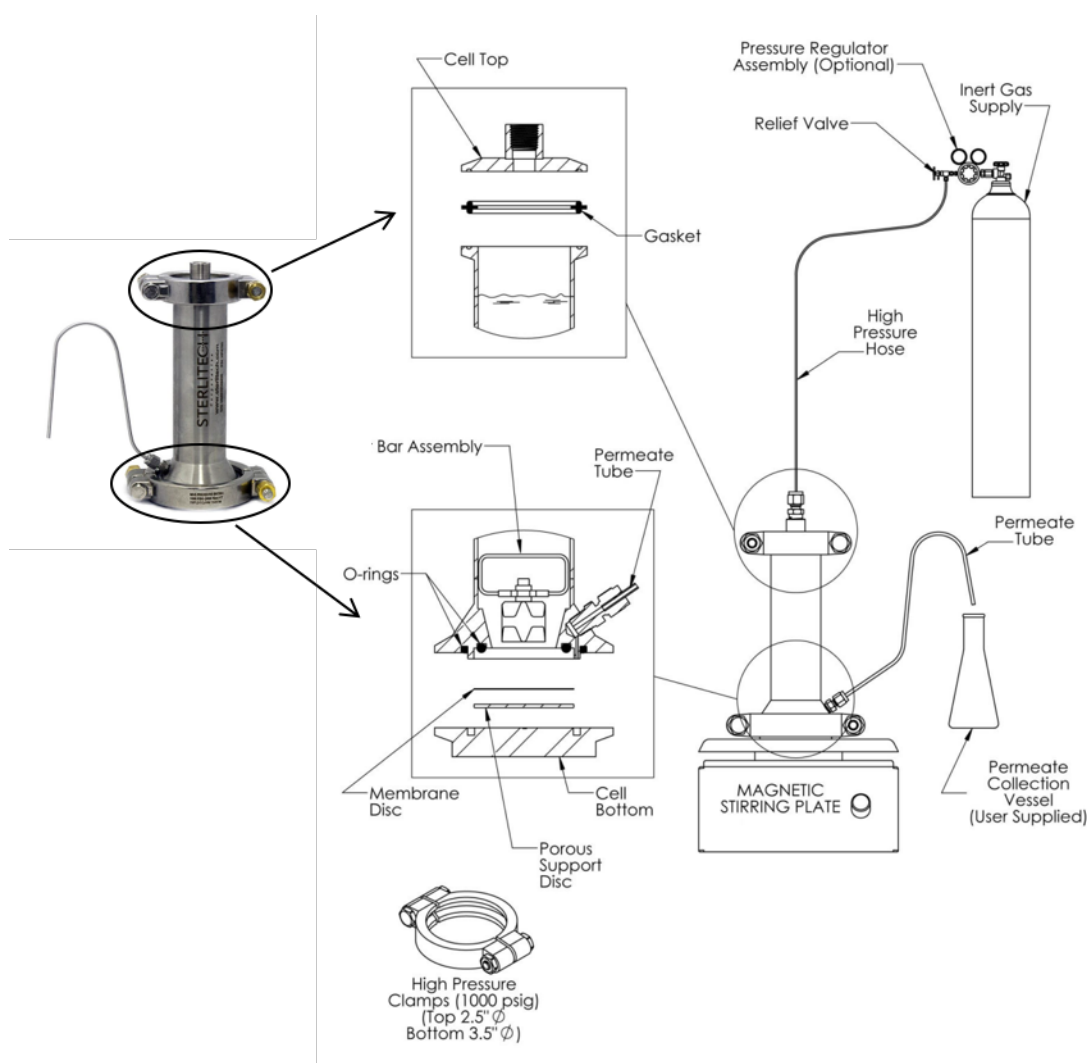


Figure 2- 1. Schematic of stirred cell showing the cell parts [2].

In this device water was forced to pass through a membrane disc. Concentration gradients is effected the flow of water through the membrane. Due to that the stirrer is

used to reduce the concentration gradients effect.

The water that passed through was collected via the permeate tube into a conical flask. A balance was used to continually weigh the permeate water per time under 16 bar pressure.

All flux and salt rejection measurements were made 50 min. after starting the experiment to obtain steady state permeate flux (J_w). The measurement of steady flux (J_w) through membrane area (A) was obtained by collected permeate volume (ΔV) during a period of time (Δt) [3, 4]. Formula (1) is used to measure the flux value and each membrane flux is presented by the average of the last 10 flux values.

$$J_w = \frac{\Delta V}{A \cdot \Delta t} \quad (2-1)$$

An example of such an experiment of water flux as a function of time is shown in Figure 2- 2. In general, the steady permeate flux was observed after 20 min. from starting the experiment.

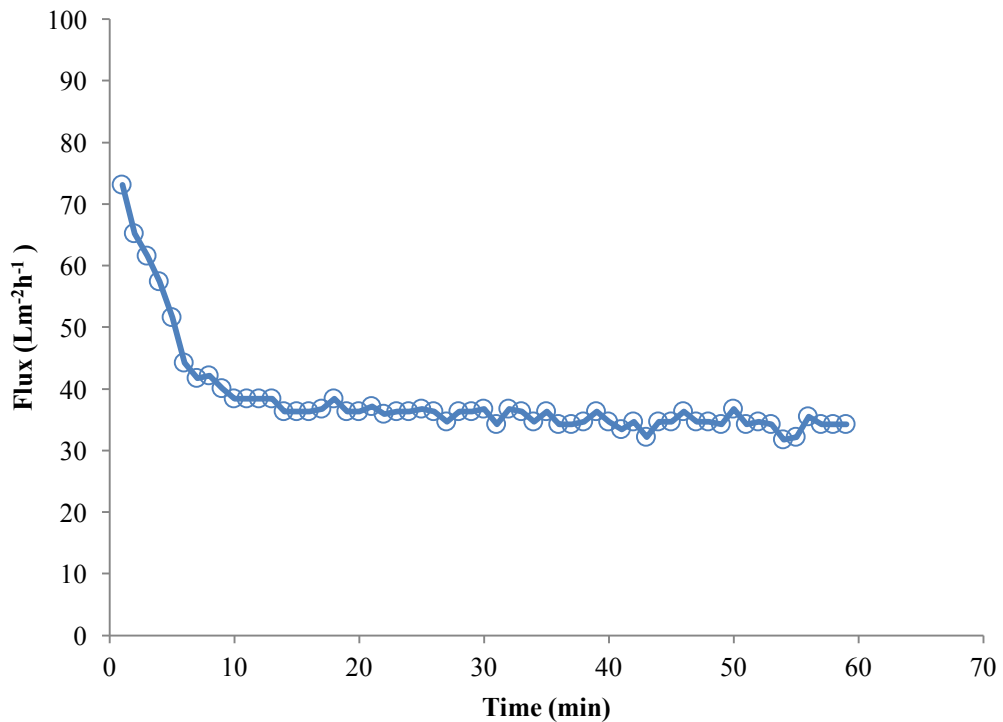


Figure 2- 2. Stirred cell water flux result of membrane embedded with SWNTs. The feed solution was 2000 ppm of NaCl. The flux was measured as a function of time.

Salt rejection was determined via the formula:

$$R = \left(1 - \frac{C_P}{C_F}\right) \times 100 \quad (2-2)$$

where C_P is the permeate concentration and C_F is the feed solution concentration [3, 4].

The calculation of salt rejection (R) was performed by measuring the conductivity of the permeate which was converted to concentration (ppm) using a calibration curve. The calibration curve was obtained by measuring the conductivity three times for six different concentrations of sodium chloride solution include the blank solution (0, 20, 40, 60, 80, 100 ppm). The average conductivity of these solutions verses the concentration is shown in Figure 2-3.

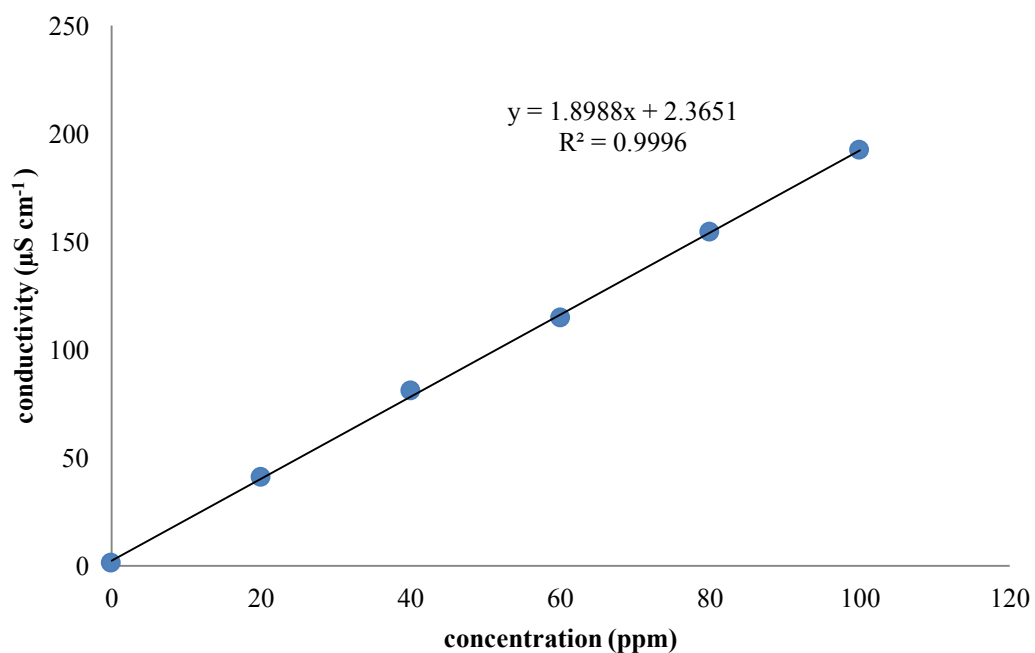


Figure 2-3. Calibration curve for the conversion of NaCl conductivity to concentration.

2.2.2 Scanning Electron Microscopy

Scanning Electron Microscopy (SEM) has been commercially available since 1965 which was 30 years after the initial demonstration of SEM [5]. This technique is a type of electron microscope that utilises a beam of electrons to study the morphology and chemical composition of solid objects. A schematic structure of SEM is illustrated in Figure 2-4. Lanthanum hexaboride and tungsten are commonly used as electron beam sources. The beam is focused by magnetic lenses to a very small resolution to obtain high magnification of the sample surface. The magnetic lenses give an ability to improve the scanning resolution and magnification. Impacting the sample surface with the focused electronic beam generates different types of reflected electrons with different energies as a result of various processes such as elastic scattering, inelastic scattering (secondary electrons) and the emission of electromagnetic radiation with x-ray frequency. Specialised detectors are used to detect these types of reflected electrons. The surface images are obtained by detecting the secondary electrons.

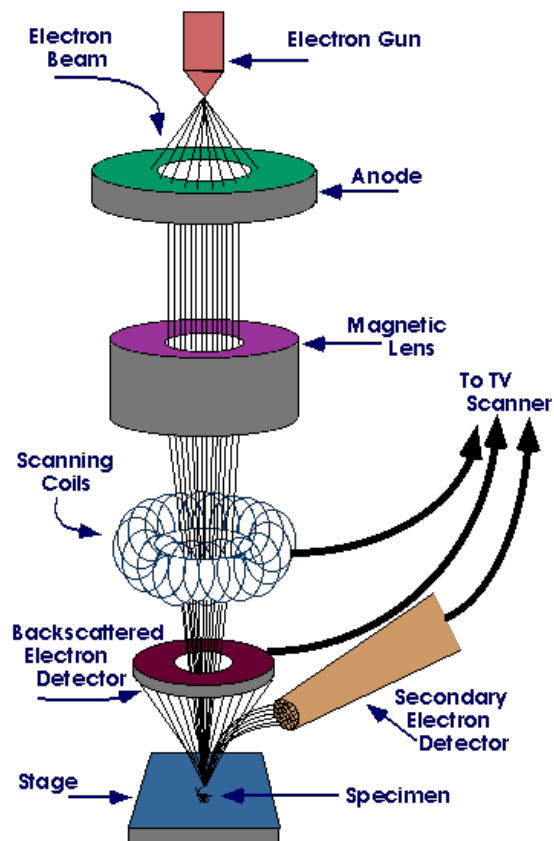


Figure 2-4. Schematic diagram of SEM parts and the electron beam path from gun to sample [6].

Clear surface images can be obtained by increasing the number of secondary electrons. Therefore, a conductive metallic layer is often placed over the surface of any sample being studied by using a sputter coater. In this thesis, all samples are coated with a gold layer for 30 seconds using a Quorum, Q300TD instrument. Once the samples are coated the SEM images were taken by using an Inspect F50 instrument.

2.2.3 Raman spectroscopy

Since 1928 when the first Raman scattering observation was recorded by Raman and Krishnan, Raman spectroscopy has been widely utilised in material characterisation. CNTs are one of the materials that can be characterised with Raman and this provides valuable information about its structure and lattice defects [7].

A Raman spectrum can be collected when a laser light is absorbed by the sample and excites it to a higher energy state. Relaxation of excited molecules to lower energy happens by releasing the absorbed energy as a photon. Depending on relaxation pathway to the original state, there are two types of photon which can be observed; namely elastic (Rayleigh) and inelastic (Stokes and anti-Stokes) as seen in Figure 2-5. Stokes scattering is observed which has lower energy than the laser light [8, 9].

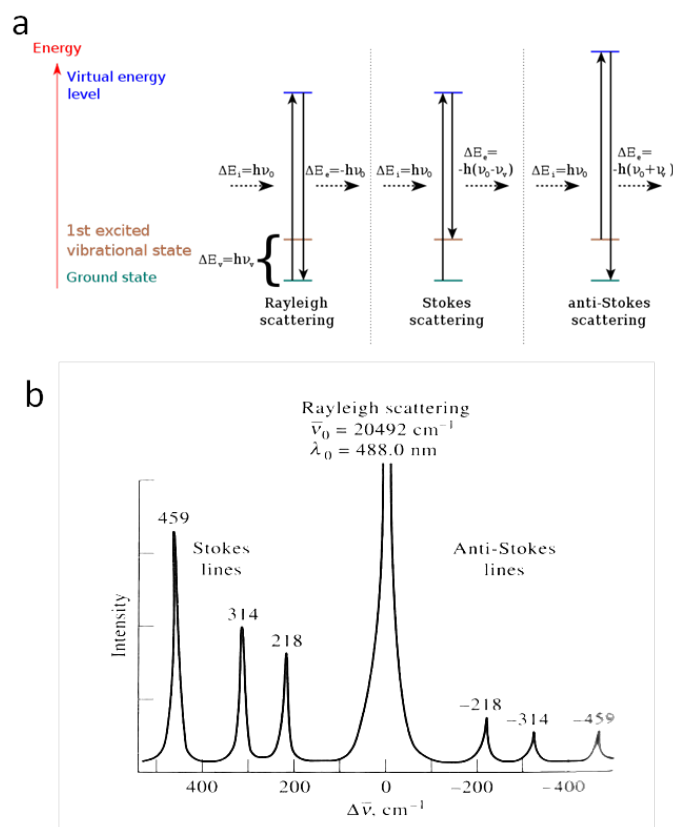


Figure 2-5. (a) Different relaxation to lower energy of excited molecule as light scattering, (b) spectrum of CCl_4 , using an Ar^+ laser at 488 nm showing Stokes, anti-Stokes and Rayleigh scattering [10, 11].

Raman spectra of CNTs have three dominant bands shown in Figure 2-6. The most dominant band is the graphitic band (G-band) which appears around $1500\text{-}1606 \text{ cm}^{-1}$. The G-band is related to sp^2 hybridised vibrations. The second band can be seen at 1350 cm^{-1} which is the disorder band (D-band) which is related to disorder or amorphous carbonaceous material or to carbon lattice defects. The radial breathing mode (RBM) which is a characteristic band of single wall carbon nanotubes (SWNTs) occurs from coherent vibrations of CNTs atoms [9, 12, 13].

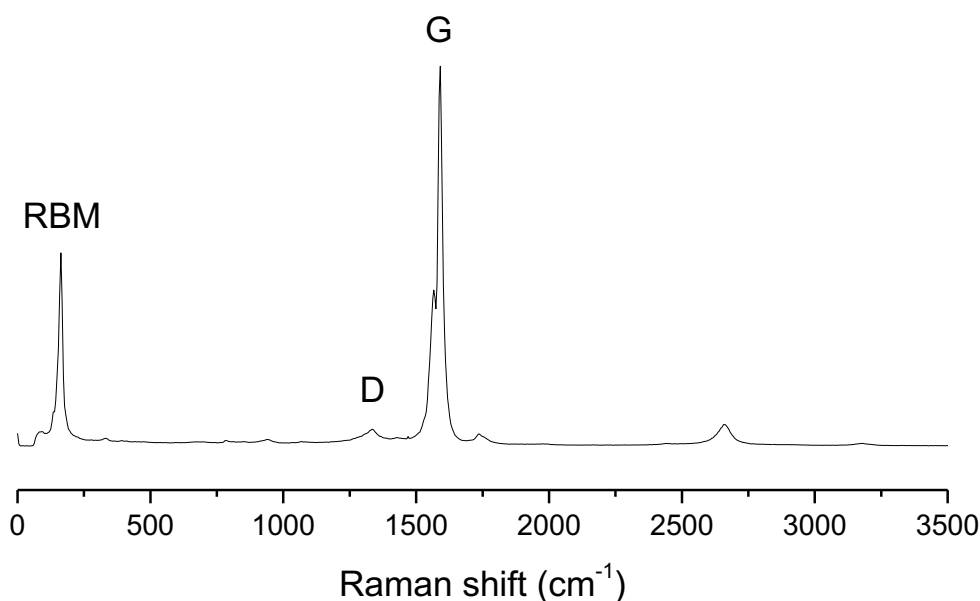


Figure 2-6. Raman spectrum at 532 nm laser of pristine SWNTs showing RBM, D and G bands.

The nanotube's diameter (d) can be determined by using RBM because its frequency depends linearly on the diameter of the CNTs using the following formula:

$$\omega_r = 223.75/d \quad (2-3)$$

where ω_r is RBM frequency and d is the tube diameter [14, 15].

In this thesis, a Witec Alpha 300R instrument using a 40× objective (numerical aperture 0.6) and 532 nm ($E_{\text{laser}} = 2.33$ eV) was used to collect the spectra. Raman spectra were recorded with typical integration times between 10 and 20 s and three accumulations.

SWNTs were dispersed in ethanol or DMF before being dropped on a clean glass slide. Solvent evaporation was achieved by keeping the sample in an oven at 60 °C overnight.

2.2.4 Nuclear Magnetic Resonance (NMR) spectroscopy

NMR spectroscopy was first developed in 1946 by utilising radar technology which was developed during the Second World War for military purposes. NMR spectroscopy is one of the most powerful tools available to chemists and biochemists for the elucidation of chemical structures[16].

NMR spectroscopy relies on the magnetic properties of the atomic nucleus. The most common nuclei in NMR are (^1H , ^{13}C , ^{19}F , ^{15}N and ^{31}P). A tiny magnetic dipole is created when the positive charge spins on axis. The magnetic dipole is determined by spin quantum numbers (I). Nuclei with spin quantum numbers $I \neq 0$ are NMR visible nuclei. In the case of $I = \pm \frac{1}{2}$, the energy of these two spin numbers are the same in the absence of external magnetic field. An energy difference will exist if an external magnetic field is applied as illustrated in Figure 2-7. The lower energy nuclei are aligned with external magnetic field while the nuclei aligned against the field will have higher energy [17-19].

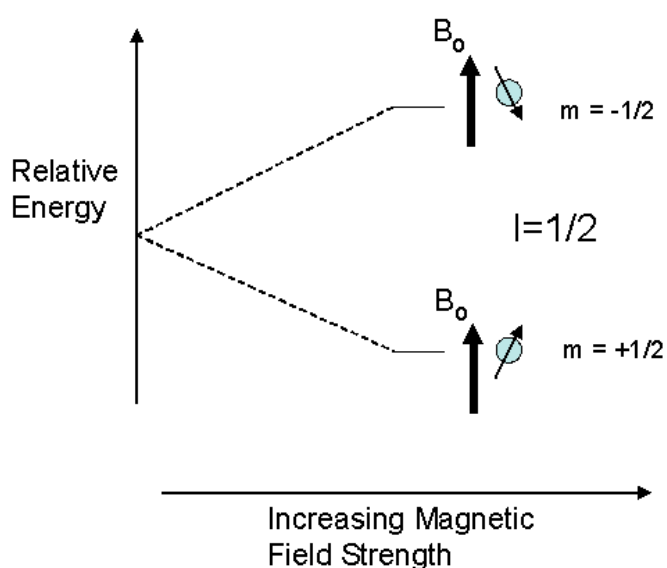


Figure 2-7. Schematic diagram showing splitting of nuclei spin states in an external magnetic field [20].

When the nuclei are irradiated by electromagnetic radiation (radiofrequency) the nuclei in lower energy will absorb the electromagnetic energy and be promoted to the higher energy state. This flipping from one energy state to another induces a voltage that can be detected by a tuned coil of wire and amplified before being displayed as signal. The NMR spectrum is a plot of radiofrequency absorption versus the resonance frequency [21, 22]. Figure 2- 8 shows the ^1H NMR spectrum of *N*-(anthracene-9-carbonyl) hexandiamine (3c).

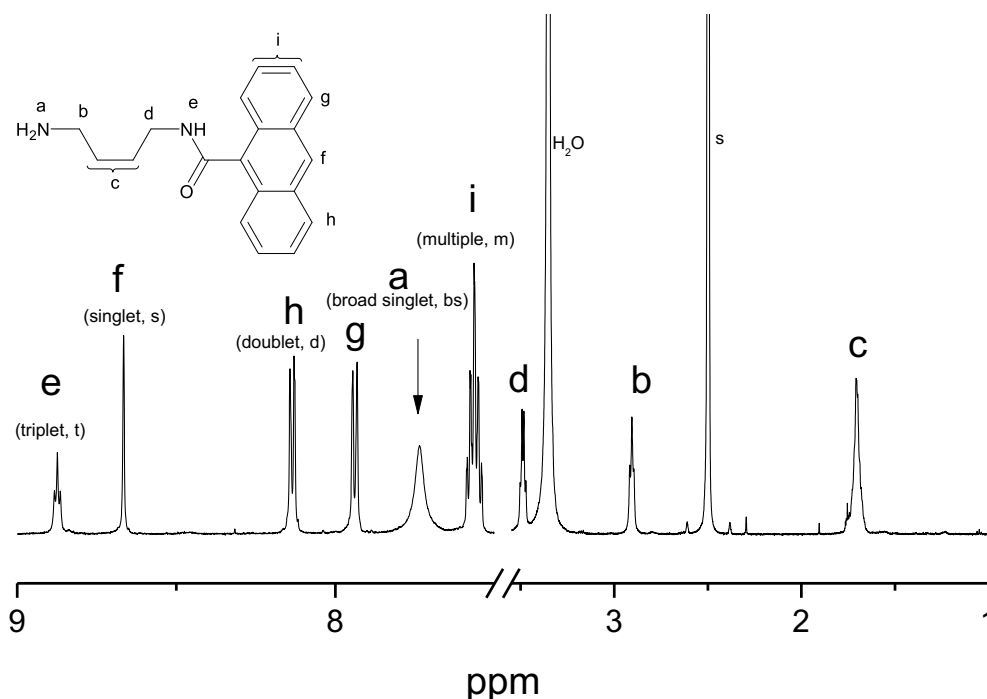


Figure 2- 8. Partial ^1H NMR (600 MHz) spectrum of *N*-(anthracene-9-carbonyl)hexandiamine (3c) showing the peaks shapes and descriptions; s = DMSO.

In this thesis, NMR spectra were recorded on a Bruker AVANCEIII 400MHz or 600MHz. The solvent peaks were used as reference signals. Solvents used included CDCl_3 , d_6 -DMSO and CD_3OD which have residual undeuterated signals at 7.26 ppm, 2.50 ppm and 3.31 ppm respectively [23].

2.2.5 Contact Angle (CA)

The solid liquid interface, which may be called wetting, has attracted scientists' attention for more than two centuries. The definition of contact angle is the angle that is formed by the intersection of liquid-solid interface and liquid-vapour interface as demonstrated in Figure 2- 9 [24]. A surface with low contact angle is described as a hydrophilic surface, while a high contact angle describes the surface as hydrophobic surface (less hydrophilicity)[25].

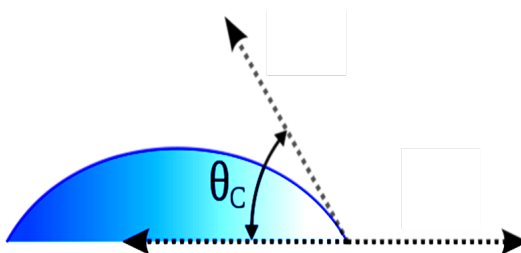


Figure 2- 9. Illustration of contact angles formed by liquid drops on smooth solid surface.

Contact angle measurements were obtained in air at room temperature with a water droplet. Membranes were attached to a glass slide facing-up with double sided sticky tape. The prepared membrane sample was placed on a horizontal platform and a Milli-Q water droplet was placed on the sample and a camera captured the image. The contact angle was calculated by the installed program on the instrument.

2.2.6 Fourier Transform Infra-Red (FT-IR) spectroscopy

FT-IR spectroscopy is used as an analytical technique to identify the functional groups in different chemical structures. There are three regions of FT-IR based on the wavelength of IR light. These regions are far infrared ($4\text{-}400\text{ cm}^{-1}$), near infrared ($4000\text{-}14000\text{ cm}^{-1}$) and the most applied region, the mid infrared ($400\text{-}4000\text{ cm}^{-1}$). Once the sample is irradiated by IR light, the functional groups absorb the radiation at different frequencies depending on their chemical functionality [17, 19].

One particular FT-IR technique is attenuated total reflectance (ATR) which was employed in this thesis for organic products and membrane samples. Membrane samples were placed active-face down on the ATR crystal and held in place by a clamp. KBr disks were used to characterise SWNTs. Pre-heated KBr powder was ground with SWNTs (1mg in 1g of KBr) until a homogenous powder mixture was obtained. After that, the homogenous powder was pressed using ten tons for 5 min to obtain the KBr disk. Another technique used NaCl windows to identify the acid chloride groups on the functionalised SWNTs in toluene/hexane solvent mixture. The mixture was placed in between two NaCl disks before insert in FT-IR instrument.

The FT-IR instrument that used in this project was Perkin Elmer Frontier. Experimental parameters were spectral range with $400\text{-}4000\text{ cm}^{-1}$, number of scans 64 and 4 cm^{-1} resolution.

2.2.7 Fluorescence

The emitted light from any compound as a result of light absorption is called luminescence. Fluorescence is one of the two categories of luminescence. This phenomenon was explained by Gabriel Stokes for the first time in 1852. Nowadays, there is a remarkable interest in the use of fluorescence in many disciplines including biological studies.

Fluorescence emission occurs after light is absorbed by a fluorophore in certain compounds. Light absorbance leads to the excitation of these compounds which raises electrons to a higher energy level.

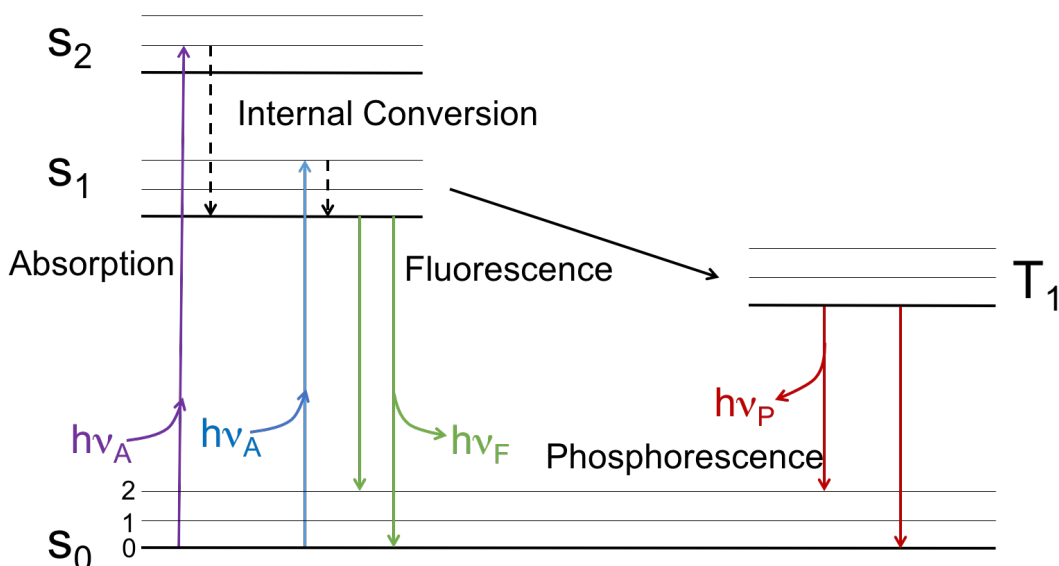


Figure 2-10. Jablonski diagram and luminescence process, figure adapted from [26].

The excited electron pathway after being excited up and returning down to the ground state (S_0) is illustrated in Figure 2-10. Once the electron is excited to higher energy level (S_1 , S_2) the return to the ground state (S_0) directly from excited state occurs by releasing the absorbed energy as light, which is known as fluorescence. The lifetime of fluorescence is very short (10^{-5} to 10^{-8} s) while phosphorescence takes longer lifetime (10^{-4} or longer) which occurs from triplet state (T_1).

In this thesis, the fluorescence instrument was Cary Eclipse Fluorescence Spectrophotometer (Varian, Australia). The investigated compound was dissolved in

chloroform with a concentration of 2 mg mL^{-1} and placed in 10 mm quartz cuvettes at room temperature. The excitation wavelength was 380 nm.

2.2.8 Thermogravimetric analysis (TGA)

TGA is a method of thermal analysis which measures the weight loss of the sample as a function of temperature or time. The thermal change in the sample can be associated with phase transitions or degradation processes. TGA data is presented as a characteristic curve as each material shows a unique pattern at specific temperature [27]. Data collection is done while the sample is subjected to a programmed heating in certain atmospheres of gas such as N_2 or air.

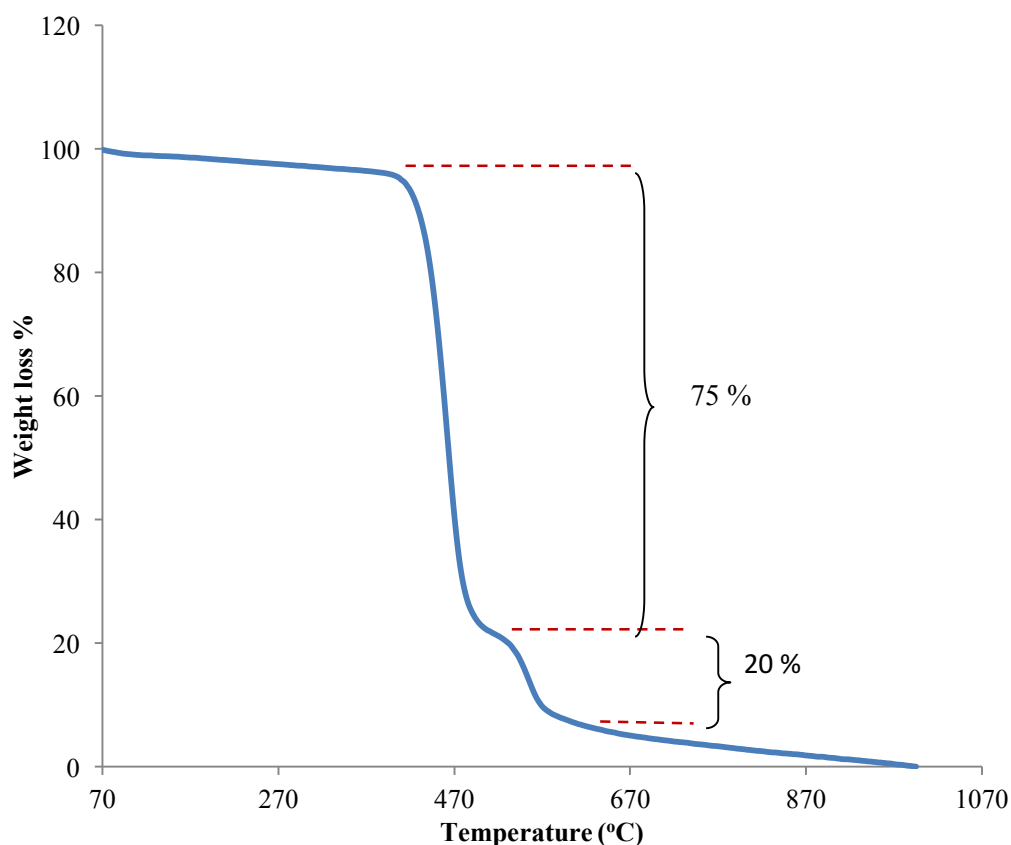


Figure 2-11. TGA curve of the TFC membrane supporting layer; polysulfone coated on polyester layer. First degradation step (75%) is attributed to the polyester layer while the second degradation step (20%) is attributed to polysulfone layer.

The TGA curve is plotted as mass loss of the sample as a function of temperature. TGA curve form is illustrated in Figure 2-11, showing how to calculate the weight change in TGA curve as a function of heating flow.

The results of TGA were recorded using a Perkin Elmer STA8000 instrument. Around 2 mg of the sample was placed in the pan which is suspended from sensitive balance arm inside a furnace with heating rate 20 °C/min.

2.2.9 Atomic Force Microscopy (AFM)

Scanning probe microscopy (SPM) techniques started with AFM as reported in 1986 by Binnig, Gerber and Quate [28]. The AFM has opened the way to many applications as it can be utilised to characterise materials (conducting or insulating) on a nanometer scale in an ambient environment [29]. The surface sample characterisation is obtained through ultraweak van der Waals interaction between the atoms at the tip of the probe and the sample surface as illustrated Figure 2-12. Due to the changes in the sample surface morphology the tip which is attached to the end of a flexible cantilever, deflects as the morphology of the sample changes during scanning [30]. The deflection of the cantilever is measured using a laser beam reflected from the back of the cantilever into a four-quadrant photodiode [28].

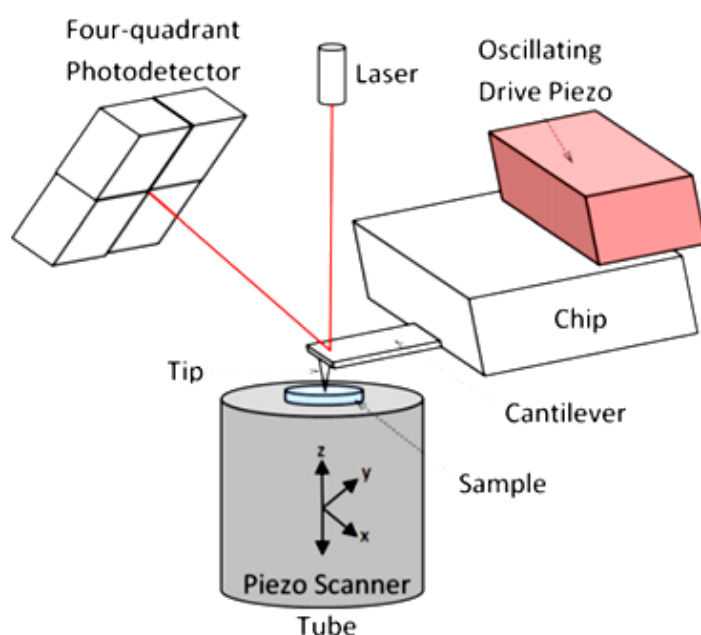


Figure 2-12. Schematic of AFM showing the basic components of the instrument [28].

The reflected laser beam spot position on the photodiode depends on the cantilever deflection. Imaging the surface is achieved by rastering the tip across the surface, using

piezoelectric movement which can be moved in the x -, y - and z - directions [28, 29]. The obtained surface image can be presented as a two or three dimensional (2D or 3D) profile as seen in Figure 2- 13.

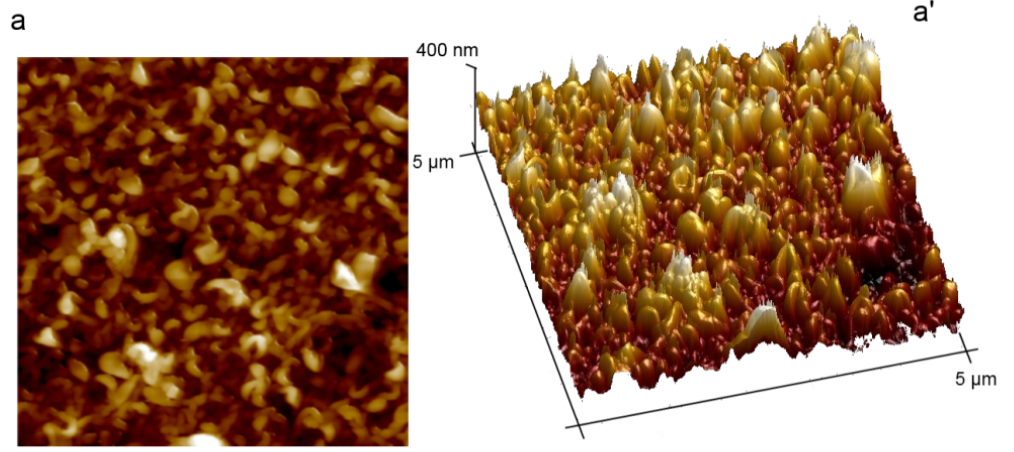


Figure 2- 13. AFM images (a) 2D and (a') 3D profile of TFC membrane.

The membrane surface roughness is quantified using two parameters which were root mean square roughness (RMS or R_q) and surface area difference (SAD) [31-33]. The SAD calculation is defined as

$$\% SAD = \left[\frac{\Sigma(\text{surface area of the sample})}{\Sigma(\text{projected surface area})} - 1 \right] \times 100 \quad (2-4)$$

The R_q parameter calculation is illustrated in Figure 2- 14 and defined as

$$R_q = \sqrt{\frac{1}{L} \int_0^L |Z^2(x)| dx} \quad (2-5)$$

where $Z^2(x)$ the function that describes the surface profile analysed in terms of height (Z) and position (x) of the sample over the evolution length L [34, 35].

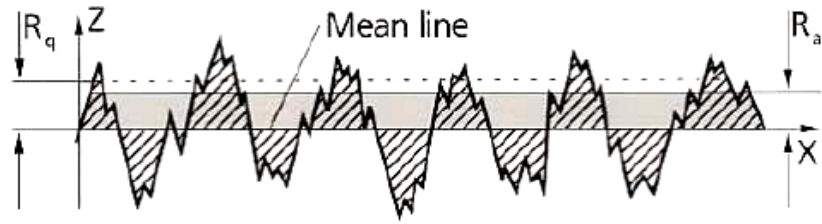


Figure 2- 14. Representation of Rq roughness measurement based on the mean line [34].

In this work, membrane samples were prepared by washing with isopropanol to remove water and then exposed to ambient conditions for 2 hours till dryness was obtained. A square sample (1 cm^2) of the membrane was attached to an AFM stub with a tape. AFM images were obtained in tapping mode in air at ambient temperature with a Bruker Multimode VIII AFM with NanoScope V controller.

2.3 References

1. Armarego, W.L. and C.L.L. Chai, *Purification of Laboratory Chemicals*. 2013: Butterworth-Heinemann.
2. TM, S., *Sterlitech TM HP4750 Stirred Cell Instruction Manual*. V.2-1.
3. Shen, J.n., C.c. Yu, H.m. Ruan, C.j. Gao, and B. Van der Bruggen, *Preparation and Characterization of Thin-Film Nanocomposite Membranes Embedded with Poly(methyl methacrylate) Hydrophobic Modified Multiwalled Carbon Nanotubes by Interfacial Polymerization*. Journal of Membrane Science, 2013. **442**: p. 18-26.
4. Zhao, H., S. Qiu, L. Wu, L. Zhang, H. Chen, and C. Gao, *Improving the Performance of Polyamide Reverse Osmosis Membrane by Incorporation of Modified Multi-Walled Carbon Nanotubes*. Journal of Membrane Science, 2014. **450**: p. 249-256.
5. McMullan, D., *Scanning Electron Microscopy 1928–1965*. Scanning, 1995. **17**(3): p. 175-185.
6. Bayo, O.B., *Production and Characterization of Mechanical Properties of Metallic Glasses*. 2009.
7. Smith, E. and G. Dent, *Modern Raman Spectroscopy: A Practical Approach*. 2013: John Wiley & Sons.
8. Larkin, P., *Infrared and Raman Spectroscopy; Principles and Spectral Interpretation*. 2011: Elsevier.
9. Dresselhaus, M.S., G. Dresselhaus, A. Jorio, A.G. Souza Filho, and R. Saito, *Raman Spectroscopy on Isolated Single Wall Carbon Nanotubes*. Carbon, 2002. **40**(12): p. 2043-2061.
10. Ferraro, J.R., *Introductory Raman Spectroscopy*. 2003: Academic press.
11. Colthup, N., *Introduction to Infrared and Raman Spectroscopy*. 2012: Elsevier.
12. Dresselhaus, M.S., A. Jorio, and M.A. Pimenta, *Resonance Raman Spectroscopy in One-dimensional Carbon Materials*. Anais da Academia Brasileira de Ciências, 2006. **78**: p. 423-439.
13. Dresselhaus, M.S., A. Jorio, M. Hofmann, G. Dresselhaus, and R. Saito, *Perspectives on Carbon Nanotubes and Graphene Raman Spectroscopy*. Nano Letters, 2010. **10**(3): p. 751-758.
14. Bandow, S., M. Takizawa, K. Hirahara, M. Yudasaka, and S. Iijima, *Raman Scattering Study of Double-wall Carbon Nanotubes Derived from the Chains of Fullerenes in Single-wall Carbon Nanotubes*. Chemical Physics Letters, 2001. **337**(1–3): p. 48-54.
15. Bandow, S., S. Asaka, Y. Saito, A.M. Rao, L. Grigorian, E. Richter, and P. Eklund, *Effect of the Growth Temperature on the Diameter Distribution and Chirality of Single-Wall Carbon Nanotubes*. Physical Review Letters, 1998. **80**(17): p. 3779.
16. Berger, S. and S. Braun, *200 and more NMR Experiments: A Practical Course*. 2004: Wiley-Vch Weinheim.
17. Vogel, A.I., *Practical Organic Chemistry*. Longman Group Ltd., London, 1971: p. 926.
18. Tosi, M., G. Fini, A. Tinti, A. Reggiani, and V. Tugnoli, *Molecular Characterization of Human Healthy and Neoplastic Cerebral and Renal Tissues by in vitro 1H NMR Spectroscopy (Review)*. International journal of

- molecular medicine, 2002. **9**(3): p. 299-310.
19. Crews, P., J. Rodriguez, M. Jaspars, and R.J. Crews, *Organic Structure Analysis*. Vol. 23. 1998: Oxford New York.
 20. Edwards, J.C. *Principles of NMR*. 2016 12 April 2016]; Available from: <http://www.process-nmr.com/nmr1.htm>.
 21. Cavanagh, J., W.J. Fairbrother, A.G. Palmer III, and N.J. Skelton, *Protein NMR Spectroscopy: Principles and Practice*. 1995: Academic Press.
 22. Jacobsen, N.E., *NMR Spectroscopy Explained: Simplified Theory, Applications and Examples for Organic Chemistry and Structural Biology*. 2007: John Wiley & Sons.
 23. Gottlieb, H.E., V. Kotlyar, and A. Nudelman, *NMR Chemical Shifts of Common Laboratory Solvents as Trace Impurities*. The Journal of organic chemistry, 1997. **62**(21): p. 7512-7515.
 24. Mittal, K.L., *Contact Angle, Wettability and Adhesion*. Vol. 4. 2006: CRC Press.
 25. Hiemenz, P.C. and R. Rajagopalan, *Principles of Colloid and Surface Chemistry, revised and expanded*. Vol. 14. 1997: CRC press.
 26. Lakowicz, J.R., *Principles of Fluorescence Spectroscopy*. 2013: Springer Science & Business Media.
 27. Stuart, B.H., *Analytical Techniques in Materials Conservation*. 2007: John Wiley & Sons.
 28. Slattery, A.D., C.T. Gibson, and J.S. Quinton, *Application of Ion Beam Processes to Scanning Probe Microscopy*, in *FIB Nanostructures*. 2013, Springer. p. 205-240.
 29. Butt, H.-J., B. Cappella, and M. Kappl, *Force Measurements with the Atomic Force Microscope: Technique, Interpretation and Applications*. Surface Science Reports, 2005. **59**(1-6): p. 1-152.
 30. Yablon, D.G., *Overview of Atomic Force Microscopy*. Scanning Probe Microscopy in Industrial Applications: Nanomechanical Characterization, 2013: p. 1-14.
 31. Gadelmawla, E.S., M.M. Koura, T.M.A. Maksoud, I.M. Elewa, and H.H. Soliman, *Roughness Parameters*. Journal of Materials Processing Technology, 2002. **123**(1): p. 133-145.
 32. Drelich, J. and K.L. Mittal, *Atomic Force Microscopy in Adhesion Studies*. 2005: CRC Press.
 33. Tiraferri, A., C.D. Vecitis, and M. Elimelech, *Covalent Binding of Single-Walled Carbon Nanotubes to Polyamide Membranes for Antimicrobial Surface Properties*. ACS Applied Materials & Interfaces, 2011. **3**(8): p. 2869-2877.
 34. De Oliveira, R., D. Albuquerque, F. Leite, F. Yamaji, and T. Cruz, *Measurement of the Nanoscale Roughness by Atomic Force Microscopy: Basic Principles and Applications*. 2012: INTECH Open Access Publisher.
 35. Yuhang, C. and H. Wenhao, *Numerical Simulation of the Geometrical Factors Affecting Surface Roughness Measurements by AFM*. Measurement Science and Technology, 2004. **15**(10): p. 2005.

CHAPTER III

3.1 Introduction

Building very large uniform structures from small molecules using non-covalent interactions is known as self-assembly and is a key method of construction within supramolecular chemistry. Individual molecules, in some conditions, can aggregate or assemble to form nano/microstructures. These structures may possess different shapes, such as micelles, vesicles, tubes, wires and helices, giving rise to the wide expansion of supramolecular chemistry in recent decades [1-4]. In 1987, the Nobel Prize was given to Jean-Marie Lehn (sharing with D.J. Cram and C. Pedersen) for his work in the field of supramolecular chemistry. He defined supramolecular chemistry as ‘chemistry beyond the molecule’ [5]. In other words, secondary interactions of the molecule as a whole influence how these molecules interact with each other. Depending on the individual molecule’s functionality, a number of spontaneous secondary interactions (forces) could be involved in the aggregation of the molecules. There is a variety of interaction forces, such as π - π stacking, van der Waals, dipole-dipole, and hydrogen bonding.

Moreover, molecules involved in supramolecular chemistry have functional groups for non-covalent interaction, but can also have other properties such as stimulus-sensitive chromogenic dyes [6], polymerisable moieties [7, 8] and photoresponsive groups [9, 10].

In supramolecular chemistry, benzene-1,3,5-tricarboxamide (BTA) is one of the simplest and most versatile motifs [11]. BTA is a disc-like molecule consisting of three arms radiating from a central core. The preferred formation of BTA’s derivatives are helical structures [11, 12], which are stabilised by strong hydrogen bonds from the three amide groups and π – π stacking using aromatic ring [13, 14]. Depending on the nature of the substituents on the arm, BTA’s derivatives are able to form a variety of materials, such as hydrogels and organogels, which can have a variety of applications [15, 16].

One of the useful groups of substituents are the anthracene derivatives, which have enormous applications. Since 1833, when anthracene was isolated from coal tar, anthracene and its derivatives have been used in a number of fields. For example, they have been used as sensors and markers in biological and supramolecular systems due

to their unique spectroscopic properties [17]. Moreover, they are used in mobile phones, car stereos and solid-state lighting as organic light-emitting diodes (OLEDs) [18].

In this work, a series of new BTA derivatives involving anthracene as the substituent at the end of the arms were synthesised. Anthracene was chosen since it mimics reactivity of SWNTs (see Chapter I, section 1.4.2). The distance between the core (BTA) and the edge of the molecule (anthracene) was altered by using aliphatic chains of various lengths. The influence of this distance on the self-assembly process was investigated by following the changes in fluorescence, FT-IR, and SEM as a function of time. The synthesised molecules will be labelled 9AC-R-BTA, where R indicates to the aliphatic chain length, and 9AC is anthracene substituted at 9- position.

3.2 Synthesis and characterisations

Different aliphatic diamines with various carbon chain lengths (ranging from two to eight carbon atoms) were used to synthesise the BTA derivatives. The synthesis of the various anthracene amine derivatives, containing different chain length, is shown in Figure 3-1.

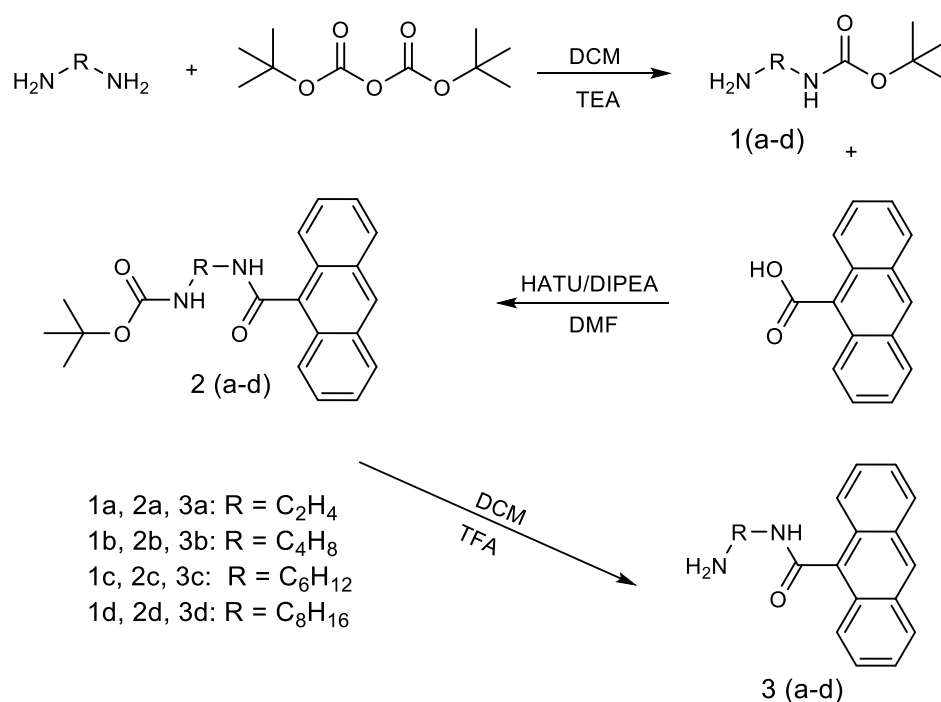


Figure 3-1. Synthesis of anthracene amine derivatives starting with aliphatic diamines.

In the first step of the reaction series, the diamine was allowed to react with di-tert-butyl dicarbonate to protect one of the amine groups in the diamine. As result, the amine group is protected by the Boc group, with good yields (95% for 1a - 41% for 1d). In the following step, protected-diamine was allowed to react with anthracene-9-carboxylic acid utilising the coupling reagent HATU. The products were washed and recrystallised from methanol yielding (98% for 2a - 65% for 2d). Subsequently, liberation of the amine group from the Boc group was achieved by using TFA with the liberated amine used without purification. Several of these compounds have been reported in literature spectral data matched that reported.

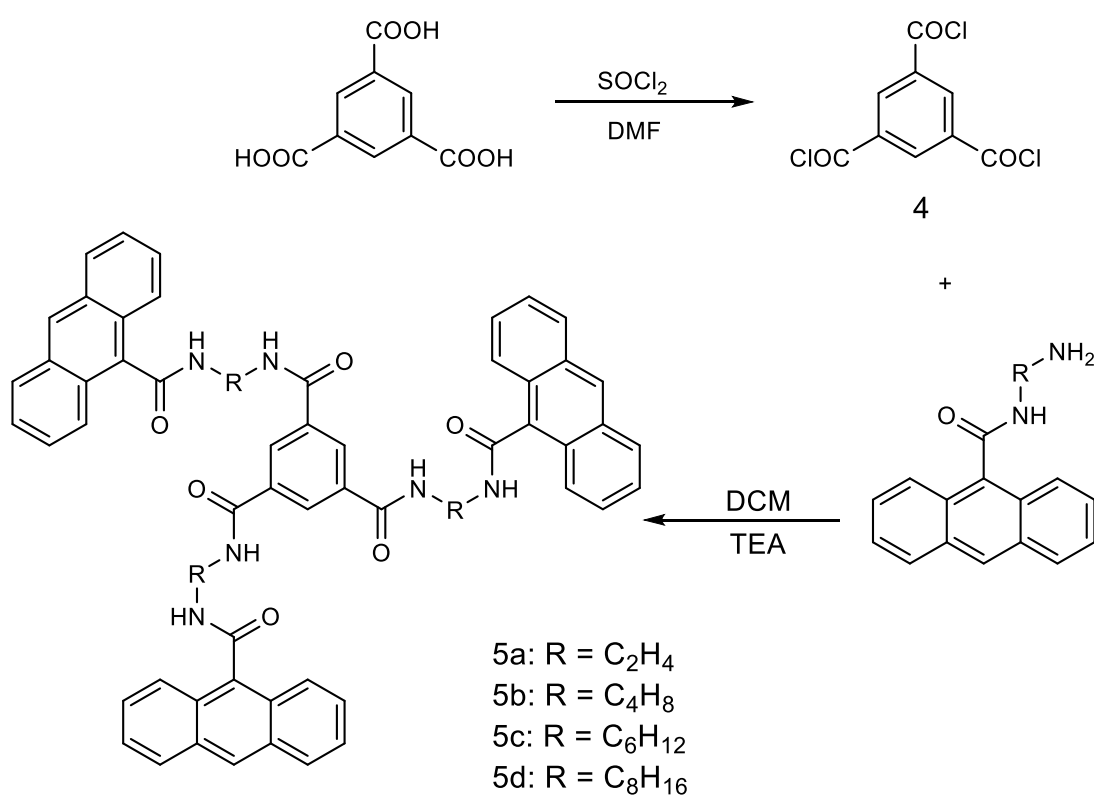


Figure 3- 2. Synthesis of BTA derivatives using amine compounds with TMC.

The synthesis of 9AC-R-BTA molecules was performed by allowing the liberated anthracene amine derivatives to react with benzene-1,3,5-tricarboxylic acid chloride (trimesoyl chloride, TMC) as presented in Figure 3- 2. The preparation of trimesoyl chloride was performed via chlorination reaction of benzene-1,3,5-tricarboxylic acid with thionyl chloride being used to convert the carboxylic acid to an acid chloride group in the presence of a trace of DMF as a catalyst. Then, the liberated anthracene amine derivative was mixed with benzene-1,3,5-tricarboxylic acid chloride in dry DCM with TEA and heated under reflux overnight. After workup of the reaction no

further purification was applied. A number of characterisation methods such as ^1H and ^{13}C NMR, FT-IR and HRMS were applied to identify and confirm the synthesised structures.

However, due to the aggregation of BTA derivatives, longer characterisation methods such as ^{13}C NMR were challenging and hence ^1H NMR, FT-IR and mass spectroscopy were used to characterise the BTA molecules using freshly made samples and with quick measurements before significant amount of aggregation had occurred.

3.2.1 ^1H NMR

A molecule with a short aliphatic chain (9AC-2-BTA) was the first synthesised molecule. A partial ^1H NMR spectrum in deuterated chloroform (CDCl_3) is illustrated in Figure 3- 3. 9AC-2-BTA exhibited two multiplet peaks at δ 3.77-3.79 and δ 3.93-3.96 ppm respectively, which were assigned to the methylene group resonances. Aromatic ring proton resonances appeared as multiplets at δ 7.50-7.57 ppm, two doublets at δ 7.97 ppm and δ 8.04 ppm, a broad singlet at δ 8.10 ppm and another singlet peak at δ 8.54 ppm. This pattern is typical of a 9-substituted anthracene and BTA core.

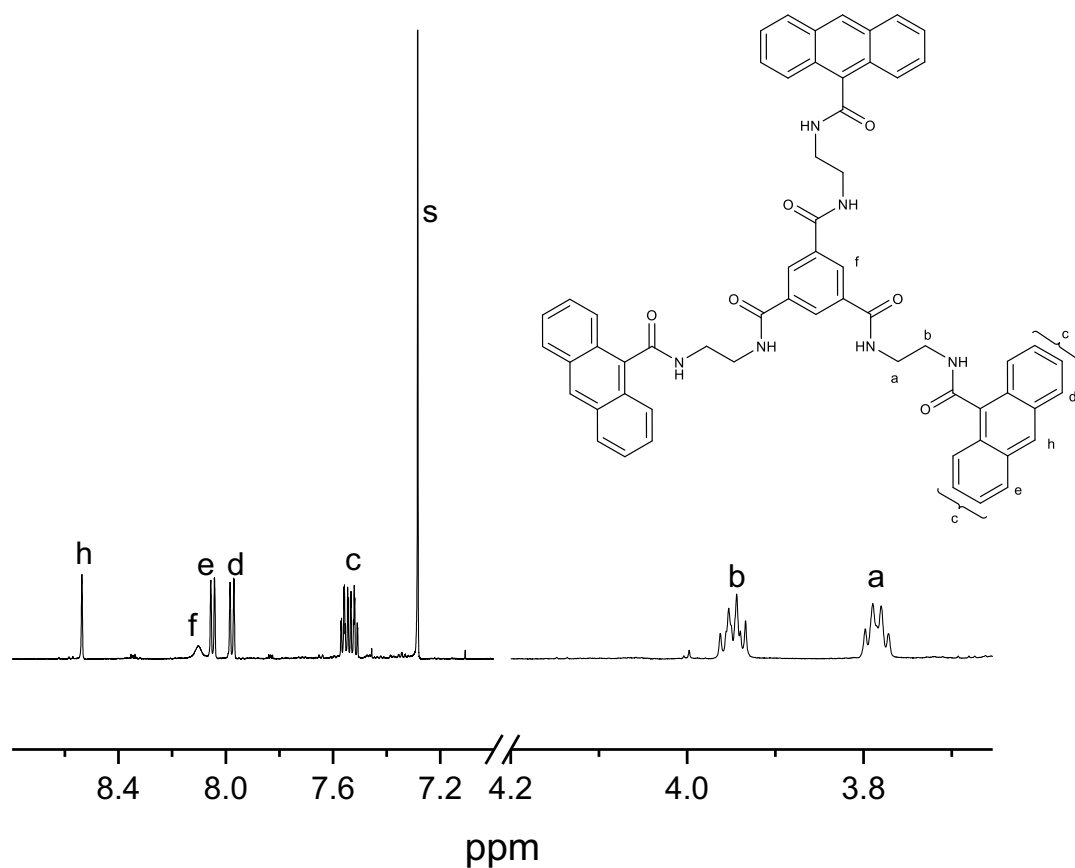


Figure 3- 3. Partial ^1H NMR spectrum (600 MHz) of *N,N',N''*-[*N*-(anthracene-9-carbonyl)ethandiamine]benzene-1,3,5-tricarboxamide (9AC-2-BTA) in CDCl_3 , (S = CHCl_3).

Five days later, the ^1H NMR spectrum of 9AC-2-BTA in CDCl_3 no longer displayed the same ^1H NMR spectrum, as seen in Figure 3- 4.

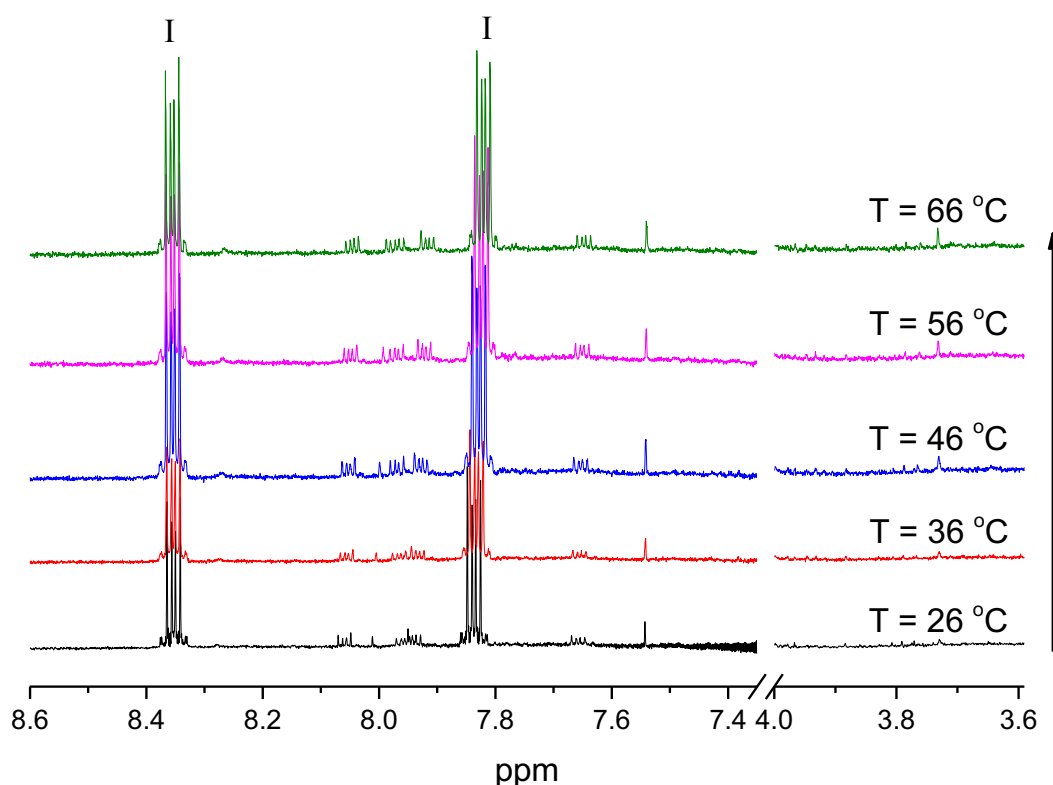


Figure 3- 5. Partial ^1H NMR spectra of 9AC-2-BTA after standing five days measured at different temperatures; (I= impurity).

3.2.2 FT-IR

The disappearance of ^1H NMR peaks after leaving the sample for five days raised the issue of stability of the compound in a chloroform solution at room temperature. Therefore, FT-IR spectroscopy was used to confirm that the molecule was still intact in the sample. BTA derivatives such as 9AC-2-BTA possess the ability to assemble themselves in solution through interaction forces such as hydrogen bonding and π -stacking [13, 19]. An ATR-FTIR spectrum of 9AC-2-BTA as seen in Figure 3-6 was obtained by evaporating drops of solution on the surface of the ATR-FTIR crystal. Inspection of Figure 3-6 shows the appearance of new bands that were not seen in the anthracene compound spectrum. For example, the existence of hydrogen bonding between the molecules was confirmed by the N-H stretching band at 3328 cm^{-1} . The appearance of bands at 3075 cm^{-1} , 2926 cm^{-1} and 2854 cm^{-1} were attributed to aromatic C-H stretching, and symmetric and asymmetric vibrations of CH_2 , respectively [21-23].

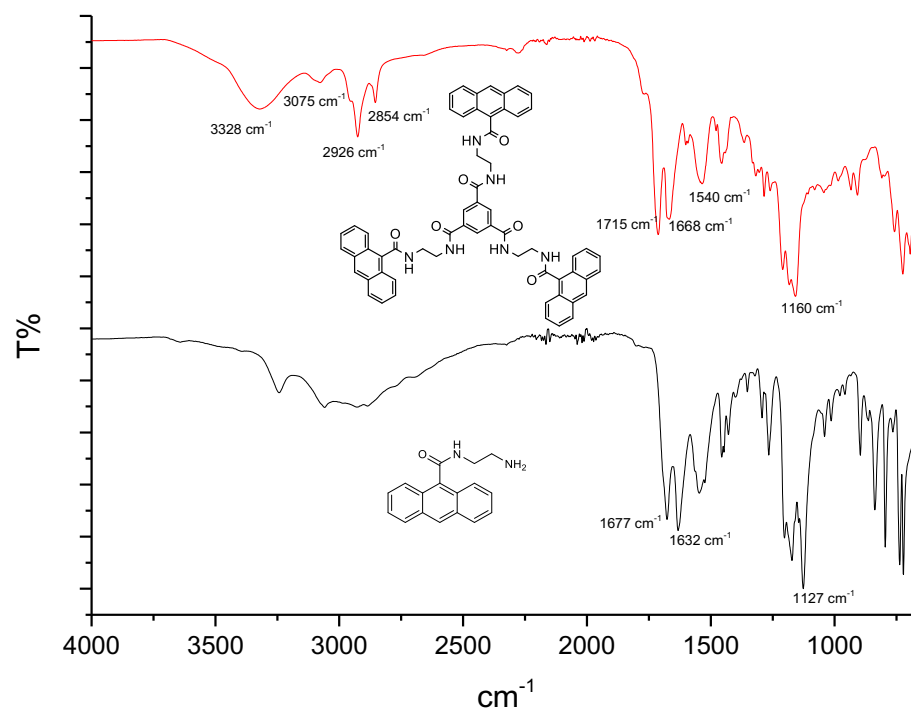


Figure 3-6. ATR-FTIR spectra for *N*-(anthracene-9-carbonyl)ethandiamine and 9AC-2-BTA.

However, carbonyl and C=C bands appeared in both spectra at different locations. The 9AC-2-BTA showed an enhanced C=C band at 1715 cm^{-1} with the carbonyl band at 1668 cm^{-1} , while these bands appeared for the anthracene compound at 1677 cm^{-1} and 1632 cm^{-1} respectively [19, 22, 24, 25]. It has been reported that the presence of bands at 3323, 3075, 1668 cm^{-1} indicate to assembly of BTA derivatives which suggests that compound was still intact and decomposition had not occurred [19, 26]. However, further characterisation was performed to investigate the self-assembly of the synthesised compound.

3.2.3 SEM

Scanning electron microscopy (SEM) was used to obtain visual images of the self-assembled structure of the synthesised compound. After five days of the chloroform solution standing at room temperature, drops of the solution were placed on a silicon wafer surface. After evaporation, the surface was imaged at different sites on the silicon wafer and showed fibers as seen in Figure 3- 7. Variation in fibre length was observed, as seen in Figure 3- 7 (a). In addition, aggregation between fibres occurred, as shown in Figure 3- 7 (b) and (c). It can be seen in Figure 3- 7 (d) that two fibres aggregate and are involved in larger fibre formation.

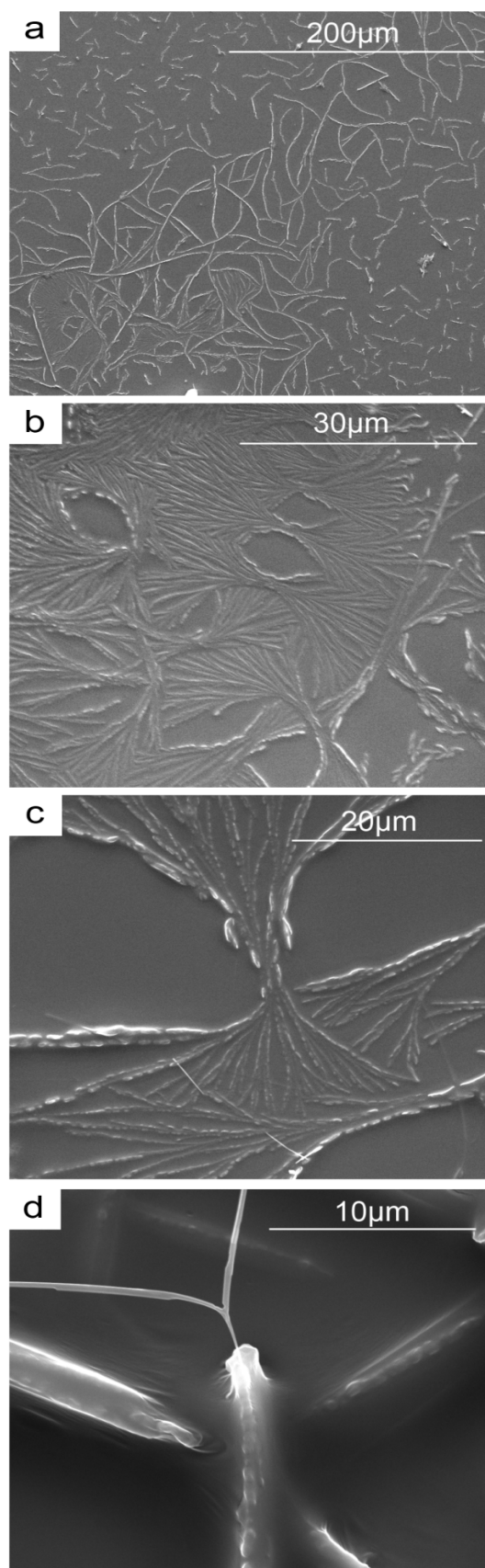


Figure 3- 7. SEM images showing fibres formed from self assembly after standing in chloroform solution for five days at room temperature.

3.2.4 Self-assembly of other molecules

Other compounds with variations in aliphatic chain length between the BTA core and anthracene were synthesised as demonstrated in Figure 3- 8. The fibres formed from the synthesised molecules in chloroform at room temperature were characterised using SEM images. As seen in Figure 3- 8, all synthesised compounds formed fibres on the silicon surface after evaporation of the chloroform solution. The shape of the fibres was variable, depending on the aliphatic chain length that connected the anthracene to the BTA core. For instance, the molecule with the four carbon atom chain length formed fibres which aggregated together to create longer fibres, as shown in Figure 3- 8 (a). A star-like shape was observed for the molecule with the six carbon atom chain length, as seen in Figure 3- 8 (b). Long chain molecules with eight carbon atoms formed long fibres, as presented in Figure 3- 8 (c). The variation in fibre shape and length provided inspiration to perform more investigations about the influence of aliphatic chain length on fibre growth as a function of time.

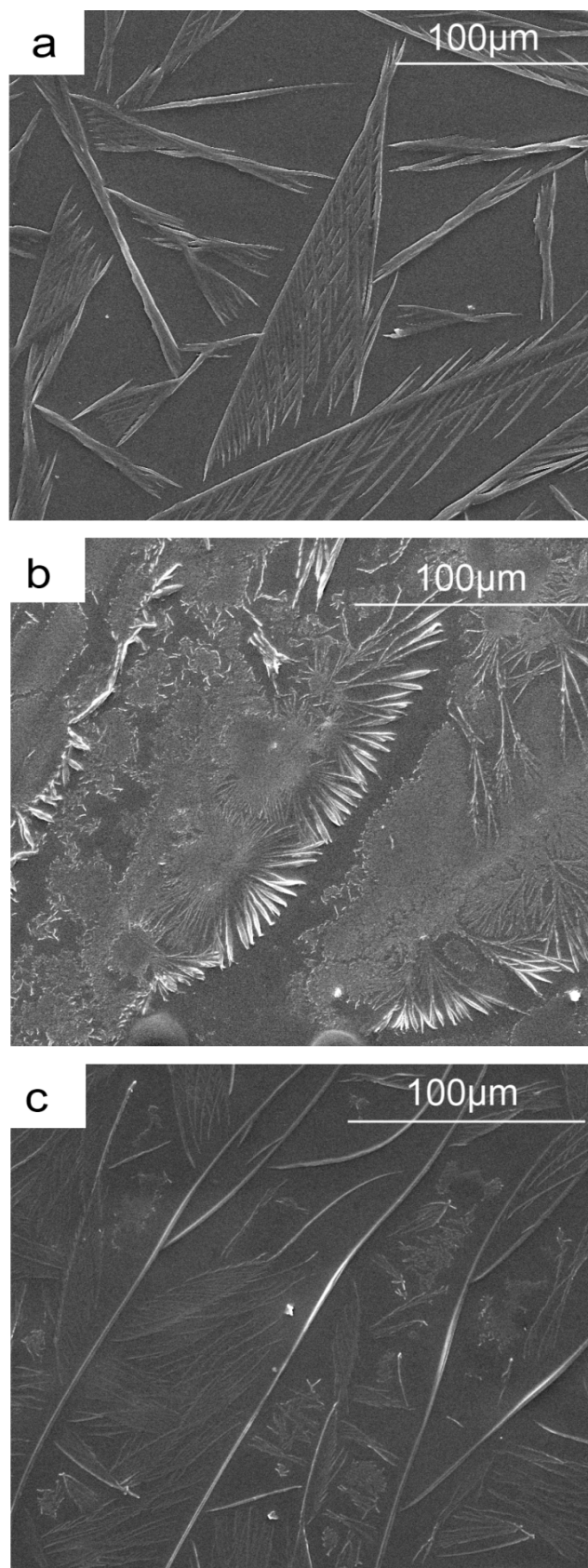


Figure 3- 8. SEM images of synthesised fibres on a silicon surface after evaporation of chloroform, (a) 9AC-4-BTA, (b) 9AC-6-BTA, (c) 9AC-8-BTA.

3.3 Self-assembly behaviour investigation

The investigation of self-assembly behaviour was conducted for two synthesised compounds with two and eight carbon atom chain lengths, namely 9AC-2-BTA and 9AC-8-BTA. In 10 mL of chloroform, 20 mg of the synthesised compound was dissolved. At room temperature, the self-assembly behaviour of the compounds as a function of time was investigated.

During the self-assembly process, a diverse range of non-covalent interactions is involved. As illustrated in Figure 3-9, the synthesised compounds have three potential types of noncovalent interactions - hydrogen bonding interactions between amide groups, van der Waals interactions between aliphatic chains, and π - π stacking interactions between the aromatic rings. The self-assembly behaviour as a function of time was investigated by utilising three different techniques namely fluorescence, FT-IR and SEM.

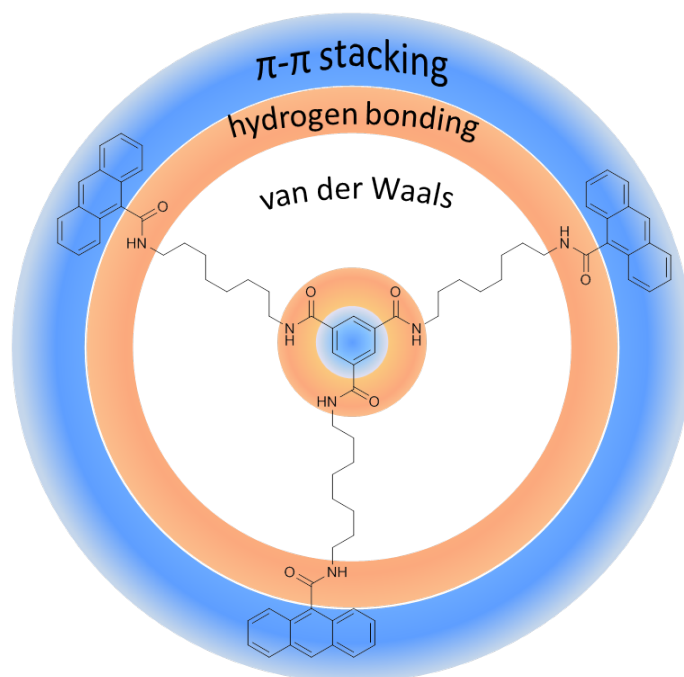


Figure 3- 9. The compound structure shows three potential aggregation forces – π - π stacking between the core and anthracene moieties, hydrogen bonding between amide groups, and van der Waals between the aliphatic chains.

The first technique used was fluorescence spectroscopy. Due to the presence of anthracene moieties in the synthesised structure, the compound was able to emit photons due to fluorescence. The advantage of using fluorescence spectroscopy was the ability to study the self-assembly process in the liquid phase. Changes in fluorescence spectra during this time reveal valuable information, which improves the understanding of the growth behaviour.

FT-IR was another technique used to study the self-assembly behaviour of the synthesised compounds. BTA derivatives form fibres with hydrogen bonding as one of the main interaction forces between the BTA derivatives. FT-IR spectroscopy is a sensitive technique for investigating the hydrogen bonding in BTAs [19, 27]. The behaviour of fibres during the growth period was studied by observing hydrogen bonding through changes in the FT-IR spectra.

Scanning electron microscopy (SEM) was used to obtain images of fibres during the study period. The change in fibre shape was observed in order to investigate fibre growth as a function of time. SEM images were taken for the BTA derivatives after evaporation of the chloroform from the silicon surface. Different sites of the solution droplet were imaged for each sample. The images provided information to understand the growth behaviour of the fibres.

3.3.1 Fluorescence spectroscopy

Fluorescence is a useful tool for investigating π - π stacking between the aromatic rings. In order to obtain a clear understanding of anthracene π - π stacking, a brief introduction is presented.

Generally, the polyacene moieties are able to pack themselves through π stacking between the aromatic rings. Three types of π - π stacking arrangement can be formed by polyacenes, namely face-to-face, edge-to-face, and end-to-face, as seen in Figure 3- 10 [28-32].

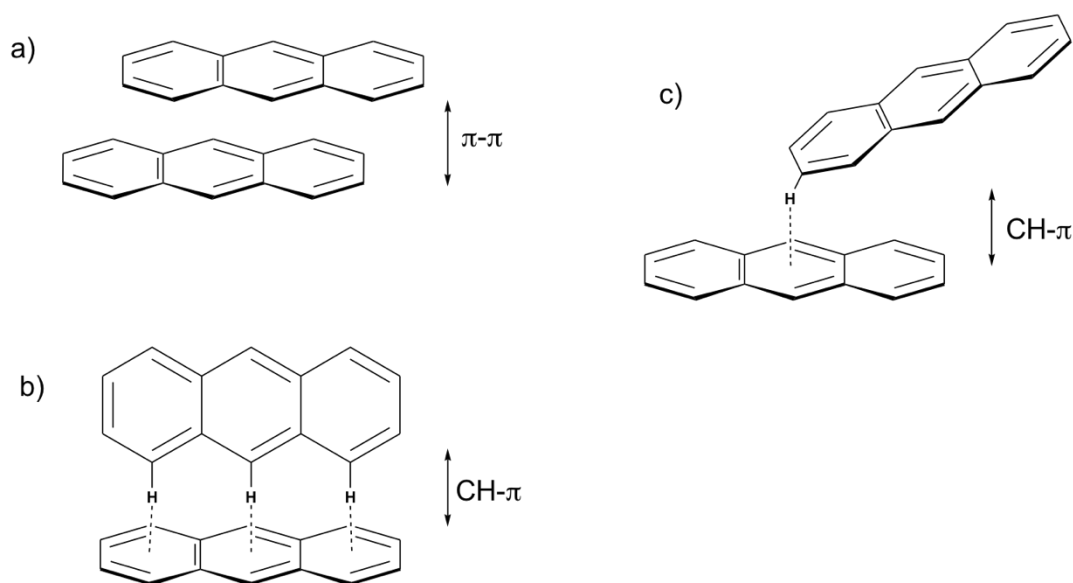


Figure 3- 10. π - π stacking geometries of anthracene (a) face-to-face, (b) edge-to-face, (c) end-to-face, figure was adapted from [33].

Due to the importance of face-to-face π - π stacking in the field of organic optical and semiconductor materials, control of the π - π stacking arrangement is a challenging subject for the development of organic optoelectronic devices. There have been several attempts to control π - π stacking arrangements of polyacenes. For instance, the steric effect of substituents has been utilised to prevent CH- π contact and improve the π - π stacking arrangement [34-37]. The interaction between the substituents, such as halogen-halogen and chalcogen-chalcogen interactions, also played a significant role in the construction of the π - π stacked arrangement of polyacene compounds [38-46].

The hydrogen bonding interaction has also been used to enforce a face-to-face stacking arrangement of aromatic rings. MacGillivray and his colleagues used hydrogen bonding to design the π - π stacked arrangement of anthracene compounds. The π - π stacking or overlapping was largely increased by the anthracene derivative bearing hydrogen bonding sites [47]. Interestingly, there is a correlation between emission peak shift and the degree of overlap between the anthracene moieties. Zhang reported that the emission of an anthracene derivative was strongly related to the overlapping area of the anthracene moieties. An increase in overlapping area produces a greater red shift in the emission peak [48]. Depending on the overlapping angle values (θ) between the longitudinal axes of the monomer transition moments, J-aggregation (slipped-stacking) is induced when the angle $0^\circ < \theta < 54.7^\circ$, whereas an angle of $54.7^\circ < \theta < 90^\circ$ produces the H-aggregation [49], as seen in Figure 3- 11. Interestingly, generally in

BTA derivatives the angle was reported with values of 36.8° , 42.4° and 45.5° , which supported J-aggregation [50]. Park and his colleagues obtained a J-type aggregation of a BTA derivative. The red shift in the photoanalysis, and the calculated angle between the transition moment and the aggregate axis confirmed the aggregation type [51].

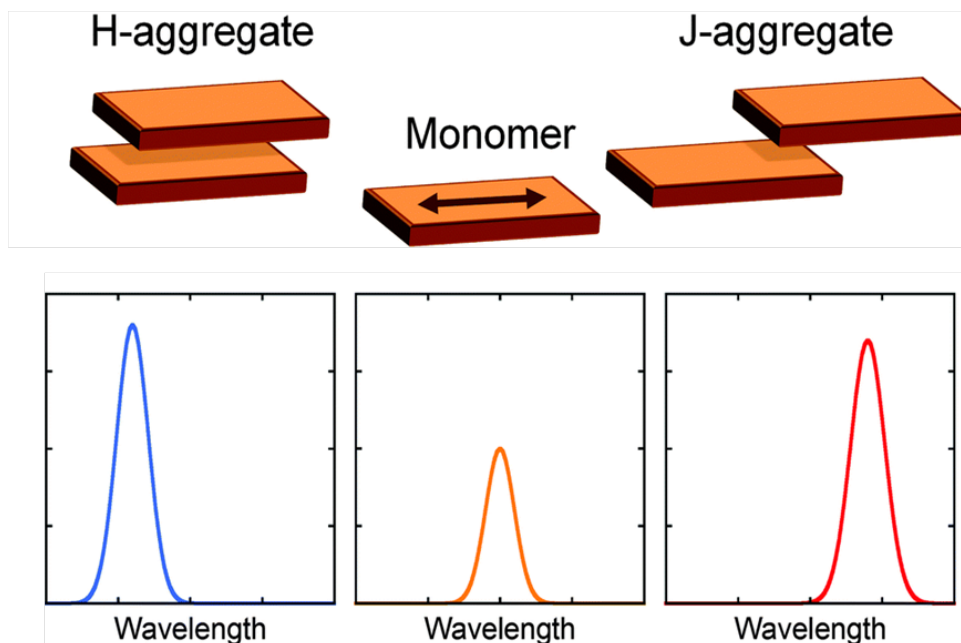


Figure 3- 11. Typical arrangements of H- and J-aggregates for a π -conjugated molecule (monomer) and corresponding effects in the fluorescence spectra [52].

Anthracene derivative aggregation in solution has also been an important subject due to its potential applications, such as fluorescence imaging and light-emitting devices [49, 53-56]. Synthesised anthracene derivatives having an amide group show π - π stacking between anthracene molecules due to the formation of hydrogen bonds between the amide groups. The change in π - π stacking was reflected in the fluorescence emission of the molecule [54, 57]. For instance, Duan and Liu reported that the combination of hydrogen bonding of amide groups and π - π stacking of the anthracene derivatives enhanced the fluorescence emission intensity of the compound. Moreover, the position of the substituted amide group on anthracene was found to be an important factor in its properties. Anthracene with substitution at the 9-position showed increased fluorescence emission in comparison to other positions. This was attributed to the different packing arrangements of the anthracene moiety. In addition, a red shift was observed for other anthracene derivatives and attributed to J-type aggregation [58].

3.3.1.1 Fluorescence analysis of 9AC-2-BTA self-assembly

In order to investigate the behaviour of the short chain length compound's (9AC-2-BTA) self-assembly via π - π stacking between the aromatic rings and H-bonding between amide groups, the fluorescence spectra were recorded as a function of time. The compound was dissolved in chloroform with a concentration of 2 mg mL^{-1} , and the first fluorescence spectrum obtained immediately after solution preparation (0 hours) as seen in Figure 3- 12. An emission peak appeared at 440 nm, which is attributed to isolated anthracene moieties, as reported in the literature [59, 60].

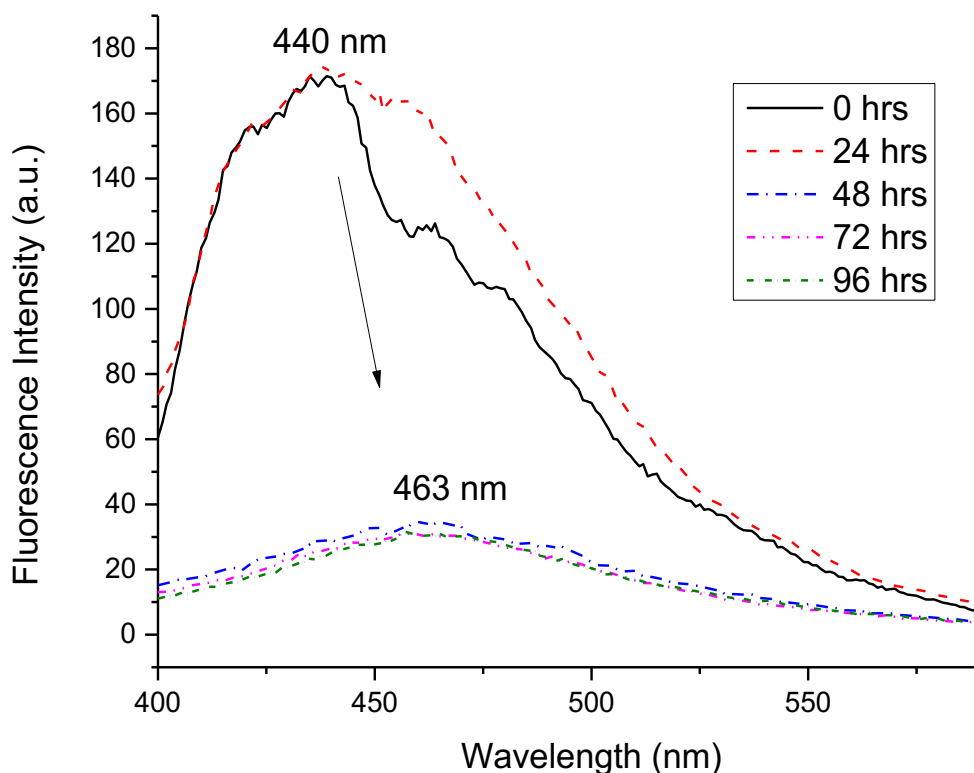


Figure 3- 12. Fluorescence emission spectra of 9AC-2-BTA in chloroform at various self-assembly times at room temperature with concentration (2 mg mL^{-1}).

The effect of a 24-hour aggregation time caused slightly red-shifted emission. With longer aggregation times (48 – 96 hours), a further shift of the emission peak to 463 nm was observed. Quenching of fluorescence emission intensity by around 80% was also observed at these longer aggregation times.

Quenching of the anthracene moiety fluorescence was attributed to the restriction of intermolecular motion as a result of aggregation of the 9AC-2-BTA molecule in solution. Motion restriction could be caused by hydrogen bonding between amide groups, which are at the 9-position on the anthracene moieties. Face-to-face π - π stacking can also restrict the intermolecular motion of the anthracene moieties. This restriction of motion enhanced charge transfer through the π -orbital overlapping of anthracene moieties, which caused quenching of the fluorescence emission intensity [33, 61].

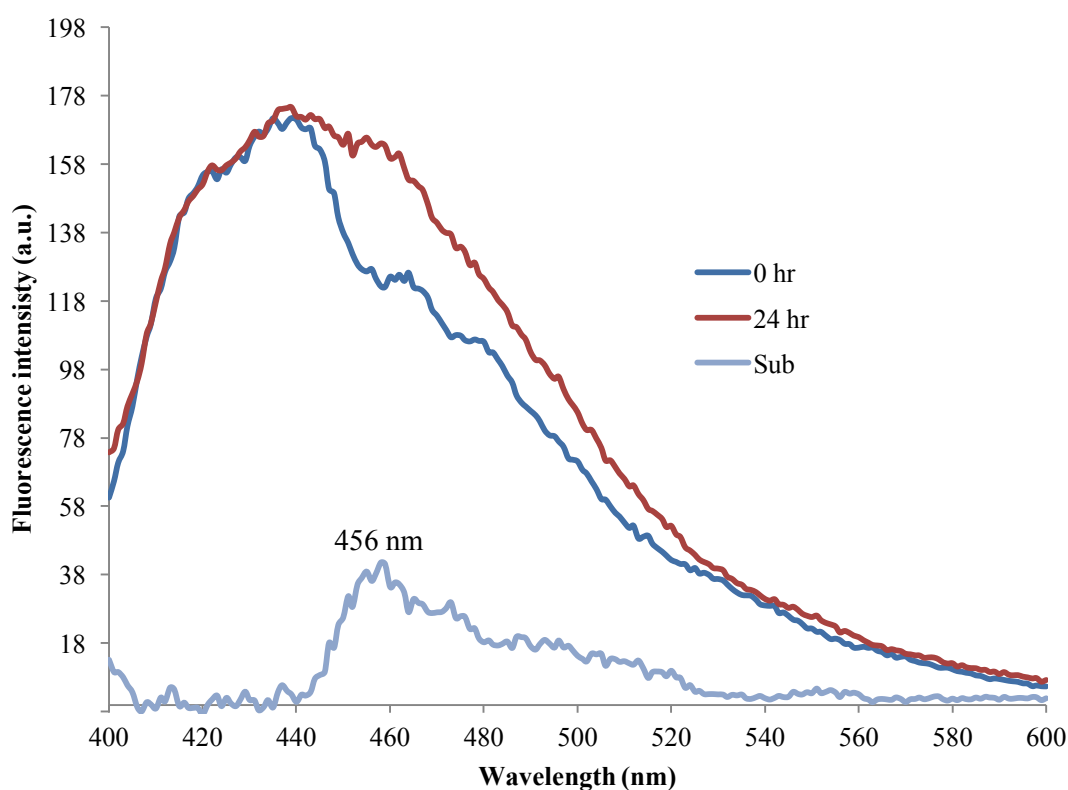


Figure 3- 13. Fluorescence spectrum shifted from 440 nm at 0 hours to 456 nm at 24 hours which indicates aggregation occurrence within 24 hours. To determine the red shift subtraction of the 24 hrs from the 0 hrs spectra was performed.

The red shift in the fluorescence intensity was initially observed at 24 hours. To determine the red shift in fluorescence spectra at 24 hours, the 24 hour fluorescence spectrum was subtracted from the 0 hour fluorescence spectrum. As seen in Figure 3-13, the fluorescence spectrum shifted from 440 nm at 0 hours to 456 nm at 24 hours.

A further shift in the emission peak to 463 nm was observed beyond 24 hours (48-96 hours). It has been discussed that the J-aggregation type, which is illustrated in Figure 3- 11, causes the red-shift in the fluorescence emission [58].

3.3.1.2 Fluorescence analysis of 9AC-8-BTA self-assembly

The longer-chain compound 9AC-8-BTA was dissolved in chloroform at 2 mg mL^{-1} concentration. The fluorescence analysis was conducted for the solution with different aggregation times, as shown in Figure 3- 14. The first fluorescence emission showed a maximum peak at 427 nm at 0 hours, which agreed with the anthracene monomer emission in the literature [59, 60].

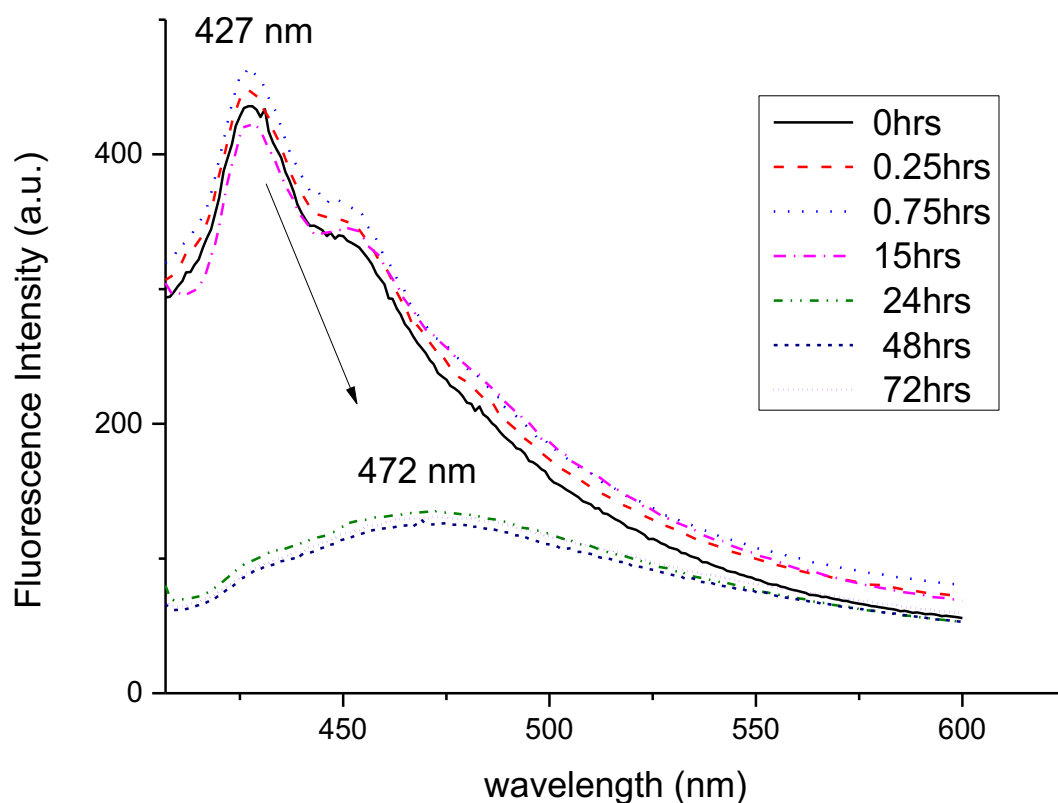


Figure 3- 14. Fluorescence emission spectra of 9AC-8-BTA in chloroform (2 mg mL^{-1}) with various self-assembly times at room temperature.

As seen in Figure 3- 14, initially there was a slight increase in fluorescence intensity at 427 nm for aggregation times from 0-0.75 hours. This increase, with no change in the wavelength, was attributed to packing of the anthracene moieties through hydrogen bonding of the amide groups that were substituted at the 9-position on the anthracene.

At 15 hours, the fluorescence intensity showed a slight decrease, and at 24-72 hours, quenching of fluorescence by around 80% was observed.

Quenching of fluorescence was attributed to the aggregation of anthracene moieties through hydrogen bonding and π - π stacking (face-to-face), which perturbed the electronic nature of the anthracene. This aggregation restricted the molecules' motion and enhanced the charge transfer through the π -orbital overlapping of anthracene moieties [33, 62-65].

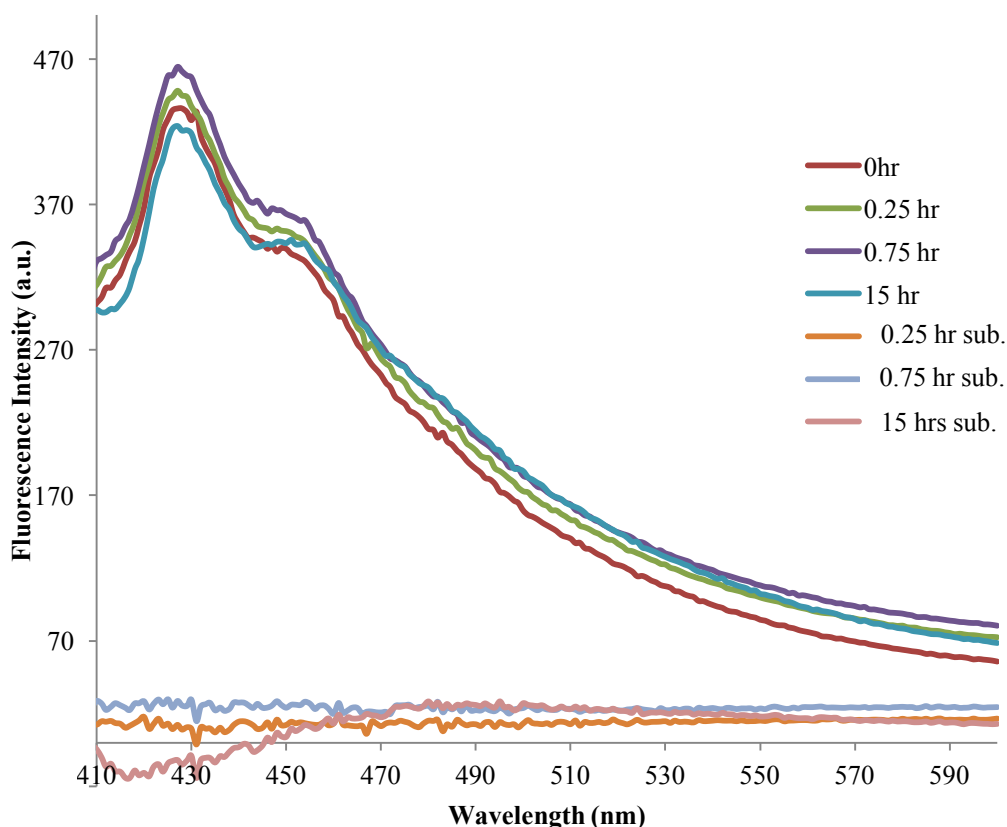


Figure 3- 15. Red shift was not observed in fluorescence spectra in time up to 15 hr which was shown by subtractions of 0.25 hr, 0.75 hr and 15 hr spectra from 0 hr spectrum.

The fluorescence emission showed a red shift from 427 nm at the initial aggregation time (0-15 hours) to 472 nm at 24-72 hours. The red shift was attributed to the J-aggregation of anthracene moieties, as represented in Figure 3- 15. At the initial aggregation time (0-15 hours), there was an absence of anthracene moiety aggregation. Subtraction of spectra at 0.25, 0.75 and 15 hours from 0 hours, as seen in Figure 3- 15, confirmed this absence of aggregation. However, for longer aggregation times (24-72 hours), the fluorescence showed a red shift of 45 nm, which was attributed to the J-

aggregation of anthracene moieties through the π - π stacking (face-to-face) and hydrogen bonding of substituted amide groups at the 9-position on the anthracene moieties [33, 62-65].

3.3.1.3 Fluorescence analysis differences

Despite the aggregation of both compounds being carried out in equivalent conditions, such as concentration, temperature, solvent and aggregation time, there was a difference in the fluorescence behaviour. According to the chemical structure of the compounds, as seen in Figure 3- 16, only the aliphatic chain length between the BTA core and the anthracene is different. The increase in aliphatic chain length increases the flexibility of the compound [66-69]. Therefore, the compound with a longer chain length (9AC-8-BTA) is more flexible than the short chain compound (9AC-2-BTA).

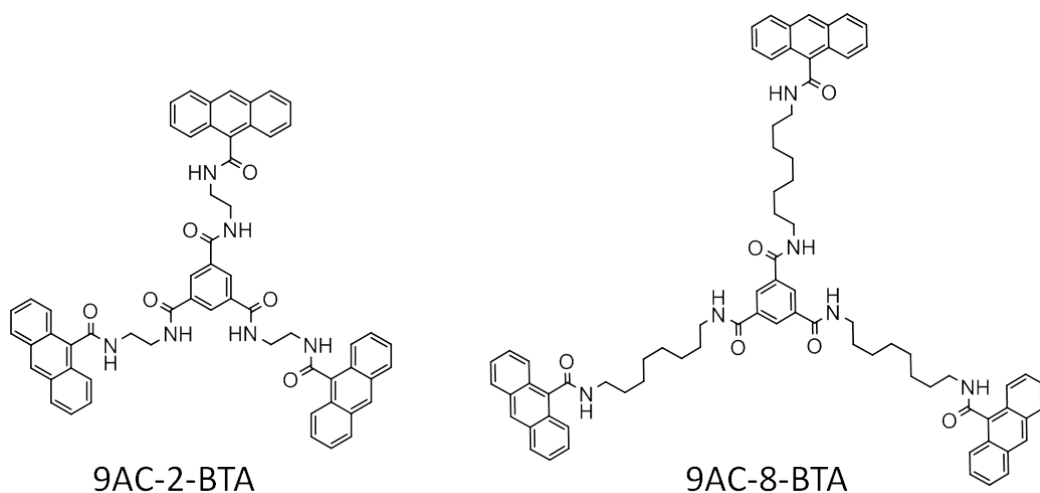


Figure 3- 16. Chemical structures of the investigated aggregation compounds showing the difference only in the aliphatic chain length.

Zhang and his colleagues reported that the flexibility of the molecule affected the anthracene moiety emission. It was found that the flexibility of anthracene compounds was related to the overlapping area between the stacked anthracene moieties. Greater red shift in the emission peak was caused by larger overlapping area of the more flexible compound[48].

Due to the variation in flexibility of the investigated compounds, the red shift for 9AC-8-BTA was almost double that of 9AC-2-BTA. The shift was 23 nm for 9AC-2-BTA,

whereas for the more flexible compound 9AC-8-BTA it was about 45 nm. This shows that the overlapping between the anthracene moieties in the more flexible compound 9AC-8-BTA was larger in area than in the less flexible compound 9AC-2-BTA, as illustrated in Figure 3- 17. Therefore, the self-quenching occurred faster in the flexible compound 9AC-8-BTA than in the less flexible compound 9AC-2-BTA. Quenching was observed at 48 hr in the 9AC-2-BTA, while 9AC-8-BTA showed quenching at 24 hr.

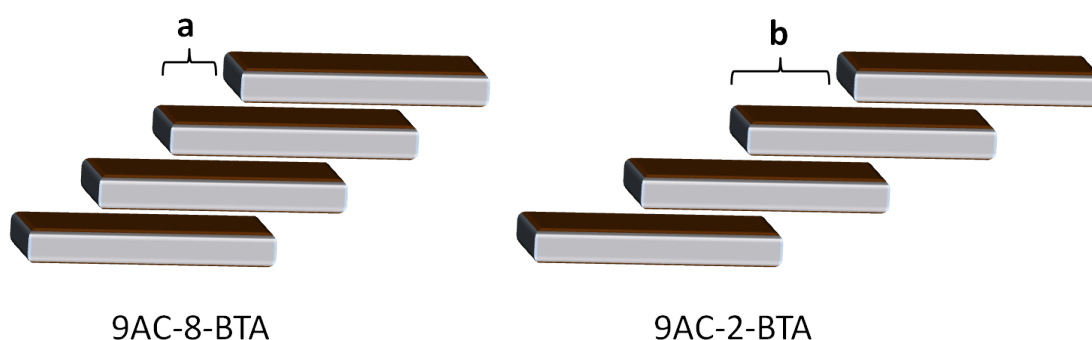


Figure 3- 17. Scheme showing the effect of flexibility of the compounds on the overlapping area ($a > b$) between the anthracene moieties.

Table 3-2. Fluorescence intensity of the flexible compound (9AC-8-BTA) and the less flexible compound (9AC-2-BTA); (AI = arbitrary units).

Time	9AC-2-BTA		9AC-8-BTA	
	Maximum Peak (nm)	Intensity (AI)	Maximum Peak (nm)	Intensity (AI)
0 hrs	440	174	427	435
24 hrs	442	174	472	134
48 hrs	463	34	472	130
72 hrs	463	31	472	131

Furthermore, the intensity of the fluorescence was different for each compound. Table 3-2 shows that the intensity of the fluorescence at 0 hr was 174 and 435 for the less flexible compound (9AC-2-BTA) and the flexible compound (9AC-8-BTA) respectively. Even after quenching, the flexible compound shows higher fluorescence emission than the less flexible compound. This may be attributed to the long chain giving the anthracene moieties more free motion than the short chain, even after aggregation.

3.3.2 FT-IR spectroscopy

Fluorescence data was limiting, as no change was observed in fluorescence intensity with an aggregation time longer than 24 hours, due to fluorescence quenching. Therefore, FT-IR was used to investigate the growth behaviour of the aggregation through hydrogen bond formation. Hydrogen bonds are formed when a donor (D) with an available acidic hydrogen atom interacts with an acceptor (A). The acceptor has to be carrying available non-bonding electron lone pair to be able to form hydrogen bonds. The strength of the hydrogen bonds depends mainly on the solvent, as well as number and sequence of both the hydrogen-bond donors and acceptors [71-73]. Hydrogen bonding is widely used in self-assembly processes because hydrogen bonds are directional and moderately strong [73]. It is known that BTA derivatives are self-assembled via hydrogen bonding as one of the most useful interaction forces [19, 27]. As illustrated in Figure 3-18, the three amide bonds are capable of forming hydrogen bonds between the BTA molecules, which builds a columnar stacking of the molecules [74, 75].

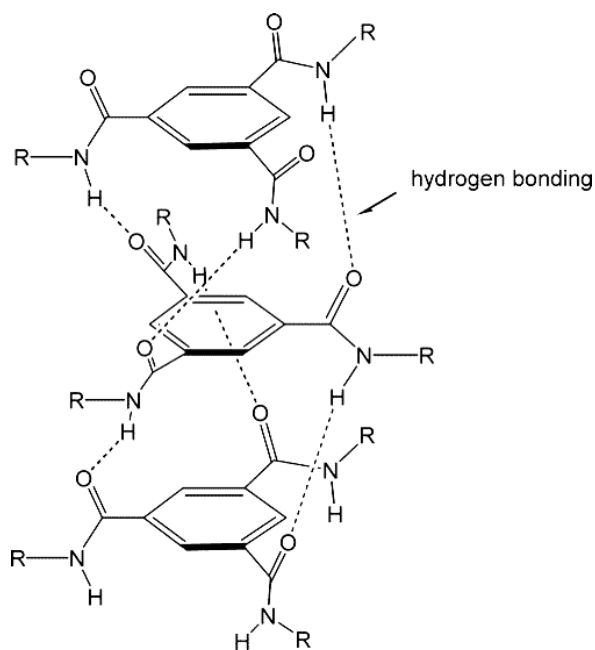


Figure 3-18. Hydrogen bonding interaction of BTA derivatives resulting in self-assembly of the derivatives.

Observation of changes in the FT-IR spectra was used to follow the growth behaviour of aggregates as a function of time. As for the fluorescence studies, the two molecules were dissolved separately in chloroform at 2 mg mL⁻¹ concentration.

The solutions were left at room temperature during the investigation. A drop was cast on the FT-IR crystal at various times after the initial preparation of the chloroform solution.

3.3.2.1 FT-IR analysis of 9AC-2-BTA self-assembly

The self-assembly behaviour of the aggregates was studied by observing the change in the FT-IR spectrum as a function of time. It can be seen in Figure 3- 19 that the 9AC-2-BTA compound shows bands at 3310 cm^{-1} , 1660 cm^{-1} and 1530 cm^{-1} , which were attributed to the N-H stretching, hydrogen bonded C=O stretching (amide I) and amide II (N-H bending and C-N stretching vibrations), respectively [19, 22, 24, 25]. The other bands are listed in Table 3-3.

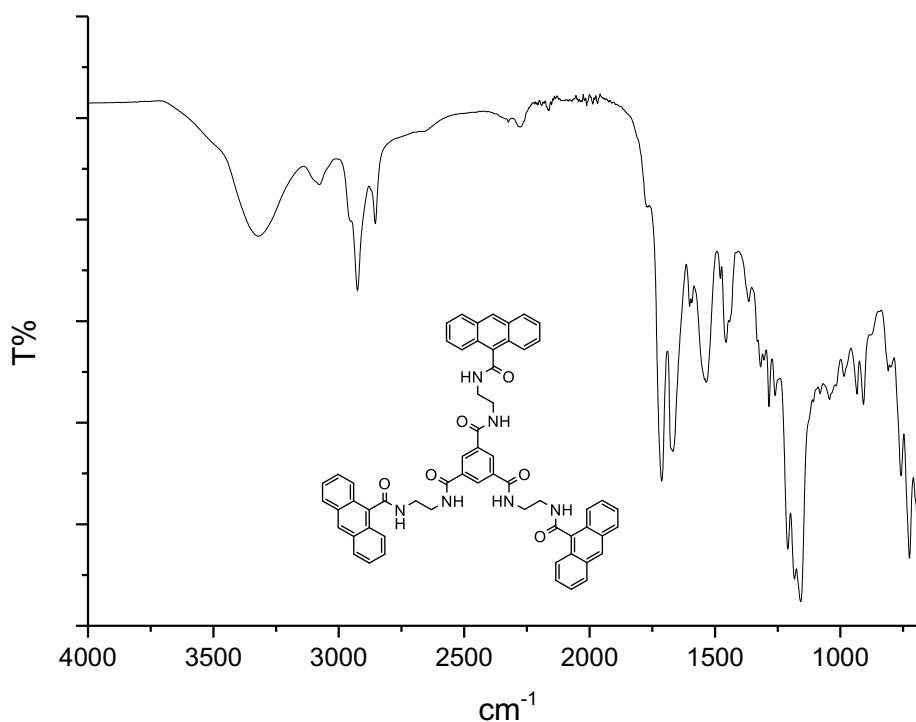


Figure 3- 19. ATR-FTIR spectrum of freshly made solution of 9AC-2-BTA in chloroform at room temperature.

Table 3-3. ATR-FTIR peaks observed for 9AC-2-BTA compound.

band/cm ⁻¹	Assignment	References
3078	Aromatic C-H stretching	[21-23]
2926	Asymmetric vibrations of alkyl chain	[22, 76]
2854	Symmetric vibrations of alkyl chain	[22, 76]
1715	Aromatic C-H out of plane vibrations/ Aromatic C=C enhanced by C=O conjugation	[21-23]
1456	Ring breathing vibration	[21-23]
1160	Symmetric bonding of aliphatic CH ₂	[22, 77]

Standing in chloroform solution at room temperature caused a change in the ATR-FTIR spectrum over time. The changes mainly occurred at the N-H band and the carbonyl band regions. Therefore, they will be discussed separately in the following sections.

Carbonyl bands

It has been reported that the compounds containing amide groups can show more than one carbonyl band between 1600 cm⁻¹ and 1700 cm⁻¹ [78-81]. These bands occur due to the variable distances and geometries of the hydrogen bonds [82, 83]. The carbonyl associated with ordered hydrogen bonding is located at lower wavenumbers than the carbonyl associated with disordered hydrogen bonding.

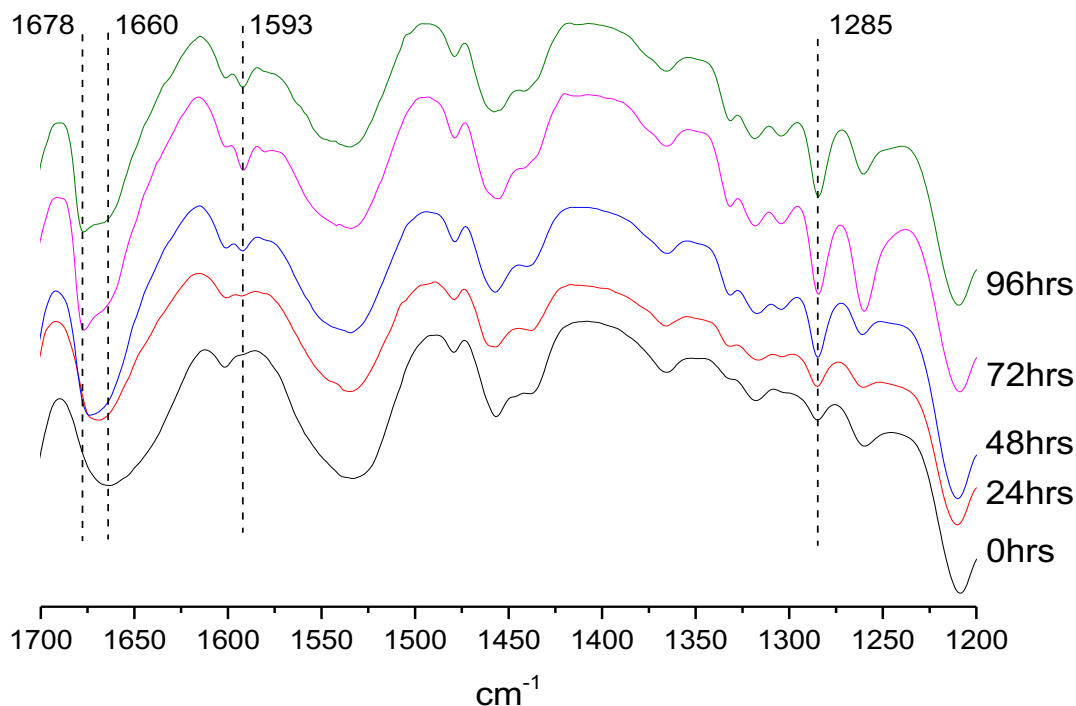


Figure 3- 20. ATR-FTIR spectra of 9AC-2-BTA as a function of time.

Inspection of Figure 3- 20 reveals that the carbonyl band at 1660 cm^{-1} changed as a function of time. At aggregation times less than one hour (0 hr) the carbonyl band appeared at 1660 cm^{-1} , whereas shifts to higher frequencies were observed at 24 hrs and 48 hrs. Two bands can be distinguished at aggregation times as long as 72 hrs and 96 hrs. A new carbonyl band appeared at 1678 cm^{-1} , in addition to the 1660 cm^{-1} band, which can be attributed to carbonyl groups with disordered and ordered hydrogen bonded carbonyl groups respectively.

It is known that the BTA derivatives form a columnar structure of fibres as a result of self-assembly [74, 75]. These fibres may aggregate and twist around each other after long aggregation times, forming bundles. Fibre twisting changes the length and geometric structure of the hydrogen bonds, and due to this, disordered hydrogen bonds appear [82, 83].

Further investigation of the change in geometric structure of the hydrogen bonds can be obtained by inspection of the change in amide III band intensity at 1285 cm^{-1} , which corresponds to the disordered structure [84-86]. The amide III band is attributed to N-H bonding and C-N stretching vibration [84-86]. Inspection of Figure 3- 20 reveals that the amide III intensity at 1285 cm^{-1} increased as aggregation time was increasing.

This was attributed to the increase in the disordered structure of hydrogen bonds as a function of aggregation time. This change in the amide III intensity was consistent with the change in the amide I band from ordered to disordered hydrogen bonds. Therefore, this change in the geometric structure of the hydrogen bonds can be attributed to the fibres twisting and forming bundles.

Moreover, π - π stacking between the aromatic rings can be observed at 1593 cm^{-1} , which is due to the benzene ring skeleton vibrations. The intensity of this band increased as the aggregation between the molecules through π - π stacking increased as a function of time [76].

N-H band

Hydrogen bond alteration can also be observed by inspection of the N-H band at 3310 cm^{-1} , as illustrated in Figure 3- 21. The shift to higher frequency from 3310 cm^{-1} to 3319 cm^{-1} and 3322 cm^{-1} at 24 hr and 48 hr respectively was observed, while no further shifts were observed at 72 hr and 96 hr. This shift to higher frequency of the N-H band also indicates changes in hydrogen bond distances and geometries during the aggregation period.

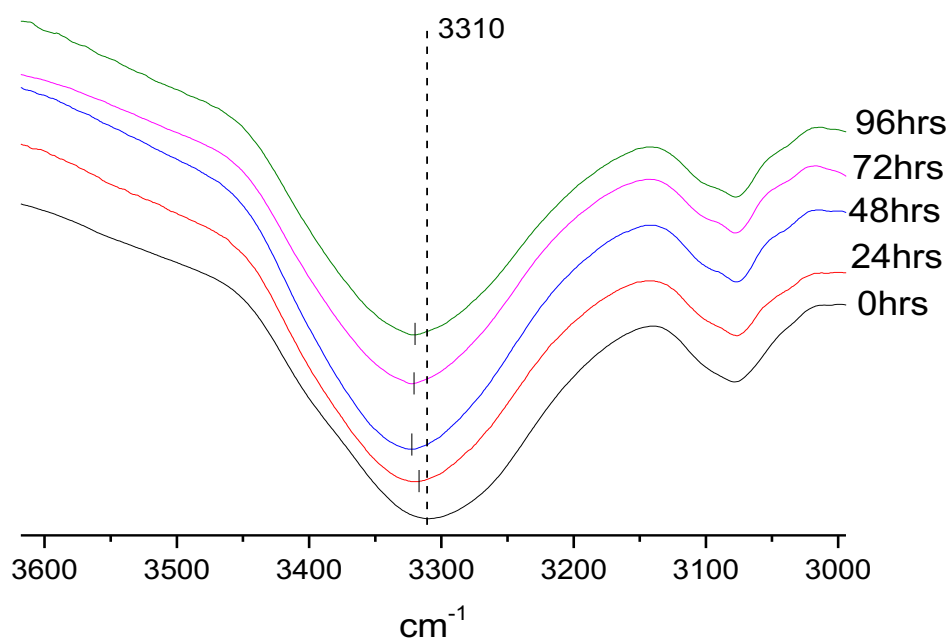


Figure 3- 21. ATR-FTIR spectra of 9AC-2-BTA N-H band at 3310 cm^{-1} showing a shift to high frequency.

3.3.2.2 FT-IR analysis of 9AC-8-BTA self-assembly

The molecule with the longer aliphatic chain, (C_8) 9AC-8-BTA, has an ATR-FTIR spectrum as seen in Figure 3- 22. Bands at 3270 cm^{-1} , 1642 cm^{-1} , and 1534 cm^{-1} represent the N-H stretching band, hydrogen bonded C=O stretching (amide I), and amide II (N-H bending and C-N stretching vibrations), respectively [19, 24, 25]. The other bands are listed in Table 3-4.

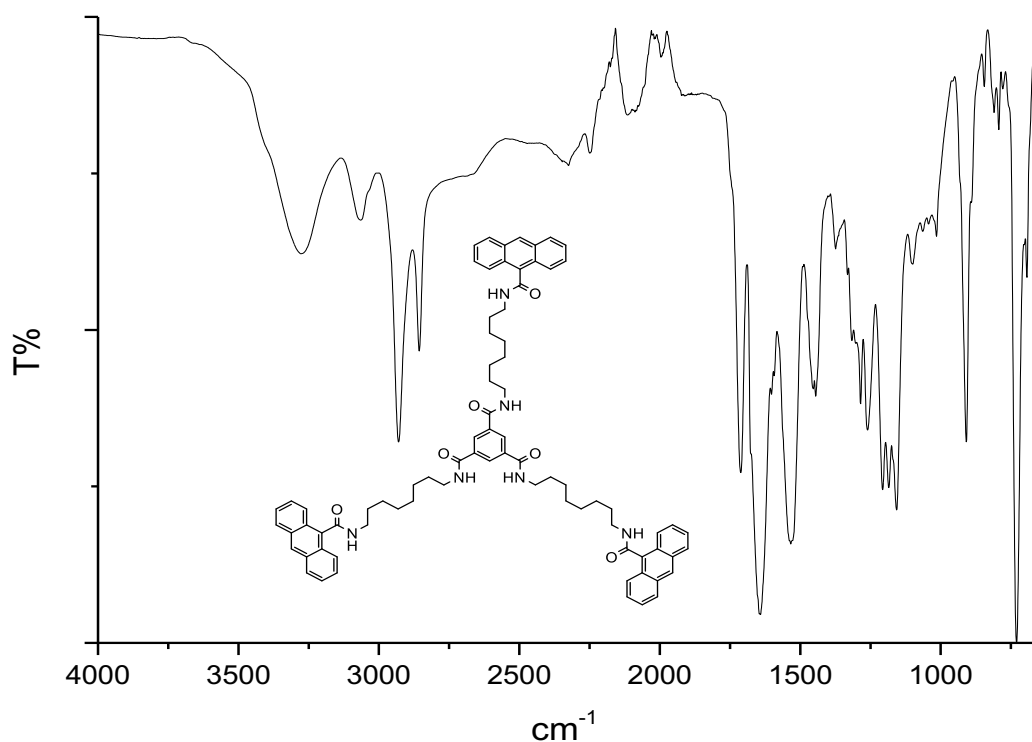


Figure 3- 22. ATR- FTIR spectra of freshly made solution of 9AC-8-BTA in chloroform at room temperature.

Table 3-4. ATR-FTIR peaks observed for the 9AC-8-BTA compound.

band/cm ⁻¹	Assignment	References
3065	Aromatic C-H stretching	[21-23]
2930	Asymmetric vibrations of alkyl chain	[22, 76]
2856	Symmetric vibrations of alkyl chain	[22, 76]
1712	Aromatic C-H out of plane vibrations/ Aromatic C=C enhanced by C=O conjugation	[21-23]
1442	Ring breathing vibration	[21-23]
1159	Symmetric bonding of aliphatic CH ₂	[22, 77]

The changes in FT-IR spectra bands as a function of time were investigated. Like 9AC-2-BTA, bands at 3270 cm⁻¹ and 1642 cm⁻¹ showed changes within the investigation period. Therefore, following the changes in these bands will assist in understanding the growth behaviour of the investigated molecule. In the following sections the bands will be discussed separately.

Carbonyl bands

The 9AC-8-BTA FT-IR spectra in the region from 1600 cm⁻¹ to 1700 cm⁻¹ as a function of time are displayed in Figure 3- 23. In the first spectrum, which was recorded immediately after dissolving in chloroform (represented as 0 hr), a carbonyl band was observed at 1642 cm⁻¹. There also was small shoulder at 1677 cm⁻¹. As mentioned before, carbonyl bands can have more than one band, depending on distances and geometries of hydrogen bonds [83, 84]. These bands are ascribed as carbonyls associated with ordered hydrogen bonding, which is located at lower wavenumbers than the carbonyl associated with disordered hydrogen bonding [82, 83].

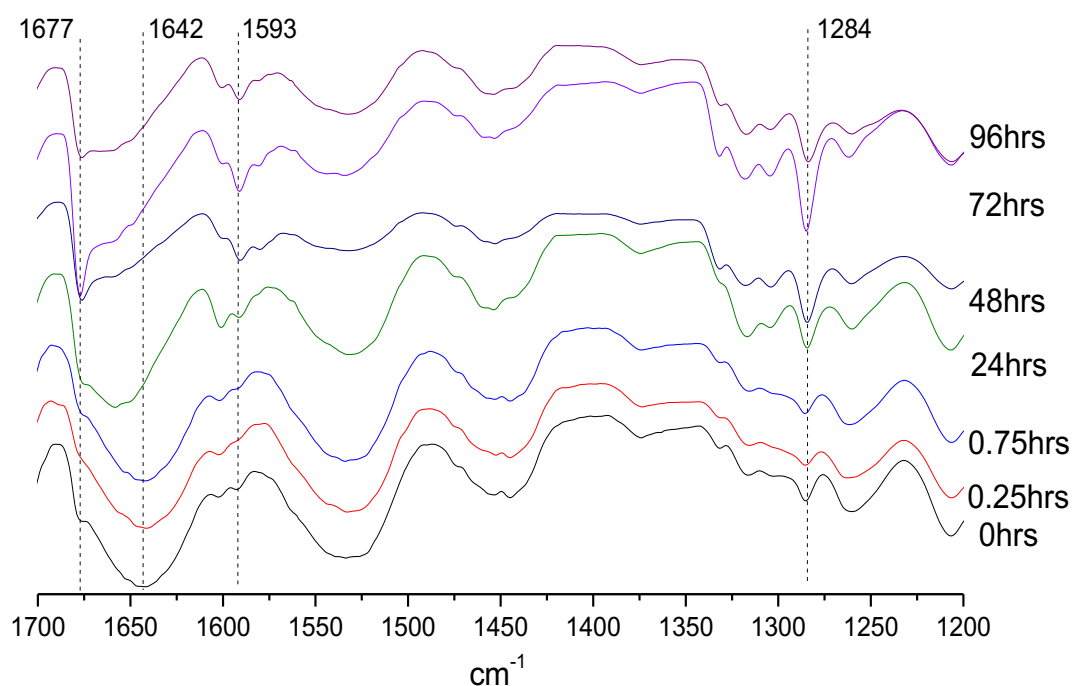


Figure 3- 23. ATR-FTIR spectra changes of 9AC-8-BTA as a function of time.

Leaving the molecules in the chloroform solution for less than 24 hours produced no shift in the band at 1642 cm^{-1} . However, a shift to 1658 cm^{-1} was observed after 24 hours in the solution, which is consistent with the fluorescence results. Aggregation times longer than 24 hours showed an increase in the shoulder intensity at 1677 cm^{-1} due to the disordered hydrogen-bonded carbonyl. This change in the carbonyl band is attributed to the fibres twisting around each other to form bundles. As a consequence, lengths and geometries of the hydrogen bonds are changed.

Further inspection of Figure 3- 23 revealed that there was an increase in the intensity of the 1284 cm^{-1} band as the aggregation time increased. This band was attributed to N-H bonding and C-N stretching vibration, namely amide III [84-86]. Due to the sensitivity of this band to the change in geometric structure of the hydrogen bonds, it was used to confirm the change in the hydrogen bond structure from ordered to disordered as a result of the fibres twisting. The observed changes in amide III were consistent with the changes in amide I, confirming the change in the hydrogen bond geometry.

Moreover, π - π stacking between the molecules was investigated by observing the intensity change in the band at 1593 cm^{-1} , which is due to the benzene ring skeleton vibrations [76]. As seen in Figure 3- 23, the intensity of this band changed through the

investigation period as a result of forming BTA fibres through π - π stacking between the aromatic moieties.

N-H band

The change in the hydrogen bonds can also be observed by inspection of the N-H band at 3270 cm^{-1} , as illustrated in Figure 3- 24. The shift to higher frequency, from 3270 cm^{-1} to 3297 cm^{-1} , was observed only after 24 hours in the chloroform solution, while no further shifts were observed for longer standing times. This shift to a higher frequency for the N-H band also indicates the changes in hydrogen bond distances and geometries during the aggregation time.

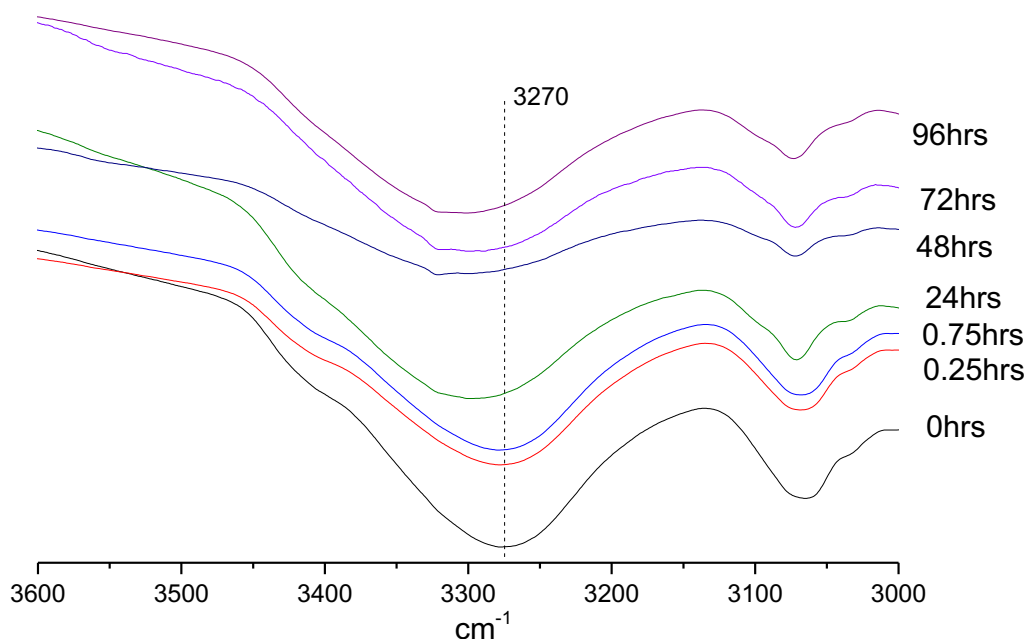


Figure 3- 24. ATR-FTIR of 9AC-8-BTA at various aggregation times showing shift of N-H band at 3270 cm^{-1} .

The conclusion from the FT-IR results was that aggregation of the BTA molecules was formed through hydrogen bonding. The geometric structure of the hydrogen bonds changed as a function of time. Twisting of the formed fibres around each other to form bundles and longer fibres was considered to be the reason for the structural change in the hydrogen bonds. In the following section, SEM images have been used to visualise the fibre growth and twisting.

In addition, π - π stacking between the aromatic moieties contributed to formation of the fibres. Compared with the fluorescence results, the red shift as a result of the J-aggregation between aromatic moieties occurred at an aggregation time of 24 hours for all molecules investigated. This was consistent with the intensity increase of the π - π stacking band at 1593 cm^{-1} , which was initially observed at 24 hours, as seen in Figure 3- 20 and Figure 3- 23.

3.3.3 SEM analysis

The next technique that was used to study aggregation was SEM. It was used to visualise the aggregation behaviour of the molecules as a function of time. The chloroform solution droplet was placed on a washed silicon wafer surface and left to evaporate at room temperature. Aggregates were observed with different shapes and at different positions on the surface after solvent evaporation.

Due to the importance of solute distribution on the surface during the evaporation of solvent in many scientific and industrial processes, controlling the distribution has been attempted previously [87-91]. For instance, protein crystallographers are attempting to use evaporation driven convection to assemble two-dimensional protein crystals. In the paint industry, a variety of additives are used to ensure a high level of pigment remains in solution and is well dispersed following drying processes [92, 93].

The aggregation of solute on a surface is thought to occur by a physical process, which is called the coffee-stain mechanism. The coffee-stain mechanism explains the formation of rings by solution droplets, where the evaporation is faster on the outer edges of droplets than on the inside surface, as illustrated in Figure 3- 25. The contact line is pinned and evaporation causes a flow within the droplet that drives the solutes to the outside, where they are deposited and form the rings [74, 94].

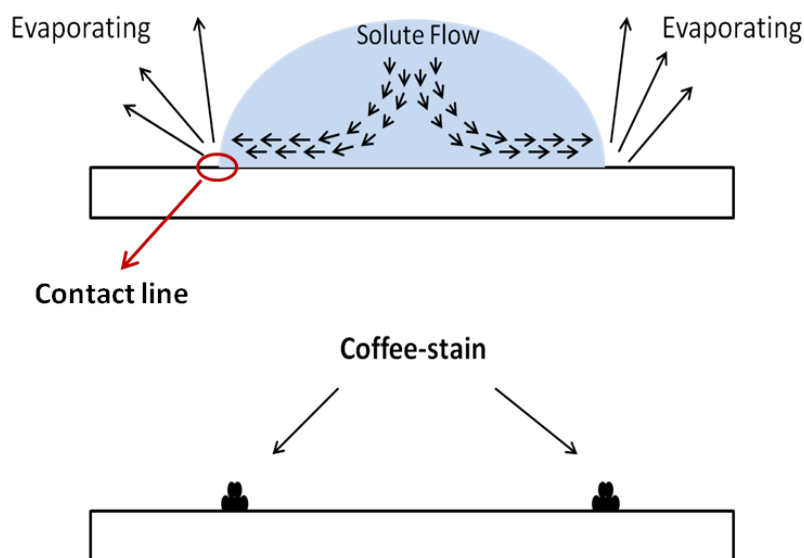


Figure 3- 25. Solute flow showing that differential evaporation rates at the edge and middle drive the solute to the edges, leading to the coffee-stain formation [95].

The chemical structure of the solute also influences the solute aggregation when a drop is cast on the surface. The ability of the solute to assemble itself through π - π stacking and hydrogen bonding is essential to obtain uniform aggregates [96]. Van Hameren and his colleagues designed a compound consisting of three porphyrin moieties that were connected to the BTA core via amide bonds [74]. The ability of these BTA derivatives to form columnar stacking via π - π stacking and hydrogen bonding caused an improvement in porphyrin aggregation. In contrast to other porphyrin compounds [97, 98], highly uniform patterns of linear aggregates were formed upon chloroform solution evaporation. Consistent stacking of bundles was obtained, with lengths up to almost 1 mm [74].

3.3.3.1 Self-assembly of short-chain compound 9AC-2-BTA

SEM images were used to study the aggregation behaviour of 9AC-2-BTA in chloroform. Droplets of chloroform solution were placed on a clean silicon wafer surface. The aggregation time in chloroform was varied between these samples, starting from less than one hour (0 hr), 24, 48, 72 and 96 hrs. Investigation of aggregate behaviour was obtained by imaging the centre and the edge of where the droplet was placed on the wafer.

At the droplet centre, there was no observation of 9AC-2-BTA aggregates at 0 hr, whereas some small aggregates appeared after 24 hrs, as seen in Figure 3- 26.

Numerous aggregates appeared, albeit small in size, after 48 and 72 hrs aggregation times, while at 96 hrs fewer aggregates were observed. The appearance of aggregates at 24, 48 and 72 hrs may be attributed to the time being sufficient to form reasonable size aggregates, while short aggregation time was not. At 96 hrs, large aggregates were formed, but according to the coffee-stain mechanism, the aggregates were shifted to the droplet edge by solvent flow.

At the droplet edge, fibres were observed for all aggregation times, even at 0 hr, as shown in Figure 3- 28. Very few fibres were observed (scale bar is 50 μm) at 0 hr, which may be due to insufficient time to form large aggregates in the solution. The shape (length and width) and the quantity of fibres increased as aggregation time increased.

The solute flow to the droplet edge (contact line) caused a shift of aggregates from the centre of the droplet to the contact line. Figure 3- 27 illustrates the formation of linear fibres rather than the ring shape of the contact line (according to the coffee-stain mechanism), which may be attributed to the fact that there are not enough compound present in solution to form a ring shape during the evaporation. The prior aggregation of compounds in the solution (according to the fluorescence results) was also thought to partially trap the solvent, hindering retraction of the contact line [74].

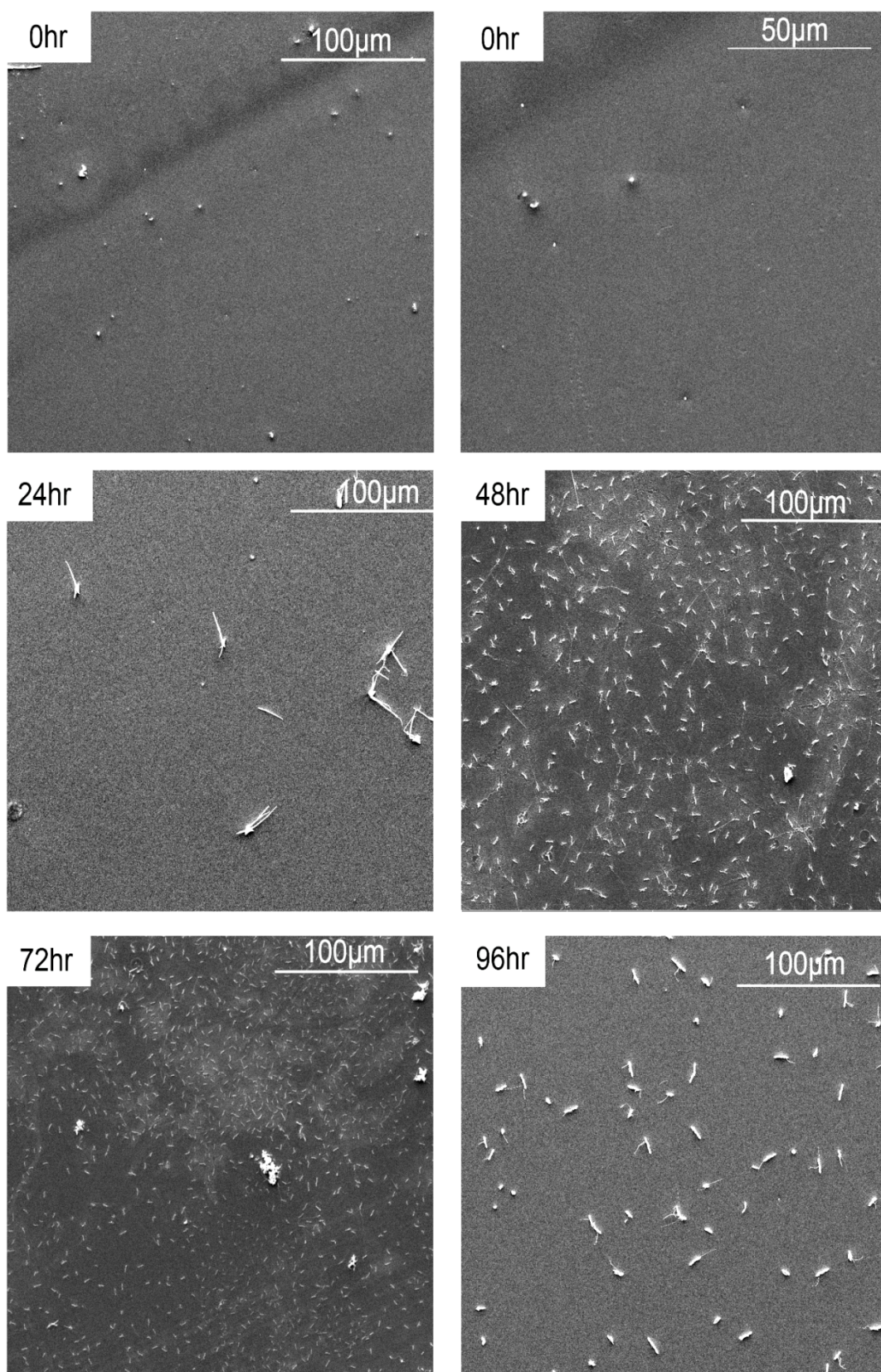


Figure 3- 26. SEM images of 9AC-2-BTA at the centre of the chloroform droplet for different aggregation times.

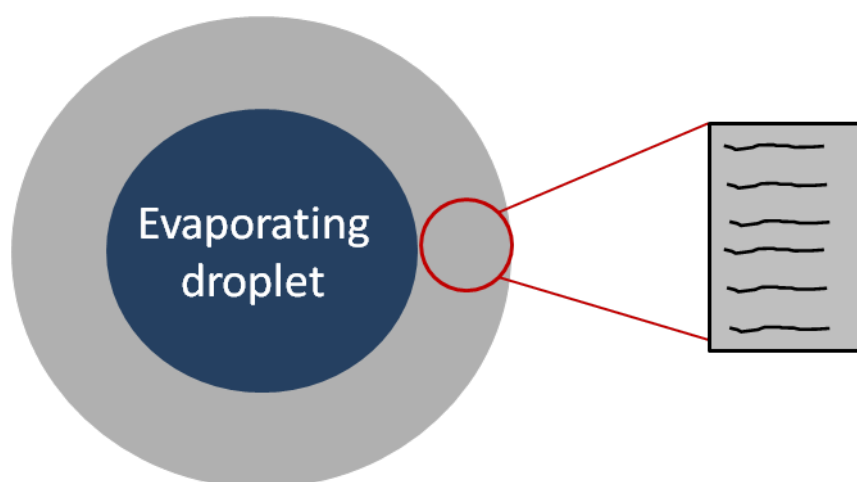


Figure 3- 27. The formation of linear fibres instead of a ring shape as a result of aggregation occurring in the chloroform solution.

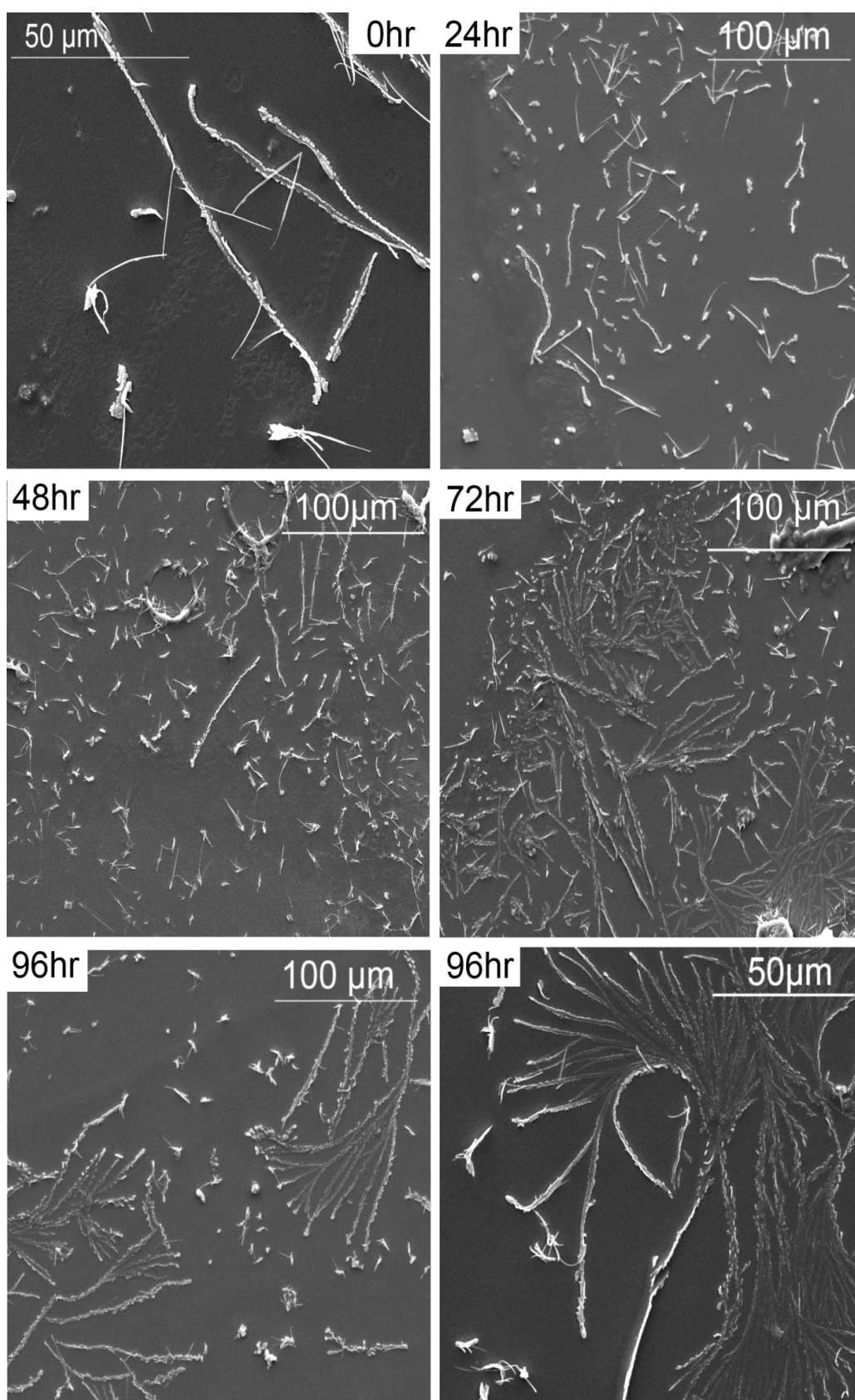


Figure 3- 28. SEM images of 9AC-2-BTA at the edge of the chloroform droplet for different aggregation times.

3.3.3.2 Self-assembly of longer-chain compound 9AC-8-BTA

The aggregation behaviour of 9AC-8-BTA in chloroform was also investigated by SEM. In a similar manner to previously outlined, droplets of chloroform solution were placed on a clean silicon wafer surface, with aggregation times starting from immediately upon dissolving (0 hr) to 0.25, 0.75, 15, 24, 48, 72 and 96 hrs. Investigation of the aggregate behaviour was obtained by imaging the centre and the edge of where the droplet was placed on wafer.

At the centre of the droplet, with short aggregation times (0 hr and 0.25 hr), there was no observation of aggregates, but at 0 hr some impurities were observed as seen in Figure 3- 29. Small aggregates were seen at 0.75 and 15 hrs, while fibres were observed for times longer than 15 hrs as shown in Figure 3- 29. The formation of small aggregates and fibres at the droplet centre in comparison to the edge is attributed to the low concentration in the centre compared with the edge. According to the coffee-stain mechanism, as illustrated in Figure 3- 25, at the contact line (droplet edge) solute concentration is higher than the middle of the droplet due to the solute flow to the fast evaporation point of the solvent at the edge [74].

At the droplet edge, the 9AC-8-BTA was able to form very long fibres with length around 1 mm at 96 hrs of aggregation in chloroform. For shorter times, aggregates were observed. However, small and short fibres were seen for aggregation times longer than 0.25 hr, as seen in Figure 3- 30. Due to the presence of molecule aggregation and insufficient compound in the solution before drop casting on the surface, pinning of the contact line occurred less often than in the 9AC-2-BTA [74]. Therefore, retraction of the contact line was hindered by partial pinning of the molecule at the solvent front. The partial pinning caused a flow of aggregates to the contact line, forming growing fibres orientated to the solvent front.

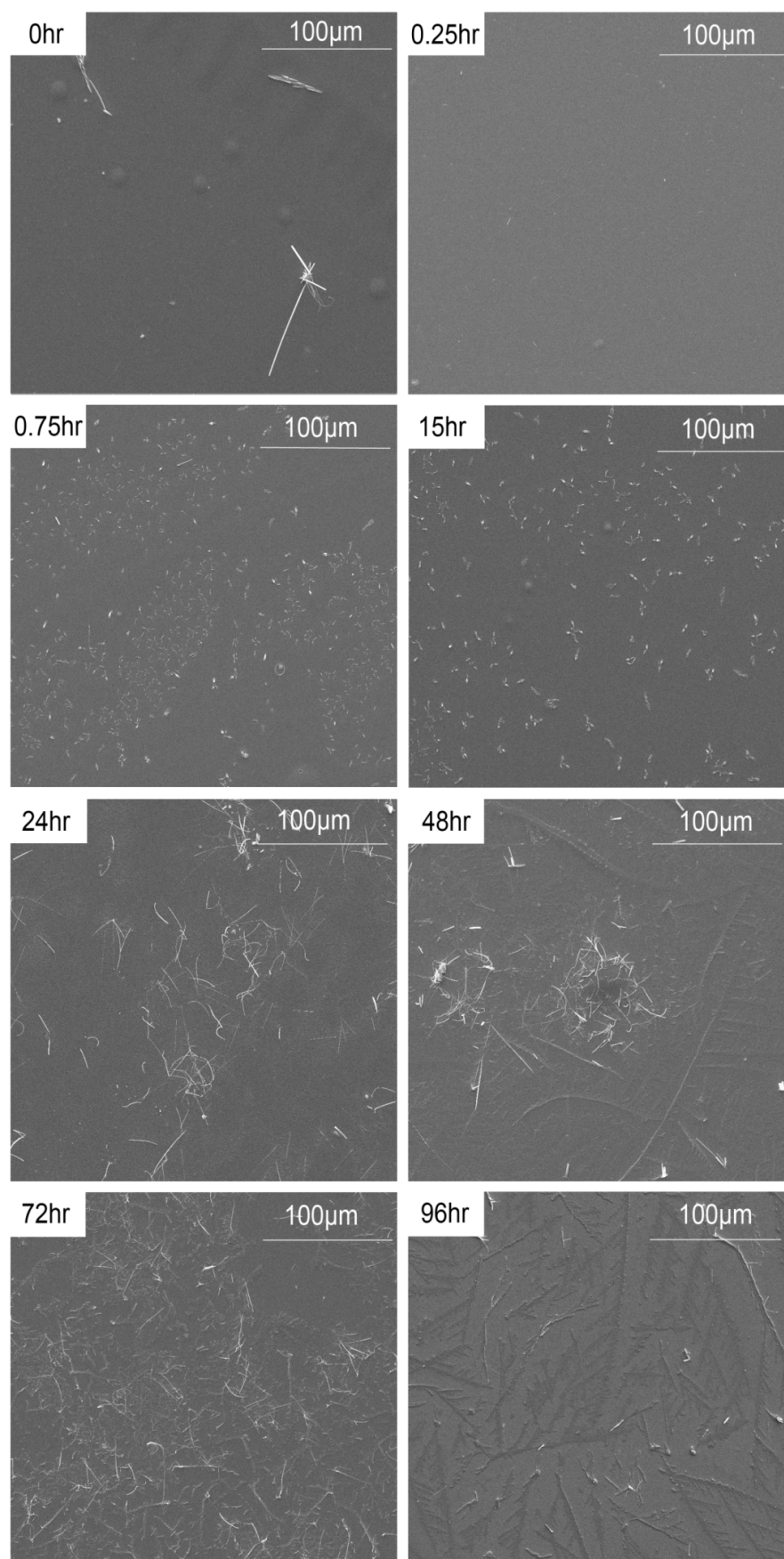


Figure 3- 29. SEM images of 9AC-8-BTA at the centre of the chloroform droplet at different aggregation times.

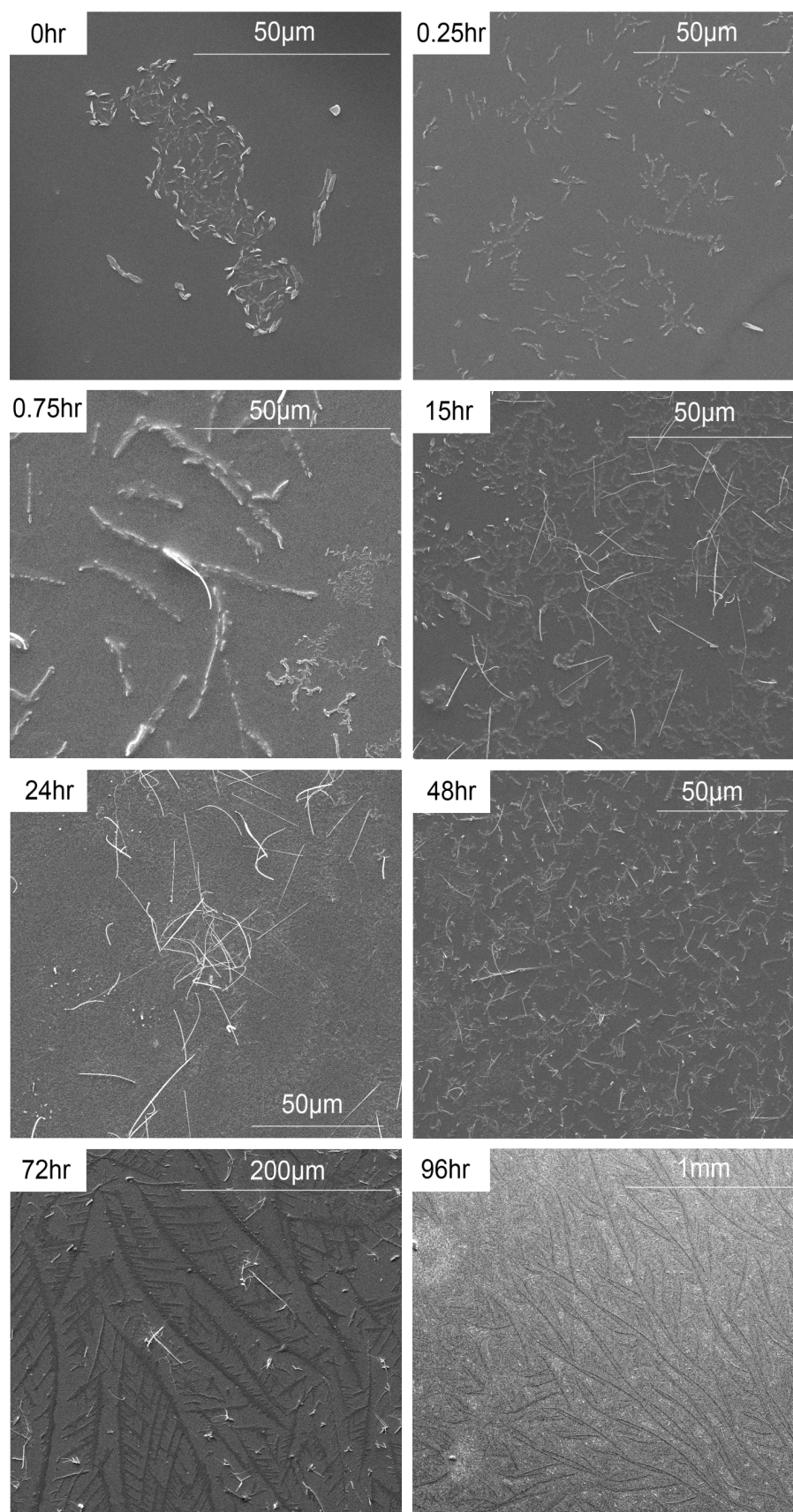


Figure 3- 30. SEM images of 9AC-8-BTA at the edge of the chloroform droplet at different aggregation times.

3.3.3.3 The effect of chain length on self-assembly

The flexibility of the compound increases with the increase in aliphatic chain length [66-69]. Therefore, the compound with the longer chain length 9AC-8-BTA is more flexible than the short chain compound 9AC-2-BTA. The flexibility of the molecule influences its self-assembly behaviour. For example, fluorescence quenching occurred for the more flexible molecule 9AC-8-BTA in less than 24 hours, while the less flexible molecule 9AC-2-BTA needed more than 24 hours to show quenching, as seen in Figure 3- 31. The red shift was greater for the more flexible molecule as a result of increased overlapping between the aromatic rings [48].

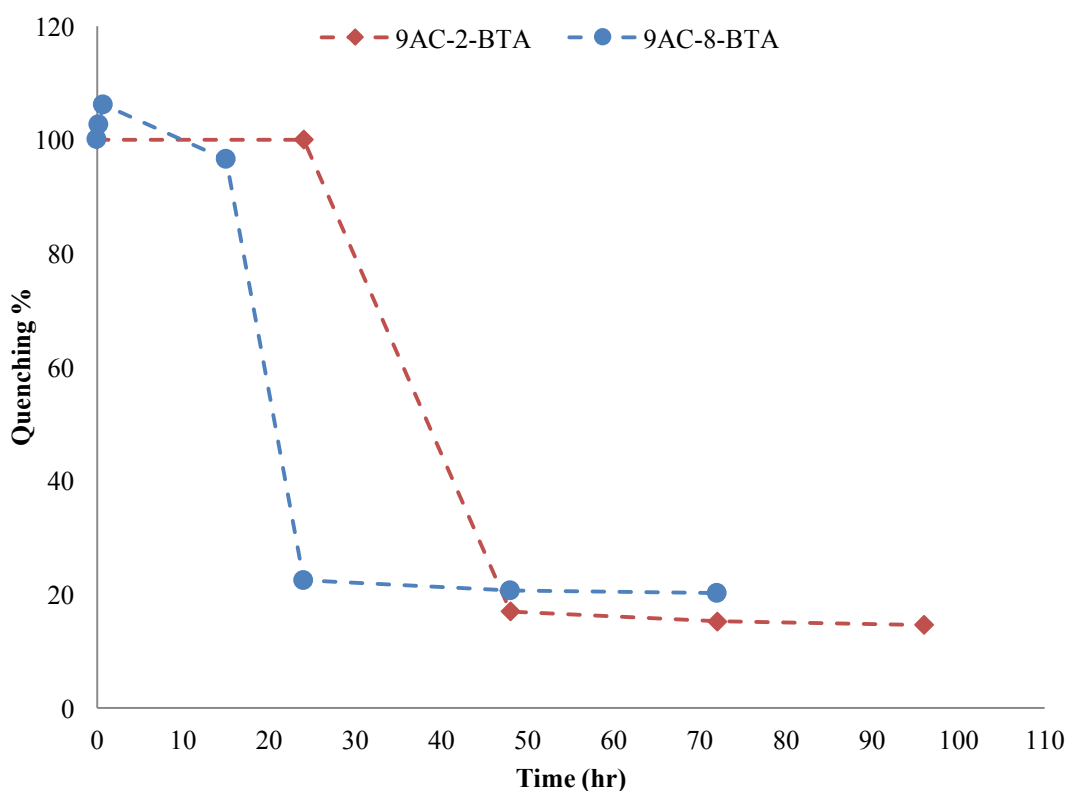


Figure 3- 31. Aggregation comparison between synthesised compounds using quenching percentage as a function of time (Lines added to guide eye).

Hydrogen bonding interactions were also affected by the flexibility of the molecule. Figure 3- 32 shows that the N-H band, as the representative band of hydrogen bonding, showed greater shift to higher wavenumbers for the more flexible molecule [99]. SEM images showed changes in the shape of aggregates as a function of the aggregation time for both compounds. Long fibres were observed for the more flexible molecule,

whereas the molecule with less flexibility was not able to form such long fibres. This is attributed to more effective stacking between the BTA core and the anthracene moieties for the long-chain molecule.

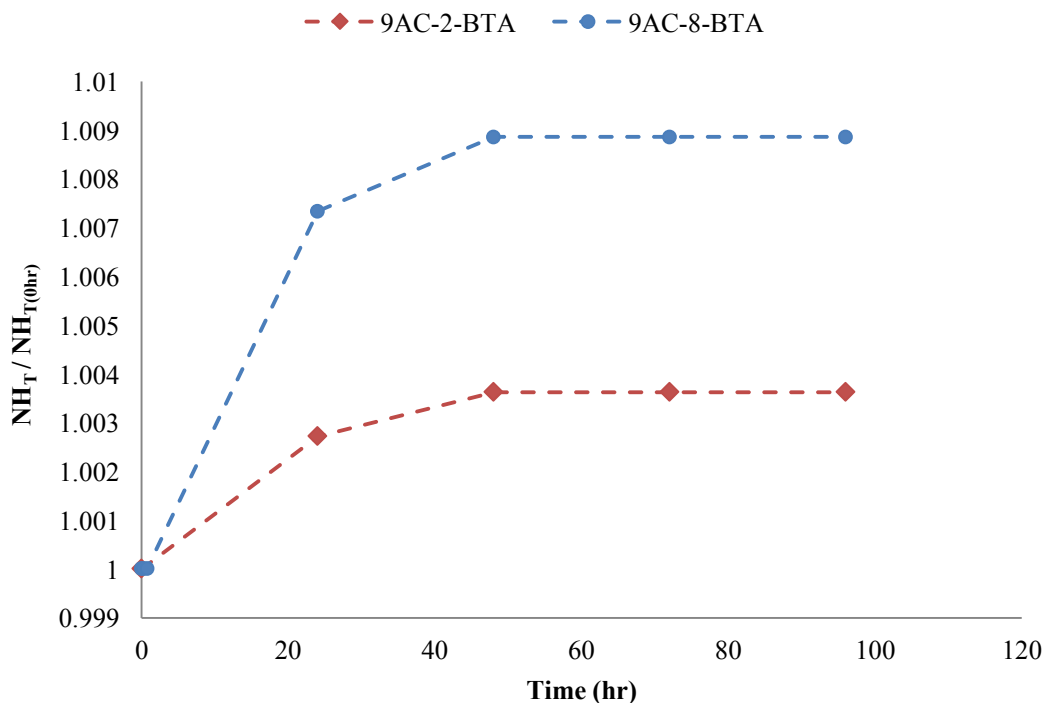


Figure 3- 32. The comparison between 9AC-2-BTA and 9AC-8-BTA to form fibres through hydrogen bonding by observing N-H stretching band shifting (Lines added to guide eye).

3.4 Conclusion

New BTA derivatives with anthracene moieties were synthesised. The self-assembly behaviour in chloroform was investigated by following the changes in fluorescence, and using FT-IR and SEM images. The distance between the BTA core and the anthracene moieties influenced the self-assembly of the molecule. It was found that the long C_8 chains showed faster self-assembly and greater overlapping between the aromatic rings than the short chains, due to the flexibility of the C_8 molecule. Moreover, C_8 molecule showed higher fluorescence and longer fibres than the molecule with less flexible C_2 based molecules.

3.5 Experimental section

General procedure for diamine protection

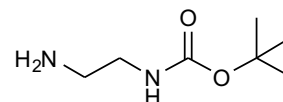
A solution of di-*tert*-butyl dicarbonate (4.36 g, 50 mmol) in CH₂Cl₂ (20 mL) was added over a period of 5 hrs to a solution of diamine (100 mmol) and triethylamine (2.78 mL, 20 mmol) in CH₂Cl₂ (40 mL) and stirred at room temperature. After 24 hrs, the solvent was removed under reduced pressure.

To purify short chain products (R = 2, 4, 6), HCl (0.5M, 50 mL) and CH₂Cl₂ (50 mL) were mixed and shaken in a separation funnel. The aqueous phase was separated, basified with NaOH (solid) to reach pH 14, and washed with CH₂Cl₂ (50 mL). CH₂Cl₂ was removed under reduced pressure.

To purify long chain product (R = 8), HCl (0.5 M, 50 mL) and CH₂Cl₂ (50 mL) were added and stirring for 15 minutes then the flask was placed in an ice bath for 30 minutes. The white solid was removed by filtration, washed CH₂Cl₂, HCl (0.5 M), and acetone to obtain the desired compound.

N-(*tert*-butoxycarbonyl)-1,2-ethandiamine (1a)

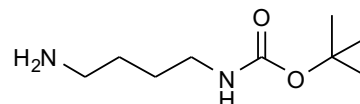
The compound 1a was obtained from di-*tert*-butyl dicarbonate (4.36 g, 50 mmol) and 1,2-ethandiamine (6 g, 100 mmol) as oily product (5.2 g, 90%) using general procedure.



¹H NMR (400 MHz, D₂O) δ: 1.47 (s, 9 H), 3.09 (t, *J* = 6 Hz, 2 H), 3.39 (t, *J* = 6 Hz, 2 H). ¹³C NMR (100 MHz, D₂O) δ: 27.74, 38.27, 39.58, 81.42, 158.23. IR: ν (cm⁻¹): 3370 (N-H stretch), 1695 (C=O amide I), 1523 (N-H amide II), 1390, 1367 (-C(CH₃)₃). HRMS calc. for C₇H₁₇N₂O₂ [M+H]⁺ 161.1290, found 161.1290.

N-(*tert*-butoxycarbonyl)-1,4-butandiamine (1b)

The compound 1b was obtained from di-*tert*-butyl dicarbonate (4.36 g, 50 mmol) and 1,4-butandiamine (8.81 g, 100 mmol) as oily product (5.8 g, 66%) using general procedure.

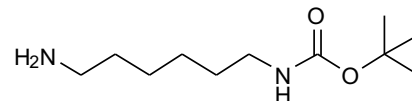


¹H NMR (600MHz, CD₃OD) δ: 1.43-1.5 (m, 13H), 2.65-2.67 (m, 2H), 3.04 (t, *J* = 6.5 Hz, 2H). ¹³C NMR (100 MHz, DMSO-*d*₆) δ: 27.5, 28.71, 31.16, 40.20, 41.91, 77.65, 156.03. IR: ν (cm⁻¹): 3360 (N-H stretch), 1690 (C=O amide I), 1520 (N-H

amide II), 1391, 1365 (-C(CH₃)₃). HRMS calc. for C₉H₂₁N₂O₂ [M+H]⁺ 189.1603, found 189.1596.

***N*-(*tert*-butoxycarbonyl)-1,6-hexandiamine (1c)**

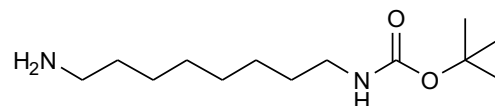
The compound 1c was obtained from di-*tert*-butyl dicarbonate (4.36 g, 50 mmol) and 1,6-hexandiamine (11.6 g, 100 mmol) as oily product (2.18 g, 45%) using general procedure.



¹H NMR (600 MHz, CDCl₃) δ: 1.31 - 1.34 (m, 4 H), 1.41 - 1.5 (m, 13 H), 2.67 (t, *J* = 7.00 Hz, 2 H), 3.1 (m, 2 H), 4.5 (bs, 1H). ¹³C NMR (150 MHz, CD₃OD) δ: 26.42, 26.62, 27.59, 32.53, 41.24, 47.27, 48.12, 78.38, 157.19. IR: ν (cm⁻¹): 3348 (N-H stretch), 1690 (C=O amide I), 1525 (N-H amide II), 1391, 1365 (-C(CH₃)₃). HRMS calc. for C₁₁H₂₅N₂O₂ [M+H]⁺ 217.1916, found 217.1908.

***N*-(*tert*-butoxycarbonyl)-1,8-octandiamine (1d)**

The compound 1d was obtained from di-*tert*-butyl dicarbonate (4.36 g, 50 mmol) and 1,8-octandiamine (14.4 g, 100 mmol) as white solid (5 g, 41%) using general procedure.



mp = 153-155 °C. ¹H NMR (600 MHz, CD₃OD) δ: 1.32-1.47 (m, 19H), 1.63-1.68 (m, 2H), 2.9-2.94 (m, 2H), 3.00-3.04 (m, 2H). ¹³C NMR (100 MHz, DMSO-*d*₆) δ: 26.27, 26.62, 27.37, 28.74, 28.97, 29.16, 29.9, 39.15, 40.26 (shoulder), 77.73, 156.04. IR: ν (cm⁻¹): 3372 (N-H stretch), 1687 (C=O amide I), 1519 (N-H amide II), 1389, 1364 (-C(CH₃)₃). HRMS calc. for C₁₃H₂₉N₂O₂ [M+H]⁺ 245.2229, found 245.2226.

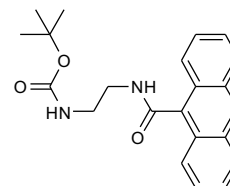
General procedure for amide coupling

Anthracene-9-carboxylic acid (444 mg, 2 mmol) was stirred in DMF (30 mL) in presence of diisopropylethylamine (DIEA) (0.35 mL, 2 mmol) and 2-(1H-7-azabenzotriazol-1-yl)-1,1,3,3-tetramethyluronium hexafluorophosphate methanaminium (HATU) (570 mg, 2.1 mmol) for one hour at room temperature. Protected diamine (2 mmol) was added to the mixture and stirred for 24 hours. Under vacuum the solvent was removed and ethyl acetate (30 mL) added. The solution was washed with aqueous solution of sodium hydroxide (0.5 M, 2x30 mL), hydrochloric acid (0.5 M, 2x30 mL), brine water (2x30 mL) and dried (MgSO₄). Finally, the solvent

was removed by evaporation. Methanol was used to recrystallise the product.

***N,N'*-(anthracene-9-carbonyl) (*tert*-butoxycarbonyl)-1,2-ethandiamine (2a)**

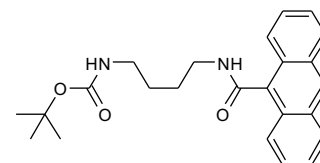
The compound 2a was obtained from *N*-(*tert*-butoxycarbonyl)-1,2-ethandiamine (320.2 mg, 2 mmol) and anthracene-9-carboxylic acid (444.4 mg, 2 mmol) as yellowish solid (714 mg, 98%) using general procedure.



mp = 194-196 °C. ^1H NMR (600 MHz, DMSO- d_6) δ : 1.42 (s, 9 H), 3.3 (q, J = 6.3 Hz, 2 H), 3.54 (q, J = 6.3 Hz, 2 H), 6.93 (t, J = 5.5 Hz, 1 H), 7.54 - 7.58 (m, 4 H), 7.98 (d, J = 8 Hz, 2 H), 8.13 (d, J = 8 Hz, 2 H), 8.66 (s, 1 H), 8.8 (t, J = 5.5 Hz, 1 H). ^{13}C NMR (150 MHz, DMSO- d_6) δ : 28.82, 39.81(shoulder), 40.29, 78.29, 125.9, 126.12, 126.96, 127.68, 127.79, 128.88, 131.21, 133.79, 156.25, 168.93. IR: ν (cm^{-1}): 3370 (N-H stretch), 1719 (C=C), 1618 (C=O amide I), 1515 (N-H amide II), 1390, 1365 (-C(CH₃)₃). HRMS calc. for C₂₂H₂₄N₂O₃Na [M+Na]⁺ 387.1685, found 387.1699.

***N,N'*-(anthracene-9-carbonyl) (*tert*-butoxycarbonyl)-1,4-butandiamine (2b)**

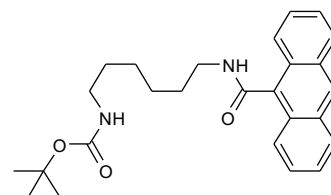
The compound 2b was obtained from *N*-(*tert*-butoxycarbonyl)-1,4-butandiamine (346.5 mg, 2 mmol) and anthracene-9-carboxylic acid (444.4 mg, 2 mmol) as yellowish solid (679 mg, 86%) using general procedure.



mp = 180 °C. ^1H NMR (600 MHz, DMSO- d_6) δ : 1.39 (s, 9 H), 1.5-1.55 (m, 2 H), 1.6-1.65 (m, 2 H), 3.00 (q, J = 6.6 Hz, 2 H), 3.45 (q, J = 6.6 Hz, 2 H), 6.89 (t, J = 5.6 Hz, 1 H), 7.53 - 7.58 (m, 4 H), 7.93 (d, J = 8 Hz, 2 H), 8.12 (d, J = 8 Hz, 2 H), 8.65 (s, 1 H), 8.81 (t, J = 5.5 Hz, 1 H). ^{13}C NMR (150 MHz, DMSO- d_6) δ : 27.11, 27.87, 28.85, 39.58, 40.17, 77.92, 125.8, 126.09, 126.91, 127.54, 127.8, 128.91, 131.24, 134.09, 156.21, 168.55. IR: ν (cm^{-1}): 3323, 3246 (N-H stretch), 1679 (C=C), 1633 (C=O amide I), 1522 (N-H amide II), 1390, 1365 (-C(CH₃)₃). HRMS calc. for C₂₄H₂₈N₂O₃Na [M+Na]⁺ 415.1998, found 415.1999.

***N,N'*-(anthracene-9-carbonyl) (*tert*-butoxycarbonyl)-1,6-hexandiamine (2c)**

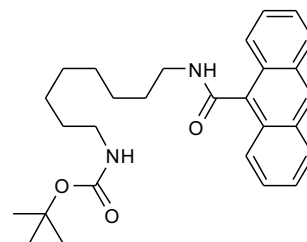
The compound 2c was obtained from *N*-(*tert*-butoxycarbonyl)-1,6-hexandiamine (402 mg, 2 mmol) and anthracene-9-carboxylic acid (444.4 mg, 2 mmol) as yellowish solid (588 mg, 75%) using general procedure.



mp= 156-158 °C. ^1H NMR (600 MHz, DMSO- d_6) δ : 1.33 - 1.43 (m, 15 H) 1.62-1.67 (m, 2 H) 2.91-2.95 (m, 2 H) 3.44-3.48 (m, 2 H) 6.83 (t, J =5.7 Hz, 1 H) 7.52 - 7.58 (m, 4 H) 7.93 (d, J =8 Hz, 2 H) 8.12 (d, J =8 Hz, 2 H) 8.65 (s, 1 H) 8.80 (t, J =5.5 Hz, 1 H). ^{13}C NMR (150 MHz, DMSO- d_6) δ : 26.58, 26.87, 28.83, 29.58, 30.09, 38.85, 39.05, 77.86, 125.77, 126.09, 126.88, 127.52, 127.79, 128.92, 131.25, 134.14, 156.16, 168.53. IR: ν (cm^{-1}): 3320 (N-H stretch), 1675 (C=C), 1633 (C=O amide I), 1525 (N-H amide II), 1391, 1364 (-C(CH $_3$) $_3$). HRMS calc. for C $_{26}$ H $_{32}$ N $_2$ O $_3$ Na [M+Na] $^+$ 443.2311, found 443.231.

***N,N'*-(anthracene-9-carbonyl) (*tert*-butoxycarbonyl)-1,8-octandiamine (2d)**

The compound 2d was obtained from *N*-(*tert*-butoxycarbonyl)-1,8-octandiamine (458.7 mg, 2 mmol) and anthracene-9-carboxylic acid (444.4 mg, 2 mmol) as yellowish solid (583 mg, 65%) using general procedure.



mp = 143-145 °C. ^1H NMR (600 MHz, CDCl $_3$) δ : 1.29 - 1.49 (m, 19 H), 1.71-1.76 (m, 2 H), 3.10 (bs, 2 H), 3.68 - 3.71 (m, 2 H), 4.5 (bs, 1 H), 6.05 (bs, 1 H), 7.47 - 7.53 (m, 4 H), 8.00 (d, J =8 Hz, 2 H), 8.06 (d, J =8 Hz, 2 H), 8.48 (s, 1 H). ^{13}C NMR (150 MHz, CDCl $_3$) δ : 26.83, 27.1, 28.55, 29.3, 29.33, 29.8, 30.17, 40.29, 40.70, 79.14, 125.22, 125.6, 126.77, 128.15, 128.26, 128.63, 131.24, 132.27, 156.1, 169.58. IR: ν (cm^{-1}): 3322 (N-H stretch), 1682 (C=C), 1633 (C=O amide I), 1522 (N-H amide II), 1390, 1364 (-C(CH $_3$) $_3$). HRMS calc. for C $_{28}$ H $_{36}$ N $_2$ O $_3$ Na [M+Na] $^+$ 471.2624, found 471.2623.

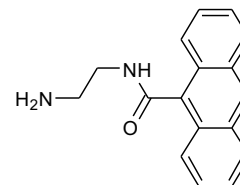
General deprotection procedure

Trifluoroacetic acid (TFA) was used to liberate the protected amine group. DCM (10 mL) was mixed with the protected amine and stirred to dissolve the solid. TFA (2

equiv.) was added slowly to the solution and the mixture stirred 2 h. The de-protection reaction was followed by ^1H NMR. The solvent was removed after ensuring that the de-protection reaction was complete. The product was used without any further purification.

***N*-(anthracene-9-carbonyl)-1,2-ethandiamine (3a)**

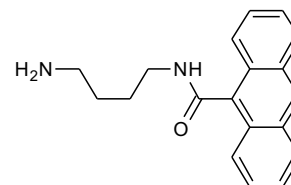
The compound 3a was obtained from *N,N'*-(anthracene-9-carbonyl) (*tert*-butoxycarbonyl)-1,2-ethandiamine (400 mg, 1.1 mmol) and trifluoroacetic acid (125.4 mg, 1.1 mmol) as yellowish oily product with quantitative yield using general procedure.



^1H NMR (600 MHz, $\text{DMSO}-d_6$) δ : 3.12-3.17 (m, 2H), 3.71-3.74 (m, 2H), 7.55-7.60 (m, 4H), 7.93 (bs, 2H), 7.97 (d, $J = 8.4$ Hz, 2H), 8.14 (d, $J = 8.4$ Hz, 2H), 8.69 (s, 1H), 8.94 (t, $J = 5.5$ Hz, 2H). ^{13}C NMR (100 MHz, CD_3OD) δ : 38.34, 40.22, 125.65, 126.54, 127.84, 129.12, 129.57, 129.63, 132.03, 132.45, 173.28. IR: ν (cm^{-1}): 3243 (N-H stretch), 1676 (C=C), 1632 (C=O amide I), 1544 (N-H amide II). HRMS calc. for $\text{C}_{17}\text{H}_{17}\text{N}_2\text{O}$ $[\text{M}+\text{H}]^+$ 256.1341, found 265.1344.

***N*-(anthracene-9-carbonyl)-1,4-butandiamine (3b)**

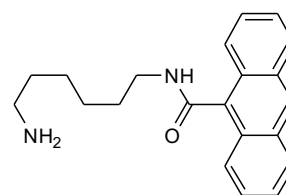
The compound 3b was obtained from *N,N'*-(anthracene-9-carbonyl) (*tert*-butoxycarbonyl)-1,4-butandiamine (400 mg, 1 mmol) and trifluoroacetic acid (114 mg, 1 mmol) as yellowish oily product with quantitative yield using general procedure.



^1H NMR (600 MHz, $\text{DMSO}-d_6$) δ : 1.68 - 1.7 (m, 4 H), 2.86-2.92 (m, 2 H), 3.47-3.51 (m, 2 H), 7.54 - 7.56 (m, 4 H), 7.72 (bs, 2 H), 7.94 (d, $J = 8.4$ Hz, 2 H), 8.13 (d, $J = 8.4$ Hz, 2 H), 8.66 (s, 1 H), 8.87 (t, $J = 5.5$ Hz, 1 H). ^{13}C NMR (100 MHz, $\text{DMSO}-d_6$) δ : 24.96, 26.25, 38.70, 38.80, 125.26, 125.63, 126.52, 127.19, 127.30, 128.47, 130.75, 133.41, 168.21. IR: ν (cm^{-1}): 3218 (N-H stretch), 1670 (C=C), 1614 (C=O amide I), 1568 (N-H amide II). HRMS calc. for $\text{C}_{19}\text{H}_{21}\text{N}_2\text{O}$ $[\text{M}+\text{H}]^+$ 293.1654, found 293.1665.

***N*-(anthracene-9-carbonyl)-1,6-hexandiamine (3c)**

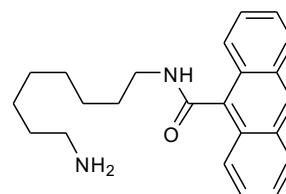
The compound 3c was obtained from *N,N'*-(anthracene-9-carbonyl) (*tert*-butoxycarbonyl)-1,6-hexandiamine (400 mg, 0.95 mmol) and trifluoroacetic acid (108.4 mg, 0.95 mmol) as yellowish oily product with quantitative yield using general procedure.



^1H NMR (600 MHz, $\text{DMSO-}d_6$) δ : 1.4 - 1.45 (m, 4 H), 1.57-1.6 (m, 2 H), 1.65-1.68 (m, 2 H), 2.8 - 2.83 (m, 2 H), 3.46-3.49 (m, 2 H), 7.54 - 7.59 (m, 4 H), 7.66 (bs, 2 H), 7.93 (d, $J = 8.4$ Hz, 2 H), 8.13 (d, $J = 8.4$ Hz, 2 H), 8.66 (s, 1 H), 8.82 (t, $J = 5.5$ Hz, 1 H). ^{13}C NMR (150 MHz, $\text{DMSO-}d_6$) δ : 2.55, 26.12, 27.05, 28.90, 38.85, 39.05, 125.20, 125.58, 126.39, 127.06, 127.26, 128.43, 130.73, 133.56, 172.13. IR: ν (cm^{-1}): 3229 (N-H stretch), 1679 (C=C), 1633 (C=O amide I), 1525 (N-H amide II). HRMS calc. for $\text{C}_{21}\text{H}_{25}\text{N}_2\text{O}$ $[\text{M}+\text{H}]^+$ 321.1967, found 321.1958.

***N*-(anthracene-9-carbonyl)-1,8-octandiamine (3d)**

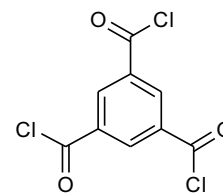
The compound 3d was obtained from *N,N'*-(anthracene-9-carbonyl) (*tert*-butoxycarbonyl)-1,8-octandiamine (400 mg, 0.89 mmol) and trifluoroacetic acid (101.6 mg, 0.89 mmol) as yellowish oily product with quantitative yield using general procedure.



^1H NMR (600 MHz, $\text{DMSO-}d_6$) δ : 1.34 - 1.45 (m, 8 H), 1.55-1.57 (m, 2 H), 1.64-1.69 (m, 2 H), 2.77-2.8 (m, 2 H), 3.46-3.49 (m, 2 H), 7.53 - 7.58 (m, 4 H), 7.76 (bs, 2H), 7.93 (d, $J = 8$ Hz, 2 H), 8.13 (d, $J = 8$ Hz, 2 H), 8.65 (s, 1 H), 8.79 (t, $J = 5.5$ Hz, 1 H). ^{13}C NMR (150 MHz, $\text{DMSO-}d_6$) δ : 25.76, 26.45, 26.98, 28.48, 28.54, 29.00, 38.12, 125.19, 125.53, 126.31, 127.00, 127.23, 128.38, 130.70, 133.56, 168 (one peak missing). IR: ν (cm^{-1}): 3318 (N-H stretch), 1676 (C=C), 1633 (C=O amide I), 1523 (N-H amide II). HRMS calc. for $\text{C}_{23}\text{H}_{29}\text{N}_2\text{O}$ $[\text{M}+\text{H}]^+$ 349.2280, found 349.2289.

Benzene-1,3,5-tricarboxylic acid chloride (4)

Thionyl chloride (30 mL) was added to benzene-1,3,5-tricarboxylic acid (4 g, 19 mmol) and DMF (anhydrous, 3 drops) and heated under reflux for 3 hours. After that, thionyl chloride was distilled off and DCM (2x30 mL) was added and removed by the distillation process to totally remove thionyl chloride. The product as yellow oily solution was obtained.



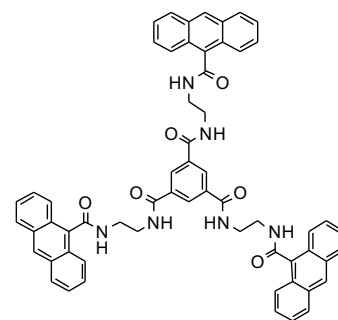
^1H NMR (400 MHz, CDCl_3) δ : 9.06 (s). ^{13}C NMR (100 MHz, CDCl_3) δ : 166.14, 138.19, 135.59. IR: ν (cm^{-1}): 3085 (C=C-H stretching), 1753 (C=O), 1591 (C=C stretching). HRMS calc. for $\text{C}_9\text{H}_3\text{Cl}_3\text{O}_3$ $[\text{M}]^+$ 253.0712, found 253.0709.

General procedure for BTA derivatives

Benzene-1,3,5-tricarboxylic acid chloride was dissolved in dry DCM (50 mL) and catalytic amount of TEA was added. Mono amine was added drop-wise and the solution heated under reflux overnight. Water (50 mL) was added and the organic phase washed with HCl (0.5M, 2x30 mL), NaOH (0.5M, 2x30 mL) brine water and dried (MgSO_4). Solvent evaporated under vacuum. Characterisation was done with the freshly prepared sample to avoid aggregation.

N,N',N''-[N-(anthracene-9-carbonyl)ethandiamine]benzene-1,3,5-tricarboxamide (5a)

The compound 5a was obtained from benzene-1,3,5-tricarboxylic acid chloride (250 mg, 0.95 mmol) *N*-(anthracene-9-carbonyl)-1,2-ethandiamine (1 g, 3.8 mmol) as a waxy product (1.13 g, 90%) using general procedure.



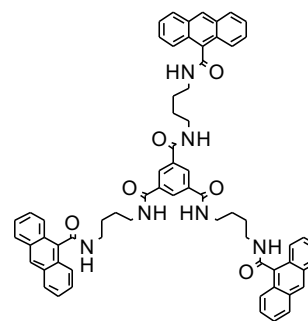
^1H NMR (600 MHz, CDCl_3) δ : 3.37-3.8 (m, 6 H), 3.93 - 3.96 (m, 6 H), 6.53 (bs, 3H), 7.5 - 7.57 (m, 12 H), 7.97 (d, $J=7.8$ Hz, 6 H), 8.04 (d, $J=7.8$ Hz, 6 H), 8.1 (bs, 3H), 8.5 (s, 3 H). IR: ν (cm^{-1}): 3310 (N-H stretch), 3078 (C=C-H stretching), 1715 (C=C), 1660 (C=O amide I), 1530 (N-H amide II).

N,N',N''-[N-(anthracene-9-carbonyl)butandiamine]benzene-1,3,5-tricarboxamide (5b)

The compound 5b was obtained from benzene-1,3,5-tricarboxylic acid chloride (250 mg, 0.95 mmol) *N*-(anthracene-9-carbonyl)-1,4-butandiamine (1.1 g, 3.8 mmol) as a

waxy product (0.98 g, 73%) using general procedure.

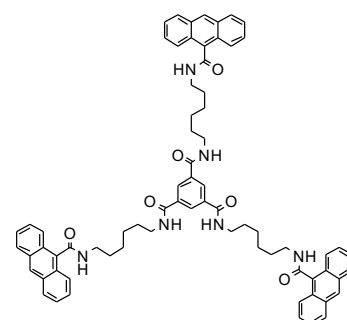
^1H NMR (600 MHz, $\text{DMSO}-d_6$) δ : 1.65-1.67(m, 12 H), 3.28-3.29 (m, 6 H), 3.47 - 3.5 (m, 6H), 7.55-7.58 (m, 12H), 7.93 - 7.95 (m, 6H), 8.11-8.13 (m, 6 H), 8.46 (s, 3 H), 8.65(s, 3H), 8.8-8.82 (m, 3 H), 9.5 (t, $J=5.5$ Hz, 3H). IR: ν (cm^{-1}): 3300 (N-H stretch), 1650 (C=O amide I), 1531 (N-H amide II).



***N,N',N''*-[N-(anthracene-9-carbonyl)hexandiamine]benzene-1,3,5-tricarboxamide (5c)**

The compound 5c was obtained from benzene-1,3,5-tricarboxylic acid chloride (250 mg, 0.95 mmol) *N*-(anthracene-9-carbonyl)-1,6-hexandiamine (1.22 g, 3.8 mmol) as a waxy product (0.98 g, 67%) using general procedure.

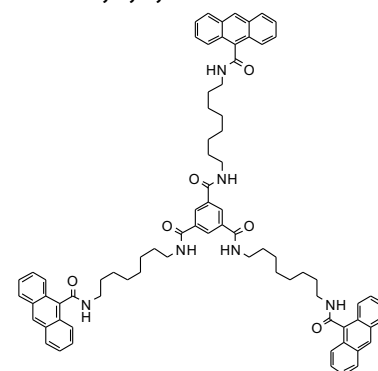
^1H NMR (400 MHz, $\text{DMSO}-d_6$) δ : 1.30 - 1.51 (m, 12 H), 1.51 - 1.62 (m, 6 H), 1.62 - 1.73 (m, 6 H), 3.25 - 3.34 (m, 6 H), 3.48-3.50 (m, 6 H), 7.47 - 7.60 (m, 12 H), 7.94 (d, $J = 8$ Hz, 6 H), 8.11 (d, $J = 8$ Hz, 6 H), 8.41 (s, 3 H), 8.63 (s, 3 H), 8.73 (t, $J = 5.5$ Hz, 3 H), 8.80 (t, $J = 5.5$ Hz, 3 H). IR: ν (cm^{-1}): 3280 (N-H stretch), 3050 (C=C-H stretching), 1713 (C=C), 1648 (C=O amide I), 1530 (N-H amide II). HRMS calc. for $\text{C}_{72}\text{H}_{72}\text{N}_6\text{O}_6$ $[\text{M}]^+$ 1139.5411, found 1139.5360.



***N,N',N''*-[N-(anthracene-9-carbonyl)octandiamine]benzene-1,3,5-tricarboxamide (5d)**

The compound 5d was obtained from benzene-1,3,5-tricarboxylic acid chloride (250 mg, 0.95 mmol) *N*-(anthracene-9-carbonyl)-1,8-octandiamine (1.3 g, 3.8 mmol) as a waxy product (0.96 g, 62%) using general procedure.

^1H NMR (400 MHz, $\text{DMSO}-d_6$) δ : 1.13 - 1.41 (m, 24 H), 1.49-1.51 (m, 6 H), 1.57 - 1.59 (m, 6 H), 2.88 - 2.91 (m, 6 H), 3.2 - 3.25 (m, 6 H), 7.44 - 7.5 (m, 12 H), 7.85 - 7.87 (m, 6 H), 8.04 - 8.06 (m, 6 H), 8.3 (s, 3 H), 8.57- 8.6 (m, 6 H), 8.68 - 8.77 (m, 3 H). IR: ν (cm^{-1}): 3270 (N-H stretch), 3065 (C=C-H stretching), 1712 (C=C), 1642 (C=O amide I), 1534 (N-H amide II). MS.MALDI calc. for $\text{C}_{78}\text{H}_{84}\text{N}_6\text{O}_6$ $[\text{M}]^+$ 1224.5, found 1223.6.



3.6 References

1. Chakrabarty, R., P.S. Mukherjee, and P.J. Stang, *Supramolecular Coordination: Self-Assembly of Finite Two- and Three-Dimensional Ensembles*. Chemical Reviews, 2011. **111**(11): p. 6810-6918.
2. Zhang, Z., Y. Luo, J. Chen, S. Dong, Y. Yu, Z. Ma, and F. Huang, *Formation of Linear Supramolecular Polymers That Is Driven by C-H... π Interactions in Solution and in the Solid State*. *Angew. chem*, 2011.50: p.1397-1401
3. Astruc, D., E. Boisselier, and C. Ornelas, *Dendrimers Designed for Functions: From Physical, Photophysical, and Supramolecular Properties to Applications in Sensing, Catalysis, Molecular Electronics, Photonics, and Nanomedicine*. Chemical Reviews, 2010. **110**(4): p. 1857-1959.
4. Aida, T., E.W. Meijer, and S.I. Stupp, *Functional Supramolecular Polymers*. Science, 2012. **335**(6070): p. 813-817.
5. Lehn, J.-M., *Constitutional dynamic chemistry: bridge from supramolecular chemistry to adaptive chemistry*, in *Constitutional Dynamic Chemistry*. 2012, Springer. p. 1-32.
6. Che, Y., D.E. Gross, H. Huang, D. Yang, X. Yang, E. Discekici, Z. Xue, H. Zhao, J.S. Moore, and L. Zang, *Diffusion-Controlled Detection of Trinitrotoluene: Interior Nanoporous Structure and Low Highest Occupied Molecular Orbital Level of Building Blocks Enhance Selectivity and Sensitivity*. Journal of the American Chemical Society, 2012. **134**(10): p. 4978-4982.
7. Ahn, D.J. and J.-M. Kim, *Fluorogenic Polydiacetylene Supramolecules: Immobilization, Micropatterning, and Application to Label-Free Chemosensors*. Accounts of Chemical Research, 2008. **41**(7): p. 805-816.
8. Masuda, M., P. Jonkhøj, R.P. Sijbesma, and E.W. Meijer, *Photoinitiated Polymerization of Columnar Stacks of Self-Assembled Trialkyl-1,3,5-benzenetricarboxamide Derivatives*. Journal of the American Chemical Society, 2003. **125**(51): p. 15935-15940.
9. Wang, S., W. Shen, Y. Feng, and H. Tian, *A multiple switching bisthiénylene and its photochromic fluorescent organogelator*. Chemical Communications, 2006(14): p. 1497-1499.
10. Zhu, L., R.O. Al-Kaysi, and C.J. Bardeen, *Reversible Photoinduced Twisting of Molecular Crystal Microribbons*. Journal of the American Chemical Society, 2011. **133**(32): p. 12569-12575.
11. Pop, F., C. Melan, I. Danila, M. Linares, D. Beljonne, D.B. Amabilino, and N. Avarvari, *Hierarchical Self-Assembly of Supramolecular Helical Fibres from Amphiphilic C3-Symmetrical Functional Tris(tetrathiafulvalenes)*. Chemistry – A European Journal, 2014. **20**(52): p. 17443-17453.
12. Albuquerque, R.Q., A. Timme, R. Kress, J. Senker, and H.-W. Schmidt, *Theoretical Investigation of Macrodipoles in Supramolecular Columnar Stacks*. Chemistry – A European Journal, 2013. **19**(5): p. 1647-1657.
13. Nakano, Y., T. Hirose, P.J.M. Stals, E.W. Meijer, and A.R.A. Palmans, *Conformational analysis of supramolecular polymerization processes of disc-like molecules*. Chemical Science, 2012. **3**(1): p. 148-155.
14. Veld, M.A.J., D. Haveman, A.R.A. Palmans, and E.W. Meijer*, *Sterically demanding benzene-1,3,5-tricarboxamides: tuning the mechanisms of supramolecular polymerization and chiral amplification*. Soft Matter, 2011. **7**(2): p. 524-531.
15. Leenders, C.M.A., T. Mes, M.B. Baker, M.M.E. Koenigs, P. Besenius, A.R.A.

- Palmans, and E.W. Meijer, *From supramolecular polymers to hydrogel materials*. Materials Horizons, 2014. **1**(1): p. 116-120.
16. García-Iglesias, M., B.F.M. de Waal, I. de Feijter, A.R.A. Palmans, and E.W. Meijer, *Nanopatterned Superlattices in Self-Assembled C₂-Symmetric Oligodimethylsiloxane-Based Benzene-1,3,5-Tricarboxamides*. Chemistry – A European Journal, 2015. **21**(1): p. 377-385.
 17. Adel, A.-S. and M. Farooqui, *(4+ 2) Cycloaddition Reactions of 9-Substituted Anthracene Compounds*. Oriental Journal of Chemistry, 2013. **29**(3): p. 1033-1039.
 18. Huang, J., J.-H. Su, and H. Tian, *The development of anthracene derivatives for organic light-emitting diodes*. Journal of Materials Chemistry, 2012. **22**(22): p. 10977-10989.
 19. Stals, P.J.M., M.M.J. Smulders, R. Martín-Rapún, A.R.A. Palmans, and E.W. Meijer, *Asymmetrically Substituted Benzene-1,3,5-tricarboxamides: Self-Assembly and Odd–Even Effects in the Solid State and in Dilute Solution*. Chemistry – A European Journal, 2009. **15**(9): p. 2071-2080.
 20. Ogata, D., T. Shikata, and K. Hanabusa, *Chiral Amplification of the Structure and Viscoelasticity of a Supramolecular Polymeric System Consisting of N, N', N''-Tris (3, 7-Dimethyloctyl) Benzene-1, 3, 5-Tricarboxamide and n-Decane*. The Journal of Physical Chemistry B, 2004. **108**(40): p. 15503-15510.
 21. Cain, J.P., P.L. Gassman, H. Wang, and A. Laskin, *Micro-FTIR study of soot chemical composition-evidence of aliphatic hydrocarbons on nascent soot surfaces*. Physical Chemistry Chemical Physics, 2010. **12**(20): p. 5206-5218.
 22. Furnish, *Textbook of practical organic chemistry*. 1986: Longman.
 23. Crews, P., J. Rodriguez, M. Jaspars, and R.J. Crews, *Organic structure analysis*. Vol. 23. 1998: Oxford New York.
 24. van Hameren, R., A.M. van Buul, D. Visser, R.K. Heenan, S.M. King, A.E. Rowan, R.J. Nolte, W. Pyckhout-Hintzen, J.A. Elemans, and M.C. Feiters, *Solution scattering studies of the hierarchical assembly of porphyrin trimers based on benzene triscarboxamide*. Soft Matter, 2014. **10**(48): p. 9688-9694.
 25. Narayan, B., C. Kulkarni, and S.J. George, *Synthesis and self-assembly of a C₃-symmetric benzene-1,3,5-tricarboxamide (BTA) anchored naphthalene diimide disc*. Journal of Materials Chemistry C, 2013. **1**(4): p. 626-629.
 26. Lee, S., S. Oh, J. Lee, Y. Malpani, Y.-S. Jung, B. Kang, J.Y. Lee, K. Ozasa, T. Isoshima, S.Y. Lee, M. Hara, D. Hashizume, and J.-M. Kim, *Stimulus-Responsive Azobenzene Supramolecules: Fibers, Gels, and Hollow Spheres*. Langmuir, 2013. **29**(19): p. 5869-5877.
 27. Mes, T., S. Cantekin, D.W.R. Balkenende, M.M.M. Frissen, M.A.J. Gillissen, B.F.M. De Waal, I.K. Voets, E.W. Meijer, and A.R.A. Palmans, *Thioamides: Versatile Bonds To Induce Directional and Cooperative Hydrogen Bonding in Supramolecular Polymers*. Chemistry – A European Journal, 2013. **19**(26): p. 8642-8649.
 28. Salonen, L.M., M. Ellermann, and F. Diederich, *Aromatic Rings in Chemical and Biological Recognition: Energetics and Structures*. Angew. Chem. International Edition, 2011. **50**(21): p. 4808-4842.
 29. Meyer, E.A., R.K. Castellano, and F. Diederich, *Wechselwirkungen mit aromatischen Ringen in chemischen und biologischen Erkennungsprozessen*. Angew. Chem., 2003. **115**(11): p. 1244-1287.
 30. Curtis, M.D., J. Cao, and J.W. Kampf, *Solid-State Packing of Conjugated Oligomers: From π -Stacks to the Herringbone Structure*. Journal of the

- American Chemical Society, 2004. **126**(13): p. 4318-4328.
31. Hunter, C.A., K.R. Lawson, J. Perkins, and C.J. Urch, *Aromatic interactions*. Journal of the Chemical Society, Perkin Transactions 2, 2001(5): p. 651-669.
 32. Tsuzuki, S., K. Honda, T. Uchamaru, M. Mikami, and K. Tanabe, *Origin of Attraction and Directionality of the π/π Interaction: Model Chemistry Calculations of Benzene Dimer Interaction*. Journal of the American Chemical Society, 2002. **124**(1): p. 104-112.
 33. Hinoue, T., Y. Shigenoi, M. Sugino, Y. Mizobe, I. Hisaki, M. Miyata, and N. Tohnai, *Regulation of π -Stacked Anthracene Arrangement for Fluorescence Modulation of Organic Solid from Monomer to Excited Oligomer Emission*. Chemistry-A European Journal, 2012. **18**(15): p. 4634-4643.
 34. Chen, J., S. Subramanian, S.R. Parkin, M. Siegler, K. Gallup, C. Haughn, D.C. Martin, and J.E. Anthony, *The influence of side chains on the structures and properties of functionalized pentacenes*. Journal of Materials Chemistry, 2008. **18**(17): p. 1961-1969.
 35. Payne, M.M., S.R. Parkin, J.E. Anthony, C.-C. Kuo, and T.N. Jackson, *Organic Field-Effect Transistors from Solution-Deposited Functionalized Acenes with Mobilities as High as 1 cm²/V·s*. Journal of the American Chemical Society, 2005. **127**(14): p. 4986-4987.
 36. Anthony, J.E., D.L. Eaton, and S.R. Parkin, *A Road Map to Stable, Soluble, Easily Crystallized Pentacene Derivatives*. Organic Letters, 2002. **4**(1): p. 15-18.
 37. Anthony, J.E., J.S. Brooks, D.L. Eaton, and S.R. Parkin, *Functionalized Pentacene: Improved Electronic Properties from Control of Solid-State Order*. Journal of the American Chemical Society, 2001. **123**(38): p. 9482-9483.
 38. Moon, H., R. Zeis, E.-J. Borkent, C. Besnard, A.J. Lovinger, T. Siegrist, C. Kloc, and Z. Bao, *Synthesis, Crystal Structure, and Transistor Performance of Tetracene Derivatives*. Journal of the American Chemical Society, 2004. **126**(47): p. 15322-15323.
 39. Kimoto, T., K. Tanaka, M. Kawahata, K. Yamaguchi, S. Otsubo, Y. Sakai, Y. Ono, A. Ohno, and K. Kobayashi, *Bis(methylthio)tetracenes: Synthesis, Crystal-Packing Structures, and OFET Properties*. The Journal of Organic Chemistry, 2011. **76**(12): p. 5018-5025.
 40. Kobayashi, K., R. Shimaoka, M. Kawahata, M. Yamanaka, and K. Yamaguchi, *Synthesis and Cofacial π -Stacked Packing Arrangement of 6,13-Bis(alkylthio)pentacene*. Organic Letters, 2006. **8**(11): p. 2385-2388.
 41. Sasaki, H., Y. Wakayama, T. Chikyow, E. Barrena, H. Dosch, and K. Kobayashi, *Growth of anthracene derivative thin films with a π -stacking structure*. Applied Physics Letters, 2006. **88**(8): p. 081907.
 42. Kobayashi, K., H. Masu, A. Shuto, and K. Yamaguchi, *Control of Face-to-Face π - π Stacked Packing Arrangement of Anthracene Rings via Chalcogen-Chalcogen Interaction: 9,10-Bis(methylchalcogeno)anthracenes*. Chemistry of Materials, 2005. **17**(26): p. 6666-6673.
 43. Pedireddi, V.R., D.S. Reddy, B.S. Goud, D.C. Craig, A.D. Rae, and G.R. Desiraju, *The nature of halogen [three dots, centered] halogen interactions and the crystal structure of 1,3,5,7-tetraiodoadamantane*. Journal of the Chemical Society, Perkin Transactions 2, 1994(11): p. 2353-2360.
 44. Sarma, J.A.R.P. and G.R. Desiraju, *The role of Cl.cntdot..cntdot..cntdot.Cl and C-H.cntdot..cntdot..cntdot.O interactions in the crystal engineering of 4-ANG short-axis structures*. Accounts of Chemical Research, 1986. **19**(7): p. 222-

228.

45. Bleiholder, C., D.B. Werz, H. Köppel, and R. Gleiter, *Theoretical Investigations on Chalcogen–Chalcogen Interactions: What Makes These Nonbonded Interactions Bonding?* Journal of the American Chemical Society, 2006. **128**(8): p. 2666-2674.
46. Gleiter, R., D.B. Werz, and B.J. Rausch, *A World Beyond Hydrogen Bonds?—Chalcogen–Chalcogen Interactions Yielding Tubular Structures*. Chemistry – A European Journal, 2003. **9**(12): p. 2676-2683.
47. Sokolov, A.N., T. Frišćić, and L.R. MacGillivray, *Enforced Face-to-Face Stacking of Organic Semiconductor Building Blocks within Hydrogen-Bonded Molecular Cocrystals*. Journal of the American Chemical Society, 2006. **128**(9): p. 2806-2807.
48. Zhang, Z., Y. Zhang, D. Yao, H. Bi, I. Javed, Y. Fan, H. Zhang, and Y. Wang, *Anthracene-Arrangement-Dependent Emissions of Crystals of 9-Anthrylpyrazole Derivatives*. Crystal Growth & Design, 2009. **9**(12): p. 5069-5076.
49. Kim, S., M. Fujitsuka, N. Tohnai, T. Tachikawa, I. Hisaki, M. Miyata, and T. Majima, *The unprecedented J-aggregate formation of rhodamine moieties induced by 9-phenylanthracenyl substitution*. Chemical Communications, 2015. **51**(58): p. 11580-11583.
50. Cantekin, S., T.F.A. de Greef, and A.R.A. Palmans, *Benzene-1,3,5-tricarboxamide: a versatile ordering moiety for supramolecular chemistry*. Chemical Society Reviews, 2012. **41**(18): p. 6125-6137.
51. Park, H.-g., S.G. Youm, M. Jeon, S.Y. Park, and D. Sohn, *Molecular J-aggregation for the Langmuir–Blodgett film of a novel tripodal dye*. Colloids and Surfaces A: Physicochemical and Engineering Aspects, 2010. **366**(1–3): p. 34-37.
52. Pescitelli, G., L. Di Bari, and N. Berova, *Application of electronic circular dichroism in the study of supramolecular systems*. Chemical Society Reviews, 2014. **43**(15): p. 5211-5233.
53. Babu, S.S., V.K. Praveen, and A. Ajayaghosh, *Functional π -Gelators and Their Applications*. Chemical Reviews, 2014. **114**(4): p. 1973-2129.
54. Lu, L., T.M. Cocker, R.E. Bachman, and R.G. Weiss, *Gelation of Organic Liquids by Some 5 α -Cholestan-3 β -yl N-(2-Aryl)carbamates and 3 β -Cholesteryl 4-(2-Anthrylamino)butanoates. How Important Are H-Bonding Interactions in the Gel and Neat Assemblies of Aza Aromatic-Linker-Steroid Gelators?*†. Langmuir, 2000. **16**(1): p. 20-34.
55. Rajamalli, P. and E. Prasad, *Luminescent micro and nanogel formation from AB3 type poly(aryl ether) dendron derivatives without conventional multi-interactive gelation motifs*. New Journal of Chemistry, 2011. **35**(7): p. 1541-1548.
56. Kim, S., Q. Zheng, G.S. He, D.J. Bharali, H.E. Pudavar, A. Baev, and P.N. Prasad, *Aggregation-Enhanced Fluorescence and Two-Photon Absorption in Nanoaggregates of a 9,10-Bis[4'-(4"-aminostyryl)styryl]anthracene Derivative*. Advanced Functional Materials, 2006. **16**(18): p. 2317-2323.
57. Sako, Y. and Y. Takaguchi, *A photo-responsive hydrogelator having gluconamides at its peripheral branches*. Organic & Biomolecular Chemistry, 2008. **6**(20): p. 3843-3847.
58. Duan, P. and M. Liu, *Design and Self-Assembly of L-Glutamate-Based Aromatic Dendrons as Ambidextrous Gelators of Water and Organic Solvents*.

- Langmuir, 2009. **25**(15): p. 8706-8713.
59. Akatsuka, R., A. Momotake, Y. Shinohara, Y. Kanna, T. Sato, M. Moriyama, K. Takahashi, Y. Nishimura, and T. Arai, *Observation of anthracene excimer fluorescence at very low concentrations utilizing dendritic structures*. Journal of Photochemistry and Photobiology A: Chemistry, 2011. **223**(1): p. 1-5.
 60. Wang, C., D. Zhang, J. Xiang, and D. Zhu, *New Organogels Based on an Anthracene Derivative with One Urea Group and Its Photodimer: Fluorescence Enhancement after Gelation*. Langmuir, 2007. **23**(18): p. 9195-9200.
 61. Cho, D.W. and D.W. Cho, *Excimer and exciplex emissions of 1,8-naphthalimides caused by aggregation in extremely polar or nonpolar solvents*. New Journal of Chemistry, 2014. **38**(6): p. 2233-2236.
 62. Ryu, S.Y., S. Kim, J. Seo, Y.-W. Kim, O.-H. Kwon, D.-J. Jang, and S.Y. Park, *Strong fluorescence emission induced by supramolecular assembly and gelation: luminescent organogel from nonemissive oxadiazole-based benzene-1,3,5-tricarboxamide gelator*. Chemical Communications, 2004(1): p. 70-71.
 63. An, B.-K., D.-S. Lee, J.-S. Lee, Y.-S. Park, H.-S. Song, and S.Y. Park, *Strongly Fluorescent Organogel System Comprising Fibrillar Self-Assembly of a Trifluoromethyl-Based Cyanostilbene Derivative*. Journal of the American Chemical Society, 2004. **126**(33): p. 10232-10233.
 64. Bao, C., R. Lu, M. Jin, P. Xue, C. Tan, G. Liu, and Y. Zhao, *l-Tartaric acid assisted binary organogel system: strongly enhanced fluorescence induced by supramolecular assembly*. Organic & Biomolecular Chemistry, 2005. **3**(14): p. 2508-2512.
 65. Kim, T.H., M.S. Choi, B.-H. Sohn, S.-Y. Park, W.S. Lyoo, and T.S. Lee, *Gelation-induced fluorescence enhancement of benzoxazole-based organogel and its naked-eye fluoride detection*. Chemical Communications, 2008(20): p. 2364-2366.
 66. Allen, D.J. and H. Ishida, *Physical and mechanical properties of flexible polybenzoxazine resins: effect of aliphatic diamine chain length*. Journal of applied polymer science, 2006. **101**(5): p. 2798-2809.
 67. Watanabe, J., N. Sekine, T. Nematsu, M. Sone, and H.R. Kricheldorf, *Rigid-rod polyesters with flexible side chains. 6. Appearance of hexagonal columnar phase as a consequence of microsegregation of aromatic main chains and aliphatic side chains*. Macromolecules, 1996. **29**(13): p. 4816-4818.
 68. Zeng, L., L. Zhang, and A.R. Barron, *Tailoring aqueous solubility of functionalized single-wall carbon nanotubes over a wide pH range through substituent chain length*. Nano Letters, 2005. **5**(10): p. 2001-2004.
 69. Bunn, C., *The melting points of chain polymers*. Journal of Polymer Science Part B: Polymer Physics, 1996. **34**(5): p. 799-819.
 70. González-Rodríguez, D. and A.P.H.J. Schenning, *Hydrogen-bonded Supramolecular π -Functional Materials*. Chemistry of Materials, 2011. **23**(3): p. 310-325.
 71. Steiner, T., *The Hydrogen Bond in the Solid State*. Angew. Chem. International Edition, 2002. **41**(1): p. 48-76.
 72. Prins, L.J., D.N. Reinhoudt, and P. Timmerman, *Noncovalent Synthesis Using Hydrogen Bonding*. Angew. Chem. International Edition, 2001. **40**(13): p. 2382-2426.
 73. Sijbesma, R.P. and E.W. Meijer, *Quadruple Hydrogen Bonded Systems*. Chemical Communications, 2003(1): p. 5-16.

74. van Hameren, R., P. Schön, A.M. van Buul, J. Hoogboom, S.V. Lazarenko, J.W. Gerritsen, H. Engelkamp, P.C.M. Christianen, H.A. Heus, J.C. Maan, T. Rasing, S. Speller, A.E. Rowan, J.A.A.W. Elemans, and R.J.M. Nolte, *Macroscopic Hierarchical Surface Patterning of Porphyrin Trimers via Self-Assembly and Dewetting*. Science, 2006. **314**(5804): p. 1433-1436.
75. Leung, M.k., Y.S. Lin, C.C. Lee, C.C. Chang, Y.X. Wang, C.P. Kuo, N. Singh, K.-R. Lin, C.-W. Hu, and C.Y. Tseng, *Benzenetricarboxamide-cored triphenylamine Dendrimer: Nanoparticle Film Formation by an Electrochemical Method*. RSC Advances, 2013. **3**(44): p. 22219-22228.
76. Lv, K., L. Zhang, and M. Liu, *Self-Assembly of Triangular Amphiphiles into Diverse Nano/Microstructures and Release Behavior of the Hollow Sphere*. Langmuir, 2014. **30**(31): p. 9295-9302.
77. Huang, G.F., Q.T. Wu, J.W.C. Wong, and B.B. Nagar, *Transformation of organic matter during co-composting of pig manure with sawdust*. Bioresource Technology, 2006. **97**(15): p. 1834-1842.
78. Coleman, M.M., D.J. Skrovanek, and P.C. Painter, *Hydrogen bonding in polymers: III further infrared temperature studies of polyamides*. Makromolekulare Chemie. Macromolecular Symposia, 1986. **5**(1): p. 21-33.
79. Skrovanek, D.J. and M.M. Coleman, *A miscible nylon blend with poly(2-vinyl pyridine)*. Polymer Engineering & Science, 1987. **27**(11): p. 857-860.
80. Skrovanek, D.J., P.C. Painter, and M.M. Coleman, *Hydrogen bonding in polymers. 2. Infrared temperature studies of nylon 11*. Macromolecules, 1986. **19**(3): p. 699-705.
81. Fernández, C., M. Bermúdez, S. Muñoz-Guerra, S. León, R. Versteegen, and E. Meijer, *Crystal structure and morphology of linear aliphatic n-polyurethanes*. Macromolecules, 2010. **43**(9): p. 4161-4171.
82. Fernández, C.E., M. Bermúdez, S. Muñoz-Guerra, S. León, R.M. Versteegen, and E.W. Meijer, *Crystal Structure and Morphology of Linear Aliphatic n-Polyurethanes*. Macromolecules, 2010. **43**(9): p. 4161-4171.
83. Skrovanek, D.J., S.E. Howe, P.C. Painter, and M.M. Coleman, *Hydrogen bonding in polymers: infrared temperature studies of an amorphous polyamide*. Macromolecules, 1985. **18**(9): p. 1676-1683.
84. Li, D., H. Zhang, and G. Ma, *Secondary structure investigation of bovine serum albumin (BSA) by Fourier transform infrared (FTIR) spectroscopy in the amide III region*. European Journal of Chemistry, 2014. **5**(2): p. 287-290.
85. Suganya, S., J. Venugopal, S.A. Mary, S. Ramakrishna, B. Lakshmi, and V.G. Dev, *Aloe vera incorporated biomimetic nanofibrous scaffold: a regenerative approach for skin tissue engineering*. Iranian Polymer Journal, 2014. **23**(3): p. 237-248.
86. Kazemimostaghimi, M., R. Rajkhowa, K. Patil, T. Tsuzuki, and X. Wang, *Structure and characteristics of milled silk particles*. Powder technology, 2014. **254**: p. 488-493.
87. Zhang, H., Y.G. Shan, L. Li, M. Lu, and R. Li, *Modeling the self-assembly of nanoparticles into branched aggregates from a sessile nanofluid droplet*. Applied Thermal Engineering, 2016. **94**: p. 650-656.
88. Zhang, J., M.K. Borg, K. Ritos, and J.M. Reese, *Electrowetting controls the deposit patterns of evaporated salt water nanodroplets*. Langmuir, 2016.
89. Shaikeeva, A.J.D. and S. Basu, *Insight into the Evaporation Dynamics of a Pair of Sessile Droplets on Hydrophobic Substrate*. Langmuir, 2016.
90. Liu, H., W. Xu, W. Tan, X. Zhu, J. Wang, J. Peng, and Y. Cao, *Line printing*

- solution-processable small molecules with uniform surface profile via ink-jet printer*. Journal of Colloid and Interface Science, 2016. **465**: p. 106-111.
91. Concetta, N., C. Luigi, F. Angela, C. Roberto, M. Liberato, and K. Roman, *Self-assembly of highly fluorescent semiconductor nanorods into large scale smectic liquid crystal structures by coffee stain evaporation dynamics*. Journal of Physics: Condensed Matter, 2009. **21**(26): p. 264013.
 92. Deegan, R.D., O. Bakajin, T.F. Dupont, G. Huber, S.R. Nagel, and T.A. Witten, *Contact line deposits in an evaporating drop*. Physical Review E, 2000. **62**(1): p. 756-765.
 93. Eral, H.B., D.M. Augustine, M.H.G. Duits, and F. Mugele, *Suppressing the coffee stain effect: how to control colloidal self-assembly in evaporating drops using electrowetting*. Soft Matter, 2011. **7**(10): p. 4954-4958.
 94. Kadish, K.M., K.M. Smith, and R. Guilard, *Handbook of porphyrin science*. World Scientific: Singapore, 2010. **2014**: p. 1-35.
 95. Majumder, M., C.S. Rendall, J.A. Eukel, J.Y.L. Wang, N. Behabtu, C.L. Pint, T.-Y. Liu, A.W. Orbaek, F. Mirri, J. Nam, A.R. Barron, R.H. Hauge, H.K. Schmidt, and M. Pasquali, *Overcoming the "Coffee-Stain" Effect by Compositional Marangoni-Flow-Assisted Drop-Drying*. The Journal of Physical Chemistry B, 2012. **116**(22): p. 6536-6542.
 96. Hoogboom, J., J.A.A.W. Elemans, A.E. Rowan, T.H.M. Rasing, and R.J.M. Nolte, *The development of self-assembled liquid crystal display alignment layers*. Philosophical Transactions of the Royal Society of London A: Mathematical, Physical and Engineering Sciences, 2007. **365**(1855): p. 1553-1576.
 97. Elemans, J.A.A.W., M.C. Lensen, J.W. Gerritsen, H. van Kempen, S. Speller, R.J.M. Nolte, and A.E. Rowan, *Scanning Probe Studies of Porphyrin Assemblies and Their Supramolecular Manipulation at a Solid-Liquid Interface*. Advanced Materials, 2003. **15**(24): p. 2070-2073.
 98. Lensen, M.C., S.J.T. van Dingenen, J.A.A.W. Elemans, H.P. Dijkstra, G.P.M. van Klink, G. van Koten, J.W. Gerritsen, S. Speller, R.J.M. Nolte, and A.E. Rowan, *Synthesis and self-assembly of giant porphyrin discs*. Chemical Communications, 2004(7): p. 762-763.
 99. Sukul, P.K. and S. Malik, *Supramolecular hydrogels of adenine: morphological, structural and rheological investigations*. Soft Matter, 2011. **7**(9): p. 4234-4241.

CHAPTER IV

4.1 Introduction

Water is one of the most essential natural resources for humankind due to its use for food production, industrial activities, energy generation and human consumption [1]. With the continuous decrease in freshwater supplies, thin film composite (TFC) membranes have emerged as an attractive solution for water filtration. They have been widely used due to their low operating temperature and efficiency compared with other filtration systems, such as thermal distillation and electrodialysis processes [2, 3]. The TFC membrane consists of three layers: polyester fabric base layer; porous support layer (such as polysulfone cast on the base layer) and on top of these layers is polyamide as an active skin layer as illustrated in Figure 4- 1. The performance of the TFC membrane is mainly dependent on the active skin layer, while the mechanical support comes from the base and porous layers.

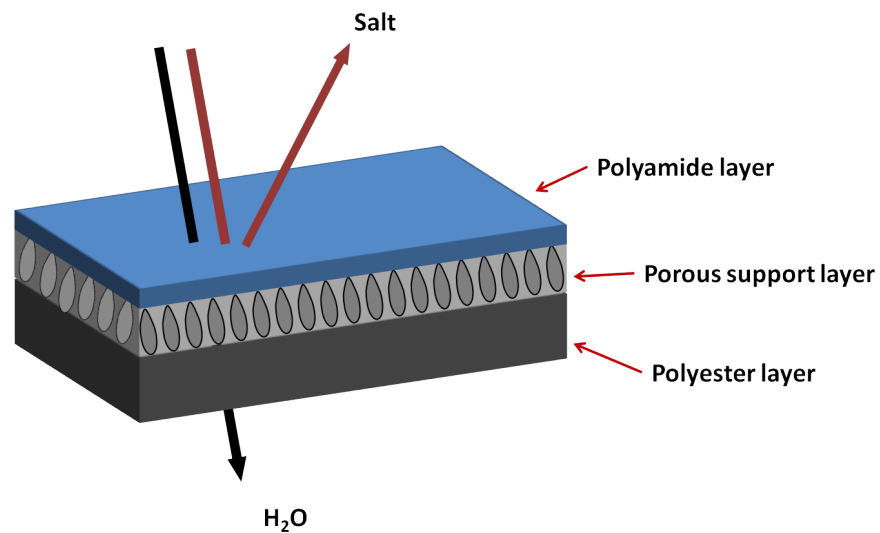


Figure 4- 1. Schematic structure showing the thin film composite (TFC) membrane, with the active polyamide layer on top, supported by polysulfone, and with polyester as the base layer[3].

Commercially, TFC polyamide membranes are fabricated by an interfacial polymerisation technique using benzene-1,3,5-tricarboxylic acid chloride (trimesoyl chloride, TMC) and *m*-phenylenediamine (MPD) in the organic and aqueous phases respectively. TFC membranes of polyamide show high salt rejection and water flux compare to other membranes [3]. The key performance parameters of a TFC membrane are the flux and salt rejection.

Nanotechnology has been utilised to improve the properties of TFC membranes. Recent studies have demonstrated that membrane properties were improved by embedding nanoparticles in polyamide thin films due to the unique properties of nanoparticles such as large surface area and large number of functional groups. The new concept of embedding nanoparticles in the polyamide layer of TFC membranes has emerged as a thin film nanocomposite (TFN) [4-6]. For example, embedding zeolite nanoparticles in the polyamide membrane improved the water flux without a significant decrease in salt rejection [7, 8]. Silver nanoparticles and titanium oxide nanoparticles also were embedded in the polyamide membrane to improve the membrane properties such as the water flux, chemical and physical resistance [9, 10].

CNTs have unique thermal, electrical and mechanical properties [11]. Moreover, the high transport rate of solvents such as ethanol and water through the tubes has caught the attention of many researchers [12-16]. Given this, CNTs have been embedded in polymers for ultrafiltration [17, 18], pervaporation [19, 20], distillation [21, 22], reverse osmosis [23, 24] and forward osmosis membranes [25, 26]. There are, however, some difficulties with embedding CNTs in membrane polymers, such as their dispersion in, and grafting with, the polymer.

It is known that agents incorporated by physical methods can be washed away from membranes during long-term operation and under high pressure [27-29]. As such, it is quite probable that CNTs physically embedded in membranes will be lost during the filtration process. The loss of CNTs will negatively influence the membrane's performance and properties [30]. Thus, it is preferred that CNTs are grafted to the membrane via a covalent attachment to the polymer chains. Distributing the CNTs in the polymer is one of the most difficult steps, especially when CNTs are involved in the interfacial polymerisation by dispersing in the organic phase.

Very little literature has been published about modified polyamide membranes with dispersion of CNTs in the organic phase (non-polar solvent). This is due to the challenge of obtaining high dispersion of CNTs in such solvents. Thus, the distribution of CNTs in polyamide membrane will be limited.

Shen et al. reported synthesis of thin film nanocomposite membranes containing functionalised MWNTs. The improvement of MWNTs dispersion in the organic phase

was obtained by functionalising the MWNTs with poly(methyl methacrylate). Morphology studies showed that MWNTs had been successfully embedded in the polyamide membrane. Membrane water flux and salt rejection also improved [31].

In this work, the interfacial polymerisation between TMC and MPD was chosen due to its popularity in TFC membrane preparation. SWNTs were covalently attached to the polyamide membrane *in situ* during the interfacial polymerisation. SWNTs were dispersed in the organic phase by functionalising them with organic compounds with different chain lengths. The effect of chain length on SWNT distribution in the polyamide was investigated. In addition, there was an investigation of the membrane's flux, salt rejection and hydrophilicity.

4.2 Synthesis and functionalisation

Embedding SWNTs in a polyamide membrane via interfacial polymerisation was performed by functionalising the SWNTs. In the first step, suitable organic reactive moieties for incorporation into the polymerisation reaction were synthesised. Characterisation was performed before commencing the next step. Covalent attachment of the synthesised moieties to SWNTs was achieved by amide coupling reactions. In the next sections, synthesis of the organic compounds and functionalisation of SWNTs will be described.

4.2.1 Synthesis of organic compounds

The synthesis of the organic compounds is illustrated in Figure 4- 2, which shows the synthetic route of the two organic compounds (10a, 10b). The synthesis procedure was the same for both compounds. The difference between compounds being the aliphatic chain length, which was either two or six carbon atoms.

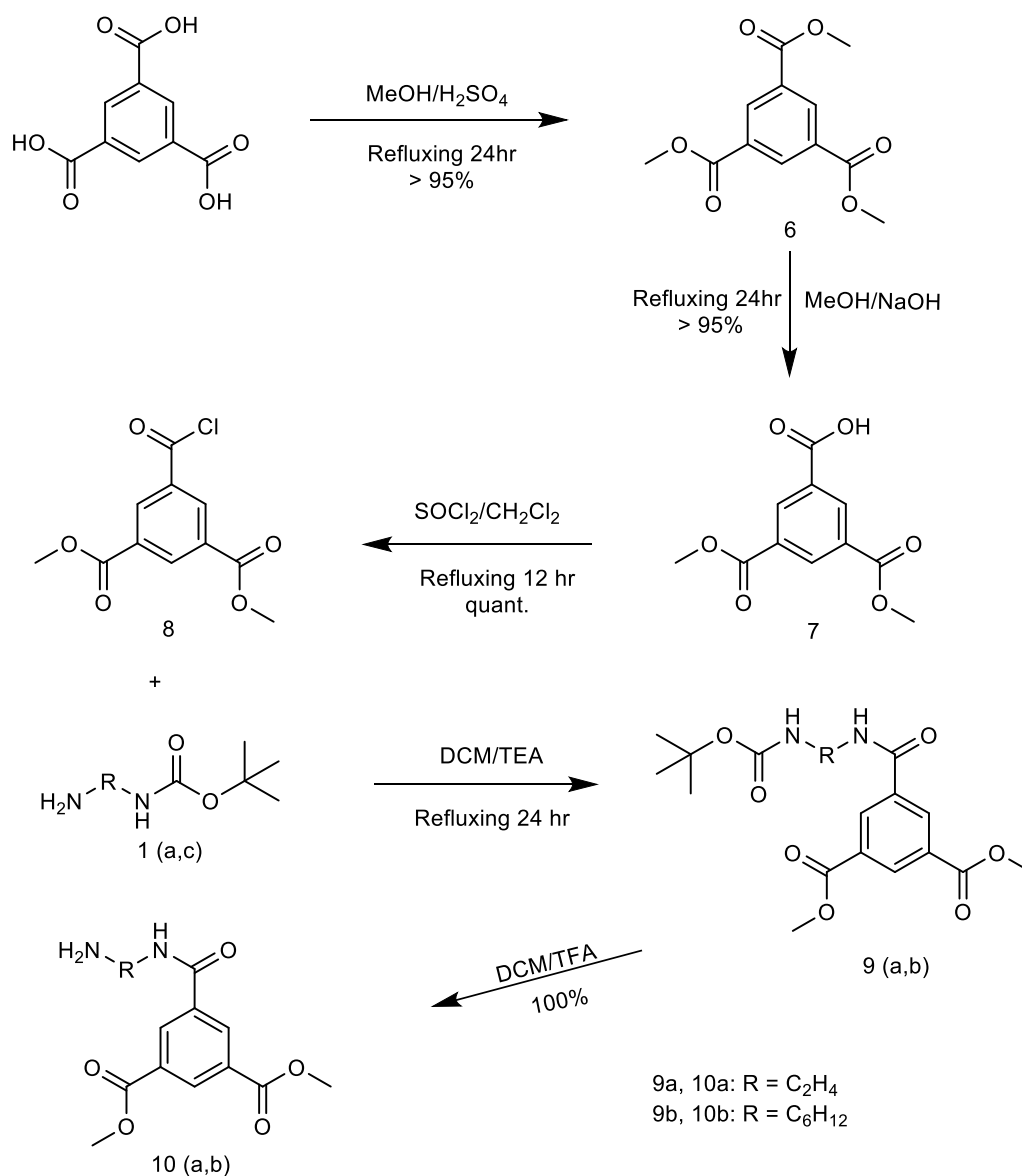


Figure 4- 2. Synthetic route of organic compounds synthesis.

Synthesis of the compounds proceeded from benzene-1,3,5-tricarboxylic acid, and a quantitative yield of trimethyl 1,3,5-benzenetricarboxylate (6) was achieved by heating benzene-1,3,5-tricarboxylic acid in methanol and sulphuric acid under reflux. The product was characterised in *d*₆-dimethyl sulfoxide by ¹H NMR, showing the methyl component of the ester functional group at 3.94 ppm as a singlet. FT-IR also confirmed the ester compound, as an (C=O) ester band was seen at 1724 cm⁻¹. Hydrolysis of one of the ester groups was achieved by heating trimethyl 1,3,5-benzenetricarboxylate (6) under reflux with one equivalent of sodium hydroxide with methanol as solvent, producing dimethyl 1,3,5-benzenetricarboxylate (7).

Integration of the methyl component of the ester functional group in the ^1H NMR spectrum proved that one ester group in the compound had been hydrolysed. The appearance of the acid carbonyl band ($\text{C}=\text{O}$) at 1699 cm^{-1} next to ester band in the FT-IR spectrum confirmed hydrolysis of the ester group. Dimethyl 1,3,5-benzenetricarboxylate (7) was heated under reflux in thionyl chloride to convert the acid to the acid chloride, resulting in dimethyl 1,3,5-benzenetricarboxylate acid chloride (8). The carbonyl band ($\text{C}=\text{O}$) at 1750 cm^{-1} in the FT-IR spectrum indicated successful conversion of the acid group to the acid chloride group.

Dimethyl 1,3,5-benzenetricarboxylate acid chloride (8) was allowed to react with protected diamines (1a and 1c) separately in dry DCM with heating under reflux for 24 hours. The produced compounds (9a, 9b) were characterised in d_6 -dimethyl sulfoxide by ^1H NMR showing peaks as a singlet at 1.37 and 3.94 ppm for Boc and methyl component of the ester functional groups respectively. The final step was the de-protection of the amine group from Boc group by adding TFA to the compound resulting in the production of the free amine compounds. Disappearance of the 1.37 ppm peak in ^1H NMR spectrum proved the de-protection of the amine group in compounds (10a, 10b). In addition to ^1H NMR and FT-IR, ^{13}C NMR and mass spectroscopy were used to verify the reaction products.

4.2.2 Functionalisation of single wall carbon nanotubes (SWNTs)

Single wall carbon nanotube functionalisation, as illustrated in Figure 4- 3, started with acid treatment of the SWNTs by ultrasonication in a 3:1 v/v solution of H_2SO_4 (98%) and HNO_3 (70%) at a nanotube concentration of 1 mg mL^{-1} for 6 hours, followed by quenching the reaction by adding 1L of cold Milli-Q water and washing with Milli-Q water. In this step, carboxylic groups were created on the wall as well as ends of the nanotube.

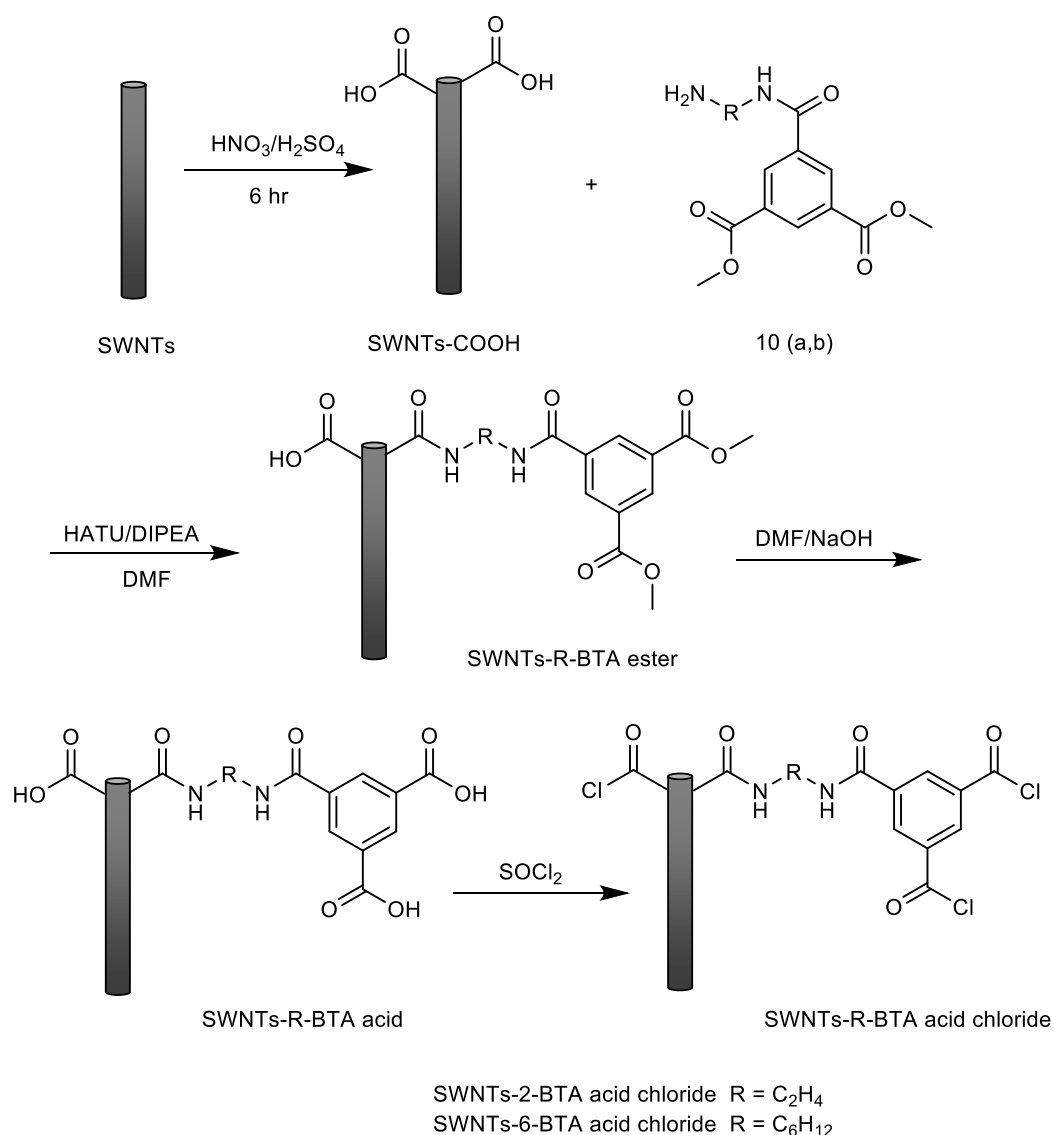


Figure 4- 3. Synthetic route of SWNT functionalisation.

Grafting of the synthesised compounds to the oxidised SWNTs was achieved via an amidation reaction using HATU as the coupling reagent. In the next step, the ester groups in grafted SWNTs were converted to acid groups by ultrasonication in a 1:3 v/v solution of 1M sodium hydroxide and DMF at a nanotube concentration of 1 mg mL^{-1} with heating at 80°C and stirring overnight as illustrated in Figure 4- 3 (SWNTS-R-BTA acid). The acid groups, either in the compounds grafted to SWNTs or unreacted on the carbon nanotubes wall, were converted to acid chloride by heating under reflux in thionyl chloride overnight. Raman and FT-IR were used to characterise the modified SWNTs.

4.2.2.1 Raman

The modification of SWNTs was characterised by Raman spectroscopy due to the technique's high sensitivity to nanotube surface changes resulting from modification as seen in Figure 4- 4 [32]. The pristine SWNT Raman spectrum shows bands at 163 cm^{-1} , 1334 cm^{-1} and 1590 cm^{-1} , which were assigned to the RBM, D and G bands respectively. The RBM is a band unique to SWNTs which arises from coherent vibrations of the carbon atoms. The D band is called the disorder band, which is attributed to sp^3 hybridised carbon atoms in the nanotube sidewall. The tangential band, or G band, is caused by movement in opposite directions of neighbouring carbon atoms [33]. Calculating the ratio of D to G bands indicates the amount of defects on the wall of CNTs [34, 35]. Due to the similarity in Raman spectrum of the two modified SWNTs, only SWNTs-2-BTA spectra are presented.

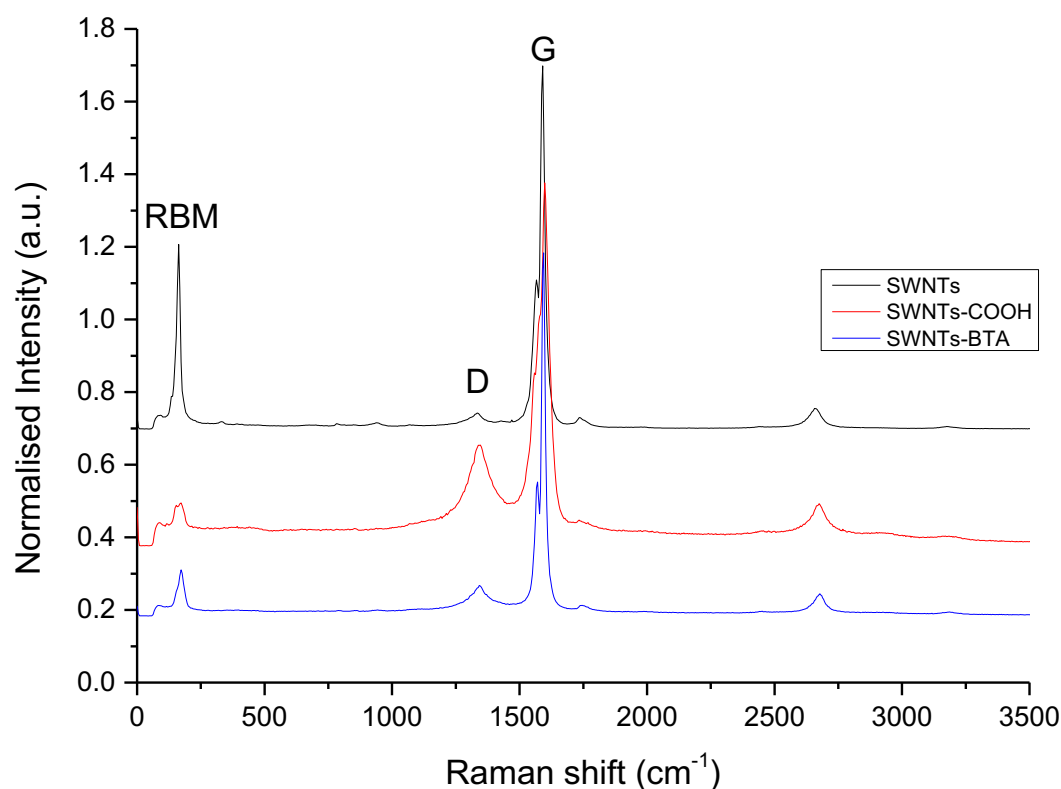


Figure 4- 4. Raman spectra with 532 nm laser of pristine SWNTs (black line), oxidised SWNTs (red line) and functionalised SWNTs with synthesised compound (blue line).

The ratio of the D/G bands was calculated determined and the results are provided in Table 4-5. This ratio increased from 0.06 to 0.25 for pristine and oxidised SWNTs

respectively indicating that the oxidation process increased the defects and the sp^3 -hybridised carbon atoms on the SWNT sidewall. A decrease in the D/G ratio to 0.07 after grafting of the amine compound to the SWNTs through the amide coupling reaction may be attributed to the presence of aromatic moieties that could increase the sp^2 over the sp^3 .

Moreover, the tube diameter can be evaluated using the following equation:

$$\omega_r = 223.75/d \quad (4-1)$$

where ω_r is the RBM frequency and d is the tube diameter [34, 36]. Using this equation, the diameters were calculated and collected in Table 4-5.

The pristine SWNTs had a diameter of 1.37 nm; however, the oxidation process for the SWNTs caused a small shift of RBM frequency from 163 cm^{-1} to 172 cm^{-1} . Grafting the amine compound to the SWNTs showed no RBM shift indicating that the diameter did not change.

Table 4-5. Raman spectra peak position using a 532 nm laser of pristine SWNTs, oxidised SWNTs and functionalised SWNTs with BTA-2-ester (SWNTs-BTA ester).

	RBM (cm^{-1})	D-band (cm^{-1})	G-band (cm^{-1})	D/G	SWNTs diameter (nm)
SWNTs	163	1334	1590	0.06	1.37
SWNTs-COOH	172	1342	1598	0.25	1.30
SWNTs-BTA ester	172	1342	1595	0.07	1.30

Further proof of the SWNTs' modification was drawn from the Raman spectra shift as seen in Figure 4- 4. Attachment of functional groups possessing oxygen, such as carboxylic acid, to the SWNTs causes a frequency shift of Raman peaks to higher wavenumbers [37]. It has been suggested that it is due to the SWNTs electronic structure changing by attaching highly electronegative atoms, which cause a change in the electronic structure of SWNTs [37, 38].

The presence of ester groups in the functionalised SWNTs could not be seen in Raman analysis. Therefore, FT-IR analysis was used to further investigate the ester group's presence and hydrolysis during the functionalisation of SWNTs.

4.2.2.2 FT-IR

The SWNTs functionalisation process steps were characterised and compared by FT-IR spectra, as seen in Figure 4- 5. The acid treated SWNTs showed bands at 3456 cm^{-1} , 2920 cm^{-1} , 2850 cm^{-1} and 1636 cm^{-1} , which were attributed to O-H stretching, C-H symmetric stretching, C-H asymmetric stretching, and C=O stretching respectively. These bands appeared in all of the FT-IR spectra examined. Once the synthesised compounds were reacted with acid treated SWNTs, new bands appeared at 1722 cm^{-1} , 1577 cm^{-1} and 1080 cm^{-1} assigned to ester carbonyl group (C=O), amide II and C-O stretching, respectively. Hydrolysing the ester led to disappearance of the ester carbonyl group band at 1722 cm^{-1} , while a new band appeared at 1200 cm^{-1} , this was assigned to O-H deformation.

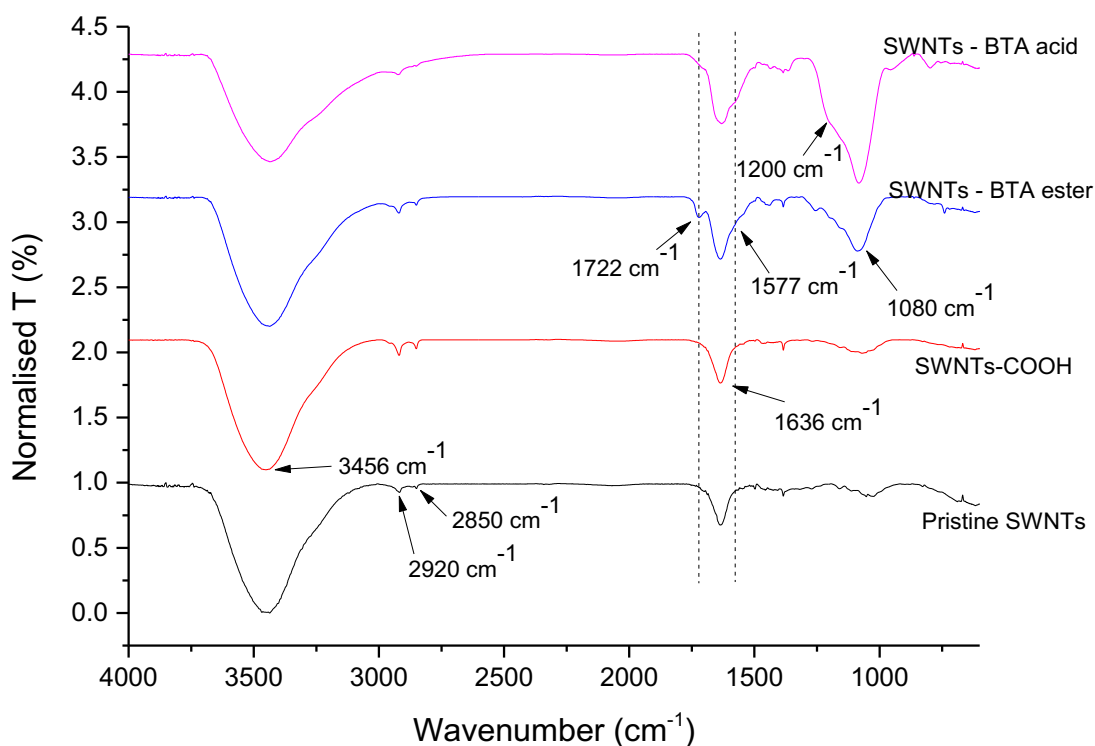


Figure 4- 5. FT-IR spectra of pristine SWNTs, oxidised SWNTs (SWNTs-COOH), functionalised SWNTs (SWNTs-BTA ester) and SWNTs after hydrolysing (SWNTs-BTA acid).

The conversion of acid groups to acid chloride groups on SWNTs was investigated by placing drops of dispersed acid chloride modified SWNTs (SWNTs-BTA-acid chloride) in toluene between two NaCl disks. The comparison between spectra of

SWNTs-BTA-acid chloride solution, pure toluene [39] and SWNTs-BTA acid is shown in Figure 4- 6. The absence of an OH band at 3456 cm^{-1} and the appearance of the acid chloride carbonyl (C=O) band at 1746 cm^{-1} after thionyl chloride treatment confirmed the conversion of the acid groups to acid chloride groups. Therefore, the successful treatment of the acid group with thionyl chloride was confirmed and attention shifted to construction of polyamide membranes.

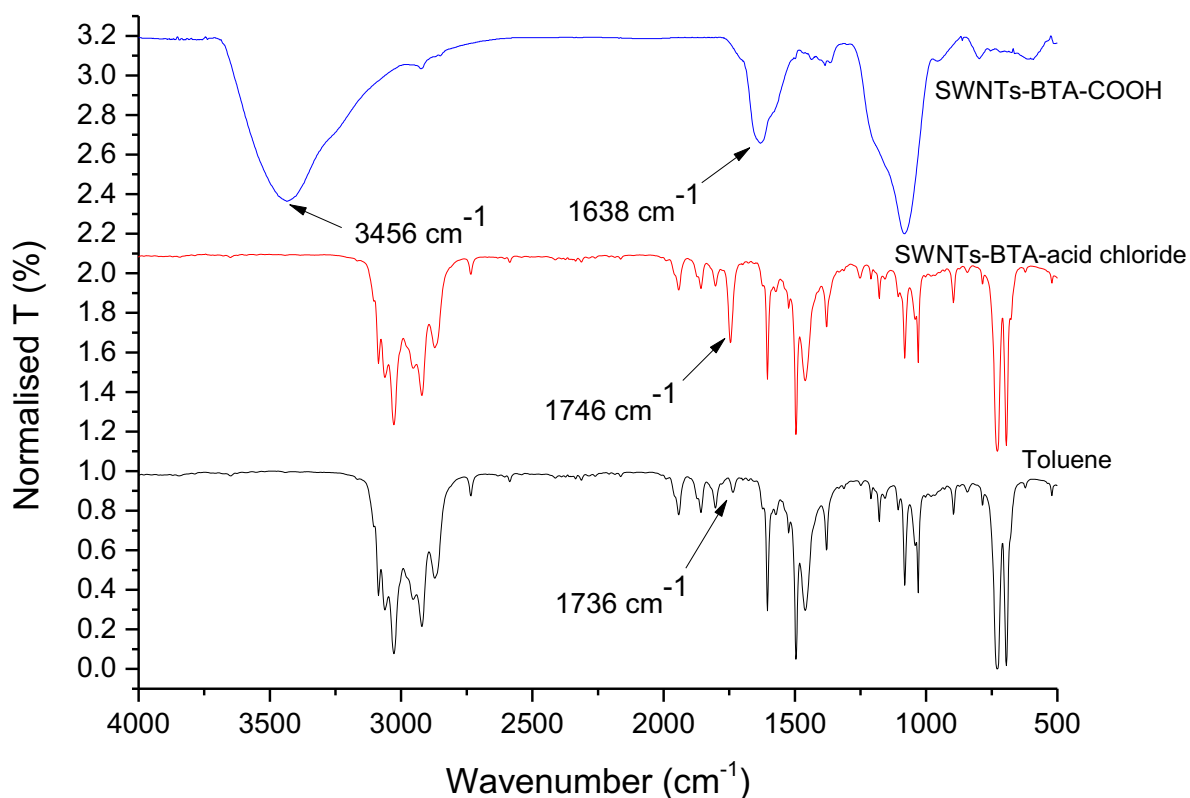


Figure 4- 6. FT-IR spectra of SWNTs-BTA-acid, SWNTs-BTA-COCl in toluene, and pure toluene recorded using NaCl disks.

4.2.3 Thin layer of polyamide in TFC membrane

The final TFC membrane structure contains a thin top polyamide layer in contact with the supporting layer surface, as illustrated in Figure 4- 1. Before examining the SWNT incorporation, conventional polyamide membranes were prepared. Using the interfacial polymerisation process, the polyamide layer was formed on the top surface of the supporting layer (PSf). The porous PSf was saturated with MPD aqueous solution (aqueous phase) and then was covered with TMC in an organic solution

(organic phase). At the interface between the aqueous and organic solutions, the reaction of MPD and TMC resulted in the formation of polyamide as a thin layer on top of the PSf surface. The adequate solubility of the MPD in the organic phase and the low solubility of TMC in the aqueous phase resulted in MPD diffusion from the aqueous phase into the organic phase to react with TMC [40-42]. Initially, a thin layer of polyamide is formed, but MPD is able to diffuse through the thin layer into the TMC organic phase and react with TMC, increasing the polyamide layer thickness. However, the increasing thickness of the polyamide layer limits transport of MPD through the layer [42, 43]. The self-limiting formation of the dense layer of polyamide occurs in a short time (seconds) due to the rapid condensation polymerisation between MPD and TMC [6]. The polyamide forming reaction is illustrated in Figure 4- 7.

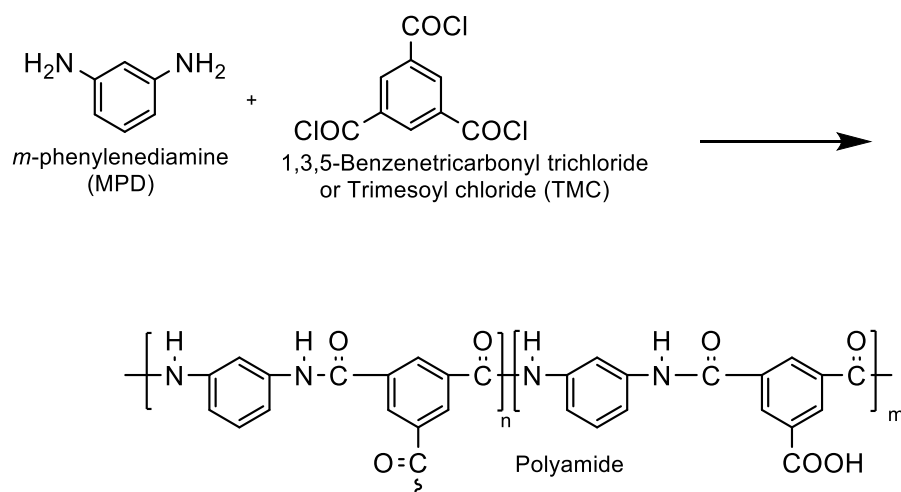


Figure 4- 7. Polyamide membrane derived from *m*-phenylenediamine (MPD) in the aqueous phase and trimesoyl chloride (TMC) in the organic phase via interfacial polymerisation [3].

The embedding of SWNTs in the thin layer of polyamide was achieved by ultrasonically functionalised SWNTs in a 4:1 v/v solution of hexane and toluene at nanotube concentrations of 0, 0.5, 1, 2.5, 5, 10 and 50 wt% based on the weight of the TMC (0.1 g in 100 mL) in organic solution. Due to the low dispersion of functionalised SWNTs in hexane, toluene (20% v/v) was added to improve the dispersion of functionalised SWNTs in the organic phase, and sonication was applied to enhance SWNT dispersion. Figure 4- 8 illustrates the preparation process of the membranes. The membranes were examined by FT-IR, and Raman spectroscopies as well as TGA.

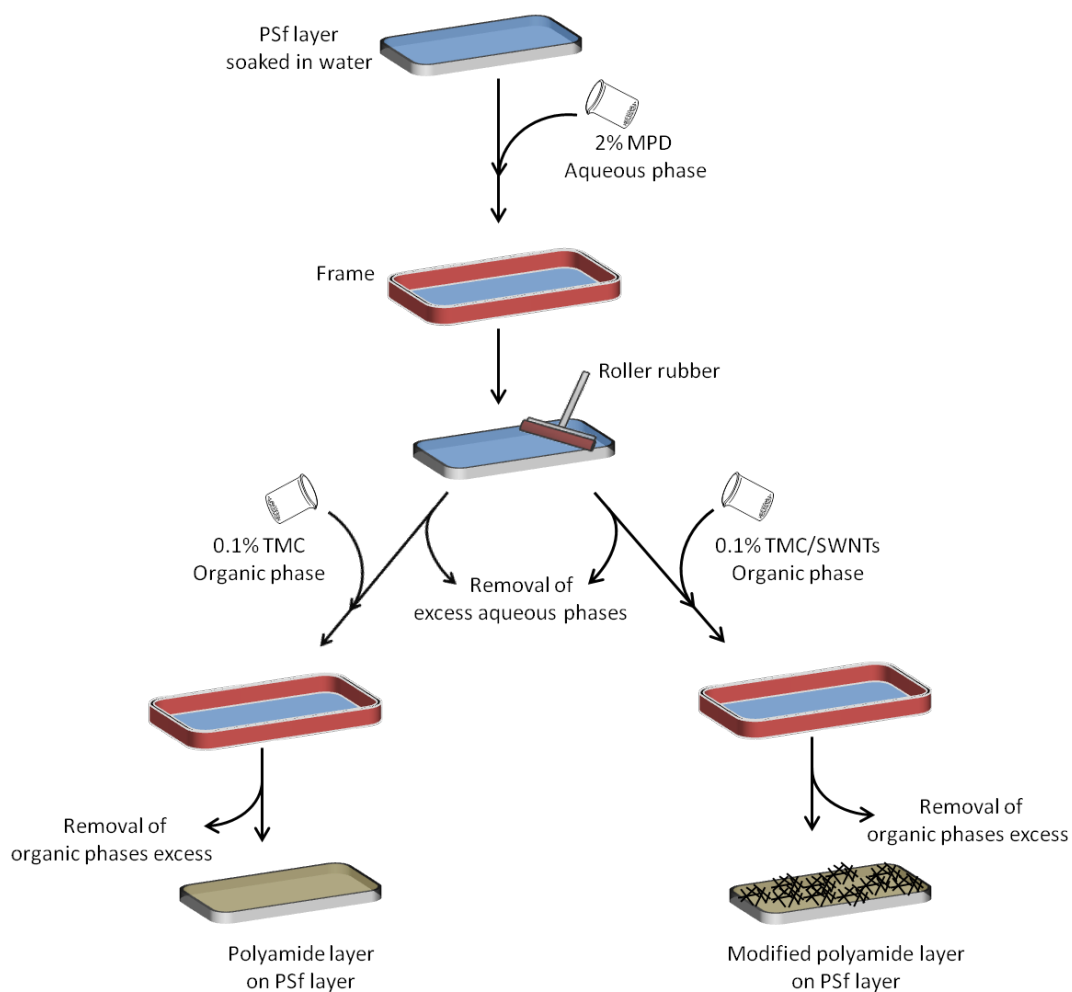


Figure 4- 8. Schematic diagram of the membrane preparation process. The PSf layer was covered with the aqueous phase (2% MPD) for 5 minutes then after removal of the excess aqueous phase contact to organic layer (0.1% TMC) was allowed for 60s. In the modified polyamide layer, SWNTs were dispersed in the organic phase.

As seen in Table 4-6, the prepared membranes were assigned PA-n-#, where PA is polyamide, n represents the chain length (2 or 6), and # is the concentration (wt%) of SWNTs in the organic phase.

Table 4-6. Polyamide membrane content of functionalised SWNTs with short-chain and long-chain compounds.

No.	SWNTs Wt% in organic phase	Polyamide membranes	
		PA/SWNT-2-BTA	PA/SWNT-6-BTA
1	0	PA	PA
2	0.5	PA-2-0.5	PA-6-0.5
3	1	PA-2-1	PA-6-1
4	2.5	PA-2-2.5	PA-6-2.5
5	5	PA-2-5	PA-6-5
6	10	PA-2-10	PA-6-10
7	50	PA-2-50	PA-6-50

4.2.3.1 FT-IR

The FT-IR spectrum of the polyamide layer on top of the support layer is quite similar to the FT-IR spectrum reported in the literature [44-46]. The spectrum shows a number of fingerprint bands as seen in Figure 4- 9.

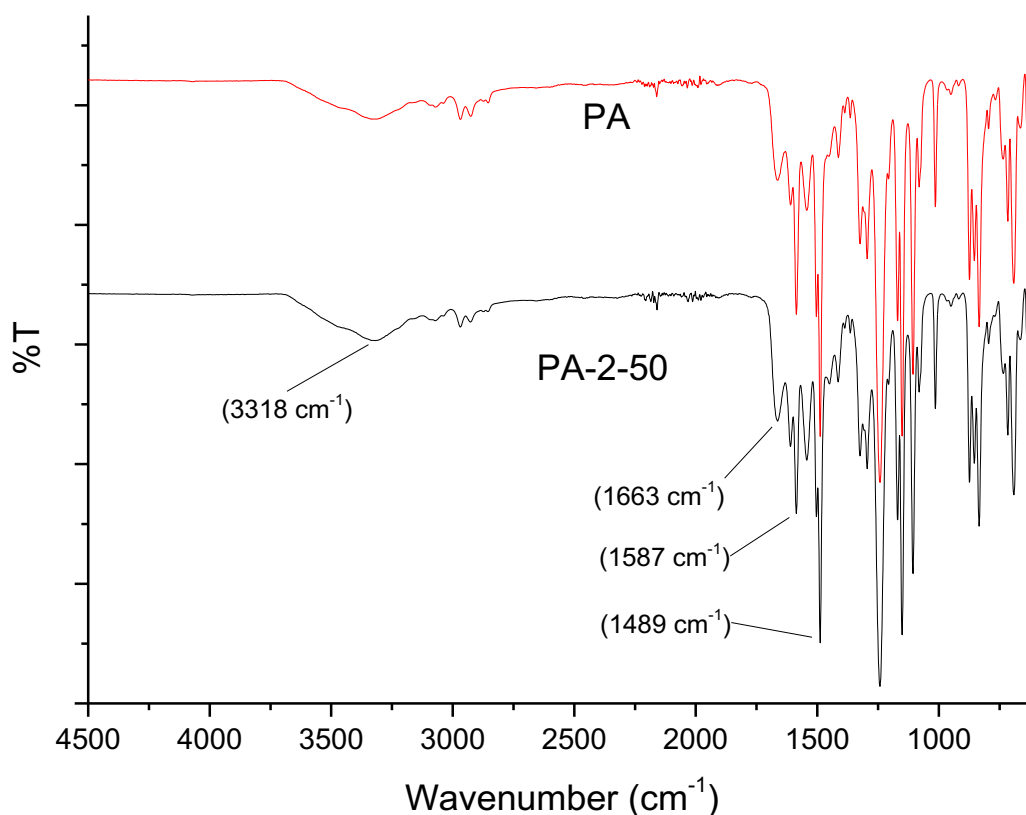


Figure 4- 9. FT-IR spectra of polyamide membrane (PA) and polyamide membrane with SWNTs (PA-2-50).

The band at 3318 cm^{-1} was assigned to the N-H stretching vibration, while bands at 1663 cm^{-1} , 1587 cm^{-1} and 1489 cm^{-1} were assigned to carbonyl stretching bands (amide I, amide II (C-N stretching and N-H bending in-plane)) and aromatic ring breathing, respectively [5]. FT-IR spectrum of PA membrane showed almost identical bands compared to SWNTs loaded membrane as shown in Figure 4- 9.

4.2.3.2 Raman

Raman spectroscopy was used to investigate the involvement of modified SWNTs in the polymerisation. Raman spectra of a conventional polyamide membrane and embedded polymer with modified SWNTs are presented in Figure 4- 10. The exposure of polyamide to Raman laser causes high fluorescence, which limits the identification of some peaks. Despite the high fluorescence of the polyamide membrane, a peak at 1583 cm^{-1} , corresponding to phenyl ring vibration, was observed [47, 48].

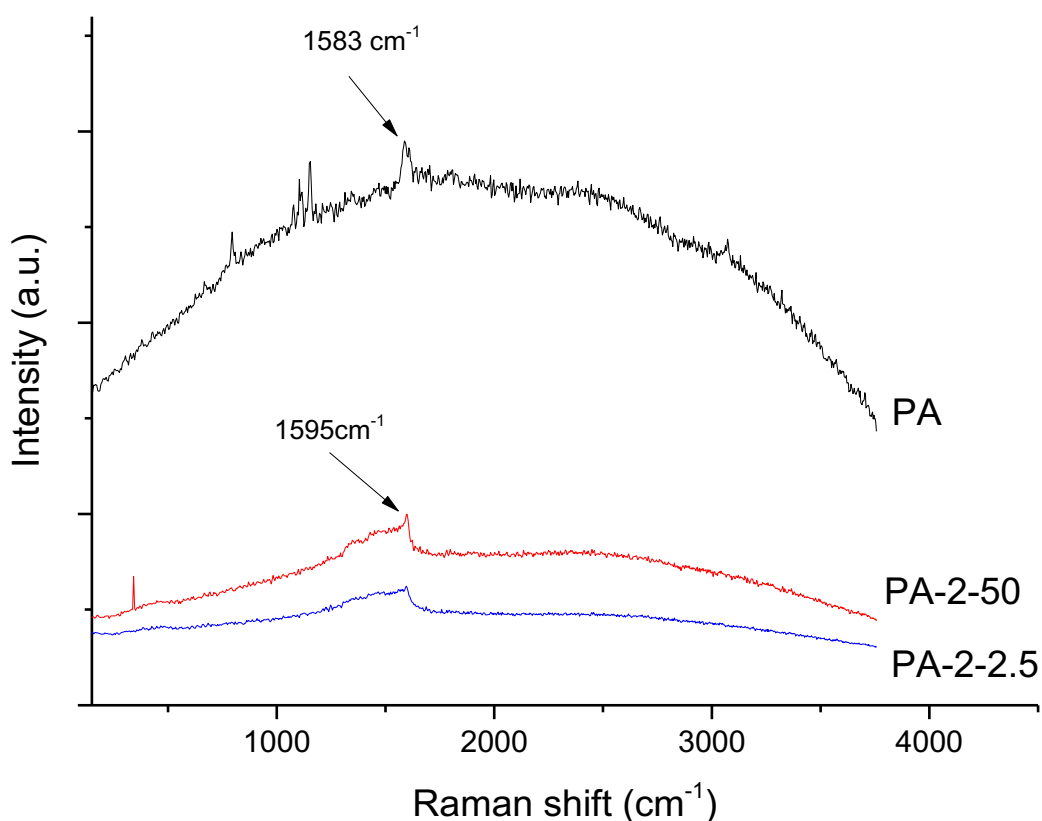


Figure 4- 10. Raman spectra of polyamide (PA), polyamide embedded with 50 wt% (PA-2-50), and 2.5 wt% (PA-2-2.5) at laser wavelength 532 nm.

A G band peak at 1595 cm^{-1} was evident in Raman spectra of the SWNTs containing membranes. The presence of this G band in the polyamide membrane with SWNTs was an indication of successful embedding of modified SWNTs in the thin polyamide layer.

4.2.3.3 TGA

TGA curves were recorded to further confirm the presence of SWNTs in the membrane. The scan rate was $20\text{ }^{\circ}\text{C}/\text{min}$ in an air atmosphere. Figure 4- 11 shows the TGA curves of the support layer polyester/polysulfone (PSf), polyamide membrane (PA), and membranes loaded with SWNTs.

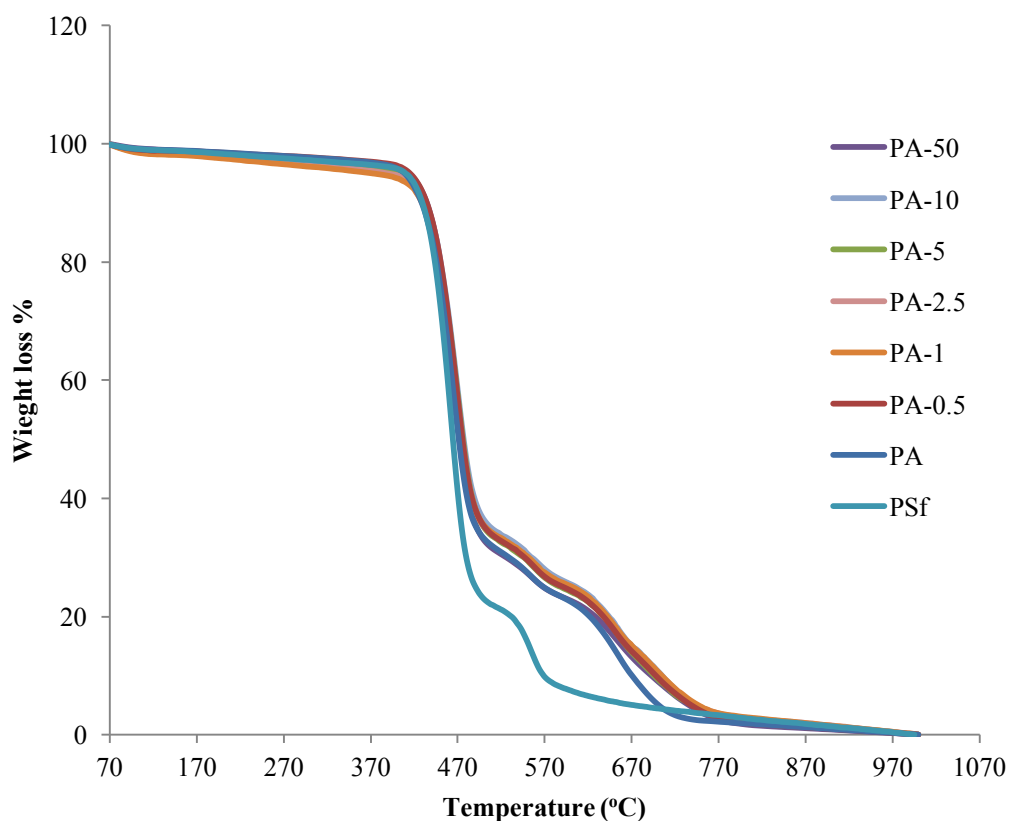


Figure 4- 11. TGA curves of all membranes, including the support layer (PSf). The scan rate was $20\text{ }^{\circ}\text{C}/\text{min}$ in an air atmosphere.

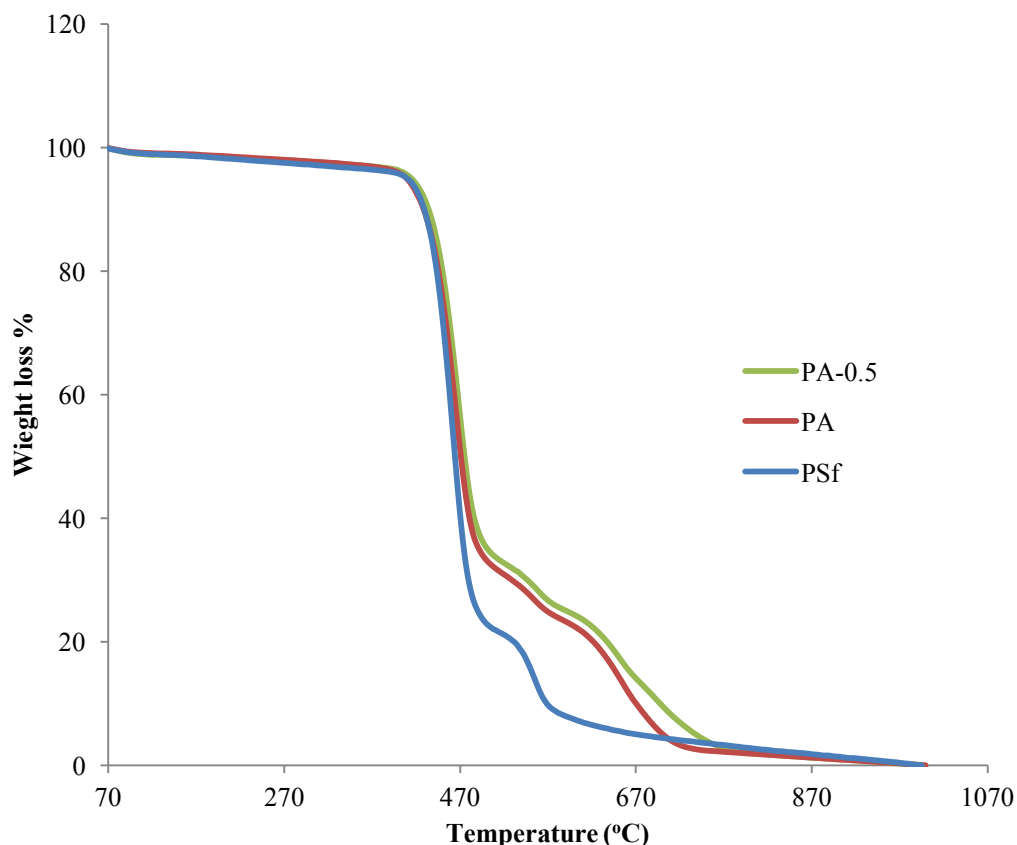


Figure 4- 12. TGA curves in air of supporting layer (PSf), polyamide (PA), and modified polyamide membrane with 0.5 wt% SWNTs in the organic phase.

The support layer (PSf) TGA had two degradation stages[49]. The first one was from around 400 °C with weight loss of around 80% and was attributed to the polyester layer [50, 51]. The second degradation stage was above 480 °C, which was caused by the polysulfone layer degradation [49, 52, 53]. A new degradation stage was also observed between 480 °C and 550 °C, which was a result of forming a thin polyamide layer on top of the support layer [54, 55].

The SWNTs' addition to the organic phase led to a shift of the TGA curves to higher temperatures. Even with a very low loading of SWNTs, such as 0.5 wt%, a shift was observed, as seen in Figure 4- 12. It has been reported that the SWNT degradation in air occurs at around 600 °C [56-58]. Thus, the improved thermal stability of the modified membrane is attributed to the SWNTs present in the polyamide. This is likely to be a result of utilising functionalised SWNTs with acyl chloride groups on the side wall and attached moieties to create covalent bonding between functionalised SWNTs and polyamide chains.

4.3 Uniformity and Repeatability

Confidence in the results being obtained was verified by measuring the uniformity and repeatability. Uniformity can be described as the ability to obtain a uniform layer across the membrane sheet, while repeatability refers to the variation in measurements made on the subject under the same conditions [59, 60]. The relative standard deviation (RSD) is used to quantify both the uniformity and repeatability [61, 62].

Three polyamide membrane sheets (a, b and c), with a size of 10 cm x 20 cm were made with 1 wt% of SWNTs concentration in the organic phase following the same method of polyamide membrane synthesis as described in experimental (Section 4.8). From each membrane sheet, three small circular membranes with a 5 cm diameter were cut out and placed in the stirring cell for testing, as explained in Chapter II.

The ability to obtain a uniform layer across the membrane sheet was evaluated by measuring the relative standard deviations in flux and salt rejection from three random sites in the membrane sheet. As seen in Table 4-7, the relative standard deviations (RSD) were 1.85, 0.92 and 1.86, while salt rejection was 2.14, 6.15 and 3.95 for sheets a, b and c respectively. These values show reasonable values of uniformity for polyamide membrane synthesis.

Table 4-7. Flux, salt rejection values and relative standard deviations (RSD) of polyamide/SWNTs membrane. SWNTs concentration in the organic phase was 1 wt% (feed water is 2000ppm of NaCl).

Membranes	Flux (L m ⁻² h ⁻¹)			Salt rejection %		
	a	b	c	a	b	c
1	17.75	25	20.87	72.76	62.61	62
2	16.44	23.4	20.68	68.93	74.9	68.85
3	20.1	25	24	72.5	69	62
Average	18.10	24.47	21.85	71.40	68.84	64.28
RSD	1.85	0.92	1.86	2.14	6.15	3.95
Total average	21.47			68.17		
Total RSD	0.54			3.60		

The average value of flux and salt rejection for each sheet (a, b and c) was used to quantify the repeatability. The RSD was 0.54 and 3.6 for flux and salt rejection respectively. Reasonable values demonstrated confidence in the results being obtained.

4.4 Surface and performance membranes characterisation

The surface morphology of the polyamide layer in the TFC membrane influences the membrane performance for water flux and salt rejection [63]. Thus, the two polyamide layers modified with SWNTs (SWNTs-2-BTA and SWNTs-6-BTA) were characterised by SEM, AFM and contact angle to investigate the surface properties, whereas the water flux and salt rejection of 2000 ppm of NaCl solution were used to determine the performance of the membranes.

4.4.1 Modified membrane with SWNTs-2-BTA

The first type of modified membrane, obtained by embedding a different mass of SWNTs-2-BTA, has been described in the experimental (section 4.8).

4.4.1.1 SEM

The SEM images of the top surface of membranes with different mass fractions of SWNTs-2-BTA (0, 0.5, 1, 2.5, 5, 10, and 50 wt%) in the organic phase are presented in Figure 4- 13. Image (a) shows the surface of the polysulfone supporting layer before coating with the polyamide layer. This image shows a smooth surface with some holes, which is consistent with the reported polysulfone membrane surface images [63]. The conventional polyamide layer was synthesised on the top surface of the polysulfone via interfacial polymerisation. The classical surface morphology of polyamide with nodules (ridges and valleys) is shown in image (b) [64, 65]. However, the addition of SWNTs-2-BTA to the organic phase caused an alteration in nodule shape, in which some nodules were connected to each other, forming larger nodule sizes, as seen in images (c, d and e). Further loading of SWNTs-2-BTA, especially when the concentration was over 2.5 wt%, caused significant disappearance of the nodular surface structure, as seen in images (f, g and h). It is thought that the connection between the nodules increased because of loading the polyamide membrane with SWNTs-2-BTA. It has been reported that nanoparticles can embed in the valleys (deeper area) of the surface which caused a disappearance of the classic surface (ridges and valleys) of the polyamide layer and the nanotubes may be playing a similar role here [4].

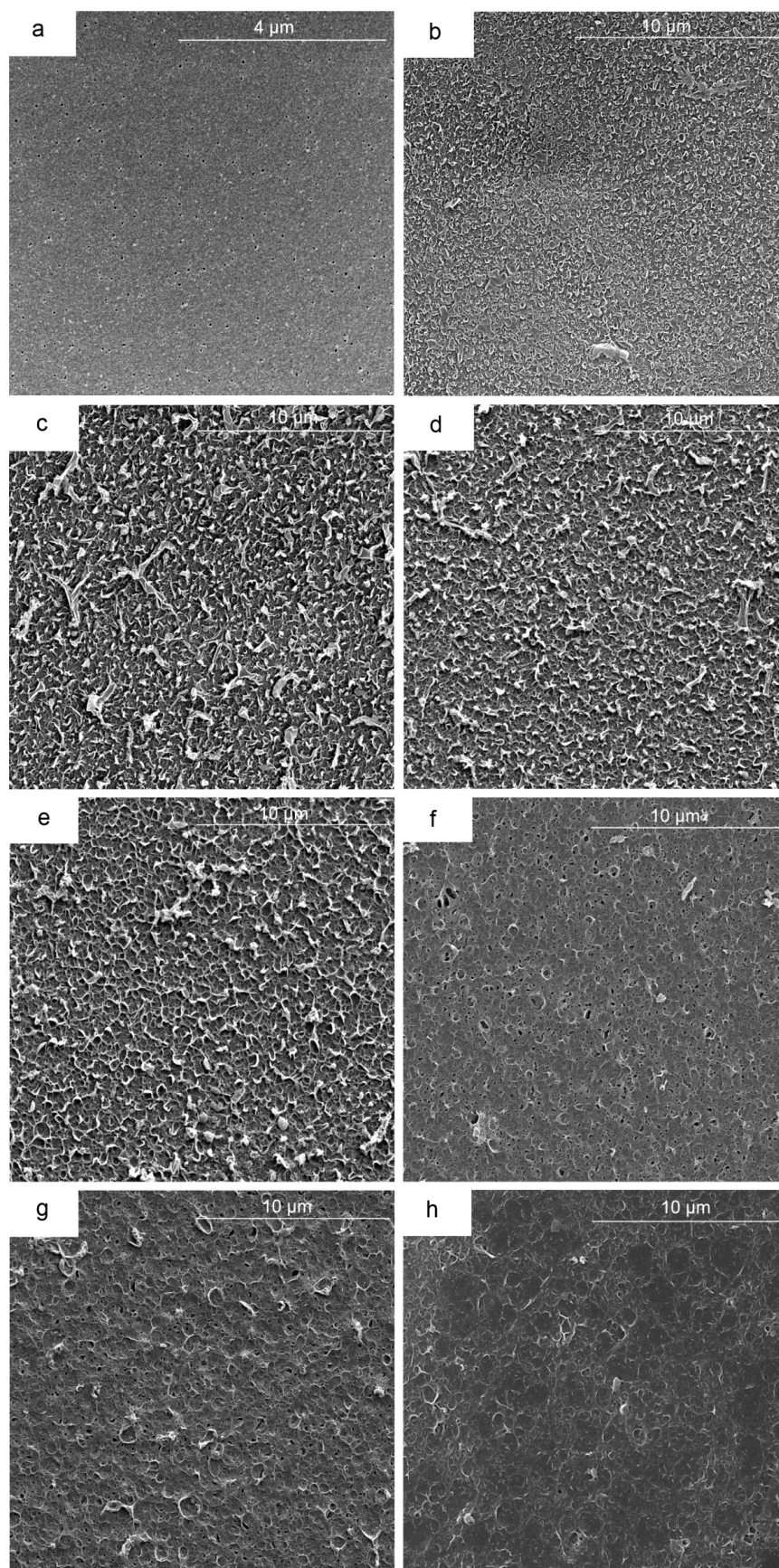


Figure 4- 13. Top surface SEM images for (a) polysulfone, (b) polyamide, (c) PA-2-0.5, (d) PA-2-1, (e) PA-2-2.5, (f) PA-2-5, (g) PA-2-10 and (h) PA-2-50.

4.4.1.2 AFM

Due to the changes that have been seen in surface morphology by SEM, attention was turned to AFM to quantify surface roughness. Figure 4- 14 presents the AFM images of membranes with various mass fractions of SWNT-2-BTA (0, 0.5, 2.5 and 50 wt%) in the organic phase. Roughness parameters are presented in Table 4-8 and are obtained from the images in Figure 4- 15. The parameter that is abbreviated as (SAD) represents surface area difference between the three-dimensional (3D) surface area (a, b, c and d) and two-dimensional (2D) surface area (a',b',c' and d') while (Rq) represents the root mean square roughness. The roughness of the surface increased as a function of SWNT concentration in the organic phase. However, when the concentration of SWNTs in the organic phase reached 50 wt%, a decrease in membrane roughness was observed. Such a change in the surface was also seen in SEM images. It was attributed to the connection between the nodules as a result of exposure of the interfacial polymerisation to a high concentration of SWNTs in the organic phase. In addition, Safarpour et al. reported that this roughness decrease could be attributed to embedding the dispersed nanoparticles in the deeper parts (valleys) of the surface, which smooths the surface [4].

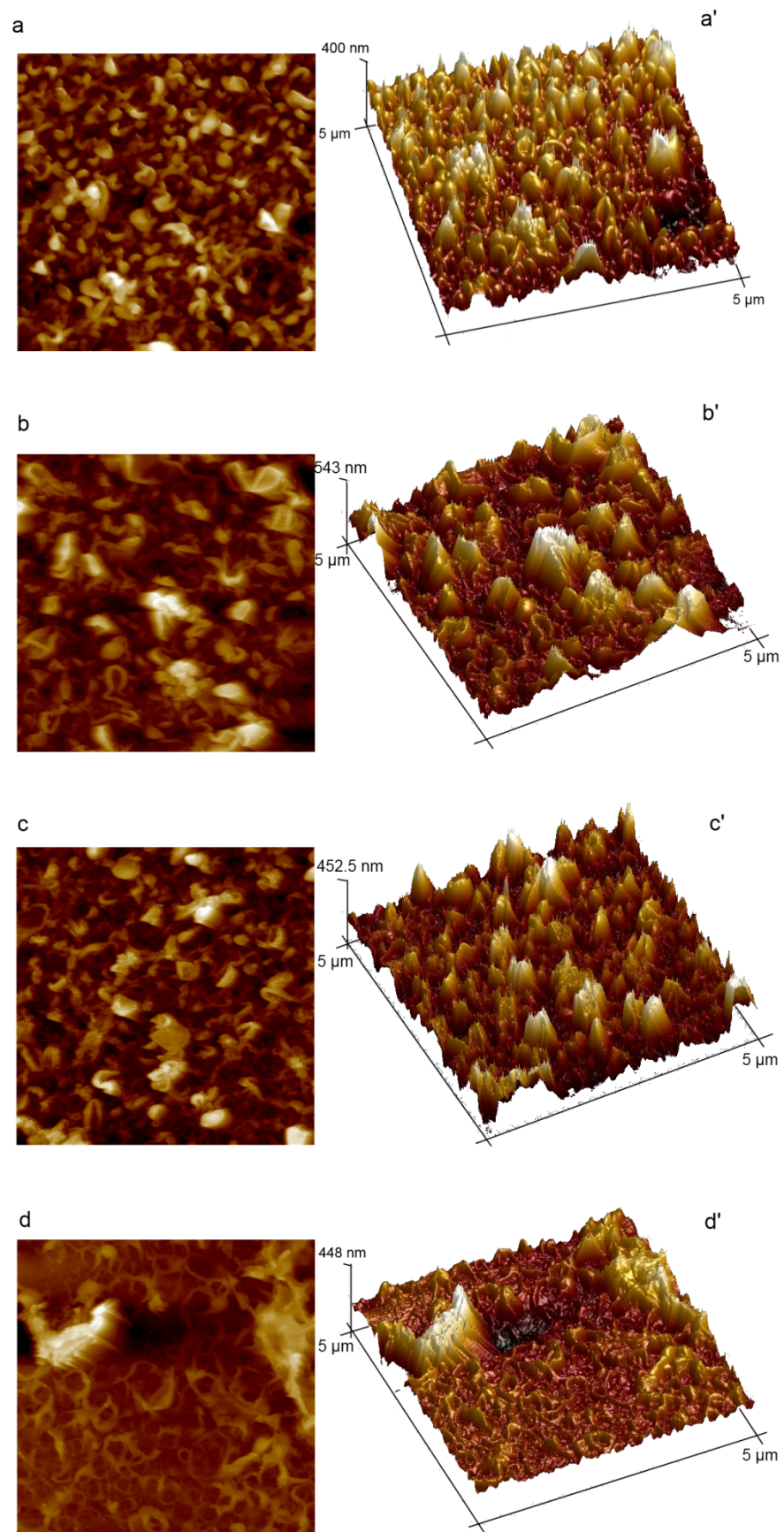


Figure 4- 14. (2D, 3D) AFM surface images of (a ,a') polyamide layer, (b,b') PA-2-0.5, (c,c'), (d,d') PA-2-2.5 and (e,e') PA-2-50.

Table 4-8. Roughness parameters of polyamide membranes. Rq represents the root mean square roughness and SAD represents the percentage of difference between the image's three-dimensional surface area and two-dimensional surface area.

Membranes	SWNTs %	Rq (nm)	SAD
PA	0.00	86.4 ± 8.2	107.4 ± 7.9
PA-2-0.5	0.5	113.4 ± 19.6	159.3 ± 18
PA-2-2.5	2.5	131 ± 32	153.7 ± 21.4
PA-2-50	50	84.8 ± 10.4	49.6 ± 9.9

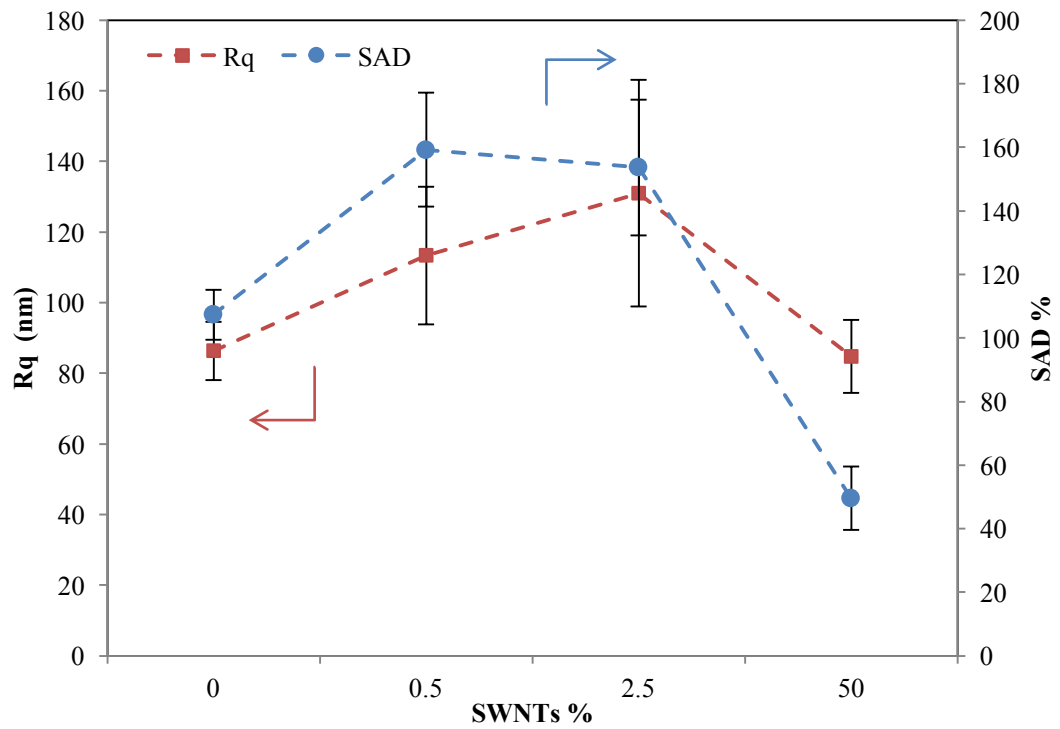


Figure 4- 15. Roughness parameters of polyamide membranes, Rq (red line) and SAD (blue line). (Lines added to guide the eye).

4.4.1.3 Contact angle

The contact angle of the polyamide layer surface influences the water flux and salt rejection of the polyamide layer. Observation of changes in the surface morphology of the polyamide layer led to an examination of the contact angle to evaluate the hydrophilicity. The contact angle values are presented in Figure 4- 16, as a function of SWNTs concentration in the organic phase.

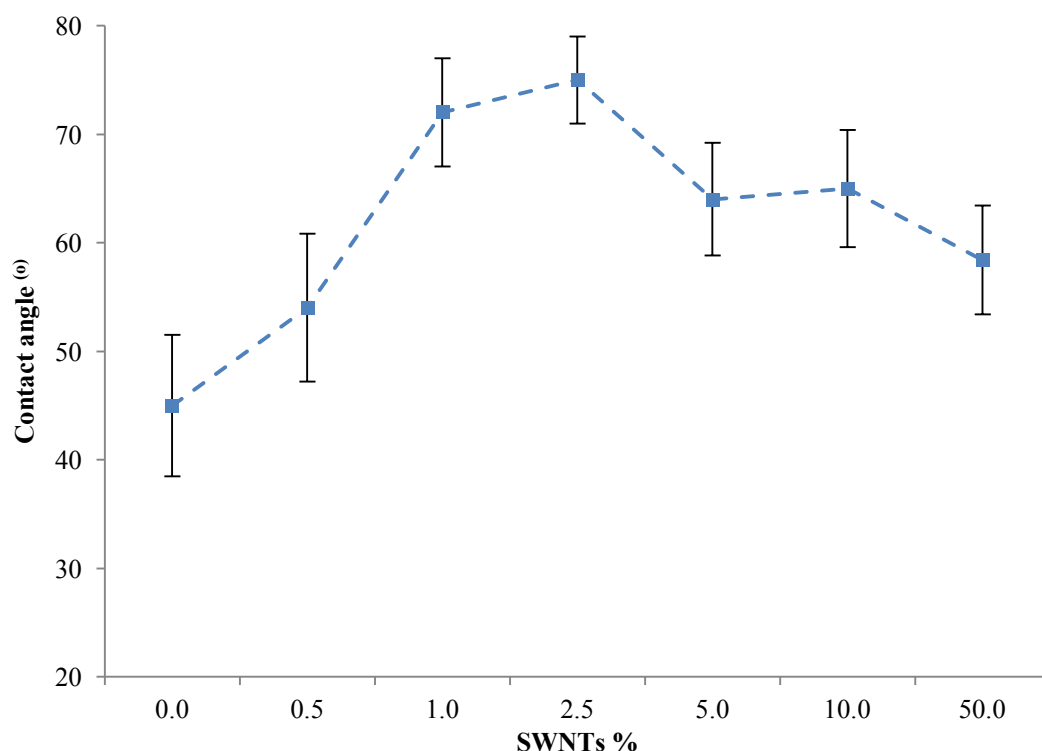


Figure 4- 16. Contact angle of polyamide (PA), PA-2-0.5, PA-2-1, PA-2-2.5, PA-2-5, PA-2-10 and PA-2-50 with SWNTs concentration 0, 0.5, 1, 2.5, 5, 10 and 50 wt% respectively. (Lines added to guide the eye).

The plain polyamide membrane contact angle was around 45° , which is consistent with a previous study [5]. The dispersion of SWNTs in the organic phase in interfacial polymerisation increased the contact angle of the produced polyamide up to around 75° at 2.5 wt% concentration. This result was consistent with the hydrophobic nature of SWNTs [5, 66]. However, at SWNTs concentrations higher than 2.5 wt%, the

contact angle decreased. This may be rationalised by the conversion of unreacted acid chloride groups on the SWNTs to carboxylic groups which increase the hydrophilicity and decrease the contact angle, as reported in the literature [64, 67].

4.4.1.4 Flux and salt rejection

The ability of the polyamide layer to reject salt molecules and permit water molecules to flow through the membrane was measured using a stirring cell as described in Chapter II. A 2000 ppm of solution NaCl was used to measure the flux and the salt rejection as a function of SWNTs concentration in the organic phase.

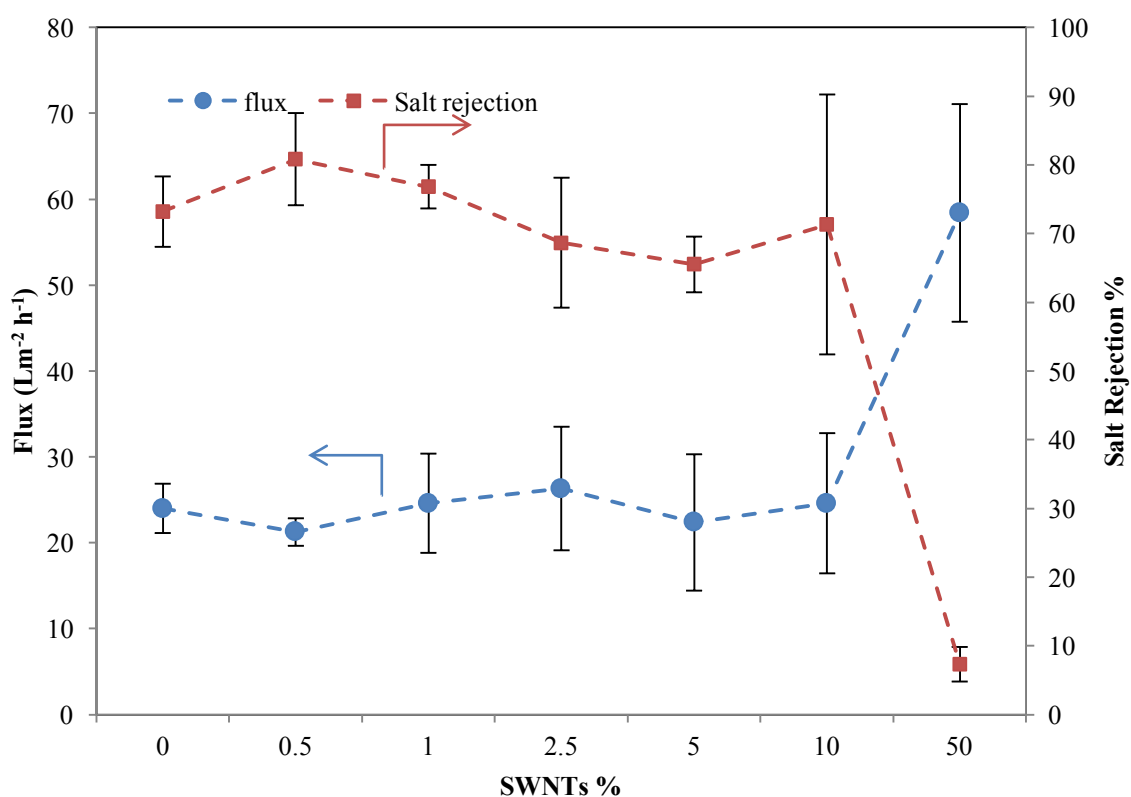


Figure 4- 17. Effect of loading of SWNTs-2-BTA in the polyamide membrane on flux and salt rejection performance. Feed solution was 2000 ppm and N_2 pressure was 16 bar. (Lines added to guide the eye).

Figure 4- 17 shows that no significant change in membrane flux was observed in SWNTs concentrations lower than 10 wt% with a value $21 \text{ Lm}^{-2} \text{h}^{-1}$ measured. Salt rejection showed a slight increase from 73% to 80% for SWNTs-free polyamide and membrane with 0.5wt% of SWNTs. At higher concentrations of SWNTs the salt

rejection presented a slight decrease. The addition of low concentrations of functionalised SWNTs with acid chloride groups increased the polymer cross-linking, but higher concentrations of SWNTs may cause defects for polymer cross-linking. At 50 wt% concentration, a significant negative change for flux and salt rejection was observed. It is thought that the high concentration of SWNTs in the organic phase disrupts the polyamide layer growth in the interfacial polymerisation. Therefore, defects in the cross-linking of the polymer were significant, causing low performance.

4.4.2 Grafting with SWNTs-6-BTA

Having examined the effect of grafting SWNTs-2-BTA onto the polyamide layer, attention was turned to the longer carbon chain analogue SWNTs-6-BTA to see whether any effect from increasing the carbon chain would be observed. The SWNTs-6-BTA was incorporated at various concentrations in a similar manner to SWNTs-2-BTA and the resulting membranes were examined using a range of techniques.

4.4.2.1 SEM

The surfaces of the polyamide membranes were investigated using SEM, as seen in Figure 4- 18. Images (a) and (b) represent the surfaces of polysulfone (PSf) and polyamide (PA) respectively, as seen before. Similar to the grafted membrane with SWNTs-2-BTA, dispersed SWNTs-6-BTA in the organic phase with concentration 0.5, 1, 2.5, 5, 10, 50 wt% changed the membrane surface. An alteration in nodule shape was observed, as some nodules connected to each other forming larger nodule sizes, as seen in images (c, d, e, f, g and h). Unlike the polyamide/SWNTs-2-BTA membrane, no significant change was observed in concentrations higher than 2.5 wt%.

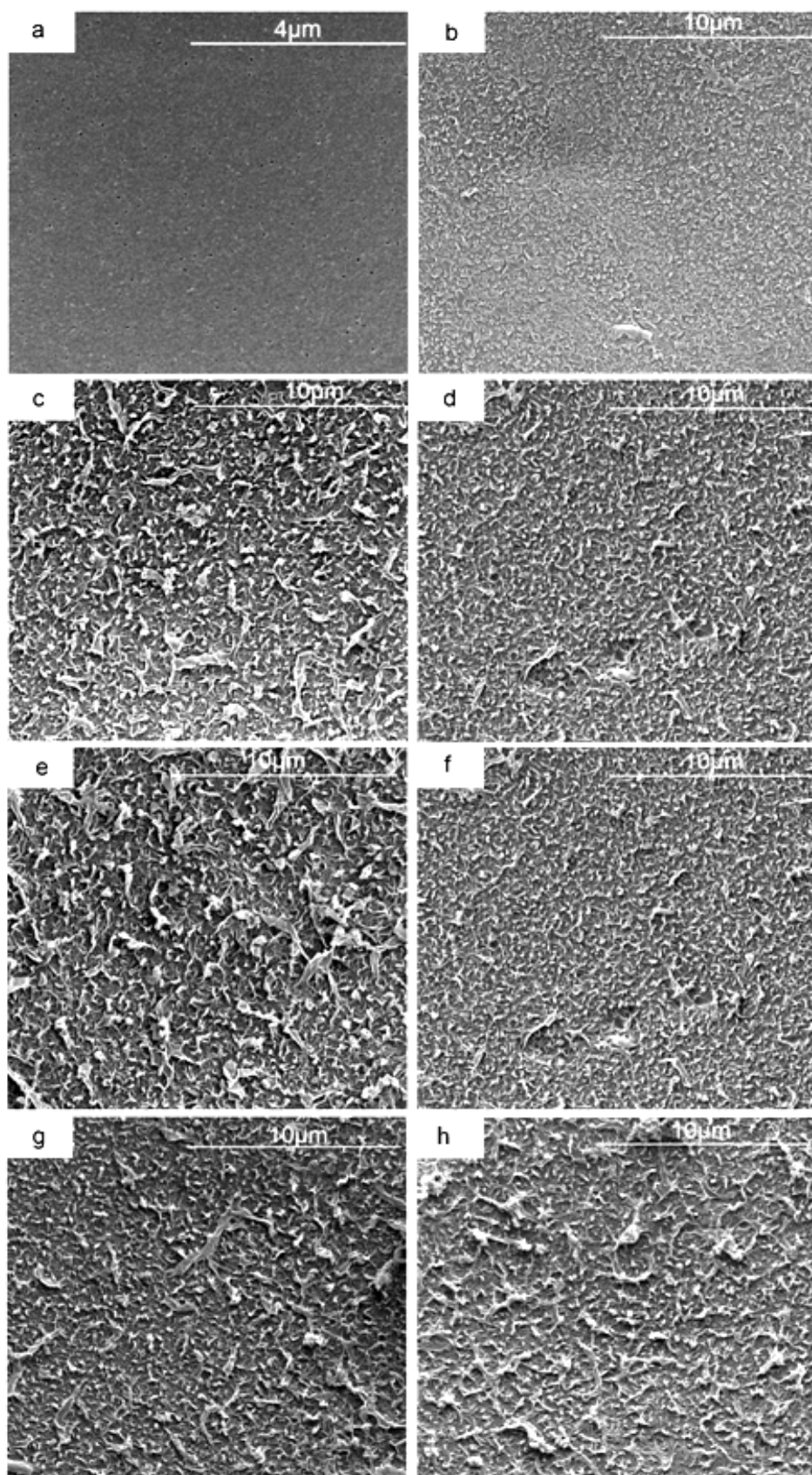


Figure 4- 18. Top surface SEM images for (a) polysulfone (PSf), (b) plain polyamide (PA), (c) PA-6-0.5, (d)PA-6-1, (e) PA-6-2.5, (f) PA-6-5, (g) PA-6-10 and (h) PA-6-50.

4.4.2.2 AFM

The membrane surface was also investigated by AFM. As seen in Figure 4- 19, AFM images were collected for polyamide layers with SWNTs concentrations 0, 0.5, 2.5 and 50 wt%. The roughness of the surface was quantified by measuring the difference between the image's three-dimensional surface area and two-dimensional surface area (SAD). In addition, the root mean square roughness (Rq) was determined, and the values are presented in Table 4-9 obtained from the images in Figure 4- 20. An increase in roughness was observed when SWNTs were added to the organic phase during interfacial polymerisation. This was consistent with SEM images showing a change in the membrane surface. This change was attributed to connections between some nodules. During the interfacial polymerisation, the tubes of the SWNTs connected some nodules of the polyamide to each other through the reaction of acid chloride groups on the SWNTs with the amine monomers. The membrane roughness generally increased as SWNTs concentration increased in the organic phase. This is attributed to the SWNTs not dispersing well in the organic phase. Therefore, bundles of aggregated SWNTs were formed, causing a rougher surface.

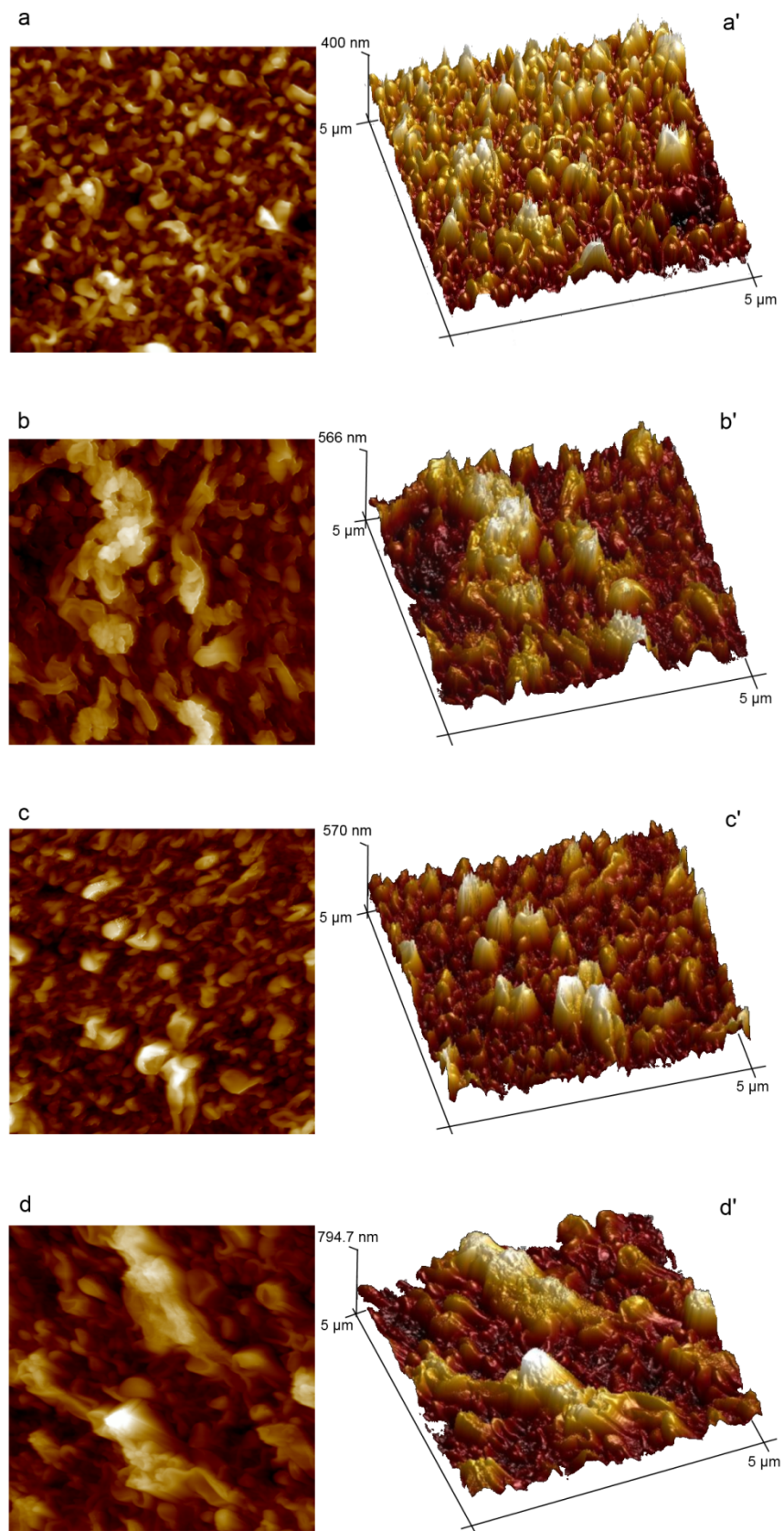


Figure 4- 19. (2D, 3D)AFM surface images for (a, a') polyamide layer (PA), (b, b') PA-6-0.5, (c, c') PA-6-2.5, (d, d') PA-6-50.

Table 4-9. Roughness parameters of polyamide/SWNTs-6-BTA membranes. Rq represents the root mean square roughness and SAD represents the percentage of difference between the image's three-dimensional surface area and two-dimensional surface area.

Membrane	SWNTs %	Rq (nm)	SAD
PA	0	86.5 ± 8.2	107.4 ± 7.9
PA-6-0.5	0.5	137.7 ± 6.8	134.7 ± 25.6
PA-6-2.5	2.5	109 ± 10.2	147.7 ± 14.6
PA-6-50	50	195 ± 24.8	152.3 ± 6

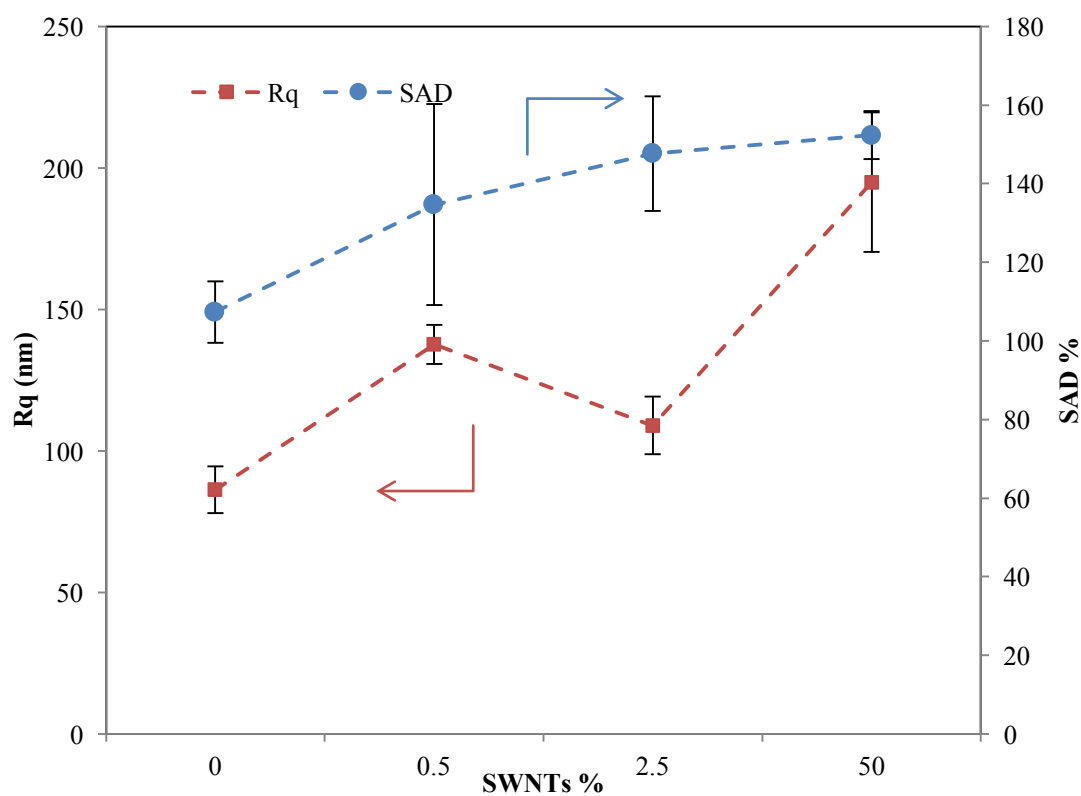


Figure 4- 20. Roughness parameters of polyamide membranes, Rq (red line) and SAD (blue line). (Lines added to guide the eye).

4.4.2.3 Contact angle

Contact angle was used to determine the hydrophilicity of the membrane surface. As seen in Figure 4- 21, loading the polyamide membranes with SWNTs changed the contact angle of the membranes.

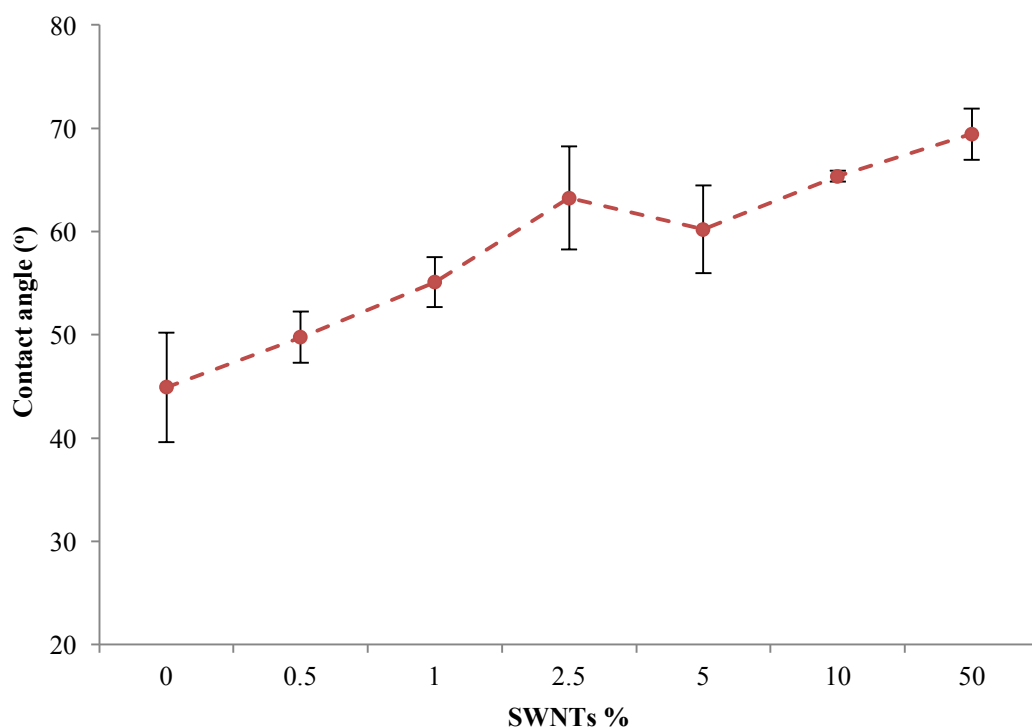


Figure 4- 21. Contact angle for polyamide/SWNT membranes with SWNT-6-BTA concentration 0, 0.5, 1, 2.5, 5, 10 and 50 wt% in the organic phase. (Line added to guide the eye).

The dispersion of SWNTs in the organic phase in the interfacial polymerisation increased the contact angle of the produced polyamide membranes from around 45° for SWNTs-free polyamide to around 63° for polyamide/SWNTs with 2.5 wt% concentration in the organic phase. Due to the hydrophobic nature of SWNTs, the contact angle continued to increase (hydrophobicity increase) as a function of SWNTs concentration in the organic phase [5, 66].

The surface properties of both membranes showed some similarities and differences. in terms of the roughness both membranes showed an increasing up to 2.5% of SWNT. However, at 50% the roughness of membrane that embedded with SWNT-2-BTA decreased while embedded membrane with SWNT-6-BTA showed slight increase.

The contact angle also showed similar behaviour. While the embedded membrane with SWNT-6-BTA showed an increasing in the contact angle in general, the membrane that embedded with SWNT-2-BTA showed a decreasing in the contact angle at SWNT concentration higher than 2.5%.

4.4.2.4 Flux and salt rejection

Membrane performance was determined by measuring the flux of 2000 ppm of NaCl solution through the membrane at room temperature and 16 bar pressure. Rejection of salt also was determined to measure the ability of membranes to produce fresh water from salty water. These membrane properties are presented in Figure 4- 22.

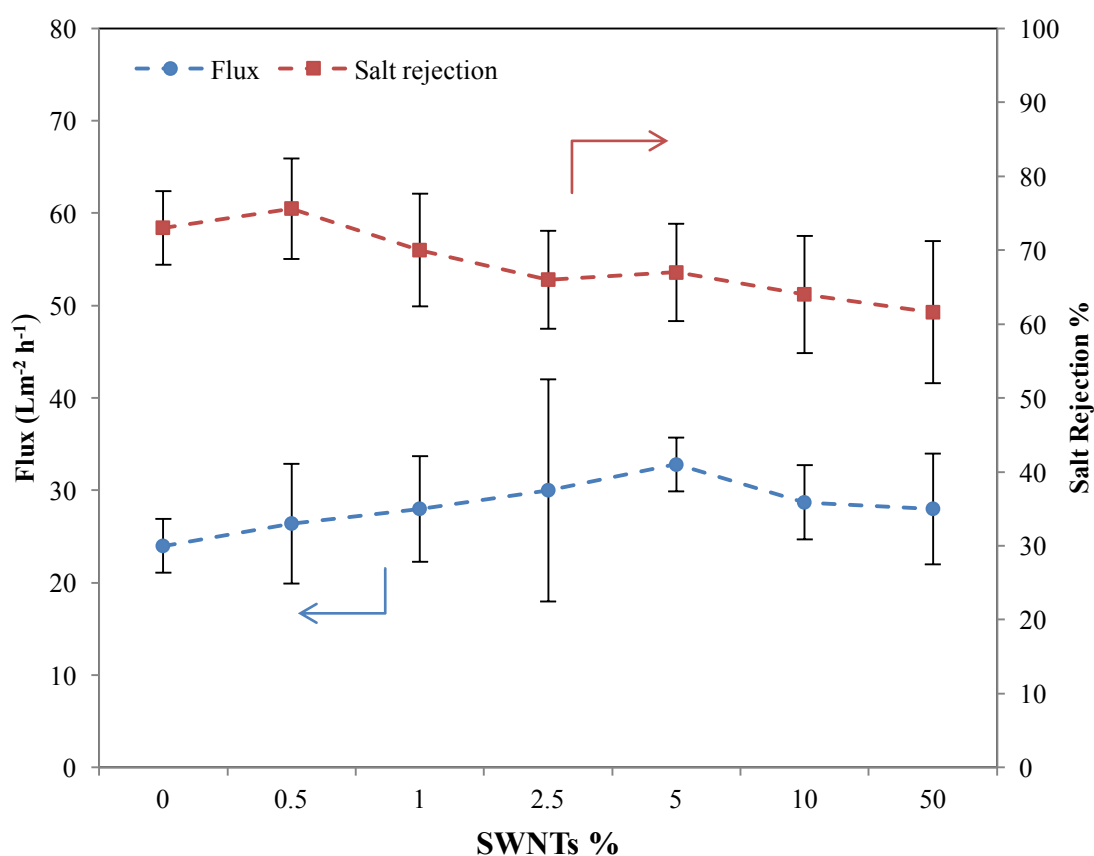


Figure 4- 22. Effect of loading of SWNT-6-BTA in the polyamide membranes on flux and salt rejection performance. Feed solution was 2000 ppm and N_2 pressure was 16 bar. (Lines added to guide the eye).

The SWNTs-free polyamide showed a flux of around $24 \text{ Lm}^{-2}\text{h}^{-1}$, while the salt rejection was around 73%. The flux increased as SWNTs concentration in the organic

phase increased from 0.5 wt% up to 5 wt%. Salt rejection slightly decreased to around 67% at 5 wt% SWNTs concentration. No significant change to performance was observed at higher concentrations.

4.5 Control membranes

Further investigation of the influence of carbon chain length was performed by synthesis of model compounds for SWNTs. As described in Chapter I, anthracene was used as a mimic compound for SWNTs. Given this, Figure 4- 23 illustrates the synthetic route for utilising anthracene mono amine compounds (3a) and (3c), which were synthesised as described in Chapter 3, and reacted with the mono acid chloride compound (8) to produce the model compounds (11a,b).

Having linked anthracene mono amines (3a and 3c) and mono acid chloride compounds (8) using amide bonds, the esters were hydrolysed to yield carboxylic acids (12a,b). Heating with thionyl chloride under reflux was performed to convert the acid groups into acid chlorides (13a,b). All compounds were characterised with ^1H and ^{13}C NMR, FT-IR and mass spectroscopy (HRMS) except the acid chloride compounds, which were only characterised with ^1H NMR and FT-IR due to the potential reactivity of these compounds. Control membranes were prepared following the same procedure and conditions as the modified membrane, and adding the model compounds instead of the SWNTs.

However, issues were encountered with the lower solubility of these model compounds in the organic phase solvent system used for interfacial polymerisation. It was decided to keep solvents the same for consistency.

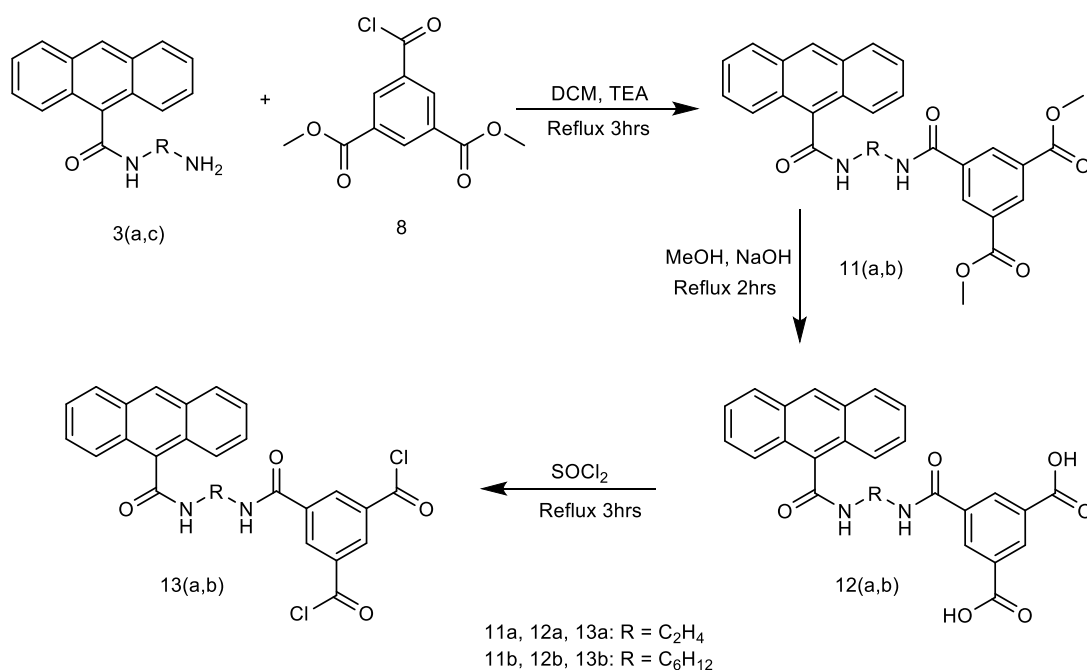


Figure 4- 23. Synthetic route of model compounds containing anthracene in place of SWNTs.

Control membrane performance was examined under the same conditions as the polyamide/SWNTs membrane tests. Flux and salt rejection for long- and short-chain compound results are presented in Table 4-10. Generally, the addition of the model compounds decreased the salt rejection, while the flux increased dramatically as seen in Figure 4- 24 and Figure 4- 25. For instance, adding the 9AC-2-BTA compound with 0.5 wt% in the organic phase increased the flux from 24.7 to 88.6 Lm⁻² h⁻¹, while the salt rejection decreased from 71.6% to zero. The same concentration of 9AC-6-BTA increased the flux to 29.4 Lm⁻² h⁻¹ and the salt rejection decreased to 49%. At high concentrations of model compounds, the salt was not rejected at all. This is attributed to the lack of solubility of the model compound in the organic phase, which caused a disruption of the polymerisation in the interface area between the organic and aqueous phases.

Table 4-10. Control membranes performance results.

Model compound %	Polyamide/9AC-2-BTA		Polyamide/9AC-6-BTA	
	Flux ($\text{Lm}^{-2} \text{h}^{-1}$)	Salt rejection%	Flux($\text{Lm}^{-2} \text{h}^{-1}$)	Salt rejection%
0	24.7 ± 0.5	71.67 ± 3	24.7 ± 0.5	71.67 ± 3
0.5	88.6 ± 24.6	-	29.4 ± 4.7	49 ± 3.7
1	85 ± 41	-	46 ± 8.4	14 ± 11
2.5	> 100	-	120 ± 2	-
5	> 100	-	73 ± 35	-
10	> 100	-	> 100	-
50	> 100	-	> 100	-

The short-chain compound (13a) had very low solubility in organic solutions that were used for polymerisation, which negatively influenced the membrane performance even at low concentrations.

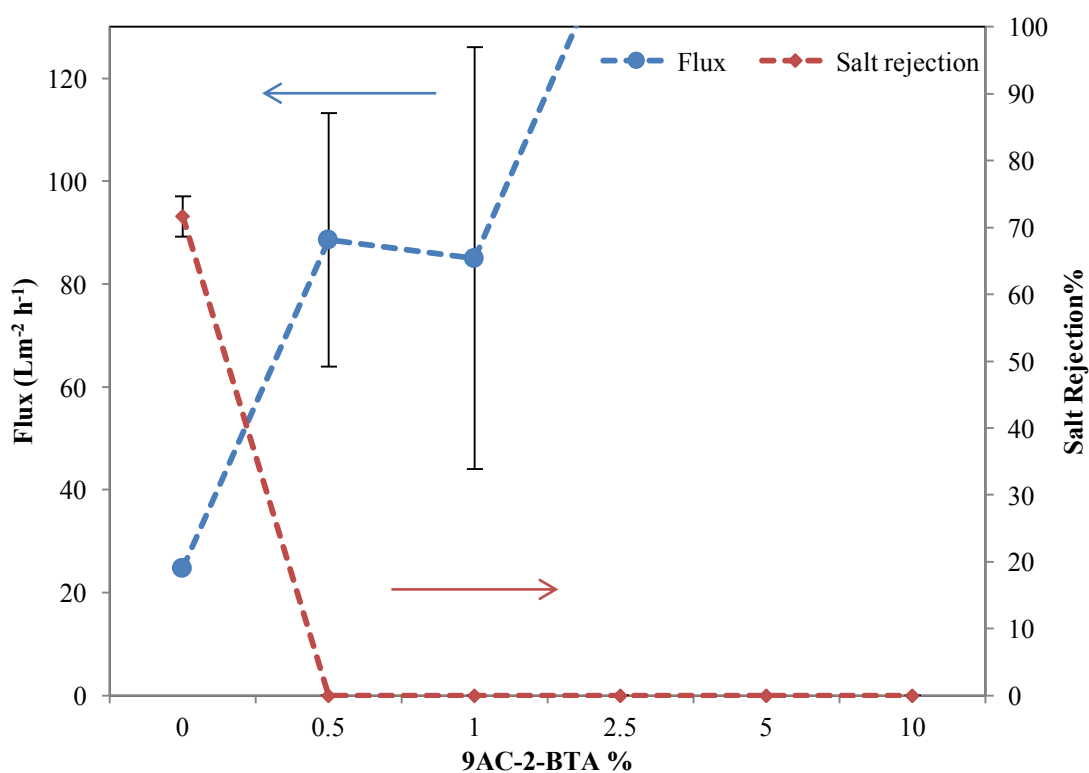


Figure 4- 24. Effect of loading 9AC-2-BTA in the polyamide membranes on flux and salt rejection performance. Feed solution was 2000 ppm NaCl and N_2 pressure was 16 bar. (Lines added to guide the eye).

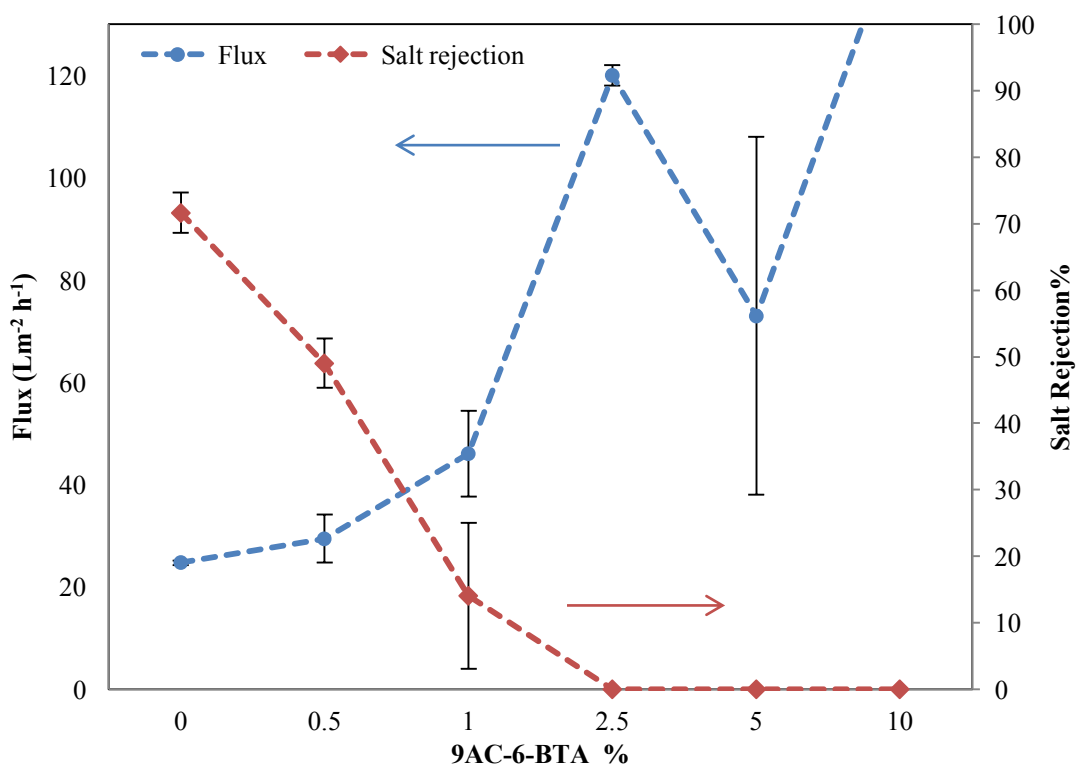


Figure 4- 25. Effect of loading 9AC-6-BTA in the polyamide membranes on flux and salt rejection performance. Feed solution was 2000 ppm NaCl and N₂ pressure was 16 bar. (Lines added to guide the eye).

4.6 Chain length influence on SWNT distribution in the membrane

The difference in the distribution of SWNTs in the polyamide membrane at concentrations higher than 2.5wt% in the organic phase may be attributed to two factors. Firstly, the quantity of the short-chain amine grafted to SWNTs was greater than of the long one, resulting in increased distribution in the polymer. According to the reaction between Mono-Boc-diamine and 9-anthracene carboxylic acid using HATU as the coupling reagent, in the resulting amide, the short-chain diamine showed a higher yield than the long-chain diamine as seen in Chapter III. The yields were 98.4% and 75% for the short-chain and long-chain respectively. The higher yield was attributed to the greater reactivity of the short-chain diamine. The short-chain amine was grafted to SWNTs in greater quantity than the long one, which increased the possible reaction sites of functionalised SWNTs and distributed them in the polymer more efficiently.

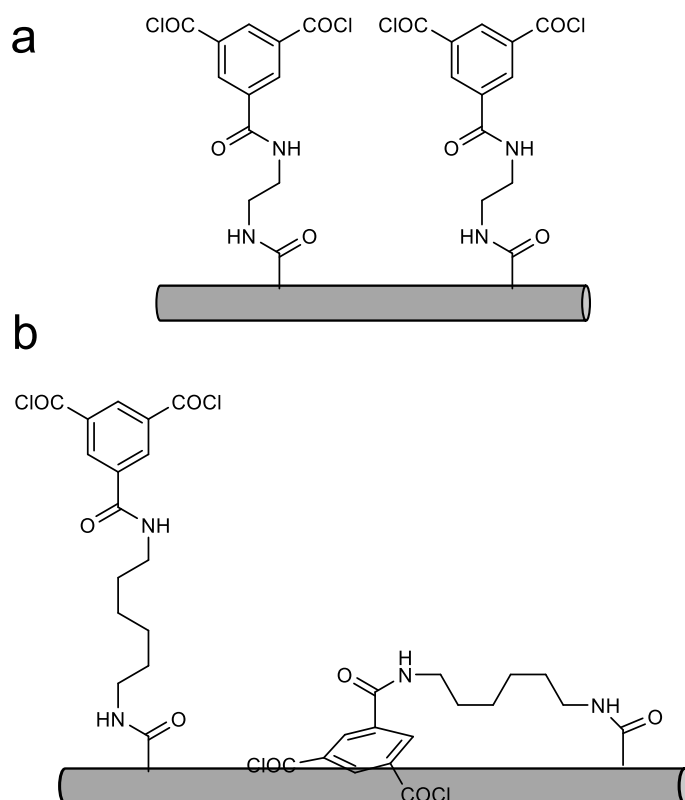


Figure 4- 26. Illustration of molecules grafted to SWNTs (a) short chain (b) long chain, showing the molecules folding over SWNTs as result of the higher flexibility of the long chain.

Secondly, the chain length of the grafted molecules affected the distribution of the SWNTs in the polyamide layer. It has been reported that the flexibility of the aliphatic chain increases with increasing chain length [68-71]. In addition, the aromatic ring molecules can attach non-covalently to the sidewall of CNTs through π - π stacking [72-75]. The short-chain molecule has less flexibility, which prevents the molecule folding over the SWNTs. However, the long-chain molecule could be folded over to interact with the sidewall of the SWNTs due to higher flexibility in the aliphatic chain and π - π stacking, as demonstrated in Figure 4- 26. Therefore, the short-chain molecule was distributed in the polyamide polymer better than the long-chain molecule during the interfacial polymerisation.

4.7 Conclusion

SWNTs were successfully functionalised with two organic amine compounds. The difference between the amine compounds was in the chain length where there were two or six carbon atoms in the aliphatic chain. Unlike other studies, functionalised SWNTs were dispersed in the organic layer and embedded in the polyamide membrane through the interfacial polymerisation technique. Characterisation with FT-IR, Raman and TGA were obtained for functionalised SWNTs and the polyamide membrane. In Raman, the G band peak was observed for SWNTs even after embedding in the membrane. The improvement in thermal stability of the polyamide membrane was confirmed by the TGA curve after embedding SWNTs into the polyamide. Moreover, the polyamide membrane surface was investigated by SEM, AFM and contact angle measurements.

Functionalised SWNTs with SWNTs-2-BTA were able to be better distributed into the polyamide layer than the SWNTs-6-BTA. The difference in SWNTs distribution in the polyamide layer was attributed to the SWNTs functionalisation with the different chain-length molecules. It was thought that due to the differences in reactivity molecules with the short chain grafted to the SWNTs in greater quantities than those with the long chain. In addition, a lack of flexibility of the short-chain molecule enhanced the distribution of SWNTs into the polyamide layer.

Performance of the membranes was investigated by measuring the water flux and salt rejection of a feed solution with 2000 ppm of NaCl. Generally, the modified membranes showed a slight improvement in water flux, but there was a decrease in salt rejection. For example, the modified membrane with SWNTs-6-BTA showed an improvement in flux from $24 \text{ Lm}^{-2} \text{ h}^{-1}$ for the SWNTs-free membrane to $32 \text{ Lm}^{-2} \text{ h}^{-1}$ for the membrane with 5 wt% SWNTs. The salt rejection decreased from 73% for the SWNTs-free membrane to 67% for the membrane with 5 wt% SWNTs.

The performance of the membrane has not showed big improvement which could be attributed to that CNTs dispersion was in the organic layer (top layer) during the interfacial polymerisation. Therefore, the embedding of CNTs in the polyamide at low loading has limited effect on the membrane performance.

Distribution of SWNTs into the polyamide layer was improved by grafting SWNTs with the short-chain mono amine molecule (10a).

The addition of BTA compounds showed negative effect on the membrane performance which could be attributed to the disruption of polymer packing chains.

4.8 Experimental

Synthesis of Polyamide Membranes

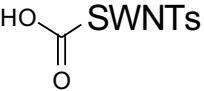
Polyamide membranes were synthesised by an interfacial polymerisation process. Polysulfone (PSf) support membranes with a size of 40 cm x 20 cm were immersed in deionised (DI) water overnight then isopropanol (IPA) for 10 min. The membrane was washed with DI water before being positioned on a PMMA (polymethylmethacrylate) plate. A silicon rubber gasket and a PMMA frame were placed on top of the PSf membrane and binder clips were used to hold the plate-membrane-gasket-frame stack together. 100 mL of 2 wt % *m*-phenylenediamine (MPD) solution (i.e., 2 g of MPD in 100 mL DI water, along with 2 wt % of camphor-10-sulfonic acid (CSA), 0.15 wt% of sodium dodecyl sulphate (SDS) and 1 wt % of isopropanol (IPA)) were poured into the frame and allowed to contact the PSf membrane for 5 min before draining the excess MPD solution. The frame and gasket were disassembled, and residual solution between the plate and the PSf membrane was removed using paper towel. Residual droplets of solution on the top surface of the PSf membrane were removed by rolling a rubber roller followed by purging with nitrogen gas flow across the membrane surface. Afterwards, the frame and gasket were reassembled on top of the PSf membrane, and 100 mL of 0.1% (w/v) trimesic acid chloride (TMC) in *n*-hexane/toluene (4:1) were poured onto the frame. After 1 min, the TMC/*n*-hexane solution was drained from the frame, and the frame and gasket were disassembled. The membrane surface was rinsed using *n*-hexane (10 mL) and DI water to wash away residual reagents, and the membrane was dried in air at ambient conditions for 1 min. Finally, the entire membrane was stored in DI water until required for further experiments.

Addition of SWNTs to the membrane was performed by sonicating the desired amount of the modified nanotubes into the organic phase just before the polymerisation reaction. Six different concentrations of functionalised nanotubes were varied between

0, 0.5, 1, 2.5, 5, 10 and 50 wt% based on the weight of the TMC (0.1 g in 100 mL) dispersed in organic solution.

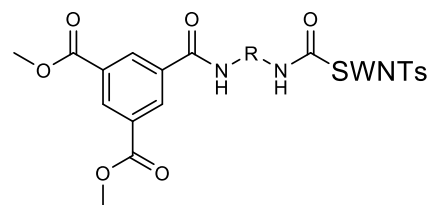
SWNTs Functionalisation

Oxidation reaction (SWNTs-COOH)

The SWNTs were functionalised with carboxyl groups by  ultrasonication in a 3:1 v/v solution of H₂SO₄ (98%) and HNO₃ (70%) at a nanotube concentration of 1 mg mL⁻¹ for 6 hrs for SWNTs at 0 °C. Quenching acid oxidation was achieved by adding of 1 L of Milli-Q water. Filtration through a 0.4 µm HTPP polycarbonate filter and further washing with Milli-Q water until filtrate naturalisation was used to recover the CNTs. An oven at 80 °C was used to dry the SWNTs for 24 hours.

Amidation reaction (SWNTs-R-BTA ester)

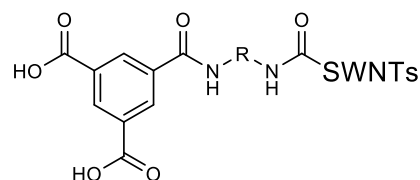
SWNTs were suspended in a solution of DMF containing 0.2 mgmL⁻¹ carbon nanotubes, 0.25 mgmL⁻¹ HATU as coupling reagent and 0.14 mgmL⁻¹ DIEA. A complete suspension was



obtained by sonicating the solution for 30 min. The desired amine compound was then added and the sonication continued for another 30 min. The solution was placed in a heated oil bath at 80 °C with stirring for overnight to complete the reaction. Reaction termination was obtained by adding 200 mL of methanol and then the solution was filtered through polycarbonate filter (HTTP) and washed with methanol extensively. The filtrate was placed in an 80 °C oven to dry the nanotubes.

Hydrolysis reaction (SWNTs-R-BTA acid)

Hydrolysing the ester groups which were attached to SWNTs by sodium hydroxide was performed by suspending the modified SWNTs with ultrasonication in a 3:1 v/v solution of DMF and 1M

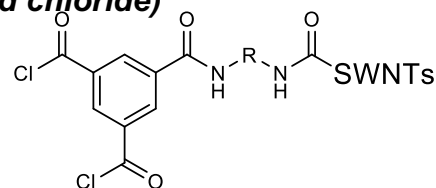


of NaOH at a nanotubes concentration of 1 mg mL⁻¹ for 1 hr. The hydrolysis reaction was completed overnight with stirring at 80 °C in an oil bath. The solution was then poured in 200 mL of methanol and was filtered through a polycarbonate filter (HTTP) and washed extensively with methanol. Nanotubes were placed in an oven at 80 °C

overnight to evaporate any solution residue.

Formation of acid chloride (SWNTs-R-BTA acid chloride)

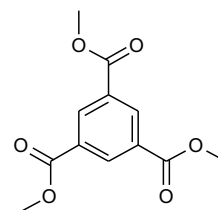
Acid groups of the either hydrolysed ester groups, or groups on the sidewall of the nanotubes, were converted to acid chloride groups by treatment with



thionyl chloride. SWNTs were suspended by ultrasonication for 1 hr in thionyl chloride solution with a catalytic amount of DMF at a nanotube concentration of 1 mgmL⁻¹. Then the mixture was heated under reflux overnight under nitrogen atmosphere. Once the reaction was completed, thionyl chloride was distilled off twice using 20 mL of dry dichloromethane under nitrogen atmosphere. SWNTs were suspended in organic phase of interfacial polymerisation.

Trimethyl 1,3,5-benzenetricarboxylate (6)

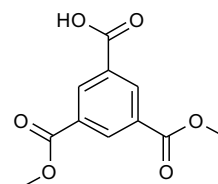
Benzenetricarboxylic acid (8.0 g, 38 mmol) was dissolved in methanol (140 mL) and concentrated sulphuric acid (2 mL) was added. The solution was heated under reflux for 24 hrs. Solvent was removed under reduced pressure. The residue was dissolved in dichloromethane (150 mL) and washed with saturated bicarbonate solution (200 mL) and the solvent was removed under reduced pressure to give the desired product as a white powder (9.15 g, 95%).



mp= 148 °C. ¹H NMR (600 MHz, CDCl₃) 3.97 (s, 9 H), 8.85 (s). ¹³C NMR (150 MHz, CDCl₃) 52.62, 131.21, 134.59, 165.42. IR: ν(cm⁻¹):2957(-CH₃), 1724(C=O), 1612 (C=C), 1237(C-O). HRMS calc. of C₁₂H₁₃O₆Na [M+Na]⁺ 253.0712, found 253.0711.

Dimethyl 1,3,5-benzenetricarboxylate (7)

Trimethyl 1,3,5-benzenetricarboxylate (2.0g, 9.79 mmol) and NaOH (0.39g, 9.79mmol) were dissolved in methanol (70 mL) with heating under reflux for 12 hrs. After that, water (200 mL) was mixed with the reaction mixture and washed with diethyl ether

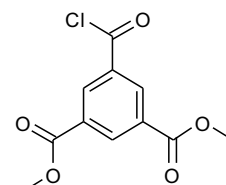


(3x100 mL). The aqueous phase was acidified with HCl (1 M) till pH 1 and extracted with diethyl ether (3x100 mL). The extracted organic phase was dried (MgSO₄), and the solvent was evaporated to give the desired product which was in quantitative yield.

mp= 145 °C. ^1H NMR (400 MHz, d_6 -DMSO) 3.90 (s, 6 H), 8.54 (t, J =1.6 Hz, 1 H), 8.59 (d, J =1.6 Hz, 2 H). ^{13}C NMR (100 MHz, d_6 -DMSO) 53.15, 131.25, 132.54, 132.70, 133.51, 133.77, 134.08, 165.13, 165.99, 166.15. IR: $\nu(\text{cm}^{-1})$: 3400(OH), 1728(C=O ester), 1699(C=O), 1607(C=C). HRMS calc. of $\text{C}_{11}\text{H}_{10}\text{O}_6\text{Na}$ $[\text{M}+\text{Na}]^+$ 261.0375, found 261.0370.

Dimethyl 1,3,5-benzenetricarboxylate acid chloride (8)

Dimethyl 1,3,5-benzenetricarboxylate (2g, 9.7 mmol) was mixed with thionyl chloride (30 mL) to which was added with three drops of DMF as a catalyst. The mixture was heated under reflux for 8 hrs. After refluxing, the excess thionyl chloride was distilled under nitrogen and dry DCM (30 mL) was added twice to ensure the removal of thionyl chloride. The product was obtained in quantitative yield and directly used for further synthesis.



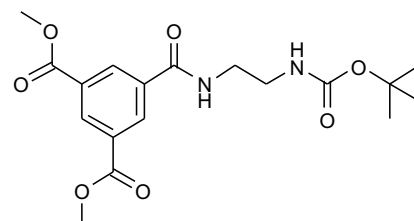
^1H NMR (600 MHz, CDCl_3) 4.01(s, 6H), 8.92 (d, J =1.6, 2H), 8.96(t, J =1.6, 1H). IR: $\nu(\text{cm}^{-1})$: 1762(C=O Cl), 1728(C=O ester), 1601(C=C).

General method of amide coupling

Protected diamine (0.5g) was dissolved in DCM (50 mL) and a catalytic amount of pyridine was poured into the flask. Dimethyl 1,3,5-Benzenetricarboxylate acid chloride was added dropwise and the mixture was heated under reflux for 2 hrs. After that, water (50 mL) was added and the organic phase washed with HCl (0.5M, 2x30 mL), NaOH (0.5M, 2x30 mL) and brine water respectively. Finally, the organic phase dried (MgSO_4) before evaporated the solvent.

N,N'-(dimethyl 1,3,5-benzenetricarboxylate) (tert-butoxycarbonyl)-1,2-ethandiamine (9a)

9a was obtained from dimethyl 1,3,5-benzenetricarboxylate chloride (0.6 g, 2.3 mmol) and *N*-(tert-butoxycarbonyl)-1,2-ethandiamine (0.5 g, 3.3 mmol) as a white solid product (0.75 g, 86%) using general procedure.

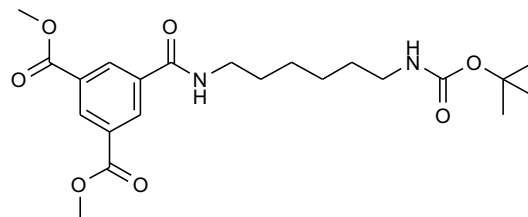


mp = 106 °C. ^1H NMR (400 MHz, d_6 -DMSO) 1.37(s,9H), 3.12(q, J =6.04, 2H), 3.31(q, J =6.2, 2H), 3.92 (s, 6H), 6.89(t, J = 5.6, 1H), 8.56(d, J = 1.4, 1H), 8.65(s, 2H), 8.90 (t,

$J = 5.2$, 1H). ^{13}C NMR (100 MHz, d_6 -DMSO) 28.67, 40.29 (shoulder), 40.50 (shoulder), 53.14, 78.15, 130.94, 132.19, 132.59, 136.22, 156.23, 164.83, 165.48. IR: $\nu(\text{cm}^{-1})$: 3342(NH), 1737(C=O ester), 1678, 1639(C=O amide), 1552, 1516(amide II), 1392, 1367(-C(CH₃)₃). HRMS calc. of C₁₈H₂₄N₂O₇Na [M+Na]⁺ 403.1481, found 403.1485.

***N,N'*-(dimethyl 1,3,5-benzenetricarboxylate) (tert-butoxycarbonyl)-1,6-hexandiamine (9b)**

9b was obtained from dimethyl 1,3,5-benzenetricarboxylate chloride (0.44 g, 1.7 mmol) and *N*-(tert-butoxycarbonyl)-1,6-hexandiamine (0.5 g, 2.3 mmol) as a white solid product (0.54 g, 73%) using general procedure.



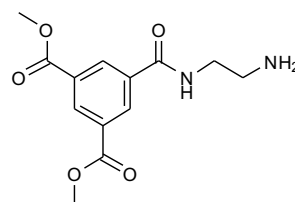
mp = 195 °C. ^1H NMR (600 MHz, d_6 -DMSO) 1.26-1.31(m, 4H), 1.37(s, 9H), 1.53(m, 2H), 2.90(q, $J = 4.3$, 2H), 3.28(m, 2H), 3.94(s, 6H), 6.77(bs, 1H), 8.58(s, 1H), 8.68(s, 1H), 8.91(t, $J = 3.6$, 1H). ^{13}C NMR (150 MHz, d_6 -DMSO) 26.48, 26.68, 28.74, 29.38, 29.9, 34.76, 40.54 (shoulder), 53.14, 77.75, 130.97, 132.14, 132.53, 136.28, 156.05, 164.5, 165.5. IR: $\nu(\text{cm}^{-1})$: 3346(NH), 1725(C=O ester), 1682, 1636(C=O amide), 1525 (amide II), 1389, 1365(-C(CH₃)₃). HRMS calc. of C₂₂H₃₂N₂O₇Na [M+Na]⁺ 459.2107, found 459.2102.

General method of amine de-protection

Trifluoroacetic acid (TFA) was used to liberate the protected amine group. DCM (10 mL) was added to the protected amine and stirred until dissolution occurred. TFA (3 mL) was added slowly to the solution and stirred for 2 hrs. The de-protection completion was traced by ^1H NMR. The solvent was removed to ensure that there was no protected amine left and the product was used without any further purification.

***N*-(dimethyl 1,3,5-benzenetricarboxylate)ethandiamine (10a)**

10a was obtained from *N,N'*-(dimethyl 1,3,5-benzenetricarboxylate) (tert-butoxycarbonyl)-1,2-ethandiamine (0.5 g, 1.9 mmol) and TFA (3 mL) as yellowish liquid product (0.54 g, 100 %) using general procedure.

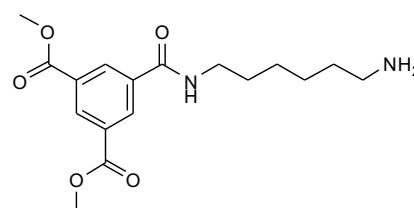


^1H NMR (600 MHz, d_6 -DMSO) 3.05 (q, $J = 5.8$, 2H), 3.56 (q, $J = 5.8$, 2H), 3.91 (s, 6H),

7.9 (s, 2H), 8.54 (s, 1H), 8.6 (s, 2H), 9.01 (t, $J=5.5$, 1H). ^{13}C NMR (150 MHz, d_6 -DMSO) 37.72, 39.05, 52.91, 130.8, 132.24, 132.64, 135.61, 158.86, 165.3, 165.94. IR: $\nu(\text{cm}^{-1})$: 3420(NH), 1784, 1728(C=O ester), 1632(C=O amide), 1549 (amide II). HRMS calc. of $\text{C}_{13}\text{H}_{17}\text{N}_2\text{O}_5\text{Na}$ $[\text{M}+\text{Na}]^+$ 281.1137, found 281.1125.

***N*-(dimethyl 1,3,5-benzenetricarboxylate)hexandiamine (10b)**

10b was obtained from *N,N'*-(dimethyl 1,3,5-benzenetricarboxylate) (tert-butoxycarbonyl)-1,6-hexandiamine (0.5 g, 1.15 mmol) and TFA (3 mL) as yellowish liquid product (0.39 g, 100 %) using general procedure.



^1H NMR (600 MHz, d_6 -DMSO) 1.29-1.37 (m, 4H), 1.52-1.58 (m, 4H), 2.78(m, 2H), 3.3 (q, $J=7$, 2H), 3.93 (s, 6H), 7.67(bs, 2H) 8.59 (t, $J=1.6$, 1H), 8.67 (d, $J=1.6$, 2H), 8.94 (t, $J=5.5$, 1H). ^{13}C NMR (150 MHz, d_6 -DMSO) 25.95, 26.41, 27.4, 29.2, 39.07, 39.26, 52.96, 130.9, 132.15, 132.78, 136.19, 158.55, 164.56, 165.45. IR: $\nu(\text{cm}^{-1})$: 3425(NH), 1782, 1716(C=O ester), 1624(C=O amide), 1555 (amide II). HRMS calc. of $\text{C}_{18}\text{H}_{24}\text{N}_2\text{O}_7\text{Na}$ $[\text{M}+\text{Na}]^+$ 403.1481, found 403.1487.

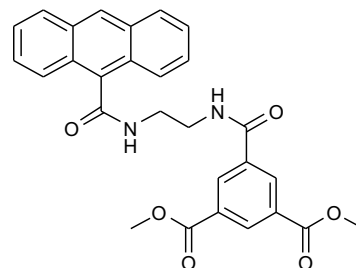
Model compounds synthesis

General method of amide coupling

Amine compounds (1g) were dissolved in DCM (50 mL) and a catalytic amount of triethylamine was added. Dimethyl 1,3,5-benzenetricarboxylate acid chloride (8) was added dropwise and the mixture was heated under reflux for 5hrs. The organic phase was washed with HCl (0.5M, 2x30 mL), NaOH (0.5M, 2x30 mL) and brine water and dried (MgSO_4). Solvent was evaporated under vacuum.

***N,N'*-(anthracene-9-carbonyl)(dimethyl 1,3,5-benzenetricarboxylate)ethandiamine (11a)**

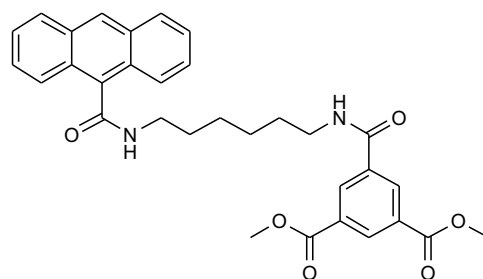
11a was obtained from *N*-(anthracene-9-carbonyl)ethandiamine (1 g, 3.8 mmol) and dimethyl 1,3,5-benzenetricarboxylate chloride (0.72 g, 2.8 mmol) as a white solid product (1.24 g, 92%) using general procedure.



^1H NMR (600 MHz, d_6 -DMSO) 3.67-3.7 (m, 2H), 3.73-3.76 (m, 2H), 3.94 (s, 6H), 7.46-7.54 (m, 4H), 7.98 (d, J = 8.5Hz, 2H), 8.11 (d, J = 8.5Hz, 2H), 8.61 (t, J = 1.5 Hz, 1H), 8.65 (s, 1H), 8.75 (d, J = 1.5 Hz, 2H), 8.91 (t, J = 5.5 Hz, 1H), 9.12 (t, J = 5.5 Hz, 1H). ^{13}C NMR (150 MHz, d_6 -DMSO) 36.31, 39.18, 53.17, 125.88, 126.02, 126.79, 127.61, 127.71, 128.77, 131.02, 131.12, 132.30, 132.62, 133.72, 136.22, 164.94, 165.49, 168.91. IR: $\nu(\text{cm}^{-1})$: 3310, 3295(NH), 1731(C=O ester), 1651, 1632(C=O amide I), 1550, 1545(amide II). HRMS calc. of $\text{C}_{28}\text{H}_{24}\text{N}_2\text{O}_6\text{Na}$ $[\text{M}+\text{Na}]^+$ 507.1532, found 507.1521.

***N,N'*-(anthracene-9-carbonyl)(dimethyl 1,3,5-benzenetricarboxylate) hexandiamine (11b)**

11b was obtained from *N*-(anthracene-9-carbonyl)hexandiamine (1 g, 3.1 mmol) and dimethyl 1,3,5-benzenetricarboxylate chloride (0.56 g, 2.3 mmol) as a white solid product (0.84 g, 81%) using general procedure.



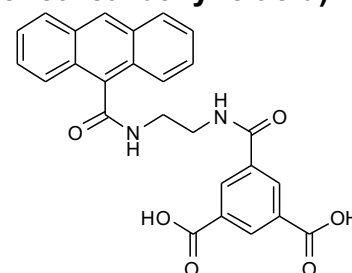
^1H NMR(600 MHz, d_6 -DMSO) 1.42-1.47 (m, 4H), 1.6-1.63 (m, 2H), 1.64-1.7 (m, 2H), 3.34-3.36 (m, 2H), 3.47-3.5 (m, 2H), 3.94 (s, 6H), 7.53-7.58 (m, 4H), 7.94 (d, J = 8.5 Hz, 2H), 8.12 (d, J = 8.5 Hz, 2H), 8.59 (t, J = 1.5 Hz, 1H), 8.65 (s, 1H), 8.69 (d, J = 1.5 Hz, 2H), 8.80 (t, J = 5.5 Hz, 1H), 8.96 (t, J = 5.5 Hz, 1H). IR: $\nu(\text{cm}^{-1})$: 3312, 3290(NH), 1735(C=O ester), 1650, 1630(C=O amide I), 1549, 1541(amide II).

General method of hydrolysis reaction

Hydrolysis of the ester groups was performed by heating under reflux the ester compounds (11a, 11b) (1g) with NaOH (1M, 20 mL) in methanol (30 mL) for 5 hrs. Then, DCM (50 mL) was added and the organic phase washed with HCl (0.5M, 3x30 mL), NaOH (0.5M, 3x30 mL) and brine water and dried (MgSO_4). Solvent was evaporated under vacuum.

***N,N'*-(anthracene-9-carbonyl)(dimethyl 1,3,5-benzenetricarboxylic acid) ethandiamine (12a)**

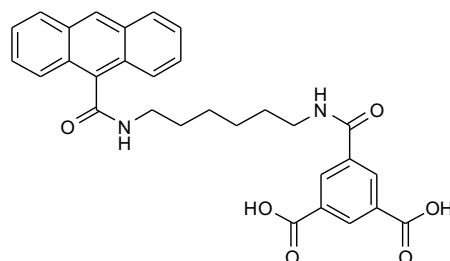
12a was obtained from *N,N'*-(anthracene-9-carbonyl)(dimethyl 1,3,5-benzenetricarboxylate) ethandiamine (1 g, 2 mmol) as a white solid product (0.8 g, 85%) using general procedure.



^1H NMR (600 MHz, d_6 -DMSO) 3.66-3.69 (m, 2H), 3.72-3.76 (m, 2H), 7.47-7.53 (m, 4H), 7.98 (d, J = 8.6 Hz, 2H), 8.11 (d, J = 8.6 Hz, 2H), 8.6 (s, 1H), 8.64 (s, 1H), 8.7 (d, J = 1.2 Hz, 2H), 8.91 (t, J = 5.5 Hz, 1H), 9.02 (t, J = 5.5 Hz, 1H). ^{13}C NMR (150 MHz, d_6 -DMSO) 39.21, 39.75 (shoulder), 125.89, 126.01, 126.78, 127.58, 127.71, 128.76, 131.11, 132.18, 132.44, 132.67, 133.74, 135.87, 165.30, 166.70, 168.90. IR: $\nu(\text{cm}^{-1})$: 3380(OH), 3291(NH), 1688(C=O acid), 1640(amide I), 1554, 1518(amide II). HRMS calc. of $\text{C}_{26}\text{H}_{20}\text{N}_2\text{O}_6\text{Na}$ $[\text{M}+\text{Na}]^+$ 479.1219, found 479.1202.

***N,N'*-(anthracene-9-carbonyl)(dimethyl 1,3,5-benzenetricarboxylic acid) hexandiamine (12b)**

12b was obtained from *N,N'*-(anthracene-9-carbonyl)(dimethyl 1,3,5-benzenetricarboxylate) hexandiamine (1 g, 1.85 mmol) as a white solid product (1.6 g, 88%) using general procedure.



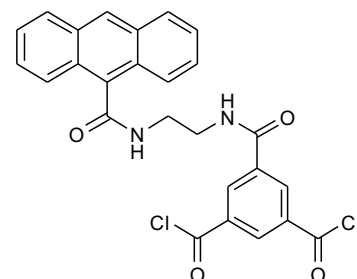
^1H NMR (600 MHz, d_6 -DMSO) 1.52-1.64 (m, 4H), 1.73-1.77 (m, 2H), 1.81-1.86 (m, 2H), 3.46-3.49 (m, 2H), 3.64-3.68 (m, 2H), 7.5-7.57 (m, 4H), 8.03 (d, J = 8.5 Hz, 2H), 8.08 (d, J = 8.5 Hz, 2H), 8.58 (s, 1H), 8.68 (d, J = 1.5 Hz, 2H), 8.78 (t, J = 1.5 Hz, 1H), 8.84 (t, J = 5.5 Hz, 1H), 8.9 (t, J = 5.5 Hz, 1H). ^{13}C NMR (150 MHz, d_6 -DMSO) 26.75, 26.85, 29.50, 29.52, 36.33, 39.9, 125.69, 126.01, 126.81, 127.44, 127.71, 128.83, 131.16, 132.02, 132.41, 132.54, 134.06, 136.04, 164.91, 166.68, 168.45. IR: $\nu(\text{cm}^{-1})$: 3382(OH), 3295(NH), 1682(C=O acid), 1643(amide I), 1550, 1520(amide II). HRMS calc. of $\text{C}_{30}\text{H}_{28}\text{N}_2\text{O}_6\text{Na}$ $[\text{M}+\text{Na}]^+$ 535.1845, found 535.1834.

General method of acid chloride formation

Thionyl chloride was added to the acid compounds (12a, 12b) with a catalytic amount of DMF and heated under reflux for 3 hrs. The excess thionyl chloride was distilled off under nitrogen and dry DCM (30 mL) was added twice to ensure the removal of thionyl chloride. The product was obtained in quantitative yield and directly used for further synthesis.

***N,N'*-(anthracene-9-carbonyl)(dimethyl 1,3,5-benzenetricarboxylate chloride)ethandiamine (13a)**

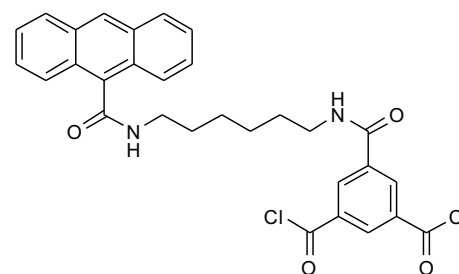
13a was obtained from *N,N'*-(anthracene-9-carbonyl)(dimethyl 1,3,5-benzenetricarboxylic acid) ethandiamine (1 g, 2.2 mmol) as yellow liquid product (1.1 g, 100%) using general procedure.



IR: $\nu(\text{cm}^{-1})$: 3295(NH), 1722(C=O Cl), 1645(C=O), 1506(amide II)

***N,N'*-(Dimethyl 1,3,5-Benzenetricarboxylate) (dimethyl 1,3,5-benzenetricarboxylate chloride)hexandiamine (13b)**

13b was obtained from *N,N'*-(anthracene-9-carbonyl)(dimethyl 1,3,5-benzenetricarboxylic acid) hexandiamine (1 g, 1.95 mmol) as yellow liquid product (1.07 g, 100%) using general procedure.



IR: $\nu(\text{cm}^{-1})$: 3291(NH), 1720(C=O Cl), 1643(C=O), 1510(amide II).

4.5 References

1. Seitz, J.L., *Globale Issues*. 2008.
2. Van der Bruggen, B. and C. Vandecasteele, *Distillation vs. Membrane Filtration: Overview of Process Evolutions in Seawater Desalination*. Desalination, 2002. **143**(3): p. 207-218.
3. Li, D. and H. Wang, *Recent Developments in Reverse Osmosis Desalination Membranes*. Journal of Materials Chemistry. **20**(22): p. 4551-4566.
4. Safarpour, M., V. Vatanpour, A. Khataee, and M. Esmaeili, *Development of a Novel High Flux and Fouling-Resistant Thin Film Composite Nanofiltration Membrane by Embedding Reduced Graphene Oxide/TiO₂*. Separation and Purification Technology, 2015. **154**: p. 96-107.
5. Shawky, H.A., S.-R. Chae, S. Lin, and M.R. Wiesner, *Synthesis and Characterization Of a Carbon Nanotube/Polymer Nanocomposite Membrane for Water Treatment*. Desalination, 2011. **272**(1): p. 46-50.
6. Shen, J.n., C.c. Yu, H.m. Ruan, C.j. Gao, and B. Van der Bruggen, *Preparation and Characterization of Thin-Film Nanocomposite Membranes Embedded With Poly(methyl methacrylate) Hydrophobic Modified Multiwalled Carbon Nanotubes by Interfacial Polymerization*. Journal of Membrane Science, 2013. **442**: p. 18-26.
7. Lind, M.L., D. Eumine Suk, T.-V. Nguyen, and E.M. Hoek, *Tailoring The Structure of Thin Film Nanocomposite Membranes to Achieve Seawater RO Membrane Performance*. Environmental science & technology, 2010. **44**(21): p. 8230-8235.
8. Lind, M.L., B.-H. Jeong, A. Subramani, X. Huang, and E. Hoek, *Effect of Mobile Cation on Zeolite-Polyamide Thin Film Nanocomposite Membranes*. Journal of Materials Research, 2009. **24**(05): p. 1624-1631.
9. Lee, H.S., S.J. Im, J.H. Kim, H.J. Kim, J.P. Kim, and B.R. Min, *Polyamide Thin-Film Nanofiltration Membranes Containing TiO₂ Nanoparticles*. Desalination, 2008. **219**(1-3): p. 48-56.
10. Lee, S.Y., H.J. Kim, R. Patel, S.J. Im, J.H. Kim, and B.R. Min, *Silver Nanoparticles Immobilized on Thin Film Composite Polyamide Membrane: Characterization, Nanofiltration, Antifouling Properties*. Polymers for Advanced Technologies, 2007. **18**(7): p. 562-568.
11. Gupta, V., O. Moradi, I. Tyagi, S. Agarwal, H. Sadegh, R. Shahryari-Ghoshekandi, A. Makhlof, M. Goodarzi, and A. Garshasbi, *Study on The Removal of Heavy Metal Ions From Industry Waste by Carbon Nanotubes: Effect of The Surface Modification: a Review*. Critical Reviews in Environmental Science and Technology, 2016. **46**(2): p. 93-118.
12. Verweij, H., M.C. Schillo, and J. Li, *Fast Mass Transport Through Carbon Nanotube Membranes*. Small, 2007. **3**(12): p. 1996-2004.
13. Noy, A., H.G. Park, F. Fornasiero, J.K. Holt, C.P. Grigoropoulos, and O. Bakajin, *Nanofluidics in Carbon Nanotubes*. Nano Today, 2007. **2**(6): p. 22-29.
14. Fan, X., H. Zhao, X. Quan, Y. Liu, and S. Chen, *Nanocarbon-based Membrane Filtration Integrated With Electric Field Driving For Effective Membrane Fouling Mitigation*. Water Research, 2016. **88**: p. 285-292.
15. Majumder, M., N. Chopra, R. Andrews, and B.J. Hinds, *Nanoscale Hydrodynamics: Enhanced Flow in Carbon Nanotubes*. Nature, 2005. **438**(7064): p. 44.

16. Chen, X., H. Ye, X. Fan, T. Ren, and G. Zhang, *A Review of Small Heat Pipes For Electronics*. Applied Thermal Engineering, 2016. **96**: p. 1-17.
17. Zhang, X., W.Z. Lang, X. Yan, Z.Y. Lou, and X.F. Chen, *Influences of The Structure Parameters of Multi-Walled Carbon Nanotubes(MWNTs) on PVDF/PFSA/O-MWNTs Hollow Fiber Ultrafiltration Membranes*. Journal of Membrane Science, 2016. **499**: p. 179-190.
18. Rahimi, Z., A.A.L. Zinatizadeh, and S. Zinadini, *Preparation of High Antibiofouling Amino Functionalized MWCNTs/PES Nanocomposite Ultrafiltration Membrane for Application in Membrane Bioreactor*. Journal of Industrial and Engineering Chemistry, 2015. **29**: p. 366-374.
19. Choi, J.H., J. Jegal, W.N. Kim, and H.S. Choi, *Incorporation of Multiwalled Carbon Nanotubes Into Poly (vinyl alcohol) Membranes For Use in The Pervaporation of Water/Ethanol Mixtures*. Journal of Applied Polymer Science, 2009. **111**(5): p. 2186-2193.
20. Panahian, S., A. Raisi, and A. Aroujalian, *Multilayer Mixed Matrix Membranes Containing Modified-MWCNTs For Dehydration of Alcohol by Pervaporation Process*. Desalination, 2015. **355**: p. 45-55.
21. Dumée, L.F., S. Smart, M.C. Duke, and S.R. Gray, *Next Generation Membranes For Membrane Distillation And Future Prospects*, In *Pervaporation, Vapour Permeation and Membrane Distillation: Principles and Applications*. 2015. p. 415-447.
22. Dumée, L., V. Germain, K. Sears, J. Schütz, N. Finn, M. Duke, S. Cerneaux, D. Cornu, and S. Gray, *Enhanced Durability And Hydrophobicity of Carbon Nanotube Bucky Paper Membranes in Membrane Distillation*. Journal of Membrane Science, 2011. **376**(1-2): p. 241-246.
23. Inukai, S., R. Cruz-Silva, J. Ortiz-Medina, A. Morelos-Gomez, K. Takeuchi, T. Hayashi, A. Tanioka, T. Araki, S. Tejima, T. Noguchi, M. Terrones, and M. Endo, *High-Performance Multi-Functional Reverse Osmosis Membranes Obtained by Carbon Nanotube-polyamide nanocomposite*. Scientific Reports, 2015. **5**: p. 13562.
24. Inukai, S., R. Cruz-Silva, J. Ortiz-Medina, A. Morelos-Gomez, K. Takeuchi, T. Hayashi, A. Tanioka, T. Araki, S. Tejima, and T. Noguchi, *High-Performance Multi-Functional Reverse Osmosis Membranes Obtained by Carbon nanotube-polyamide nanocomposite*. Scientific reports, 2015. **5**.
25. Jia, Y.X., H.L. Li, M. Wang, L.Y. Wu, and Y.D. Hu, *Carbon Nanotube: Possible Candidate For Forward Osmosis*. Separation and Purification Technology, 2010. **75**(1): p. 55-60.
26. Song, Z. and Z. Xu, *Ultimate Osmosis Engineered by The Pore Geometry And Functionalization of Carbon Nanostructures*. Scientific Reports, 2015. **5**.
27. Shi, F., Y. Ma, J. Ma, P. Wang, and W. Sun, *Preparation And Characterization of PVDF/TiO₂ Hybrid Membranes With Different Dosage of Nano-TiO₂*. Journal of Membrane Science, 2012. **389**: p. 522-531.
28. Tsai, H.A., W.H. Chen, C.Y. Kuo, K.R. Lee, and J.Y. Lai, *Study on The Pervaporation Performance And Long-Term Stability of Aqueous Iso-propanol Solution Through Chitosan/Polyacrylonitrile Hollow Fiber Membrane*. Journal of Membrane Science, 2008. **309**(1-2): p. 146-155.
29. Jang, W., S. Sundar, S. Choi, Y.G. Shul, and H. Han, *Acid-Base Polyimide Blends For The Application as Electrolyte Membranes For Fuel Cells*. Journal of Membrane Science, 2006. **280**(1-2): p. 321-329.
30. Zhao, X., J. Ma, Z. Wang, G. Wen, J. Jiang, F. Shi, and L. Sheng, *Hyperbranched-*

Polymer Functionalized Multi-Walled Carbon Nanotubes For Poly (vinylidene fluoride) Membranes: From Dispersion to Blended Fouling-Control Membrane. Desalination, 2012. **303**: p. 29-38.

31. nan Shen, J., C. chao Yu, H. min Ruan, C. jie Gao, and B. Van der Bruggen, *Preparation And Characterization of Thin-Film Nanocomposite Membranes Embedded With Poly (methyl methacrylate) Hydrophobic Modified Multiwalled Carbon Nanotubes by Interfacial Polymerization.* Journal of Membrane Science, 2013. **442**: p. 18-26.
32. Fagan, S.B., A. Souza Filho, J. Lima, J.M. Filho, O. Ferreira, I. Mazali, O. Alves, and M. Dresselhaus, *1, 2-Dichlorobenzene Interacting With Carbon Nanotubes.* Nano Letters, 2004. **4**(7): p. 1285-1288.
33. Chen, J., A.M. Rao, S. Lyuksyutov, M.E. Itkis, M.A. Hamon, H. Hu, R.W. Cohn, P.C. Eklund, D.T. Colbert, R.E. Smalley, and R.C. Haddon, *Dissolution of Full-Length Single-Walled Carbon Nanotubes.* The Journal of Physical Chemistry B, 2001. **105**(13): p. 2525-2528.
34. Bandow, S., S. Asaka, Y. Saito, A.M. Rao, L. Grigorian, E. Richter, and P. Eklund, *Effect of The Growth Temperature on The Diameter Distribution And Chirality of Single-Wall Carbon Nanotubes.* Physical Review Letters, 1998. **80**(17): p. 3779.
35. Liu, Y., Z. Yao, and A. Adronov, *Functionalization of Single-Walled Carbon Nanotubes with Well-Defined Polymers by Radical Coupling.* Macromolecules, 2005. **38**(4): p. 1172-1179.
36. Bandow, S., M. Takizawa, K. Hirahara, M. Yudasaka, and S. Iijima, *Raman Scattering Study of Double-Wall Carbon Nanotubes Derived From The Chains of Fullerenes in Single-Wall Carbon Nanotubes.* Chemical Physics Letters, 2001. **337**(1-3): p. 48-54.
37. Mevellec, J.-Y., C. Bergeret, J. Cousseau, J.-P. Buisson, C.P. Ewels, and S. Lefrant, *Tuning the Raman Resonance Behavior of Single-Walled Carbon Nanotubes via Covalent Functionalization.* Journal of the American Chemical Society, 2011. **133**(42): p. 16938-16946.
38. Corio, P., A.P. Santos, P.S. Santos, M.L.A. Temperini, V.W. Brar, M.A. Pimenta, and M.S. Dresselhaus, *Characterization of Single Wall Carbon Nanotubes Filled With Silver And With Chromium Compounds.* Chemical Physics Letters, 2004. **383**(5-6): p. 475-480.
39. Li, X., Z. Zhu, Q. Zhao, and S. Liu, *FT-IR Study of The Photocatalytic Degradation of Gaseous Toluene over UV-irradiated TiO₂ Microballs: Enhanced Performance by Hydrothermal Treatment in Alkaline Solution.* Applied Surface Science, 2011. **257**(10): p. 4709-4714.
40. Chai, G.-Y. and W.B. Krantz, *Formation And Characterization of Polyamide Membranes via Interfacial Polymerization.* Journal of Membrane Science, 1994. **93**(2): p. 175-192.
41. Ji, J., J.M. Dickson, R.F. Childs, and B.E. McCarry, *Mathematical Model for the Formation of Thin-Film Composite Membranes by Interfacial Polymerization: Porous and Dense Films.* Macromolecules, 2000. **33**(2): p. 624-633.
42. Freger, V. and S. Srebnik, *Mathematical Model of Charge And Density Distributions in Interfacial Polymerization of Thin Films.* Journal of Applied Polymer Science, 2003. **88**(5): p. 1162-1169.
43. Berezkin, A.V. and Y.V. Kudryavtsev, *Effect of Cross-Linking on the Structure and Growth of Polymer Films Prepared by Interfacial Polymerization.* Langmuir, 2015. **31**(44): p. 12279-12290.

44. Zhao, H., S. Qiu, L. Wu, L. Zhang, H. Chen, and C. Gao, *Improving the Performance of Polyamide Reverse Osmosis Membrane by Incorporation of Modified Multi-Walled Carbon Nanotubes*. Journal of Membrane Science, 2014. **450**: p. 249-256.
45. Dumée, L., J. Lee, K. Sears, B. Tardy, M. Duke, and S. Gray, *Fabrication of Thin Film Composite Poly(amide)-Carbon-Nanotube Supported Membranes for Enhanced Performance in Osmotically Driven Desalination Systems*. Journal of Membrane Science, 2013. **427**(0): p. 422-430.
46. Lee, H.S., S.J. Im, J.H. Kim, H.J. Kim, J.P. Kim, and B.R. Min, *Polyamide Thin-Film Nanofiltration Membranes Containing TiO₂ Nanoparticles*. Desalination, 2008. **219**(1-3): p. 48-56.
47. Perreault, F., M.E. Tousley, and M. Elimelech, *Thin-Film Composite Polyamide Membranes Functionalized with Biocidal Graphene Oxide Nanosheets*. Environmental Science & Technology Letters, 2014. **1**(1): p. 71-76.
48. Lamsal, R., S.G. Harroun, C.L. Brosseau, and G.A. Gagnon, *Use of surface Enhanced Raman Spectroscopy for Studying Fouling on Nanofiltration Membrane*. Separation and Purification Technology, 2012. **96**: p. 7-11.
49. Yadav, K., K. Morison, and M.P. Staiger, *Effects of Hypochlorite Treatment on the Surface Morphology and Mechanical Properties of Polyethersulfone Ultrafiltration Membranes*. Polymer Degradation and Stability, 2009. **94**(11): p. 1955-1961.
50. Hamciuc, C., T. Vlad-Bubulac, O. Petreus, and G. Lisa, *Kinetics of Thermal Degradation in Non-isothermal Conditions of Some Phosphorus-Containing Polyesters and Polyesterimides*. European Polymer Journal, 2007. **43**(3): p. 980-988.
51. Wu, B., Y.-Z. Wang, X.-L. Wang, K.-K. Yang, Y.-D. Jin, and H. Zhao, *Kinetics of Thermal Oxidative Degradation of Phosphorus-Containing Flame Retardant Copolyesters*. Polymer Degradation and Stability, 2002. **76**(3): p. 401-409.
52. Leo, C.P., W.P. Cathie Lee, A.L. Ahmad, and A.W. Mohammad, *Polysulfone Membranes Blended with ZnO Nanoparticles for Reducing Fouling by Oleic Acid*. Separation and Purification Technology, 2012. **89**: p. 51-56.
53. Guan, R., H. Zou, D. Lu, C. Gong, and Y. Liu, *Polyethersulfone Sulfonated by Chlorosulfonic Acid and its Membrane Characteristics*. European Polymer Journal, 2005. **41**(7): p. 1554-1560.
54. Kong, C., A. Kouchima, T. Kamada, T. Shintani, M. Kanezashi, T. Yoshioka, and T. Tsuru, *Enhanced Performance of Inorganic-Polyamide Nanocomposite Membranes Prepared by Metal-Alkoxide-Assisted Interfacial Polymerization*. Journal of Membrane Science, 2011. **366**(1-2): p. 382-388.
55. Rajaeian, B., A. Rahimpour, M.O. Tade, and S. Liu, *Fabrication and Characterization of Polyamide Thin Film Nanocomposite (TFN) Nanofiltration Membrane Impregnated with TiO₂ Nanoparticles*. Desalination, 2013. **313**: p. 176-188.
56. Chiang, I.W., B.E. Brinson, R.E. Smalley, J.L. Margrave, and R.H. Hauge, *Purification and Characterization of Single-Wall Carbon Nanotubes*. The Journal of Physical Chemistry B, 2001. **105**(6): p. 1157-1161.
57. Shi, Z., Y. Lian, F. Liao, X. Zhou, Z. Gu, Y. Zhang, and S. Iijima, *Purification of Single-Wall Carbon Nanotubes*. Solid State Communications, 1999. **112**(1): p. 35-37.
58. Chiang, I.W., B.E. Brinson, A.Y. Huang, P.A. Willis, M.J. Bronikowski, J.L.

- Margrave, R.E. Smalley, and R.H. Hauge, *Purification and Characterization of Single-Wall Carbon Nanotubes (SWNTs) Obtained from the Gas-Phase Decomposition of CO (HiPco Process)*. The Journal of Physical Chemistry B, 2001. **105**(35): p. 8297-8301.
59. Bartlett, J. and C. Frost, *Reliability, Repeatability and Reproducibility: Analysis of Measurement Errors in Continuous Variables*. Ultrasound in Obstetrics & Gynecology, 2008. **31**(4): p. 466-475.
 60. Joachim, G., *Are Reliability, Reproducibility and Validity the Correct Terms to Assess the Correctness of Dietary Studies?* Nutrition and health, 2001. **15**(1): p. 17-28.
 61. Pöstényi, Z., K. Tekes, E. Tóth-Molnár, and H. Kalász, *HPLC Analysis of Blood–Brain Barrier Penetration of 4-fluorodeprenyl*. Journal of Pharmaceutical and Biomedical Analysis, 2015. **102**: p. 529-534.
 62. Wei, H., L. Sun, Z. Tai, S. Gao, W. Xu, and W. Chen, *A Simple and Sensitive HPLC Method for the Simultaneous Determination of Eight Bioactive Components and Fingerprint Analysis of Schisandra Sphenanthera*. Analytica chimica acta, 2010. **662**(1): p. 97-104.
 63. Zhao, S., Z. Wang, X. Wei, B. Zhao, J. Wang, S. Yang, and S. Wang, *Performance Improvement of Polysulfone Ultrafiltration Membrane Using PANiEB as Both Pore Forming Agent and Hydrophilic Modifier*. Journal of Membrane Science, 2011. **385–386**: p. 251-262.
 64. Yu, S., M. Liu, Z. Lü, Y. Zhou, and C. Gao, *Aromatic-Cycloaliphatic Polyamide Thin-Film Composite Membrane with Improved Chlorine Resistance Prepared From m-phenylenediamine-4-methyl and Cyclohexane-1,3,5-tricarbonyl chloride*. Journal of Membrane Science, 2009. **344**(1-2): p. 155-164.
 65. Ghosh, A.K. and E.M.V. Hoek, *Impacts of Support Membrane Structure and Chemistry on Polyamide–Polysulfone Interfacial Composite Membranes*. Journal of Membrane Science, 2009. **336**(1-2): p. 140-148.
 66. Spitalsky, Z., D. Tasis, K. Papagelis, and C. Galiotis, *Carbon Nanotube–Polymer Composites: Chemistry, Processing, Mechanical and Electrical Properties*. Progress in polymer science, 2010. **35**(3): p. 357-401.
 67. Arthur, S.D., *Structure-Property Relationship in a Thin Film Composite Reverse Osmosis Membrane*. Journal of membrane science, 1989. **46**(2): p. 243-260.
 68. Allen, D.J. and H. Ishida, *Physical and Mechanical Properties of Flexible Polybenzoxazine Resins: Effect of Aliphatic Diamine Chain Length*. Journal of applied polymer science, 2006. **101**(5): p. 2798-2809.
 69. Watanabe, J., N. Sekine, T. Nematsu, M. Sone, and H.R. Kricheldorf, *Rigid-rod Polyesters with Flexible Side Chains. 6. Appearance of Hexagonal Columnar Phase as a Consequence of Microsegregation of Aromatic Main Chains and Aliphatic Side Chains*. Macromolecules, 1996. **29**(13): p. 4816-4818.
 70. Zeng, L., L. Zhang, and A.R. Barron, *Tailoring Aqueous Solubility of Functionalized Single-Wall Carbon Nanotubes over a Wide pH Range Through Substituent Chain Length*. Nano letters, 2005. **5**(10): p. 2001-2004.
 71. Bunn, C., *The Melting Points of Chain Polymers*. Journal of Polymer Science Part B: Polymer Physics, 1996. **34**(5): p. 799-819.
 72. Chen, L., H. Xie, and W. Yu, *Functionalization Methods of Carbon Nanotubes and its Applications*. 2011: INTECH Open Access Publisher.
 73. Wang, X., Y. Liu, W. Qiu, and D. Zhu, *Immobilization of Tetra-Tert-Butylphthalocyanines on Carbon Nanotubes: a First Step Towards the Development of New Nanomaterials*. Journal of Materials Chemistry, 2002.

- 12(6):** p. 1636-1639.
74. Chen, R.J., Y. Zhang, D. Wang, and H. Dai, *Noncovalent Sidewall Functionalization of Single-Walled Carbon Nanotubes for Protein Immobilization*. Journal of the American Chemical Society, 2001. **123**(16): p. 3838-3839.
75. Song, K., Y. Zhang, J. Meng, E.C. Green, N. Tajaddod, H. Li, and M.L. Minus, *Structural Polymer-Based Carbon Nanotube Composite Fibers: Understanding the Processing–Structure–Performance Relationship*. Materials, 2013. **6**(6): p. 2543-2577.

CHAPTER V

5.1 Conclusion

There are two disciplines that have been investigated in this thesis, namely are the self-assembly of BTA derivatives and RO membrane modification with SWNTs. These disciplines were addressed because the functionalisation reactions of SWNTs were studied and simulated by the model reaction. Anthracene was used to mimic the carbon nanotube wall, due to its aromatic structure. The compounds produced from the model reactions were utilised to form BTA derivatives. First, the self-assembly behaviour of the BTA derivatives was investigated, as described in Chapter III. The second discipline was modified RO membranes with functionalised SWNTs, as described in Chapter IV. Therefore, this conclusion is divided into two sections.

5.1.1 Self-assembly

BTA derivatives were synthesised and allowed to self-assemble in chloroform. The anthracene moiety was used as a substituent, connected to the BTA core through the amide bond, as seen in Figure 5-1. The distance between the BTA core and the anthracene moiety was adjusted by the aliphatic chain length. Four molecules were synthesised with aliphatic chain lengths of C_2H_4 , C_4H_8 , C_6H_{12} , and C_8H_{16} .

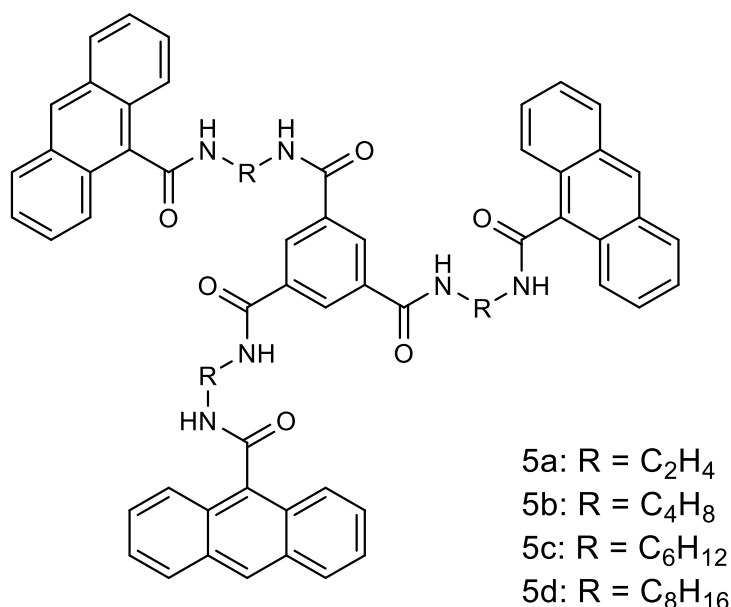


Figure 5-1. BTA derivative structure showing anthracene moieties as substituents coupled to the BTA core through amide bonds.

These molecules aggregate and form different shapes depending on the chain length. The influence of the distance between the BTA core and anthracene on the self-assembly process as a function of time was investigated by observing the change in fluorescence, and FT-IR and SEM images.

Fluorescence quenching occurred for the more flexible molecule (BTA with C_8H_{16}) in less than 24 hours, while the less flexible molecule (BTA with C_2H_4) needed more than 24 hours to show quenching. In addition, the red shift was greater for the more flexible molecule as a result of increased overlapping between the aromatic rings.

Hydrogen bonding interactions were also affected by the flexibility of the molecule. FT-IR spectra shows that the N-H band, as the representative band of hydrogen bonding, showed greater shift to higher wavenumbers for the more flexible molecule than the less flexible molecule.

Very long fibres were formed by the BTA molecule with the long chain in comparison to the short-chain molecule (C_2H_4). Figure 5- 2 (A) shows that the short-chain molecule was not able to form very long and uniform fibres on the surface, even after 96 hours of aggregation time in chloroform. In contrast, the molecule with the longer chain formed longer and more uniform fibres in identical conditions, as seen in Figure 5- 2 (B).

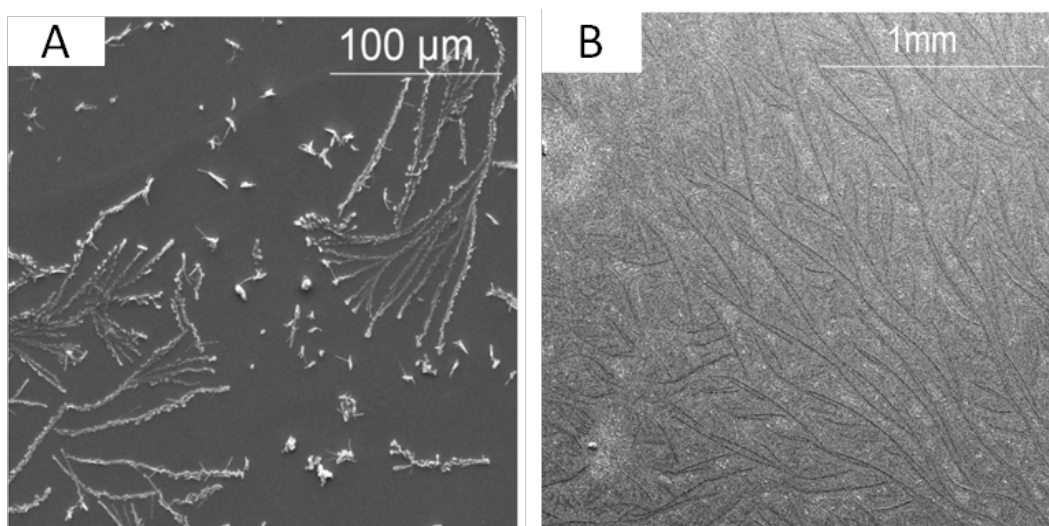


Figure 5- 2. SEM images of (A) short-chain molecule and (B) long-chain molecule on silicon surface after 96 hours of aggregation time in chloroform (presented in Chapter III). Note different scale sizes.

The difference in fibre formation was attributed to the molecule flexibility. The molecule with the long chain was more flexible than the short chain one and was able to form longer fibres than the short chain molecule.

5.1.2 RO membrane

In Chapter IV, there was an attempt to overcome the poor dispersion of SWNTs in the organic phase and their agglomeration in the polyamide membrane. To achieve this aim, two organic compounds were synthesised with the difference between them being only the aliphatic chain length as seen in Figure 5- 3. Analysis tools such as NMR, FT-IR and mass spectroscopy were used to characterise the synthesised organic compounds. SWNTs were covalently linked with the synthesised compounds through amide coupling. The functionalisation of SWNTs was characterised by Raman and FT-IR spectroscopes showing the successful functionalisation of SWNTs with the organic compounds. Interfacial polymerisation was performed to synthesise a polyamide layer on the top surface of the support layer.

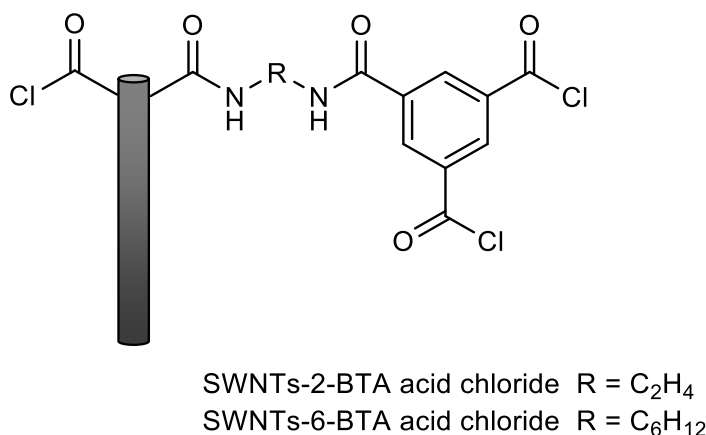


Figure 5- 3. Illustration of the functionalised SWNTs with the organic compounds.

In order to embed SWNTs in the polyamide layer, functionalised SWNTs were dispersed in organic solution at nanotube concentrations of 0, 0.5, 1, 2.5, 5, 10 and 50 wt% based on the weight of the TMC (0.1 g in 100 mL). The polyamide layer was characterised with Raman, FT-IR, AFM, SEM and contact angle measurements.

Figure 5- 4 shows the SEM images of the top surface of the polyamide layer. The comparison reveals that there is a difference in the surfaces, which was attributed to the distribution of the functionalised SWNTs. Functionalisation of SWNTs with the short (C_2H_4) aliphatic chain compound showed a decrease in surface roughness, which was due to more homogenous distribution of SWNTs in the polyamide layer.

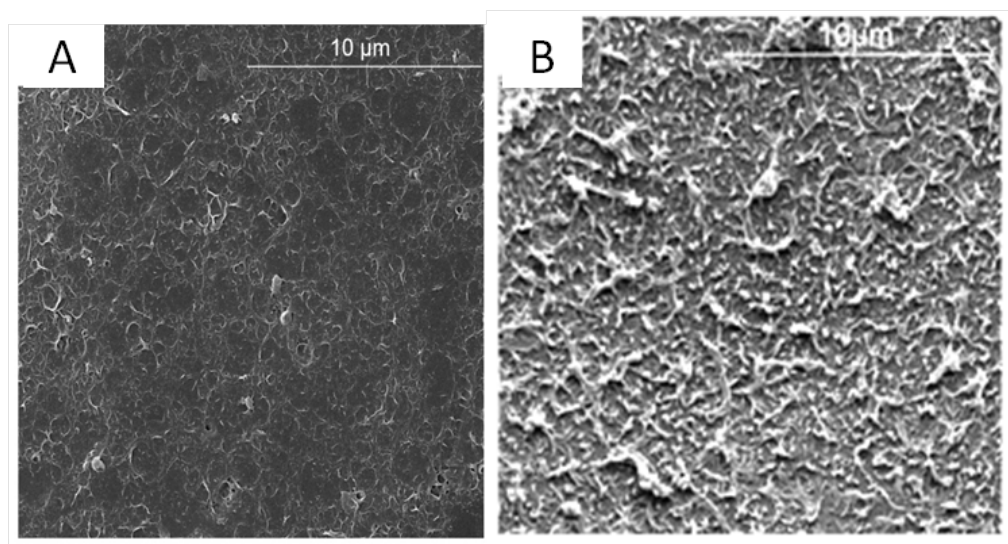


Figure 5- 4. SEM images for the embedded polyamide layer with 50 wt% of (A) functionalised SWNTs with the short-chain compound, (B) with the long-chain compound.

Generally, the water flux was improved by embedding SWNTs in the polyamide layer, while a reduction in salt rejection occurred. The embedded polyamide with 50 wt% of short-chain functionalised SWNTs showed a significant increase in water flux from $25 \text{ L m}^{-2} \text{ h}^{-1}$ to $60 \text{ L m}^{-2} \text{ h}^{-1}$, while salt rejection decreased significantly, from 70% to 10%. This was attributed to the disruption of polymer cross-linkage by embedding a high loading of SWNTs. It was attributed to the aggregation of CNTs during the polymerisation which caused a disruption of polymer growing. Imperfection in polymer growing led to low cross linking and therefore poor salt rejection.

5.2 Future work

The results obtained during this study will inspire future projects. There are two subdivisions for these future projects, depending on the two discipline results, which are the self-assembly and RO membrane projects.

5.2.1 Self-assembly

There are four future projects suggested, which depend on the results obtained in Chapter III, and there is a different application for each.

5.2.1.1 *Forming various shapes*

When BTA derivatives are allowed to self assemble under different conditions, such as different concentrations and solvents, they aggregate to form various shapes such as micelles, vesicles, tubes and fibres [1-3]. For instance, Lee et al. synthesised a BTA molecule that was able to form different shapes by changing the solvent. Fibres were formed in DMSO and DMF with H₂O, while bulk and hollow spherical shapes were formed in mixtures of THF and H₂O [4]. Figure 5- 5 shows the different shapes formed in different solvents for the synthesised molecule.

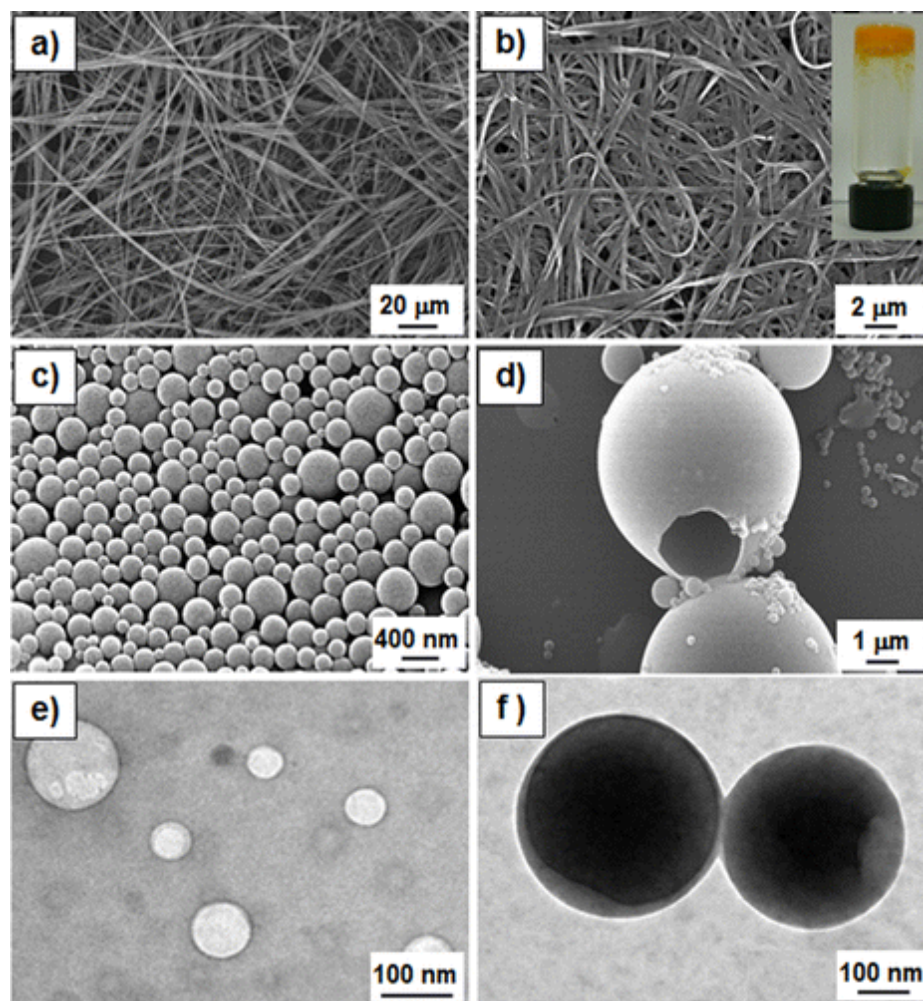


Figure 5- 5. SEM images of (10 mM) supramolecules prepared in 50% DMSO–H₂O (a), 50% DMF–H₂O (b), and 50% THF–H₂O (c and d). Transmission electron microscope (TEM) images of the spheres (e and f). The inset in (b) shows a vial containing gel, figure was adapted from [4].

Successful encapsulation of dyes inside the hollow spherical shape was obtained, indicating a possible application for drug delivery [4]. An encapsulation experiment was carried out using the fluorescent Rhodamine B (RB) dye, in order to prove that hollow spheres were generated. The optical and fluorescence images, as seen in Figure 5- 6, illustrate that the dye molecules were encapsulated inside the spherical structures [4].

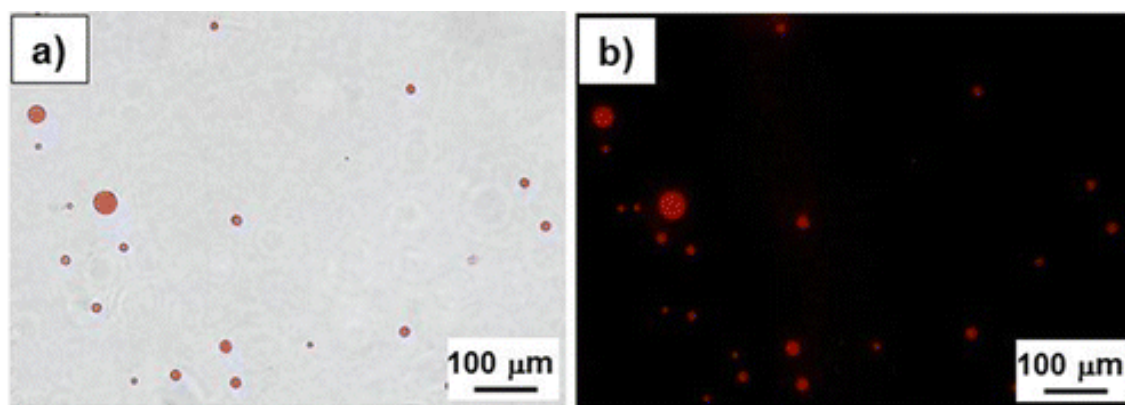


Figure 5- 6. Optical (a) and fluorescence (b) microscope images of the Rhodamine B encapsulated spheres [4].

For future work, it is recommended to allow the synthesised BTA molecules to self assemble in different solvents to, potentially, obtain supramolecular structures of different shapes. For instance, the mixture of THF/H₂O (1:1) was used to allow the synthesised BTA molecules to self assemble and spherical structures were formed.

5.2.1.2 Gel formation to enhance the optical properties

A gel can be formed as a result of self-assembly of the BTA derivatives through intermolecular interactions, such as hydrogen bonding and π - π stacking [5]. When the molecules self-assemble, the resulting supramolecular structure can immobilise a large volume of solvent, leading to gelation of the solvent mass [6]. If the gel is formed in organic solvents such as hexane, heptane and chloroform, the gel is generally called an organogel, whereas it is called a hydrogel when water is used as the solvent [5, 6]. The applications for the gel depend on the substituents of the BTA. The presence of anthracene moieties as substituents in the synthesised BTA derivatives, as seen in Figure 5-1, imparts optical properties to these molecules, particularly fluorescence emission.

It is reported that gel formation can enhance fluorescence emission [7-9]. Duan and Liu synthesised a series of L-glutamate-based dendrons containing anthracene cores. The fluorescence emission of anthracene moiety is significantly enhanced after forming the gel when compared to the solution fluorescence emission, as seen in Figure 5- 7 [9].

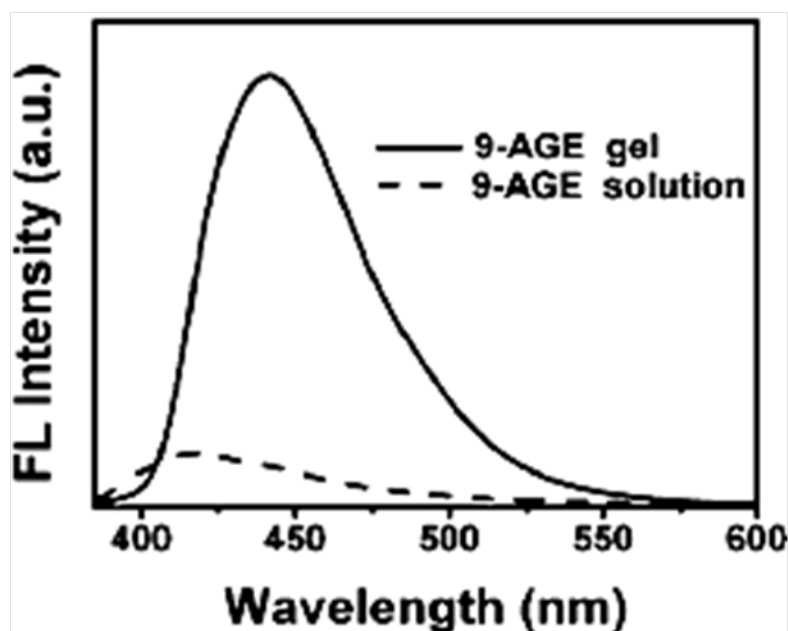


Figure 5- 7. Fluorescence spectra enhancement in the gel phase compared to the solution phase [9].

Therefore, investigation of the fluorescence emission enhancement of the synthesised BTA molecules by forming a gel in either organic or aqueous solvents is recommended.

5.2.1.3 Photoresponsive gel formation

Forming a gel also can be achieved by exposing the synthesised molecules to UV light. It is well known that anthracene and its derivatives can be transformed into photodimers after UV light irradiation. Disassociation of the photodimers into monomers can be obtained after heating or further visible light irradiation, as demonstrated in Figure 5- 8 [10].

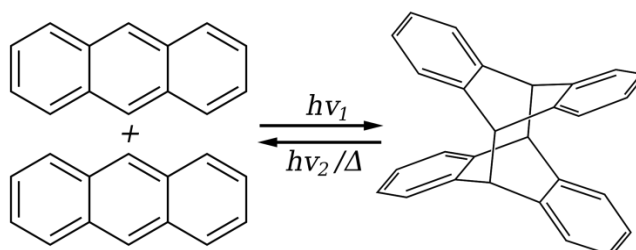


Figure 5- 8. Photodimerisation of anthracene upon UV light irradiation [11].

Wang et al. synthesised anthracene derivatives and exposed them to UV light (365 nm), as demonstrated in Figure 5- 9. Transparent organogels were formed in several organic solvents, such as THF, cyclohexane and hexane. The organogel formation reduced the fluorescence intensity due to photodimer formation [10].

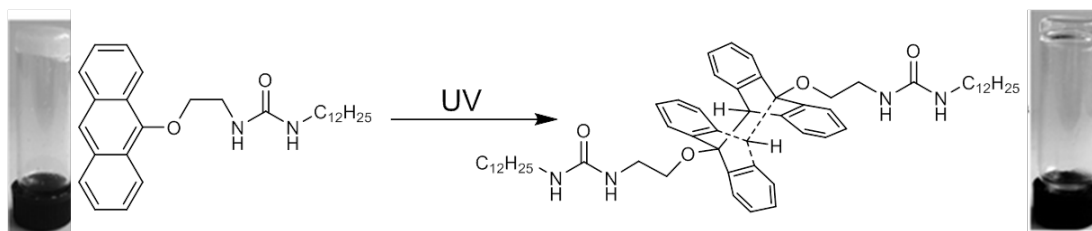


Figure 5- 9. Transparent organogel formation in THF after exposure to UV light [10].

Synthesised BTA derivatives, in this project, could form photoresponsive gels. The exposure to UV light of anthracene moieties in the synthesised BTA derivatives would form anthracene photodimers, which could potentially produce photoresponsive gels.

5.2.2 RO membrane

There are three suggested future projects which were inspired by the results obtained in Chapter IV.

5.2.2.1 Salt rejection

Due to the use of toluene to disperse CNTs in organic phase, the membrane salt rejection was below 80%. It is recommended that more investigation should be performed to figure out the mixture percent that improve the dispersion of CNTs in organic phase and salt rejection.

5.2.2.2 Antibiofouling

Membrane biofouling causes a decline in the water flux, thereby increasing energy consumption which leads to increased desalination costs. The formation of biofouling on the membrane surface is attributed to the interaction between the membrane surface and the foulants. The membrane's resistance to foulants can be altered by modifying the surface of the membrane. It has been reported that CNTs enhance the biofouling resistance of the membrane. This is due to the ability of CNTs to damage microorganism membranes and disrupt metabolic pathways, accompanied by oxidative stress. Thus, inactivation and/or death of the microorganisms can occur [12-15].

SWNTs, specifically, have been utilised in a variety environmental applications as antimicrobial agents [16, 17]. This property of SWNTs was exploited to improve TFC membranes, and showed the positive effect of resisting biofouling formation on the membrane surface. Tiraferri et al. reported that the covalent bonding of SWNTs to the polyamide layer in TFC membranes reduced the number of bacteria by around 62% compared to the SWNT-free polyamide layer, as demonstrated in Figure 5- 10 [18].

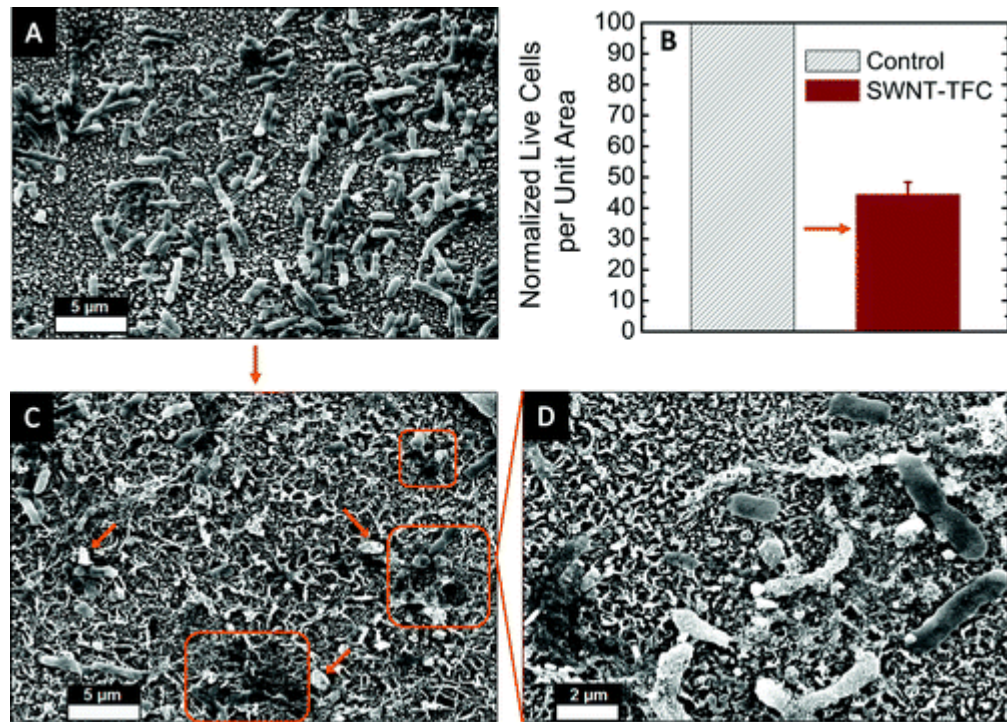


Figure 5- 10. SEM images displaying *E. coli* bacteria at the surface of (A) control membrane and (C) SWNT-functionalised membrane (some cells with lost integrity are highlighted in orange). (D) Magnified view of the surface of a SWNT-TFC membrane with *E. coli* cells [18].

Therefore, a biofouling resistance experiment is recommended to investigate the antibiofouling property of the membranes synthesised in this project.

5.2.2.3 Forward osmosis desalination

Forward osmosis (FO) is a promising desalination technique due to the very low hydraulic pressure required. Many potential advantages, such as lower energy consumption, higher fouling resistance, easier fouling removal and higher recovery of water are delivered by FO over the pressure-driven processes like RO and ultrafiltration (UF). Osmotic pressure is the driving force of water molecules across the semipermeable membrane, as opposed to pressure-driven processes [19, 20], as illustrated in Figure 5- 11.

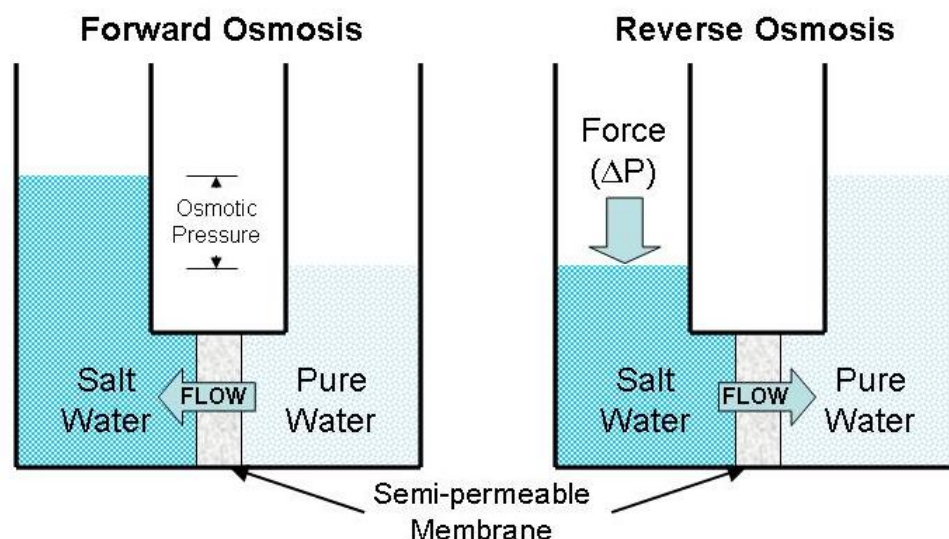


Figure 5- 11. Illustration of FO and RO schemes showing that the water flow is driven by the osmotic pressure in FO, while external pressure is applied in RO.

TFC has been used as the semipermeable membrane in FO [21-23]. Thus, the modified TFC membrane with SWNTs, as described in Chapter IV, can be used in FO. Potentially, water flux and salt rejection for FO can be improved. Moreover, SWNTs can increase the antifouling resistance of FO membranes.

5.2.2.4 RO membrane modification with graphene

Graphene is a carbon-based nanomaterial that consists of a single-atom-thick sheet of hexagonal arrayed sp^2 -bonded carbon atoms [24]. It has received increasing attention as another option for modifying the polyamide layer in TFC membranes. This is due to the extraordinary properties of graphene, such as high surface area ($2360 \text{ m}^2\text{g}^{-1}$), excellent mechanical properties and superior hydrophilicity [25].

There have been several attempts to use graphene in TFC membranes which show an improvement in fouling resistance, water flux and mechanical properties of the membrane [24, 26-29]. For instance, Yin et al. dispersed graphene oxide in the organic phase in the interfacial polymerisation method, as illustrated in Figure 5- 12. The resultant membranes were embedded with graphene oxide, which improved the membrane performance. The water flux was enhanced by around 33%, while a slight decrease was observed in salt rejection [25].

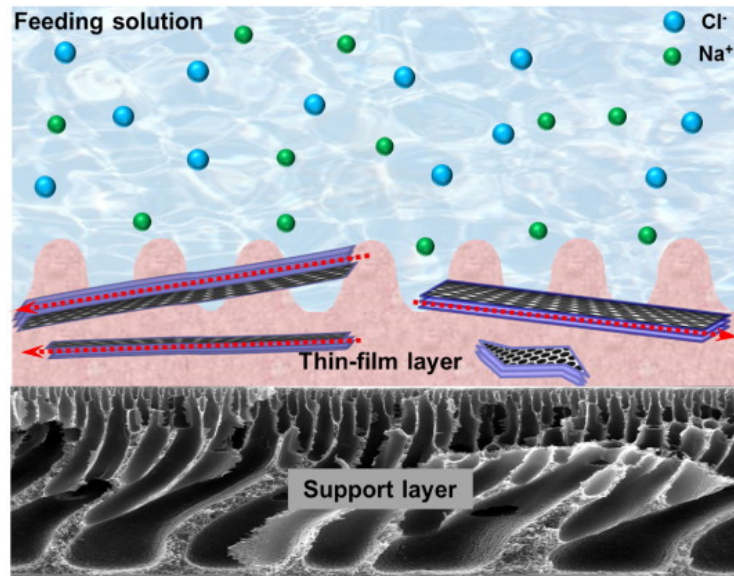


Figure 5- 12. Schematic illustration of embedded graphene oxide in the polyamide layer on top of the polysulfone layer [25].

The functionalisation process that has been used in this project to improve the dispersion of SWNTs in polyamide (Chapter IV) can be applied to graphene as well. A potential high distribution of graphene in polyamide, and water flux and salt rejection improvements are expected.

5.3 References

1. Petkau-Milroy, K., M.H. Sonntag, and L. Brunsveld, *Modular Columnar Supramolecular Polymers as Scaffolds for Biomedical Applications*. Chemistry–A European Journal, 2013. **19**(33): p. 10786-10793.
2. Stals, P.J., J.C. Everts, R. de Bruijn, I.A. Filot, M.M. Smulders, R. Martín-Rapún, E.A. Pidko, T.F. de Greef, A.R. Palmans, and E. Meijer, *Dynamic Supramolecular Polymers Based on Benzene-1, 3, 5-tricarboxamides: The Influence of Amide Connectivity on Aggregate Stability and Amplification of Chirality*. Chemistry–A European Journal, 2010. **16**(3): p. 810-821.
3. Shen, Z., T. Wang, and M. Liu, *Macroscopic Chirality of Supramolecular Gels Formed from Achiral Tris (ethyl cinnamate) Benzene-1, 3, 5-tricarboxamides*. Angewandte Chemie International Edition, 2014. **53**(49): p. 13424-13428.
4. Lee, S., S. Oh, J. Lee, Y. Malpani, Y.-S. Jung, B. Kang, J.Y. Lee, K. Ozasa, T. Isoshima, S.Y. Lee, M. Hara, D. Hashizume, and J.-M. Kim, *Stimulus-Responsive Azobenzene Supramolecules: Fibers, Gels, and Hollow Spheres*. Langmuir, 2013. **29**(19): p. 5869-5877.
5. Howe, R.C., A.P. Smalley, A.P. Guttenplan, M.W. Doggett, M.D. Eddleston, J.C. Tan, and G.O. Lloyd, *A Family of Simple Benzene 1, 3, 5-tricarboxamide (BTA) Aromatic Carboxylic Acid Hydrogels*. Chemical Communications, 2013. **49**(39): p. 4268-4270.
6. Babu, S.S., V.K. Praveen, and A. Ajayaghosh, *Functional π -Gelators and Their Applications*. Chemical Reviews, 2014. **114**(4): p. 1973-2129.
7. Bernet, A., R.Q. Albuquerque, M. Behr, S.T. Hoffmann, and H.-W. Schmidt, *Formation of a Supramolecular Chromophore: a Spectroscopic and Theoretical Study*. Soft Matter, 2012. **8**(1): p. 66-69.
8. Leung, M.-k., Y.-S. Lin, C.-C. Lee, C.-C. Chang, Y.-X. Wang, C.-P. Kuo, N. Singh, K.-R. Lin, C.-W. Hu, and C.-Y. Tseng, *Benzenetricarboxamide-cored Triphenylamine Dendrimer: Nanoparticle Film Formation by an Electrochemical Method*. RSC Advances, 2013. **3**(44): p. 22219-22228.
9. Duan, P. and M. Liu, *Design and Self-Assembly of l-Glutamate-Based Aromatic Dendrons as Ambidextrous Gelators of Water and Organic Solvents*. Langmuir, 2009. **25**(15): p. 8706-8713.
10. Wang, C., D. Zhang, J. Xiang, and D. Zhu, *New Organogels Based on an Anthracene Derivative with One Urea Group and its Photodimer: Fluorescence Enhancement After Gelation*. Langmuir, 2007. **23**(18): p. 9195-9200.
11. Breton, G.W. and X. Vang, *Photodimerization of Anthracene*. Journal of Chemical Education, 1998. **75**(1): p. 81.
12. Kim, H.J., Y. Baek, K. Choi, D.-G. Kim, H. Kang, Y.-S. Choi, J. Yoon, and J.-C. Lee, *The Improvement of Antibiofouling Properties of a Reverse Osmosis Membrane by Oxidized CNTs*. RSC Advances, 2014. **4**(62): p. 32802-32810.
13. Park, S., H.-S. Yang, D. Kim, K. Jo, and S. Jon, *Rational Design of Amphiphilic Polymers to Make Carbon Nanotubes Water-Dispersible, Anti-biofouling, and Functionalizable*. Chemical Communications, 2008(25): p. 2876-2878.
14. Hu, C., C. Yang, and S. Hu, *Hydrophobic Adsorption of Surfactants on Water-Soluble Carbon Nanotubes: A Simple Approach to Improve Sensitivity and Antifouling Capacity of Carbon Nanotubes-Based Electrochemical Sensors*. Electrochemistry Communications, 2007. **9**(1): p. 128-134.

15. Vatanpour, V., S.S. Madaeni, R. Moradian, S. Zinadini, and B. Astinchap, *Fabrication and Characterization of Novel Antifouling Nanofiltration Membrane Prepared From Oxidized Multiwalled Carbon Nanotube/Polyethersulfone Nanocomposite*. Journal of Membrane Science, 2011. **375**(1): p. 284-294.
16. Kang, S., M.S. Mauter, and M. Elimelech, *Microbial Cytotoxicity of Carbon-Based Nanomaterials: Implications for River Water and Wastewater Effluent*. Environmental Science & Technology, 2009. **43**(7): p. 2648-2653.
17. Mauter, M.S. and M. Elimelech, *Environmental Applications of Carbon-Based Nanomaterials*. Environmental Science & Technology, 2008. **42**(16): p. 5843-5859.
18. Tiraferri, A., C.D. Vecitis, and M. Elimelech, *Covalent Binding of Single-Walled Carbon Nanotubes to Polyamide Membranes for Antimicrobial Surface Properties*. ACS Applied Materials & Interfaces, 2011. **3**(8): p. 2869-2877.
19. Lutchmiah, K., A.R.D. Verliefde, K. Roest, L.C. Rietveld, and E.R. Cornelissen, *Forward Osmosis for Application in Wastewater Treatment: A review*. Water Research, 2014. **58**: p. 179-197.
20. Zhao, S., L. Zou, C.Y. Tang, and D. Mulcahy, *Recent Developments in Forward Osmosis: Opportunities and Challenges*. Journal of Membrane Science, 2012. **396**: p. 1-21.
21. Yip, N.Y., A. Tiraferri, W.A. Phillip, J.D. Schiffman, and M. Elimelech, *High Performance Thin-Film Composite Forward Osmosis Membrane*. Environmental Science & Technology, 2010. **44**(10): p. 3812-3818.
22. Widjojo, N., T.-S. Chung, M. Weber, C. Maletzko, and V. Warzelhan, *The Role of Sulphonated Polymer and Macrovoid-free Structure in the Support Layer for Thin-Film Composite (TFC) Forward Osmosis (FO) Membranes*. Journal of Membrane Science, 2011. **383**(1-2): p. 214-223.
23. Widjojo, N., T.-S. Chung, M. Weber, C. Maletzko, and V. Warzelhan, *A Sulfonated Polyphenylenesulfone (sPPSU) as the Supporting Substrate in Thin Film Composite (TFC) Membranes with Enhanced Performance for Forward Osmosis (FO)*. Chemical Engineering Journal, 2013. **220**: p. 15-23.
24. Safarpour, M., V. Vatanpour, A. Khataee, and M. Esmaeili, *Development of a Novel High Flux and Fouling-Resistant Thin Film Composite Nanofiltration Membrane by Embedding Reduced Graphene Oxide/TiO₂*. Separation and Purification Technology, 2015. **154**: p. 96-107.
25. Yin, J., G. Zhu, and B. Deng, *Graphene Oxide (GO) Enhanced Polyamide (PA) Thin-Film Nanocomposite (TFN) Membrane for Water Purification*. Desalination, 2016. **379**: p. 93-101.
26. Ali, M.E.A., L. Wang, X. Wang, and X. Feng, *Thin Film Composite Membranes Embedded with Graphene Oxide for Water Desalination*. Desalination, 2016. **386**: p. 67-76.
27. Lai, G.S., W.J. Lau, P.S. Goh, A.F. Ismail, N. Yusof, and Y.H. Tan, *Graphene Oxide Incorporated Thin Film Nanocomposite Nanofiltration Membrane for Enhanced Salt Removal Performance*. Desalination, 2016. **387**: p. 14-24.
28. Yin, J. and B. Deng, *Polymer-Matrix Nanocomposite Membranes for Water Treatment*. Journal of Membrane Science, 2015. **479**: p. 256-275.
29. Kim, S.G., D.H. Hyeon, J.H. Chun, B.-H. Chun, and S.H. Kim, *Novel Thin Nanocomposite RO Membranes for Chlorine Resistance*. Desalination and Water Treatment, 2013. **51**(31-33): p. 6338-6345.

6. Appendices

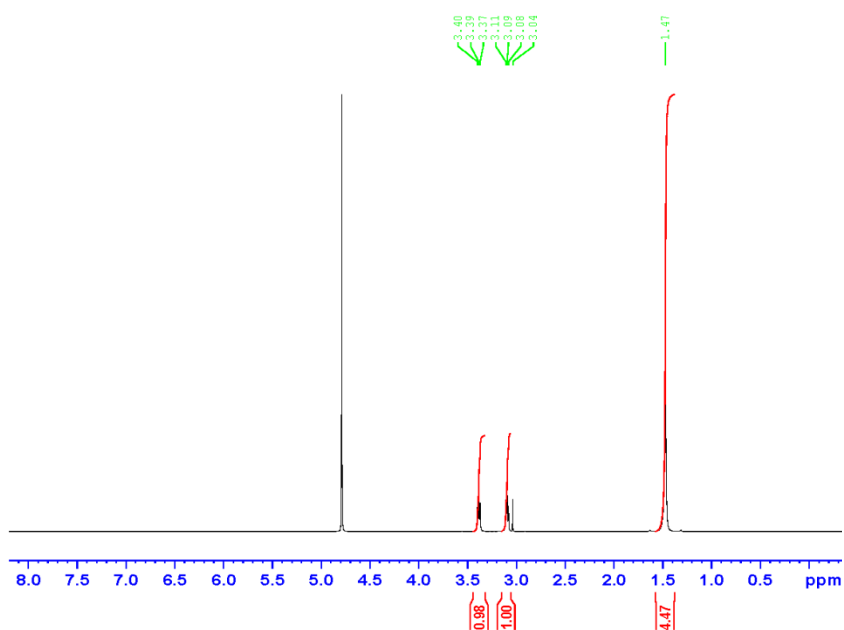


Figure 6- 1. ¹H NMR spectrum of compound 1a.

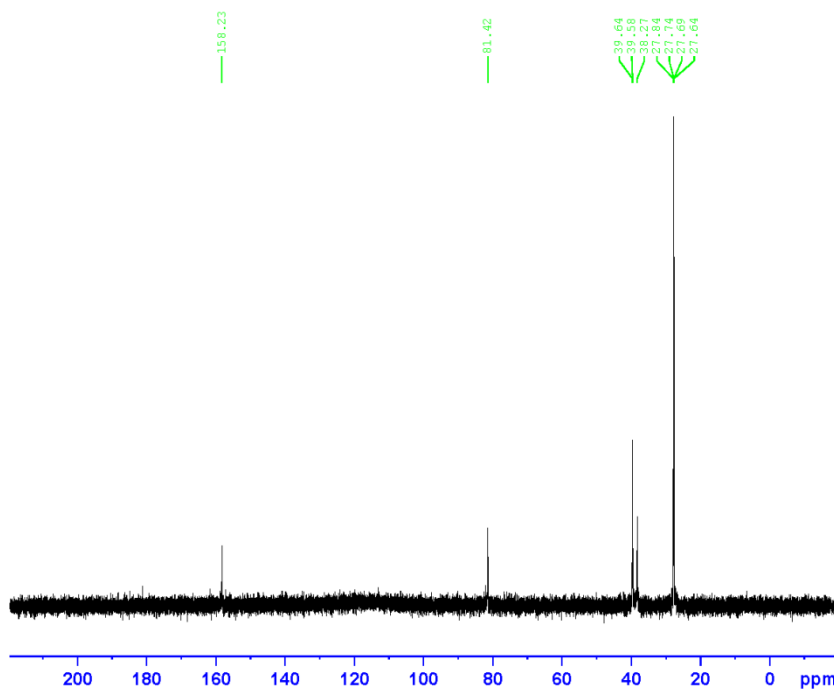


Figure 6- 2. ¹³C NMR spectrum of compound 1a.

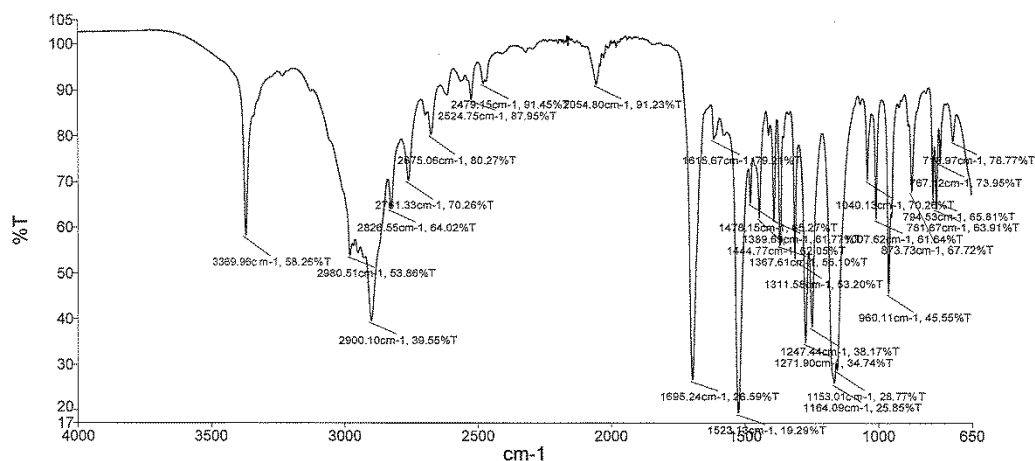
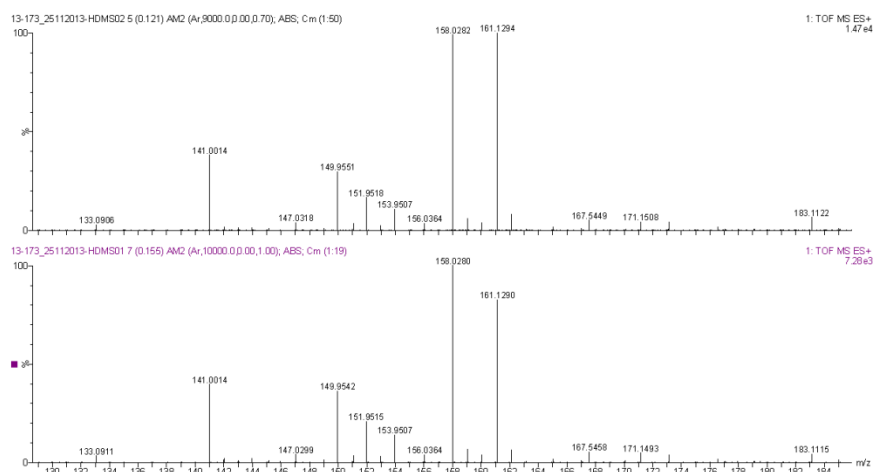


Figure 6- 3. FT-IR spectrum of compound 1a

High Resolution Spectra Positive ion



Accurate Mass Data

Observed Mass	Formula $[\text{M}+\text{H}]^+$	Calculated mass	Difference (ppm)	iFit (norm)
161.1290	$\text{C}_7\text{H}_{17}\text{N}_2\text{O}_2$	161.1290	0.0	0.0
161.1294	$\text{C}_7\text{H}_{17}\text{N}_2\text{O}_2$	161.1290	2.5	0.0

Figure 6- 4. Mass spectra of compound 1a.

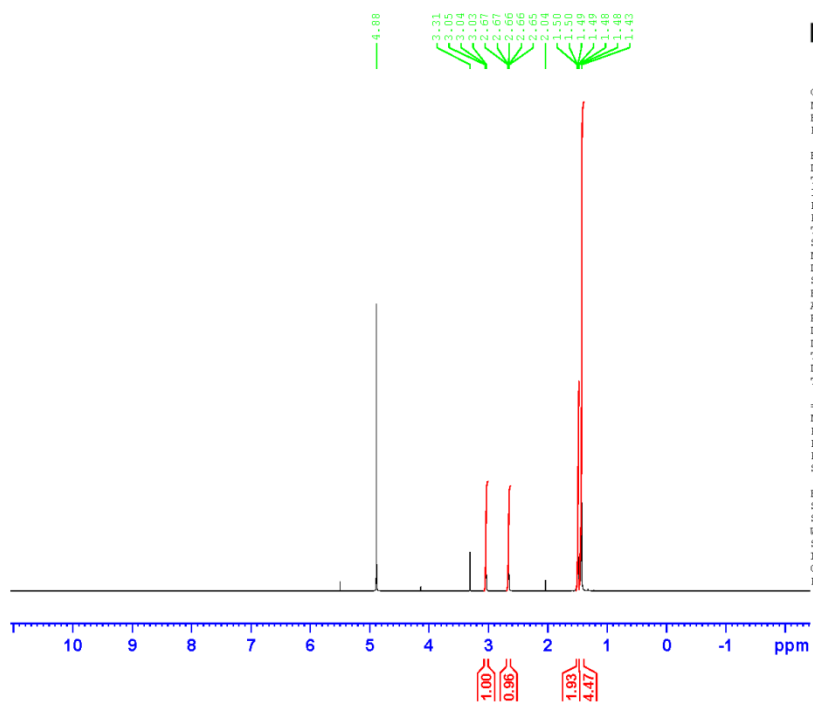


Figure 6- 5. ^1H NMR spectrum of compound 1b

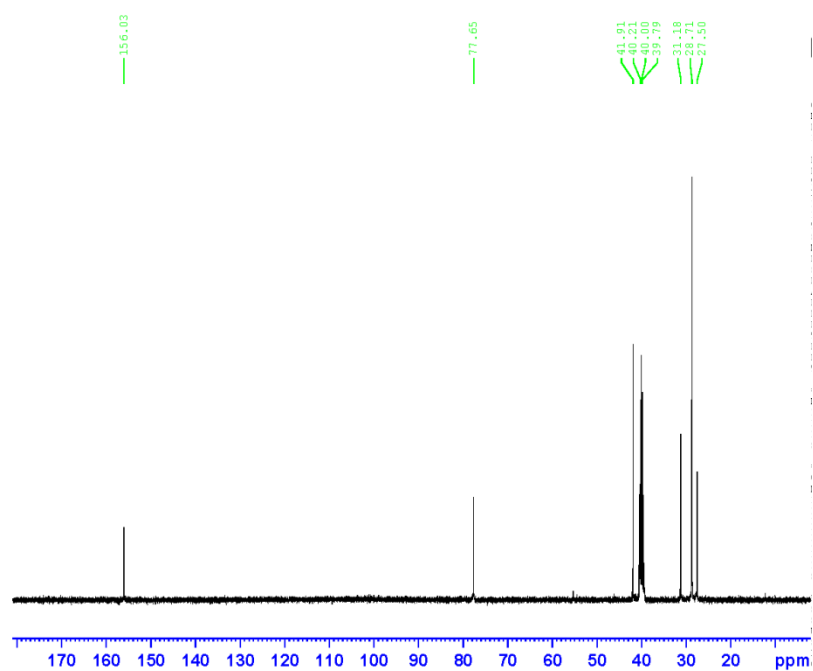


Figure 6- 6. ^{13}C NMR spectrum of compound 1b.

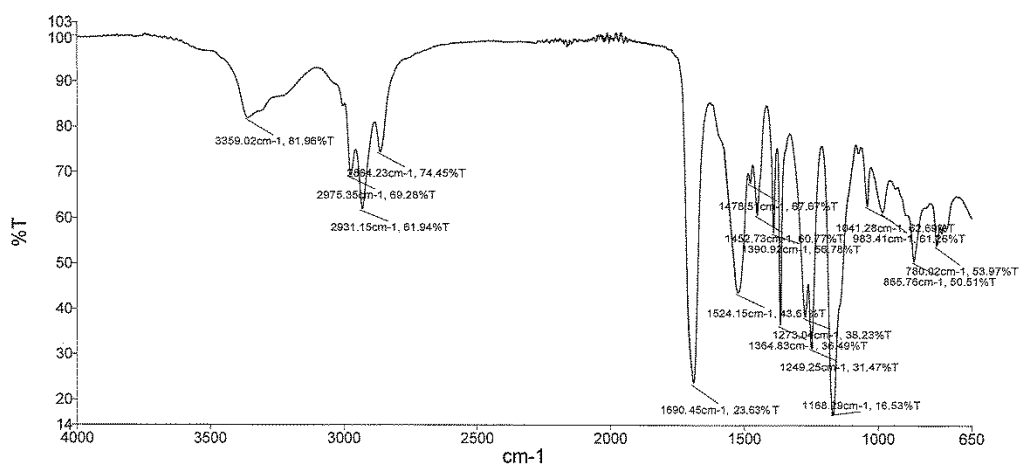
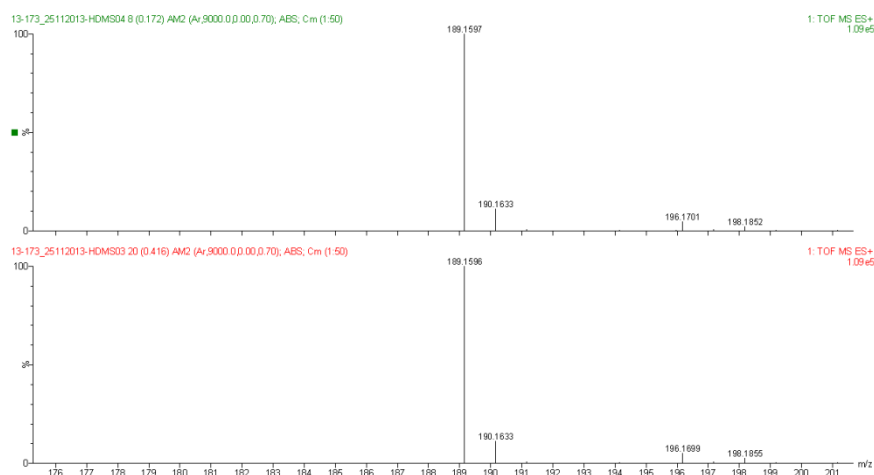


Figure 6- 7. FT-IR spectrum of compound 1b.

High Resolution Spectra Positive ion



Accurate Mass Data

Observed Mass	Formula $[M+H]^+$	Calculated mass	Difference (ppm)	iFit (norm)
189.1596	$\text{C}_9\text{H}_{21}\text{N}_2\text{O}_2$	189.1603	-3.7	0.0
189.1597	$\text{C}_9\text{H}_{21}\text{N}_2\text{O}_2$	189.1603	-3.2	0.0

Figure 6- 8. Mass spectra of compound 1b.

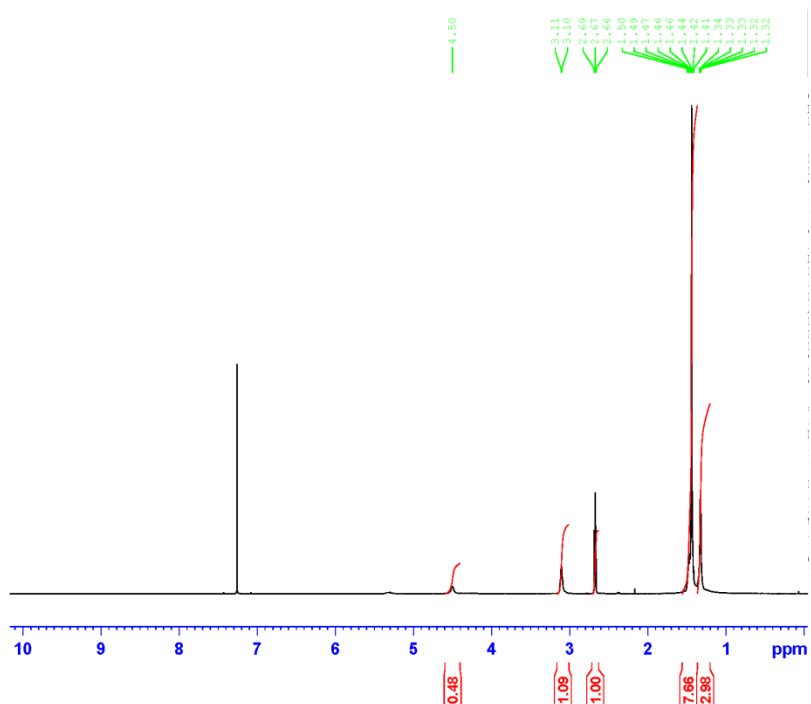


Figure 6- 9. ¹H NMR spectrum of compound 1c.

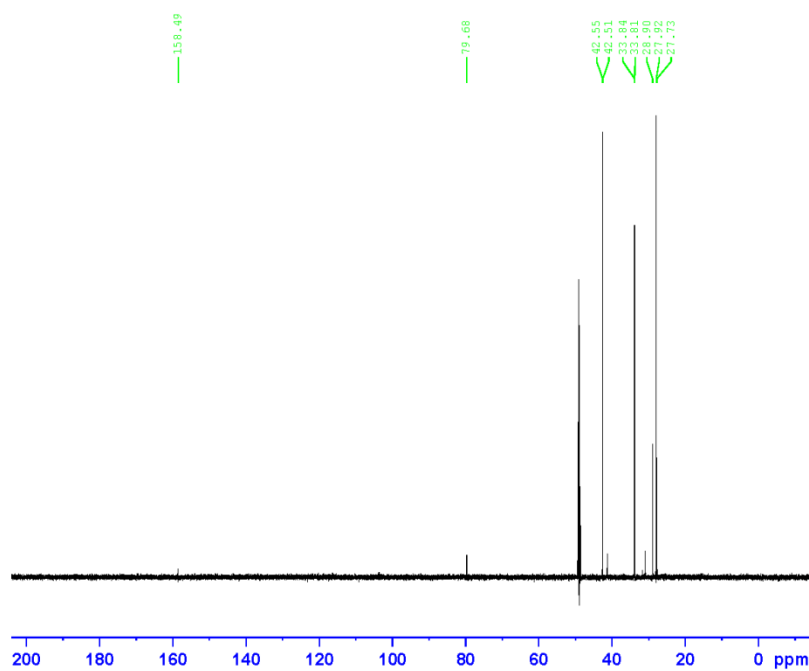


Figure 6- 10. ¹³C NMR spectrum of compound 1c.

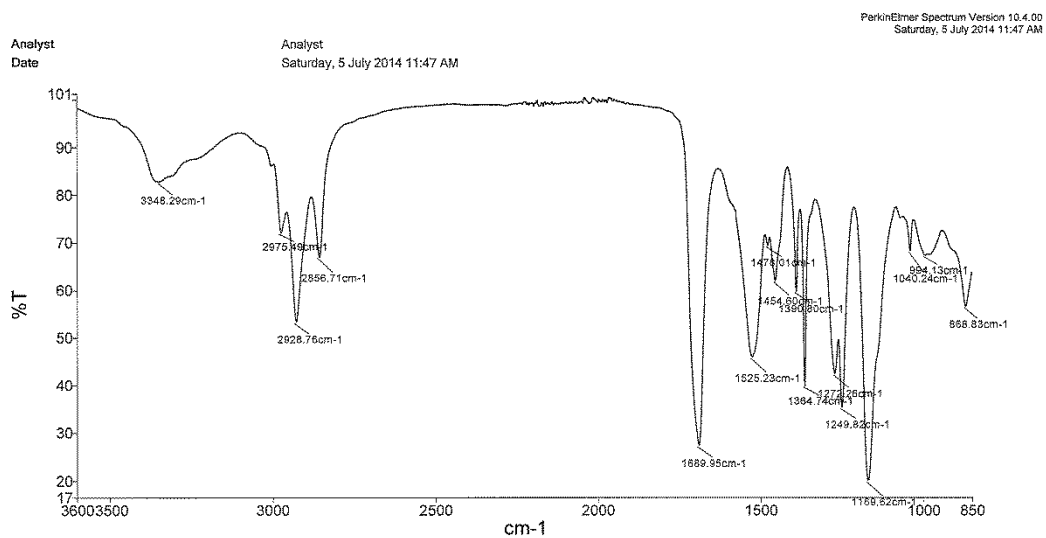
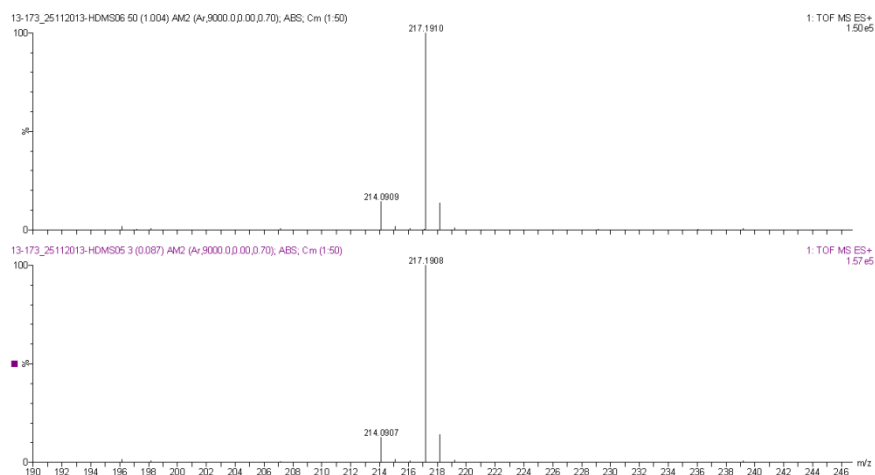


Figure 6- 11. FT-IR spectrum of compound 1c.

High Resolution Spectra Positive ion



Accurate Mass Data

Observed Mass	Formula [M+H] ⁺	Calculated mass	Difference (ppm)	iFit (norm)
217.1908	C ₁₁ H ₂₅ N ₂ O ₂	217.1916	-3.7	0.1
217.1910	C ₁₁ H ₂₅ N ₂ O ₂	217.1916	-2.8	0.0

Figure 6- 12. Mass spectra of compound 1c.

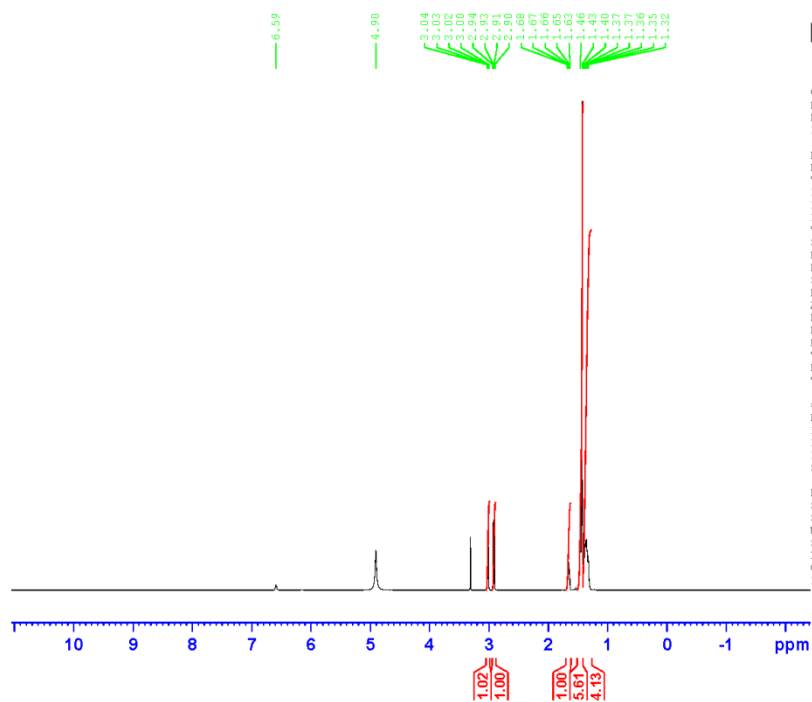


Figure 6- 13. ¹H NMR spectrum of compound 1d.

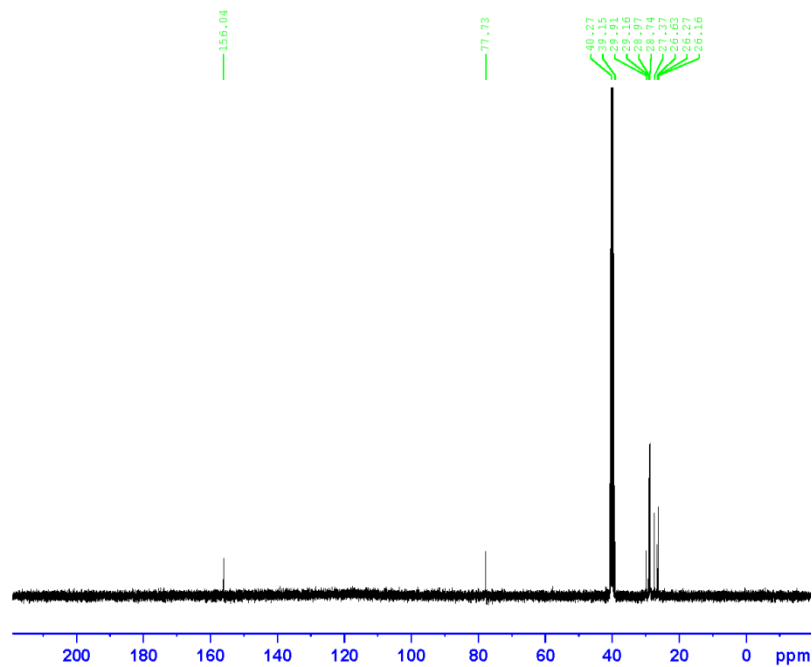


Figure 6- 14. ¹³C NMR spectrum of compound 1d.

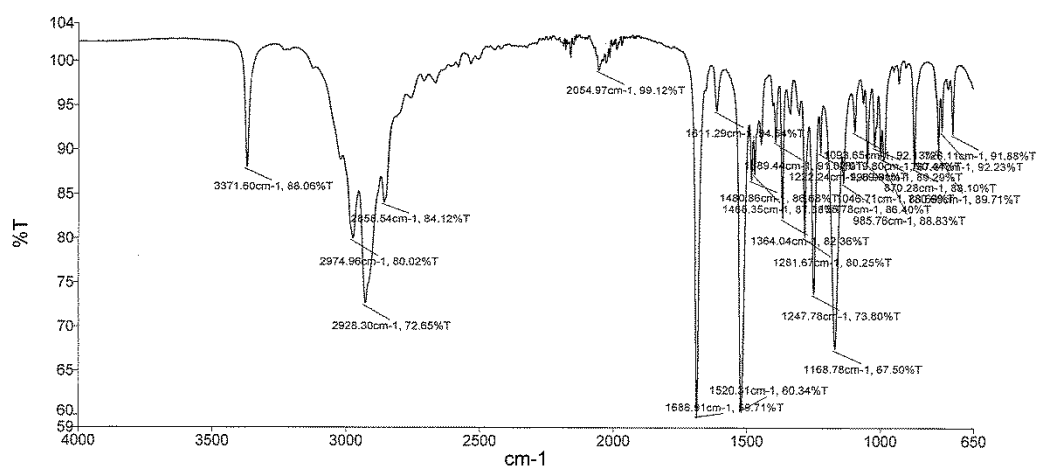
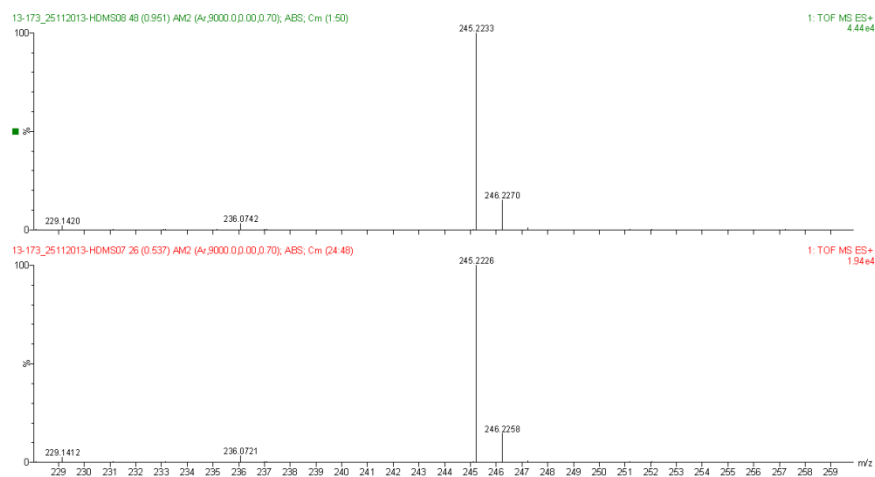


Figure 6- 15. FT-IR spectrum of compound 1d.

High Resolution Spectra Positive ion



Accurate Mass Data

Observed Mass	Formula [M+H] ⁺	Calculated mass	Difference (ppm)	iFit (norm)
245.2226	C ₁₃ H ₂₉ N ₂ O ₂	245.2229	-1.2	2.7
245.2233	C ₁₃ H ₂₉ N ₂ O ₂	245.2229	1.6	1.2

Figure 6- 16. Mass spectra of compound 1d.

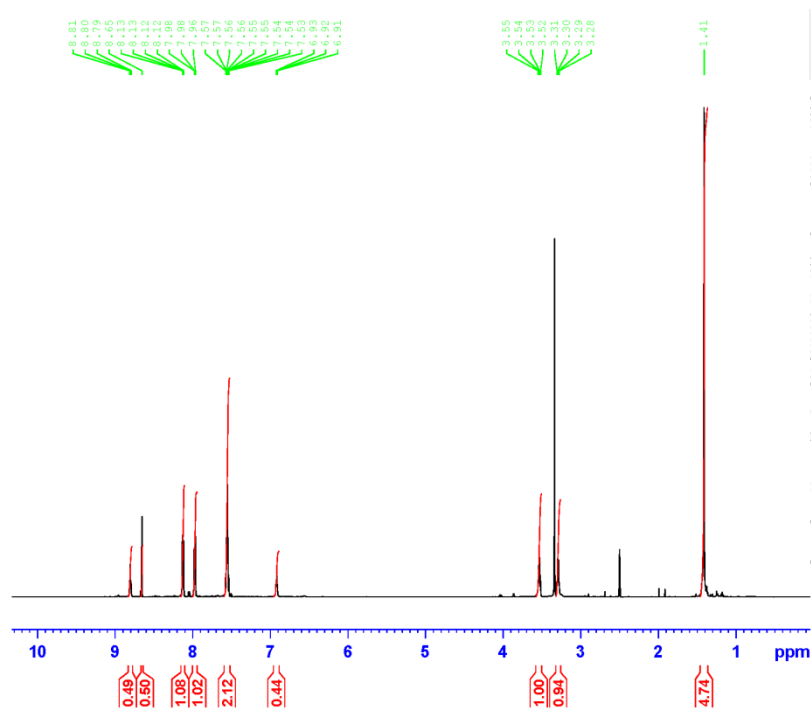


Figure 6- 17. ¹H NMR spectrum of compound 2a.

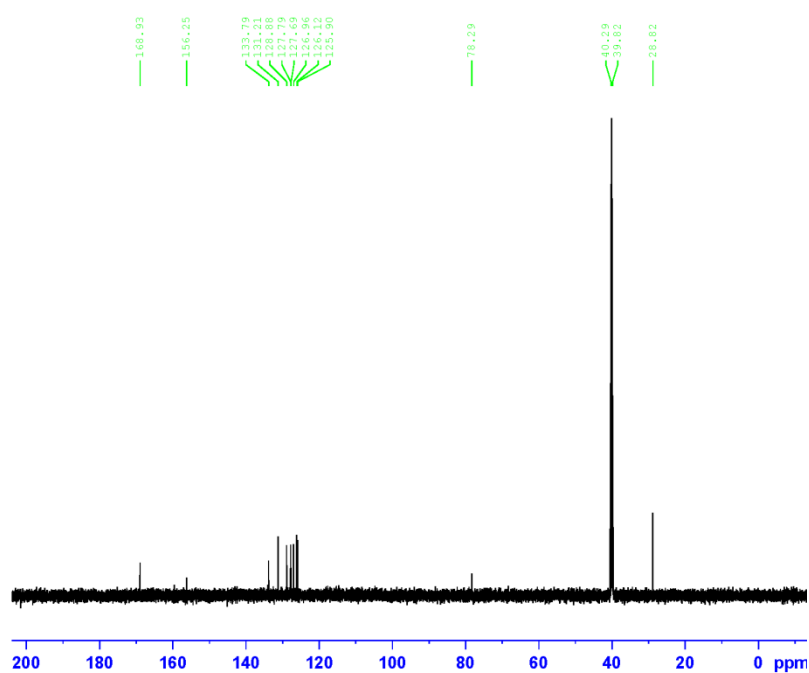


Figure 6- 18. ¹³C NMR spectrum of compound 2a.

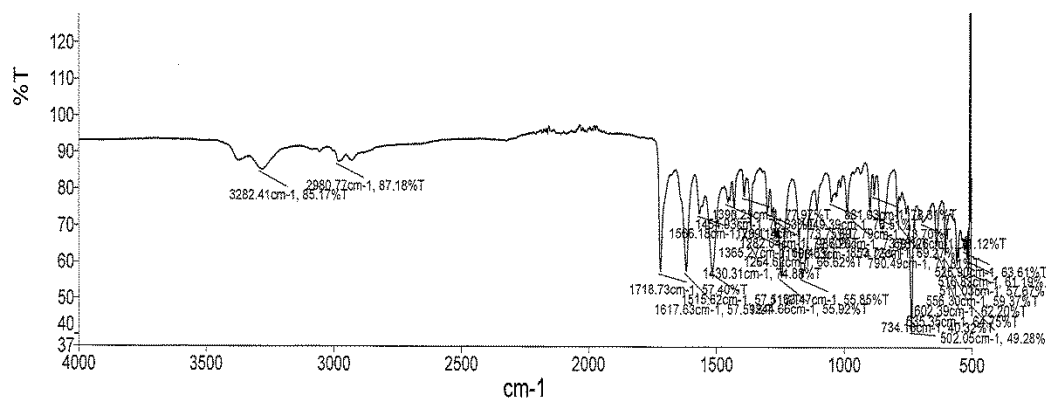
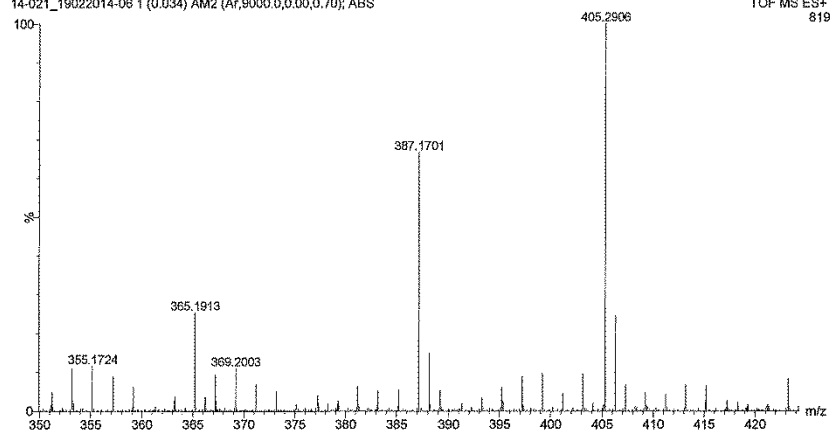


Figure 6- 19. FT-IR spectrum of compound 2a

High Resolution Spectra Positive ion

14-021_19022014-06 1 (0.034) AM2 (Ar,9000.0,0.00,0.70); ABS



Accurate Mass Data

Observed Mass	Formula [M+Na] ⁺	Calculated mass	Difference (ppm)	iFit (norm)
387.1699	C ₂₂ H ₂₄ N ₂ O ₃ Na	387.1685	3.6	2.8

Figure 6- 20. Mass spectra of compound 2a.

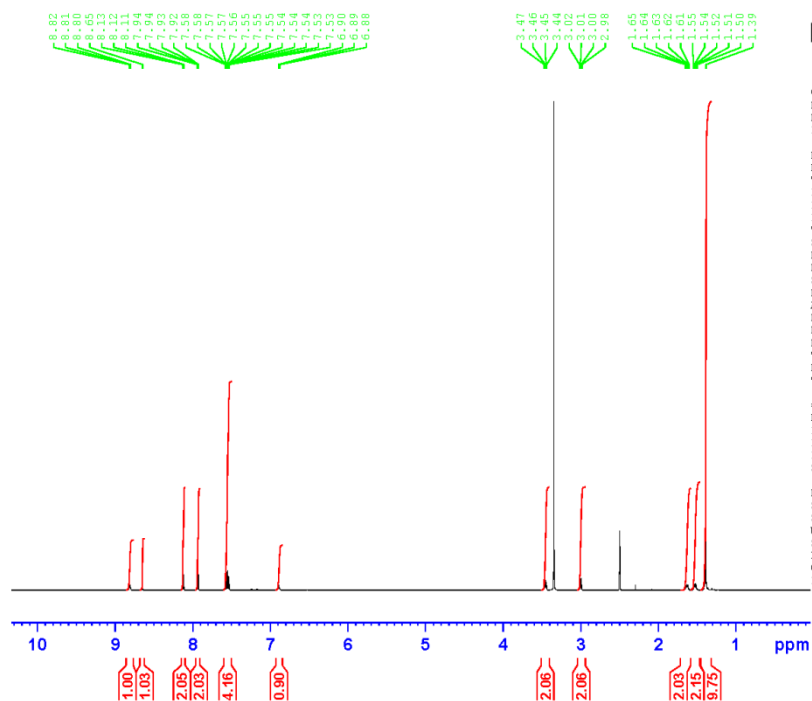


Figure 6- 21. ¹H NMR spectrum of compound 2b.

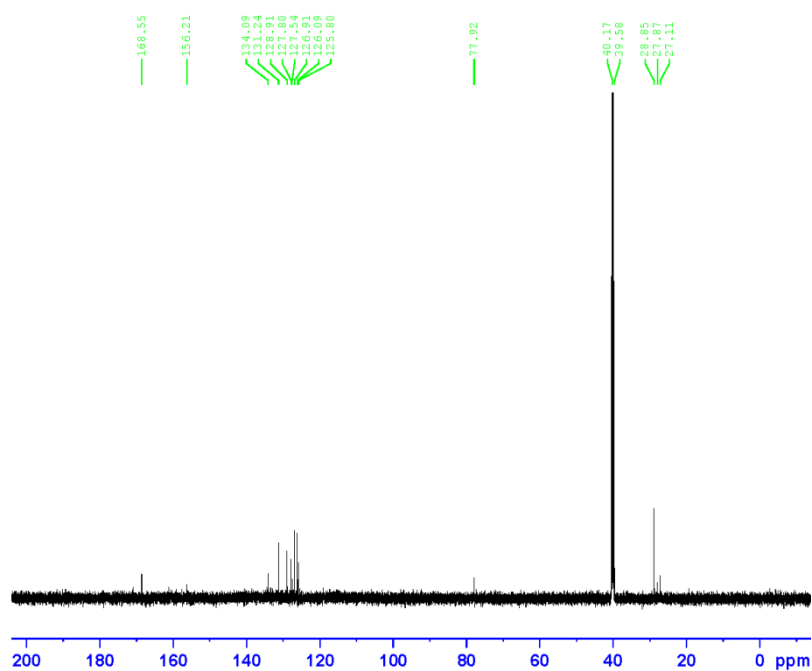


Figure 6- 22. ¹³C NMR spectrum of compound 2b.

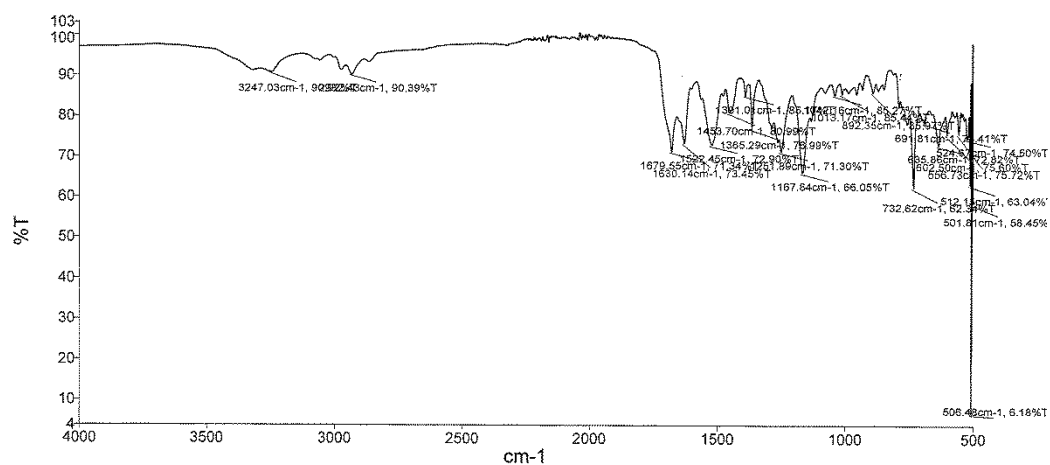
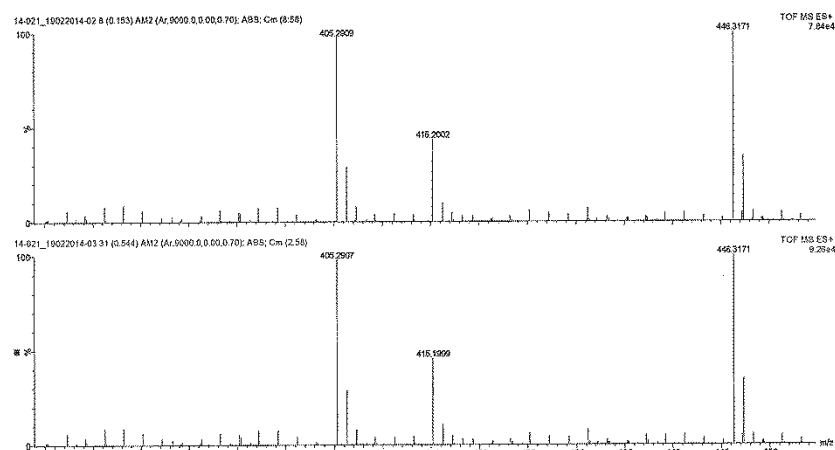


Figure 6- 23. FT-IR spectrum of compound 2b.

High Resolution Spectra Positive ion



Accurate Mass Data

Observed Mass	Formula [M+Na] ⁺	Calculated mass	Difference (ppm)	iFit (norm)
415.1999	C ₂₄ H ₂₈ N ₂ O ₃ Na	415.1998	0.2	3.5
415.2002	C ₂₄ H ₂₈ N ₂ O ₃ Na	415.1998	1.0	3.6

Figure 6- 24. Mass spectra of compound 2b.

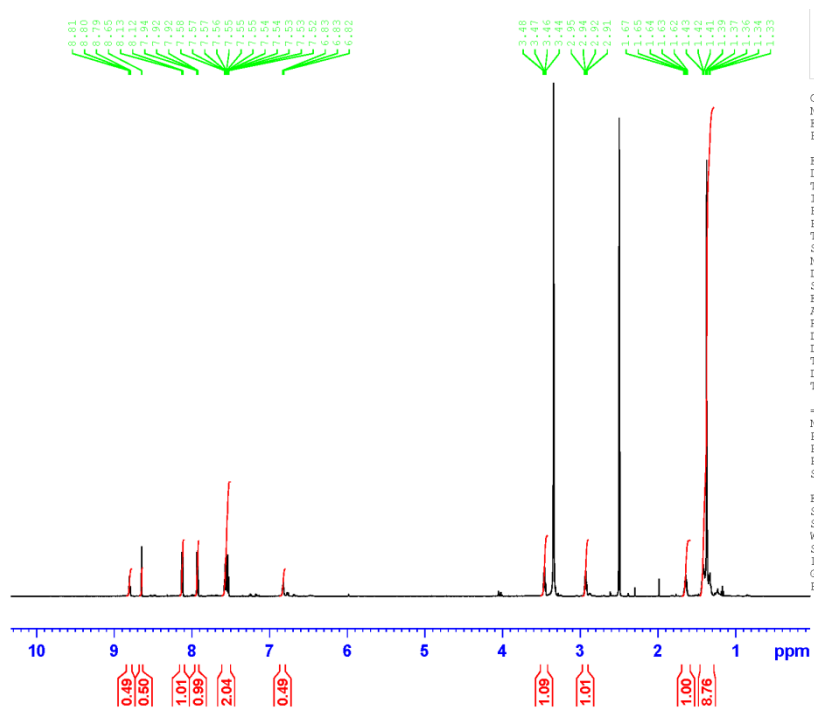


Figure 6- 25. ¹H NMR spectrum of compound 2c.

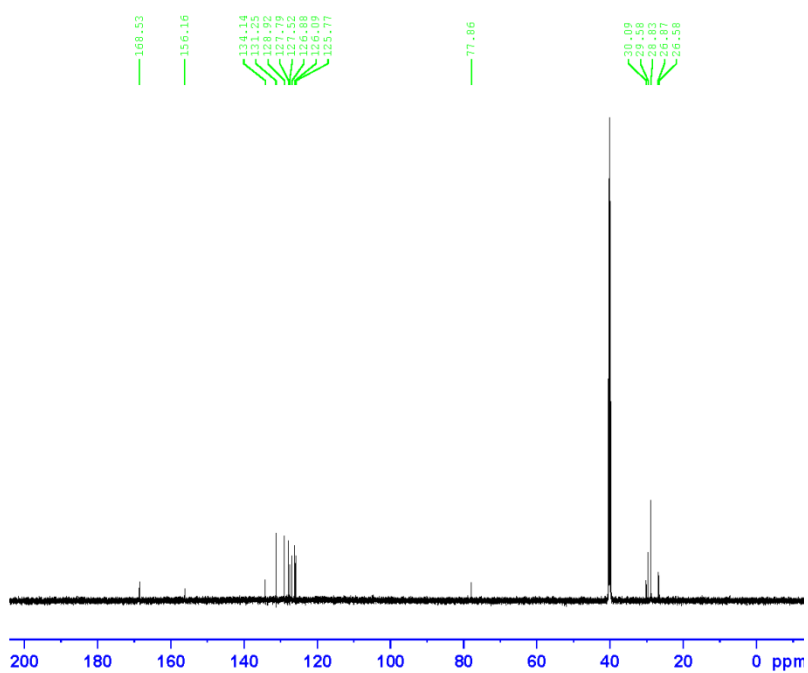


Figure 6- 26. ¹³C NMR spectrum of compound 2c.

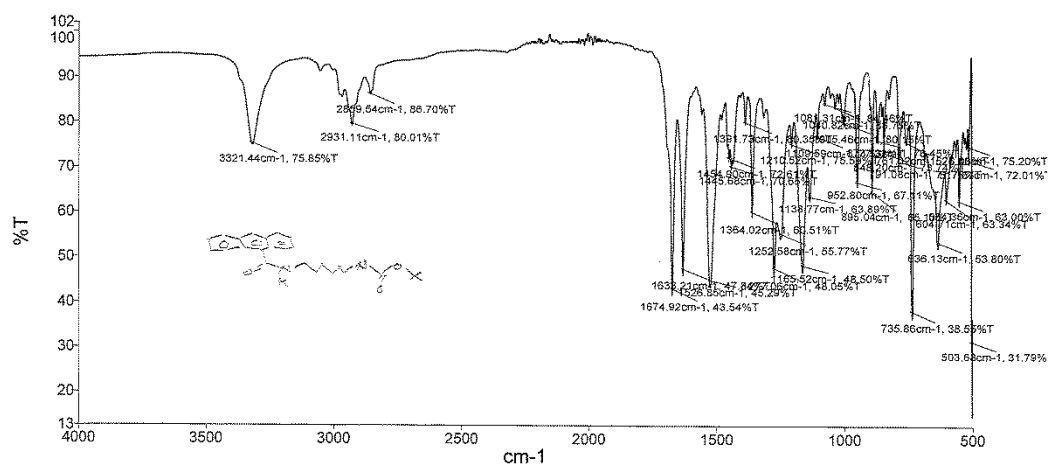
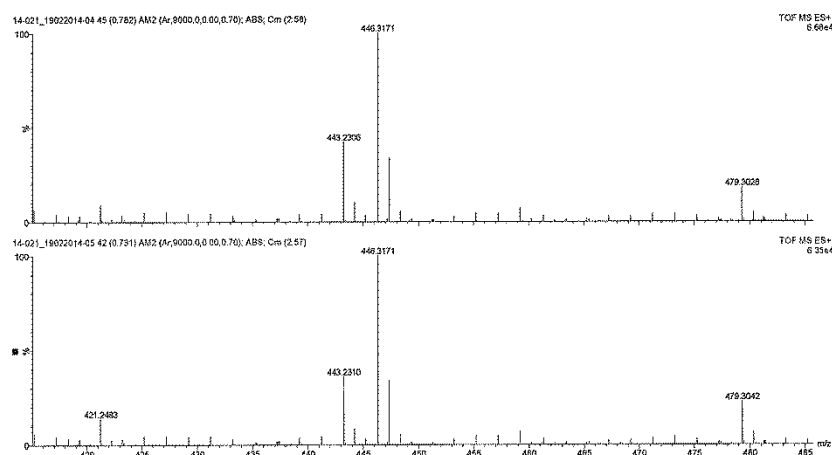


Figure 6- 27. FT-IR spectrum of compound 2c.

High Resolution Spectra Positive ion



Accurate Mass Data

Observed Mass	Formula [M+Na] ⁺	Calculated mass	Difference (ppm)	iFIT (norm)
443.2310	C ₂₆ H ₃₂ N ₂ O ₃ Na	443.2311	-0.2	4.6
443.2306	C ₂₆ H ₃₂ N ₂ O ₃ Na	443.2311	-1.1	5.0

Figure 6- 28. Mass spectra of compound 2c.

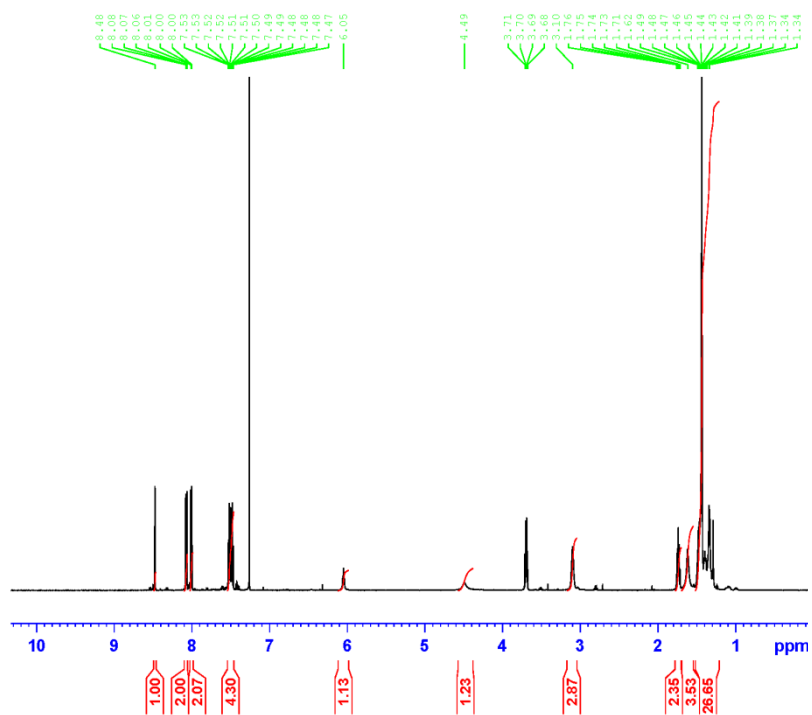


Figure 6- 29. ¹H NMR spectrum of compound 2d.

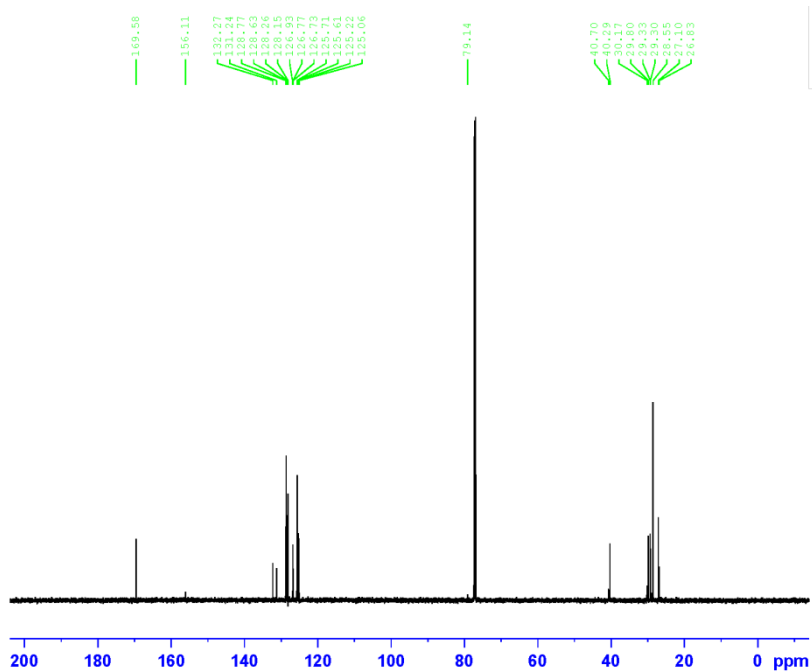


Figure 6- 30. ¹³C NMR spectrum of compound 2d.

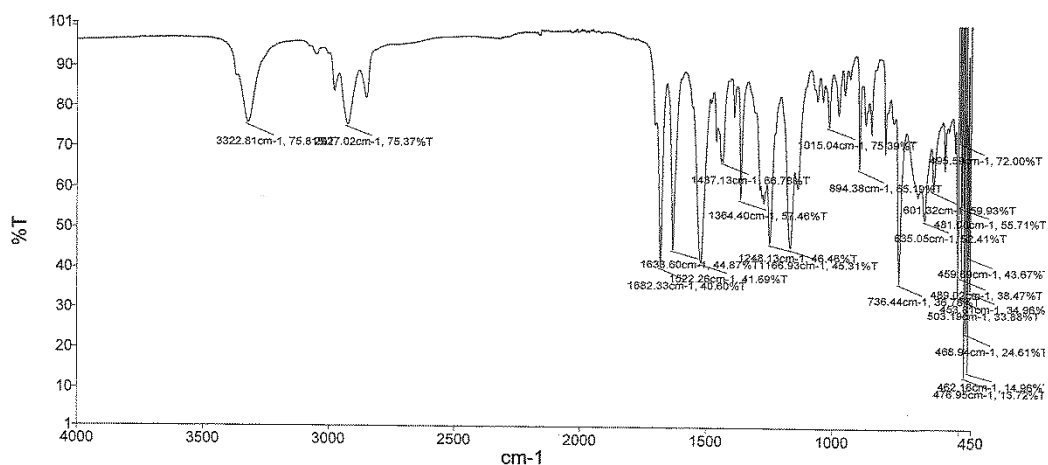
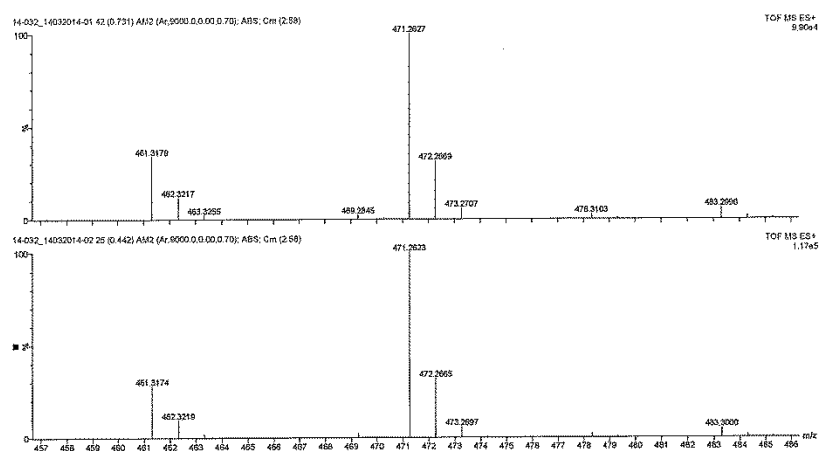


Figure 6- 31. FT-IR spectrum of compound 2d.

High Resolution Spectra Positive ion



Accurate Mass Data

Observed Mass	Formula [M+Na]⁺	Calculated mass	Difference (ppm)	IFit (norm)
471.2623	C ₂₈ H ₃₆ N ₂ O ₃ Na	471.2624	-0.2	3.3
471.2627	C ₂₈ H ₃₆ N ₂ O ₃ Na	471.2624	0.6	3.6

Figure 6- 32. Mass spectra of compound 2d.

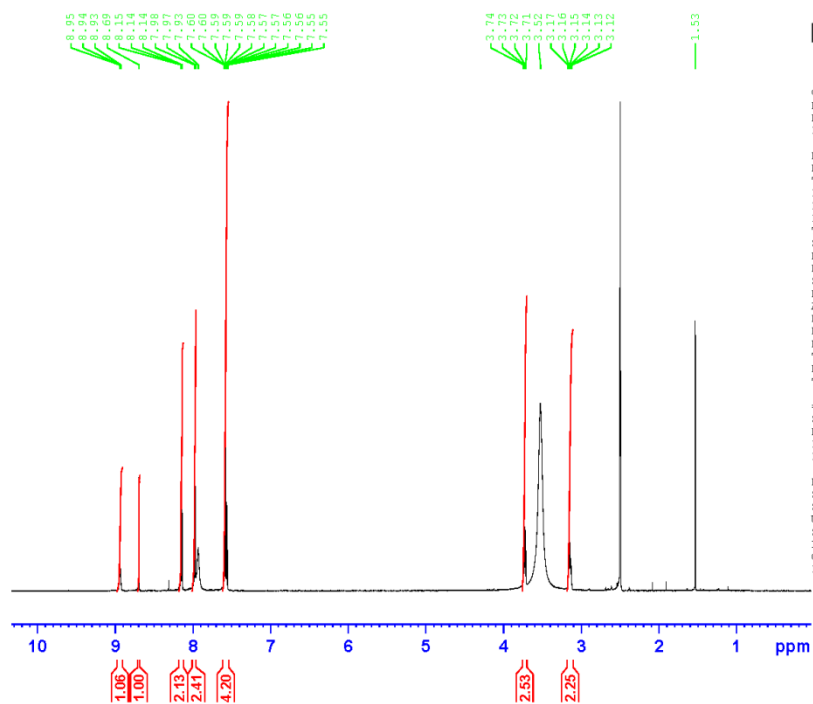


Figure 6- 33. ¹H NMR spectrum of compound 3a.

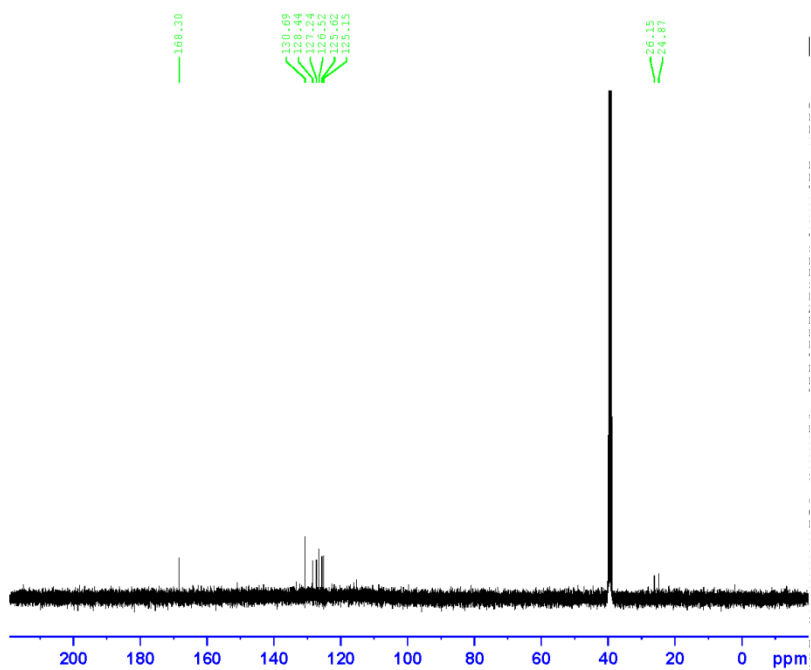


Figure 6- 34. ¹³C NMR spectrum of compound 3a.

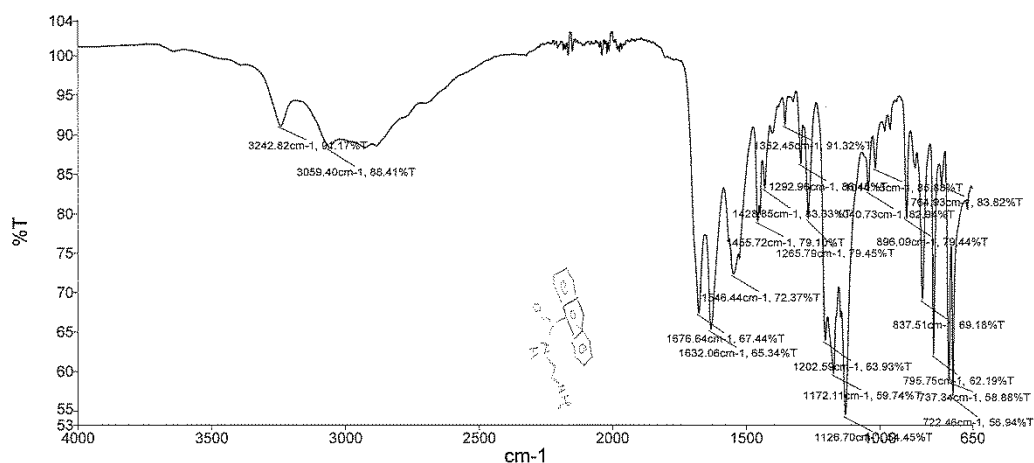
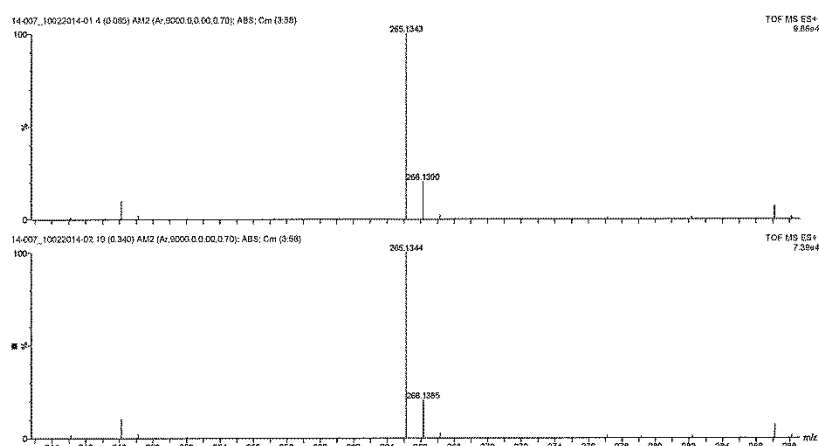


Figure 6- 35. FT-IR spectrum of compound 3a.

High Resolution Spectra Positive ion



Accurate Mass Data

Observed Mass	Formula [M+H] ⁺	Calculated mass	Difference (ppm)	iFIT (norm)
265.1344	C ₁₇ H ₁₇ N ₂ O	265.1341	1.1	5.5
265.1343	C ₁₇ H ₁₇ N ₂ O	265.1341	0.8	0.2

Figure 6- 36. Mass spectra of compound 3a.

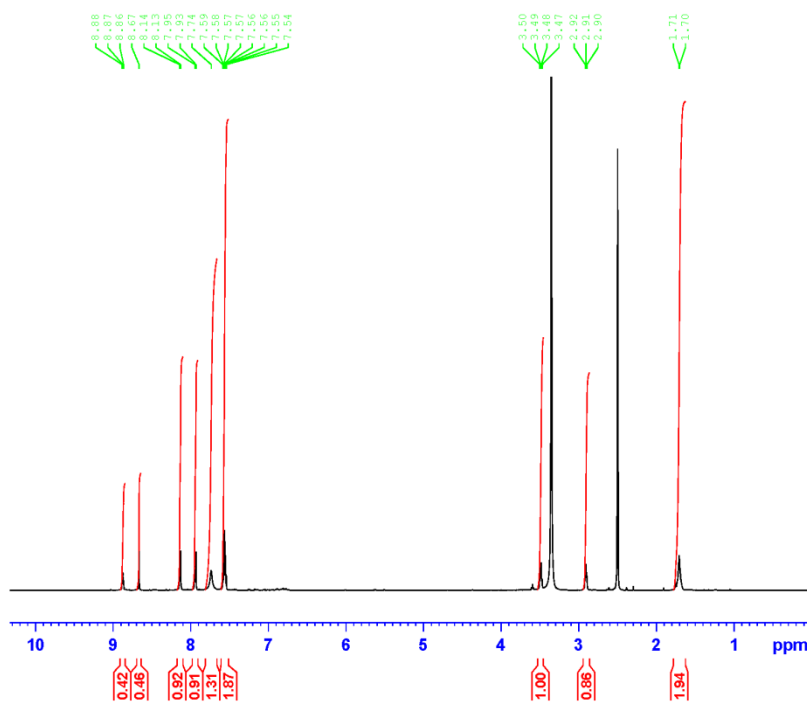


Figure 6- 37. ¹H NMR spectrum of compound 3b.

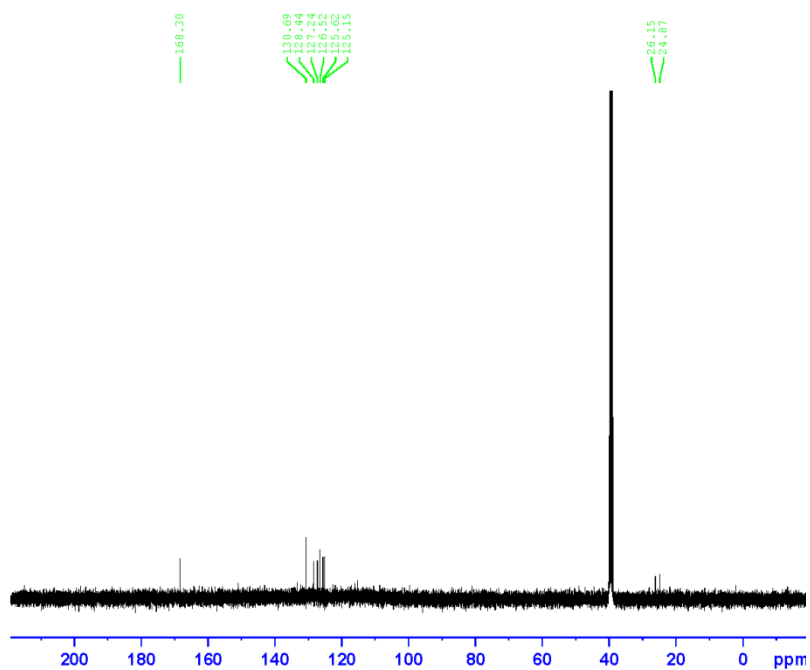


Figure 6- 38. ¹³C NMR spectrum of compound 3b.

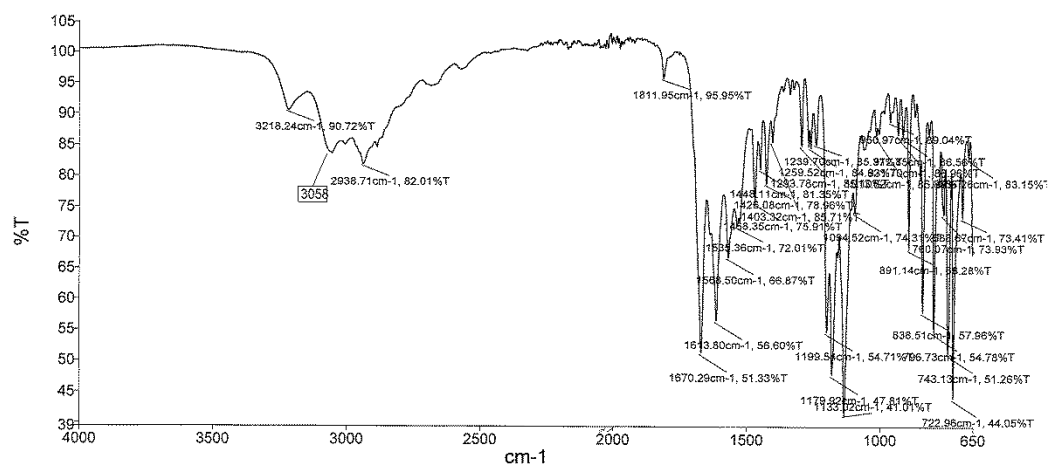


Figure 6- 39. FT-IR spectrum of compound 3b.

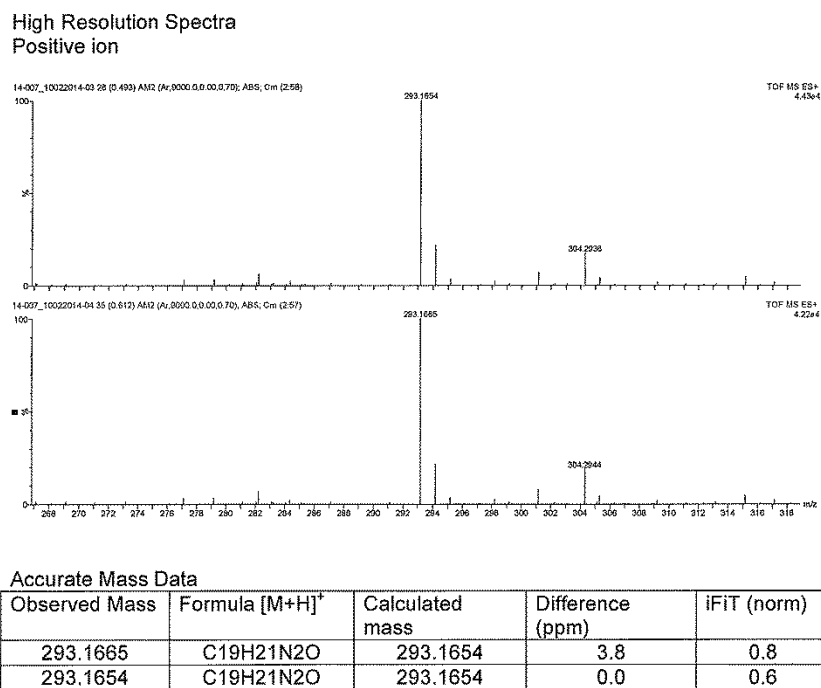


Figure 6- 40. Mass spectra of compound 3b.

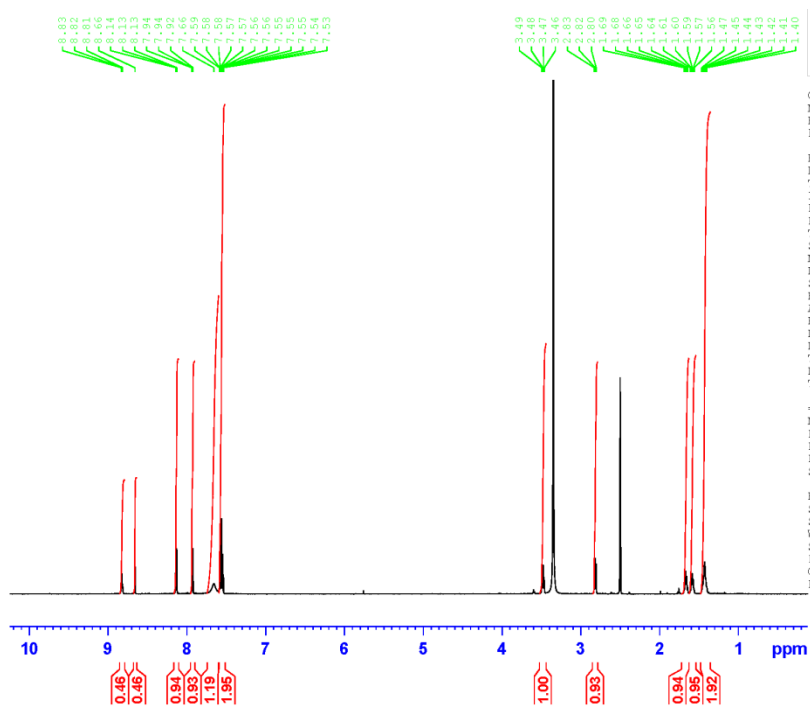


Figure 6- 41. ¹H NMR spectrum of compound 3c.

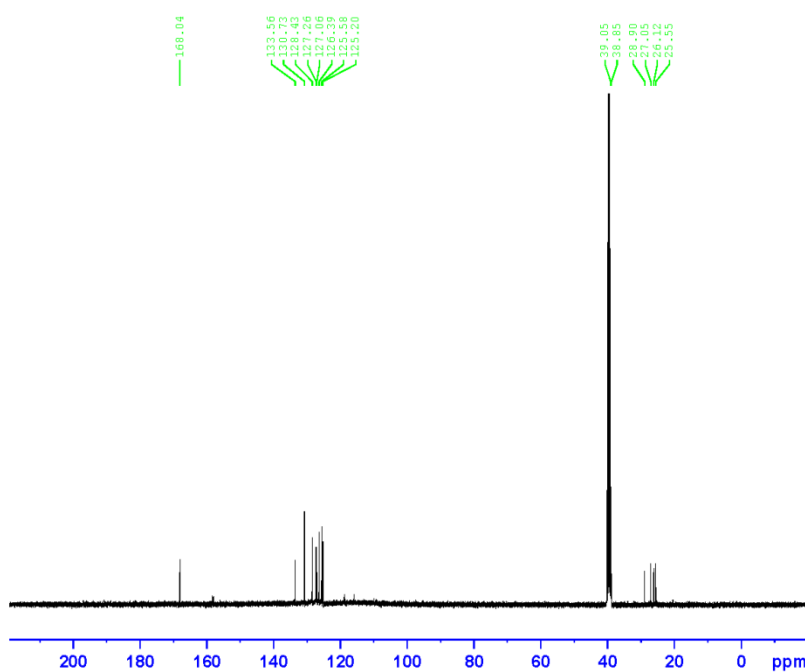


Figure 6- 42. ¹³C NMR spectrum of compound 3c.

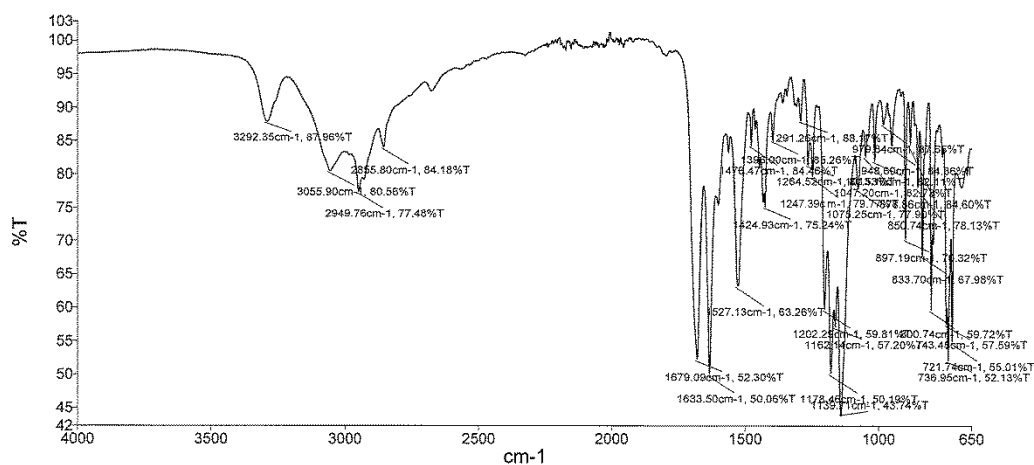
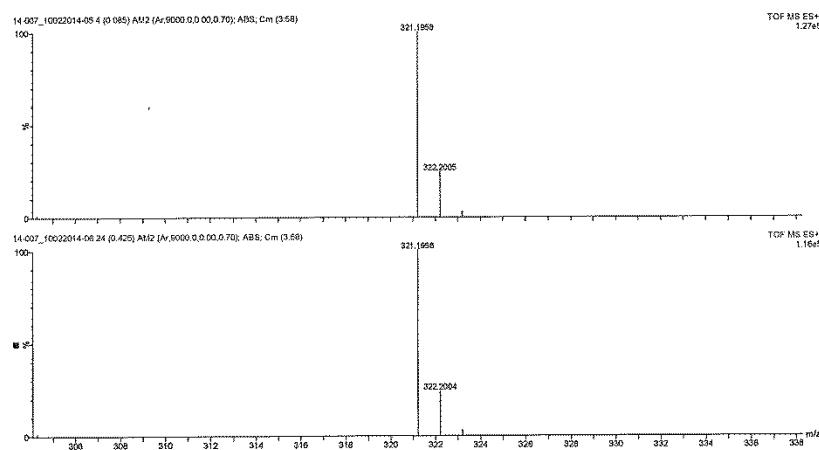


Figure 6- 43. FT-IR spectrum of compound 3c.

High Resolution Spectra Positive ion



Accurate Mass Data

Observed Mass	Formula [M+H] ⁺	Calculated mass	Difference (ppm)	iFIT (norm)
321.1958	C ₂₁ H ₂₅ N ₂ O	321.1967	-2.8	0.1
321.1958	C ₂₁ H ₂₅ N ₂ O	321.1967	-2.8	0.0

Figure 6- 44. Mass spectra of compound 3c.

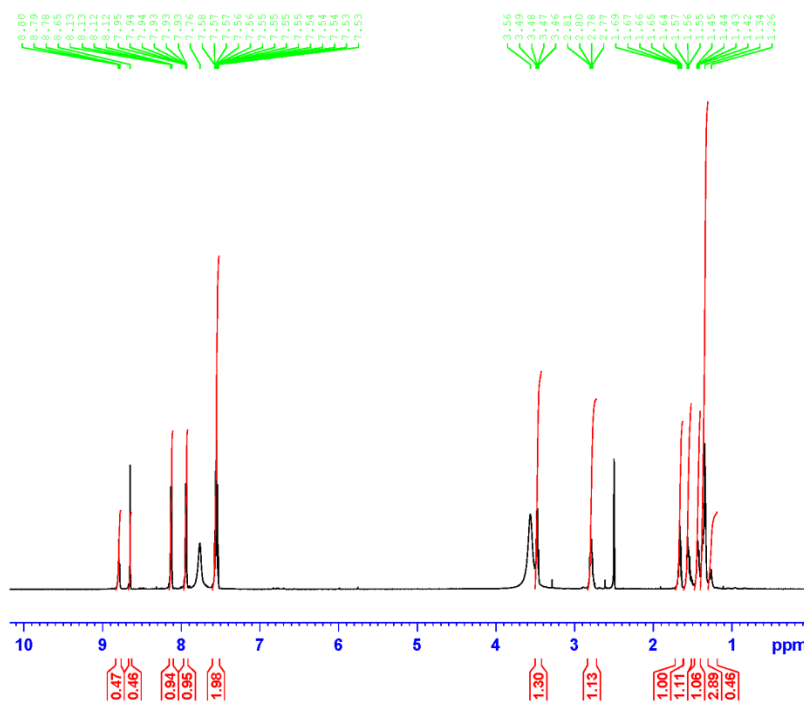


Figure 6- 45. ¹H NMR spectrum of compound 3d.

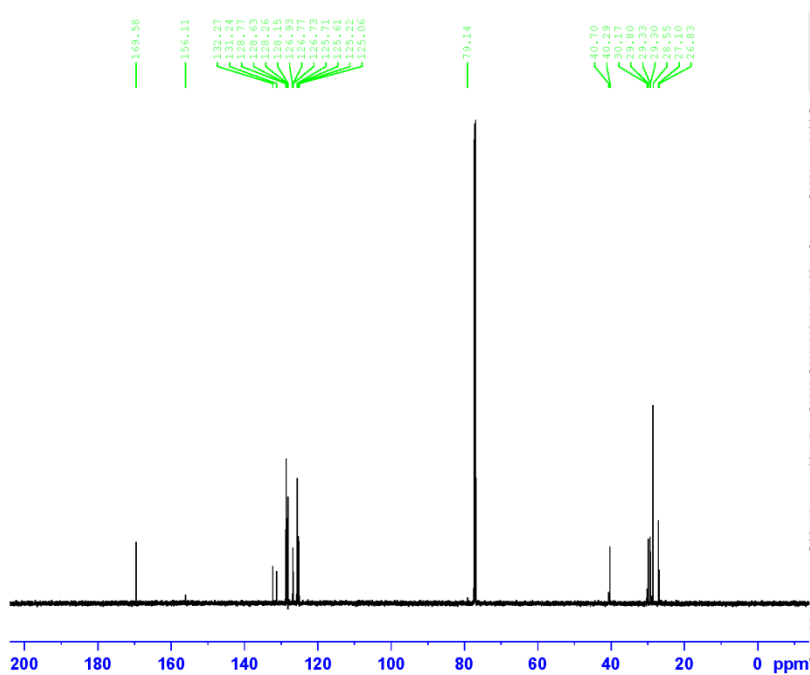


Figure 6- 46. ¹³C NMR spectrum of compound 3d.

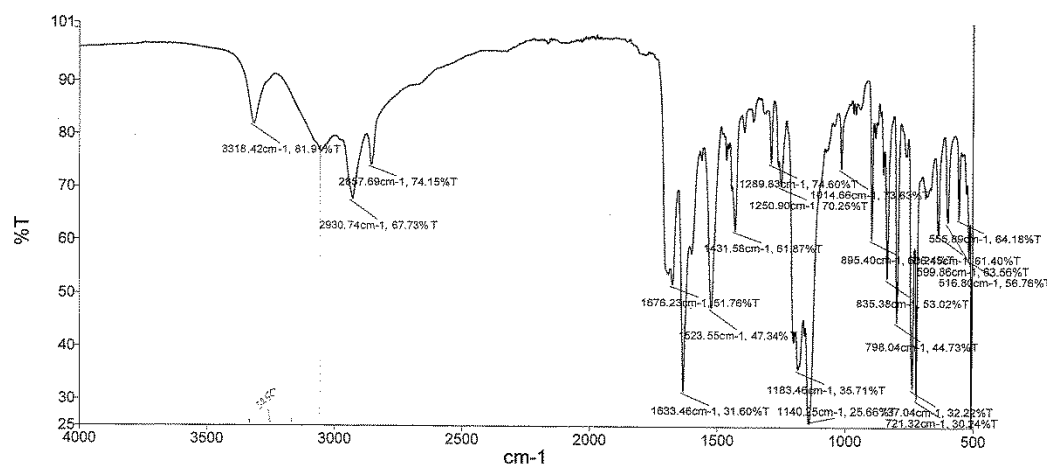
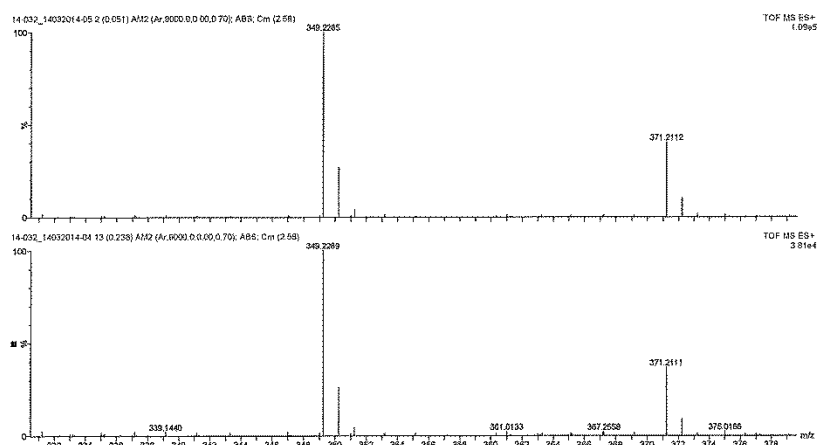


Figure 6- 47. FT-IR spectrum of compound 3d.

High Resolution Spectra Positive ion



Accurate Mass Data

Observed Mass	Formula [M+H] ⁺	Calculated mass	Difference (ppm)	iFit (norm)
349.2289	C ₂₃ H ₂₉ N ₂ O	349.2280	2.6	1.5
349.2285	C ₂₃ H ₂₉ N ₂ O	349.2280	1.4	0.6

Figure 6- 48. Mass spectra of compound 3d.

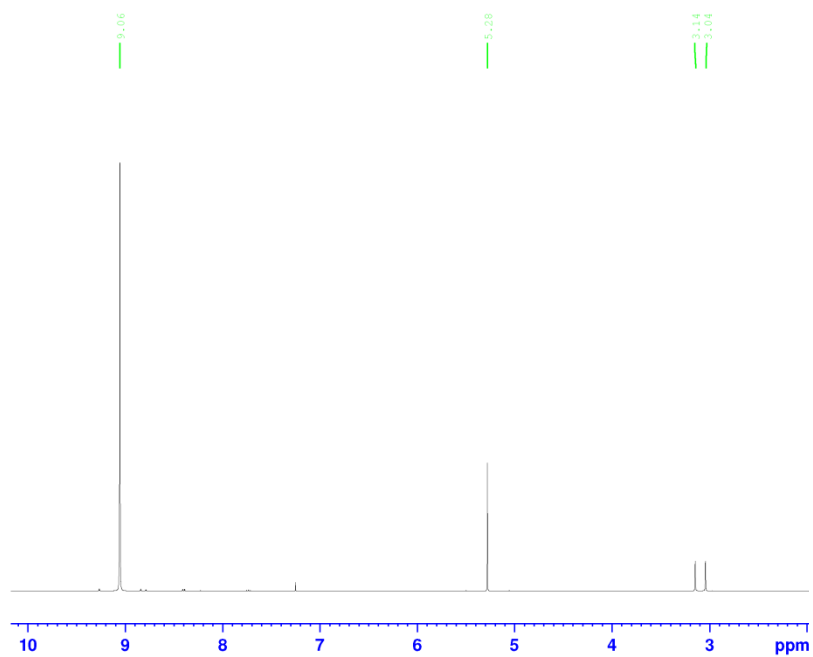


Figure 6- 49. ¹H NMR spectrum of compound 4.

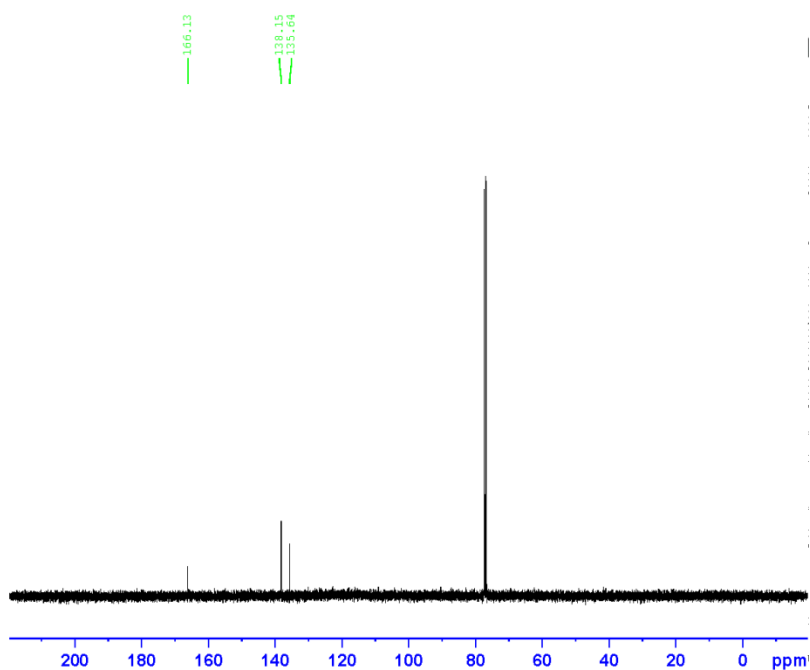


Figure 6- 50. ¹³C NMR spectrum of compound 4.

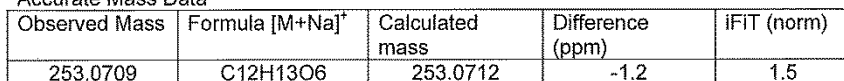


Figure 6- 52. Mass spectra of compound 4.

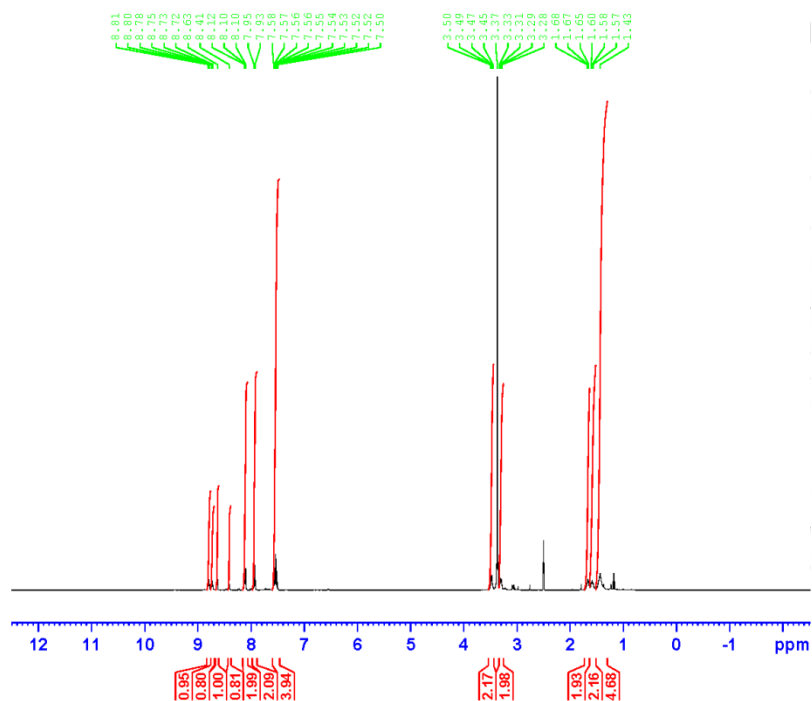


Figure 6- 55. ¹H NMR spectrum of compound 5c.

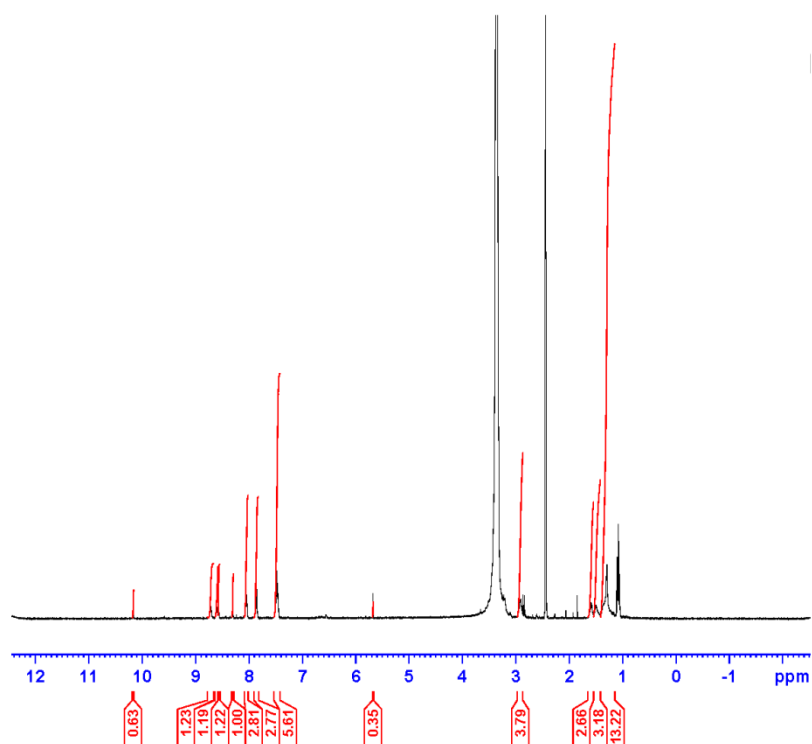


Figure 6- 56. ¹H NMR spectrum of compound 5d.

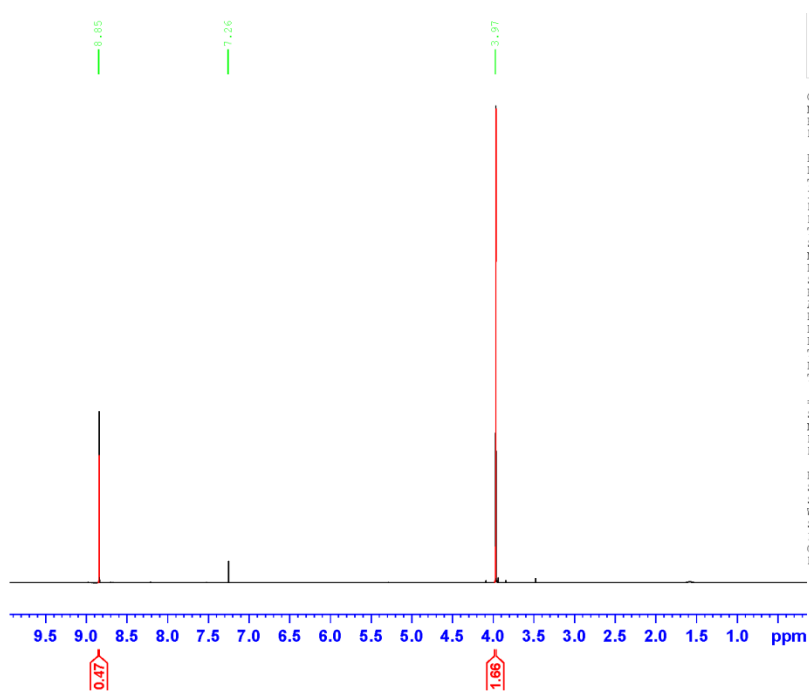


Figure 6- 57. ¹H NMR spectrum of compound 6.

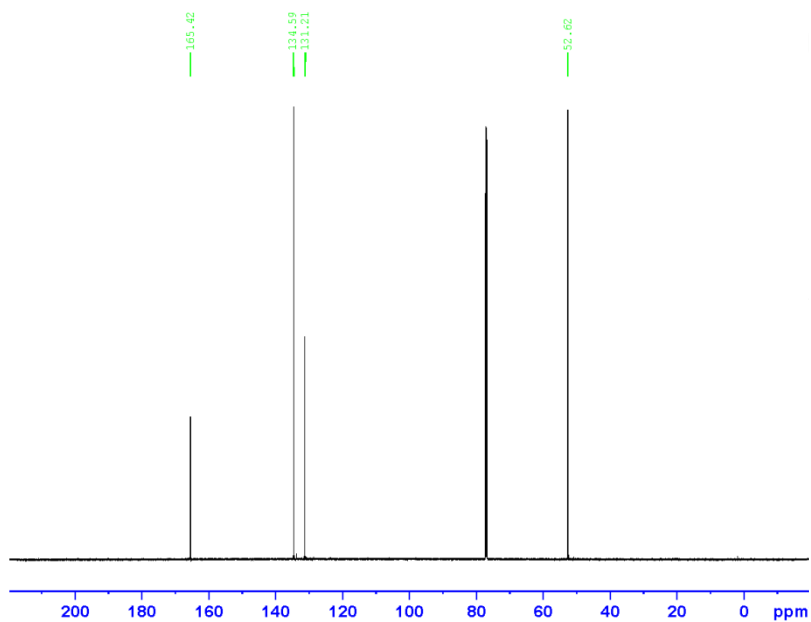


Figure 6- 58. ¹³C NMR spectrum of compound 6.

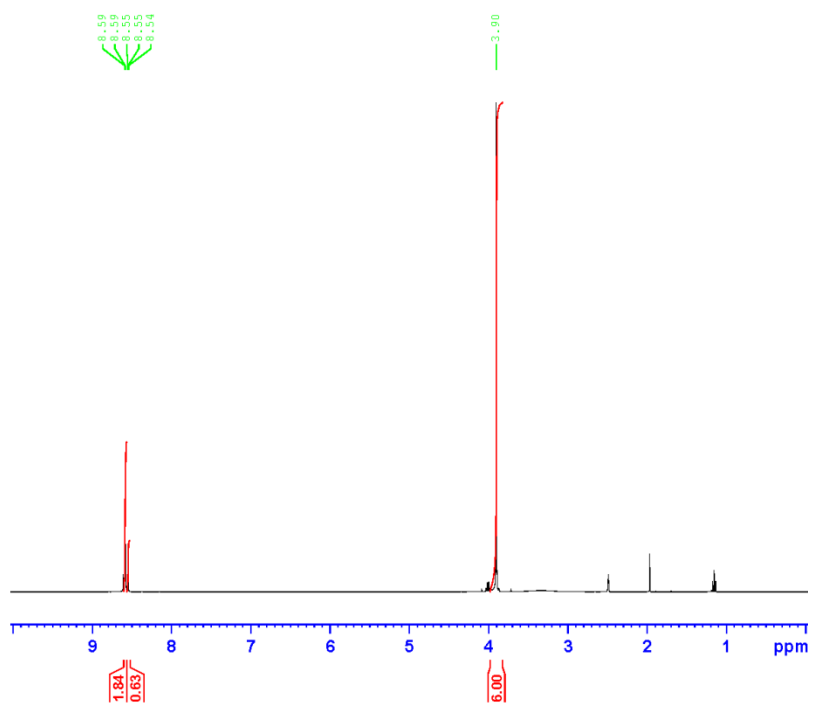


Figure 6- 61. ¹H NMR spectrum of compound 7.

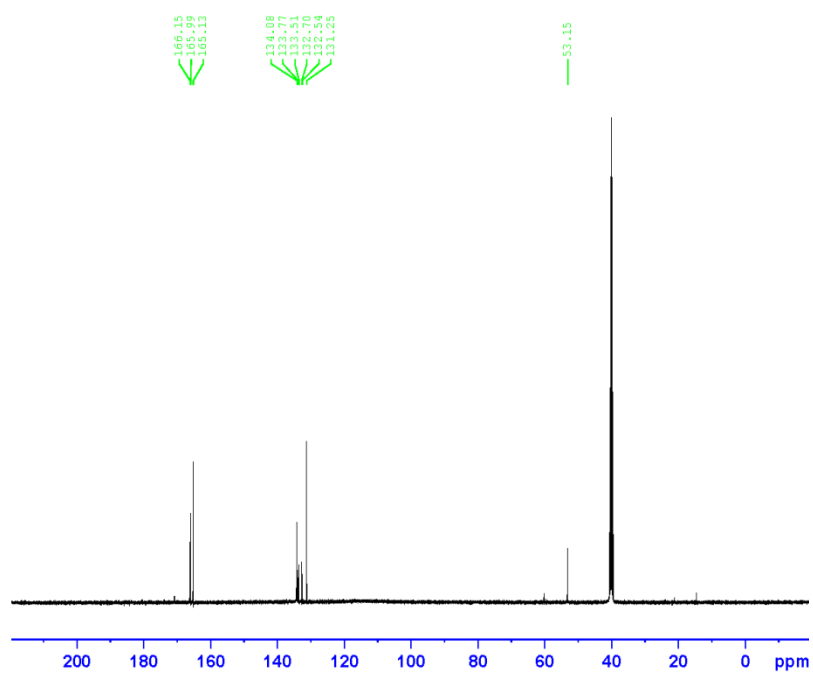


Figure 6- 62. ¹³C NMR spectrum of compound 7.

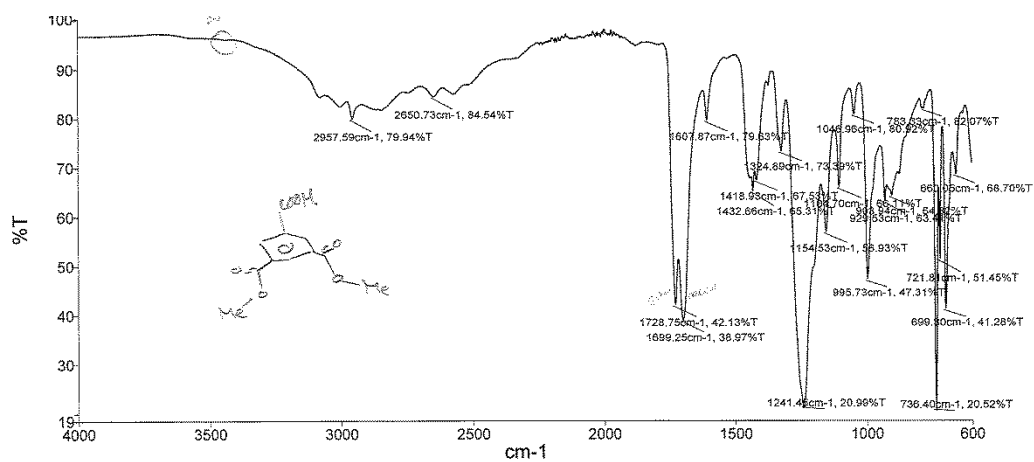
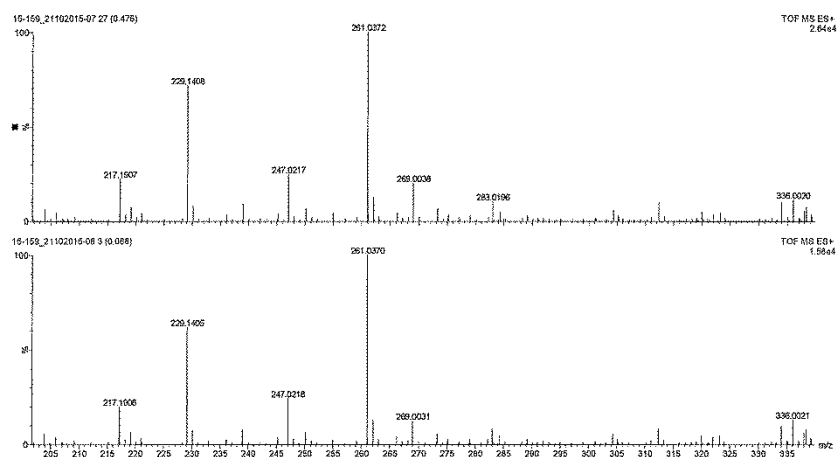


Figure 6- 63. FT-IR spectrum of compound 7.



Accurate Mass Data

Observed Mass	Formula [M+Na] ⁺	Calculated mass	Difference (ppm)	iFit (norm)
261.0370	C ₁₁ H ₁₀ O ₆ Na	261.0375	-1.9	0.7
261.0372	C ₁₁ H ₁₀ O ₆ Na	261.0375	-1.1	1.3

Figure 6- 64. Mass spectra of compound 7.

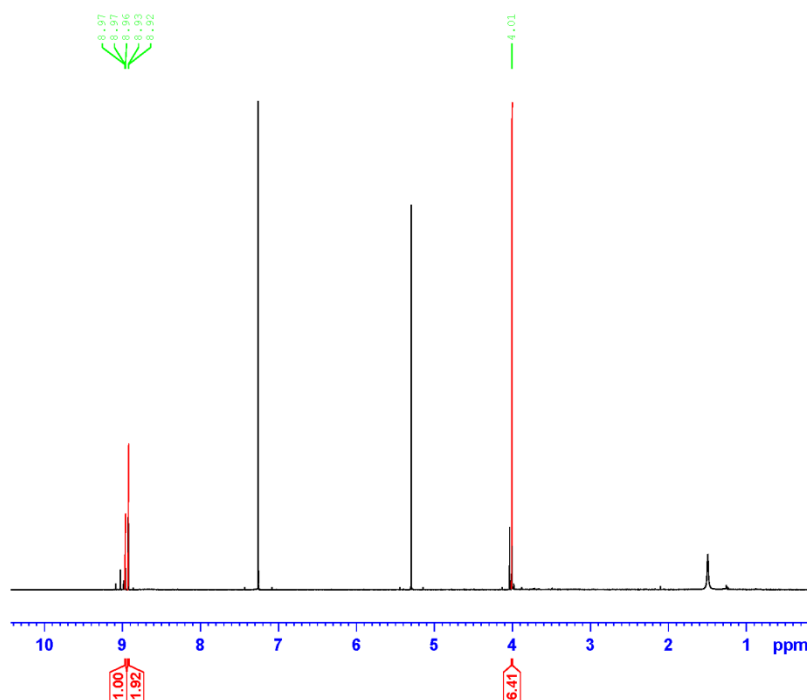


Figure 6- 65. ^1H NMR spectrum of compound 8.

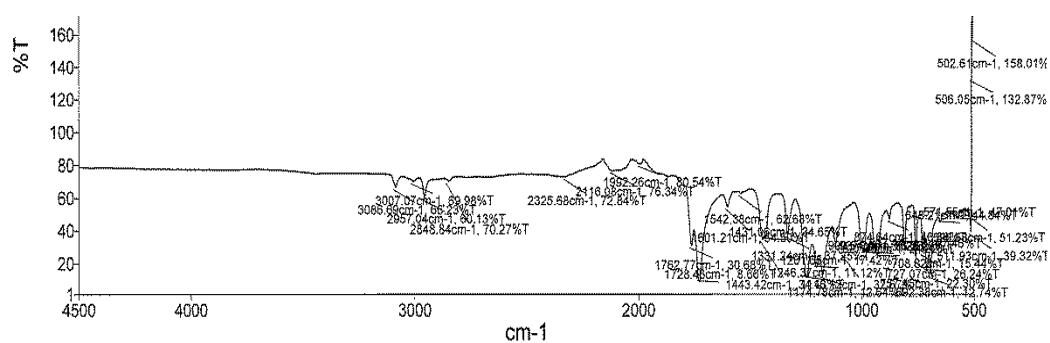


Figure 6- 66. FT-IR spectrum of compound 8.

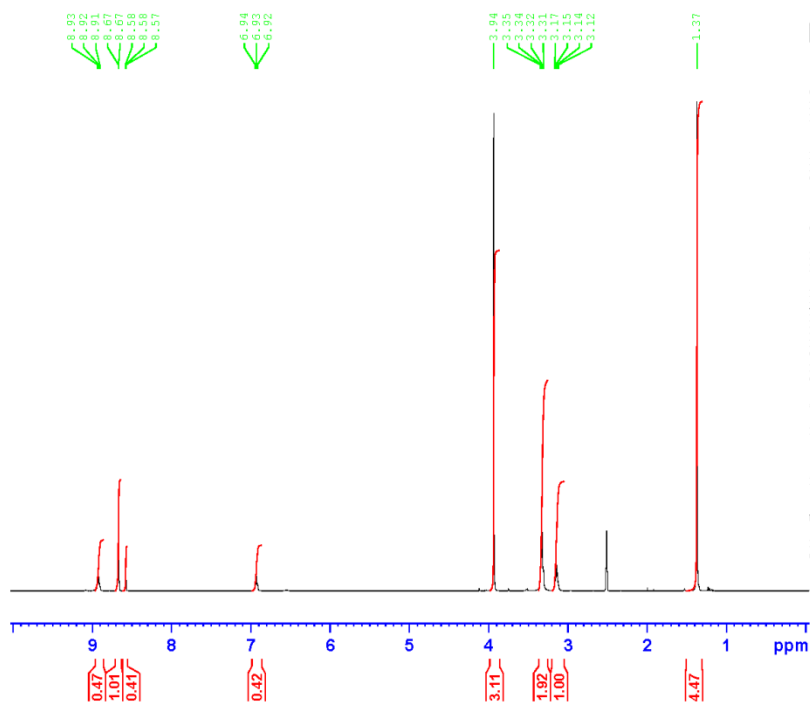


Figure 6- 67. ¹H NMR spectrum of compound 9a.

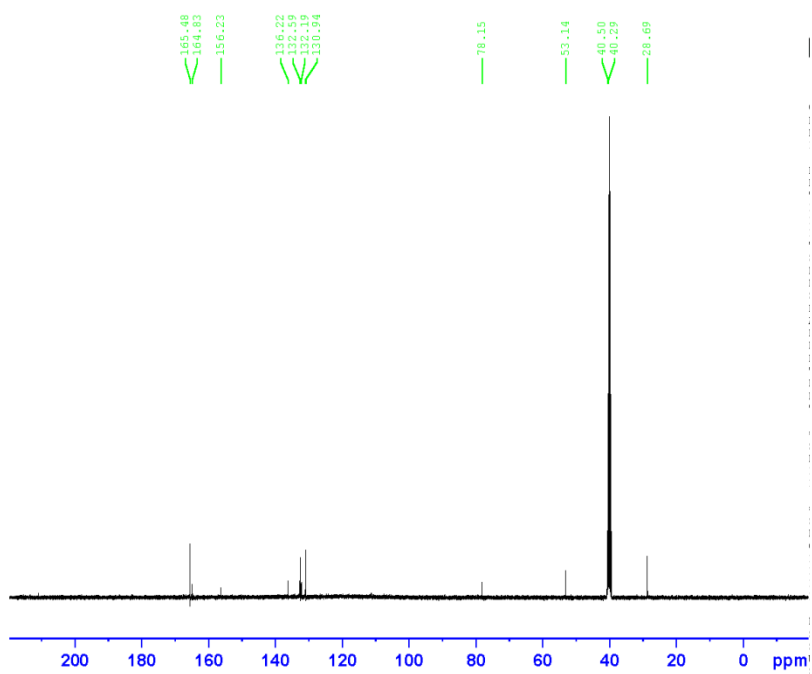


Figure 6- 68. ¹³C NMR spectrum of compound 9a.

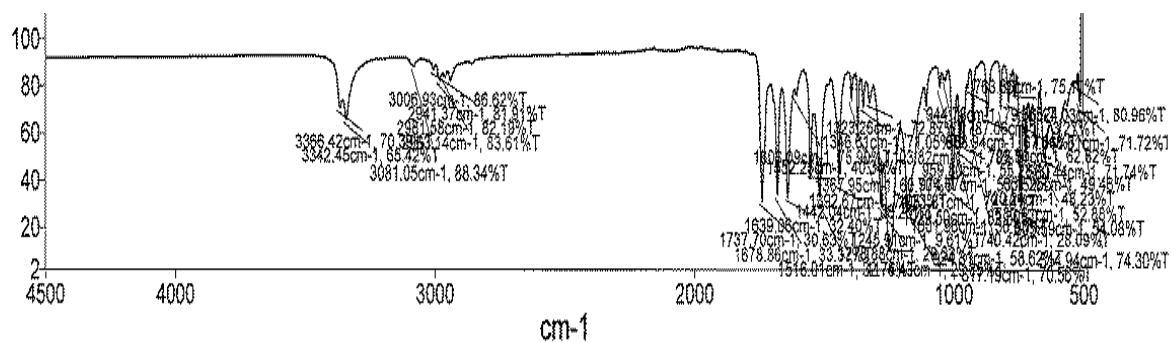
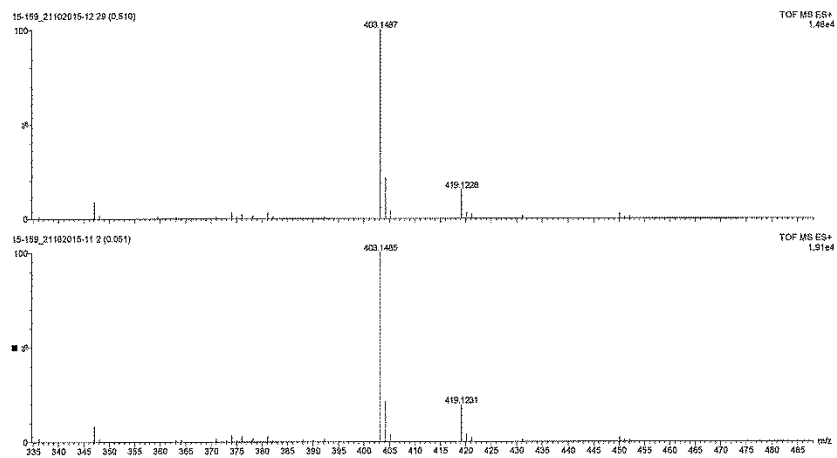


Figure 6- 69. FT-IR spectrum of compound 9a.



Accurate Mass Data				
Observed Mass	Formula [M+Na] ⁺	Calculated mass	Difference (ppm)	iFit (norm)
403.1485	C ₁₈ H ₂₄ N ₂ O ₇ Na	403.1481	1.0	2.4
403.1487	C ₁₈ H ₂₄ N ₂ O ₇ Na	403.1481	1.5	3.1

Figure 6- 70. Mass spectra of compound 9a.

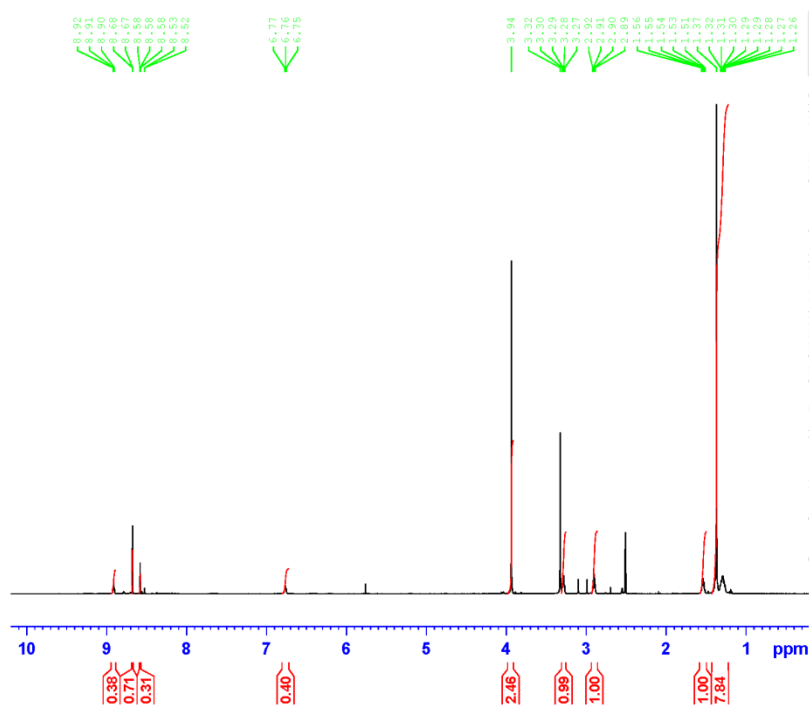


Figure 6- 71. ¹H NMR spectrum of compound 9b.

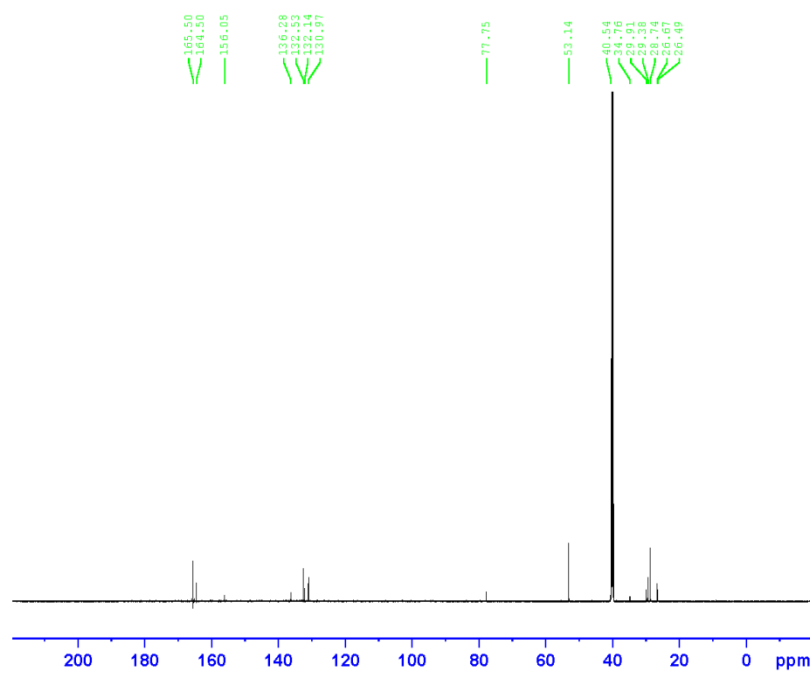


Figure 6- 72. ¹³C NMR spectrum of compound 9b.

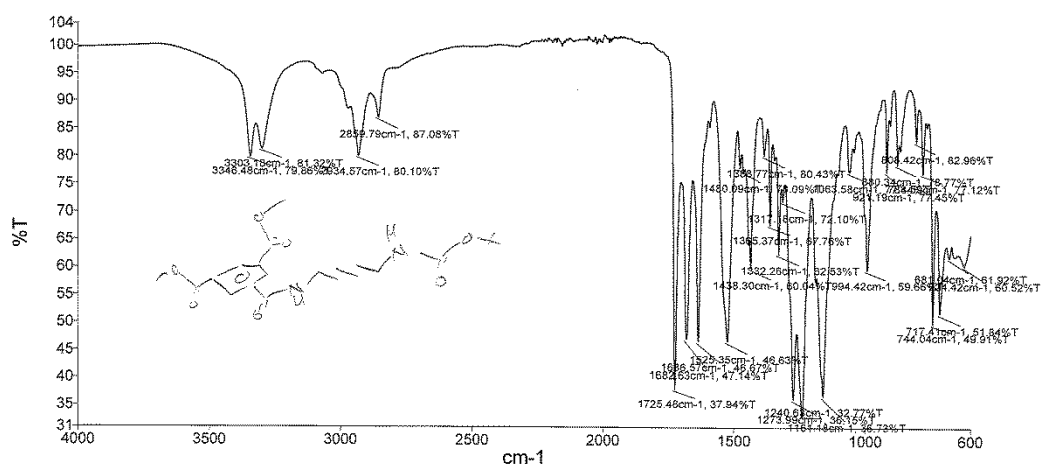
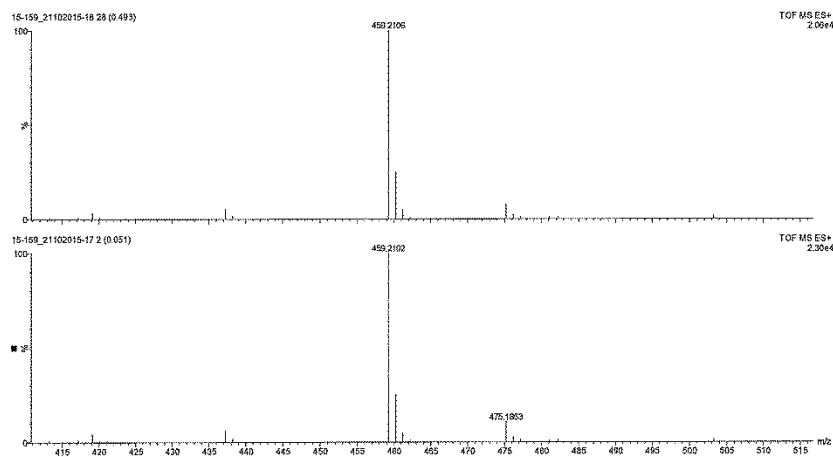


Figure 6- 73. FT-IR spectrum of compound 9b.



Accurate Mass Data

Observed Mass	Formula [M+Na] ⁺	Calculated mass	Difference (ppm)	iFit (norm)
459.2102	C ₂₂ H ₃₂ N ₂ O ₇ Na	459.2107	-1.1	0.1
459.2106	C ₂₂ H ₃₂ N ₂ O ₇ Na	459.2107	-0.2	0.2

Figure 6- 74. Mass spectra of compound 9b.

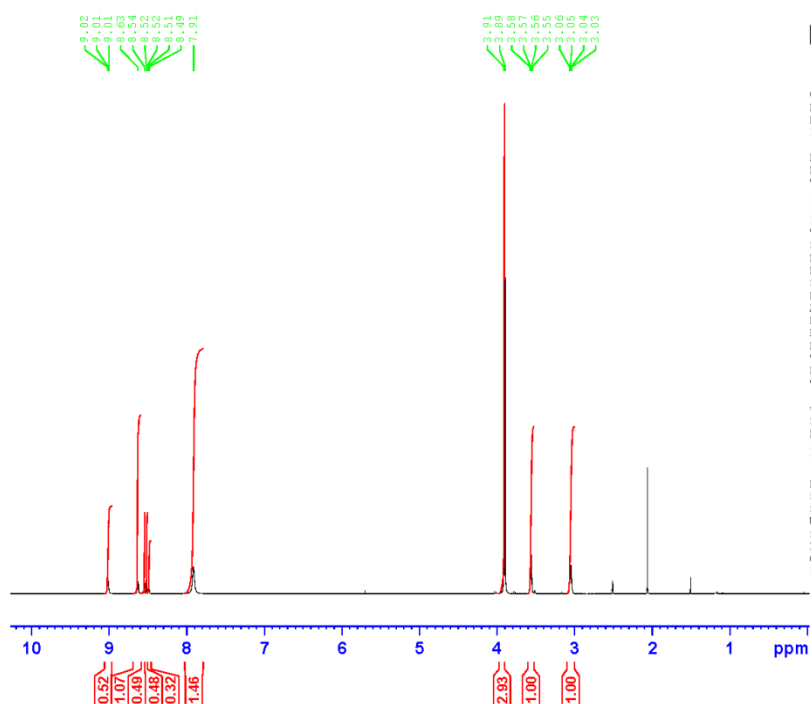


Figure 6- 75. ¹H NMR spectrum of compound 10a.

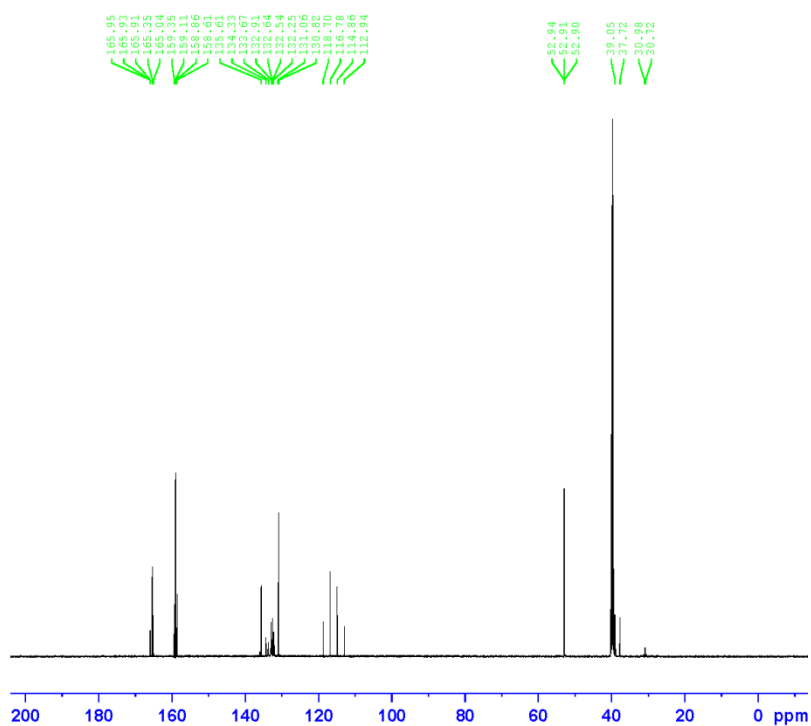


Figure 6- 76. ¹³C NMR spectrum of compound 10a.

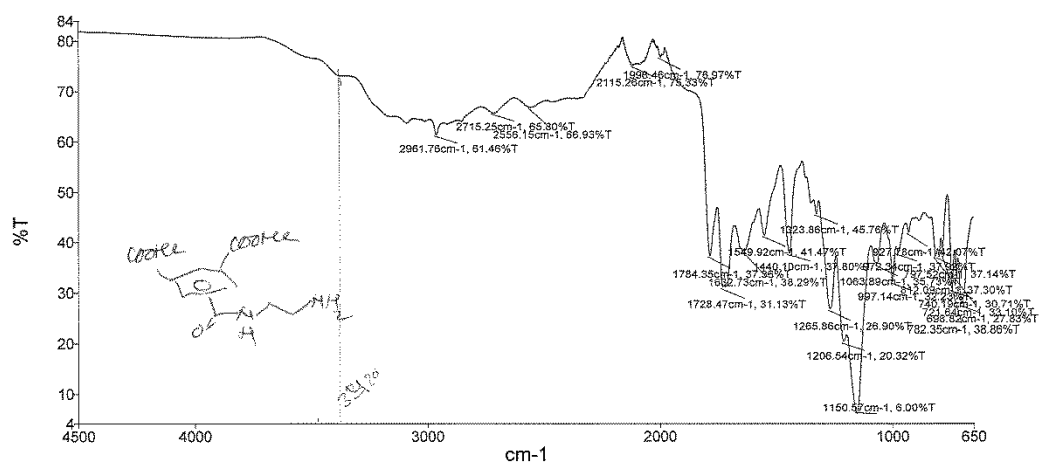
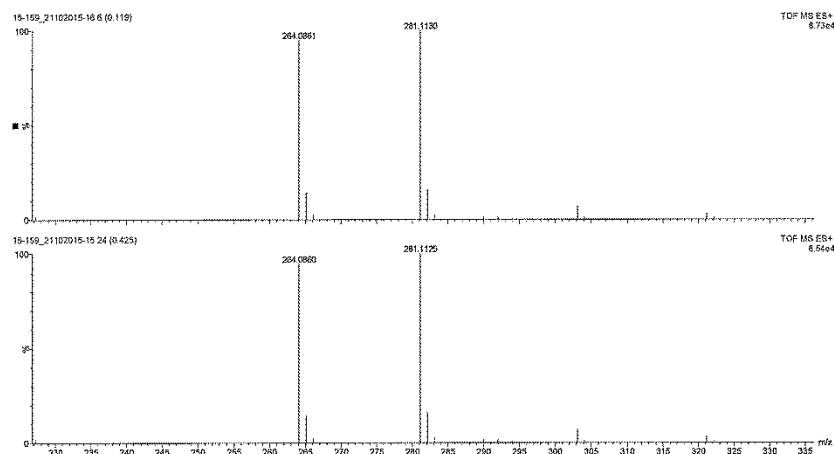


Figure 6- 77. FT-IR spectrum of compound 10a.



Accurate Mass Data

Observed Mass	Formula [M+H] ⁺	Calculated mass	Difference (ppm)	iFit (norm)
281.1125	C ₁₃ H ₁₇ N ₂ O ₅	281.1137	-4.3	2.4
281.1130	C ₁₃ H ₁₇ N ₂ O ₅	281.1137	-2.5	2.3

Figure 6- 78. Mass spectra of compound 10a.

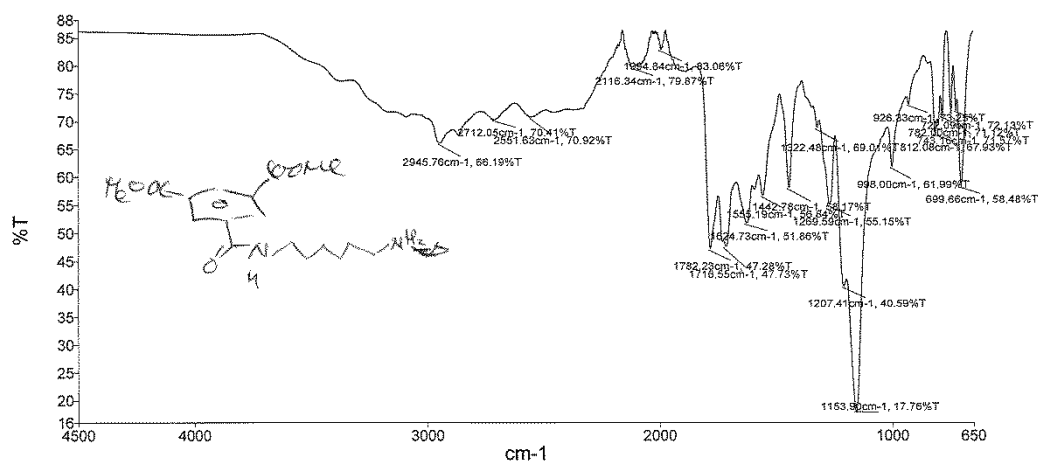
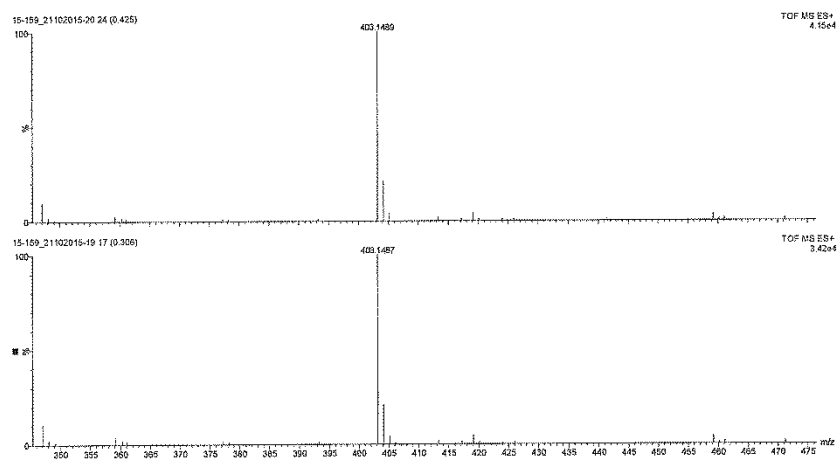


Figure 6- 81. FT-IR spectrum of compound 10b.



Accurate Mass Data

Observed Mass	Formula [M+Na] ⁺	Calculated mass	Difference (ppm)	iFit (norm)
403.1487	C ₁₈ H ₂₄ N ₂ O ₇ Na	403.1481	1.5	0.1
403.1489	C ₁₈ H ₂₄ N ₂ O ₇ Na	403.1481	2.0	3.3

Figure 6- 82. Mass spectra of compound 10b.

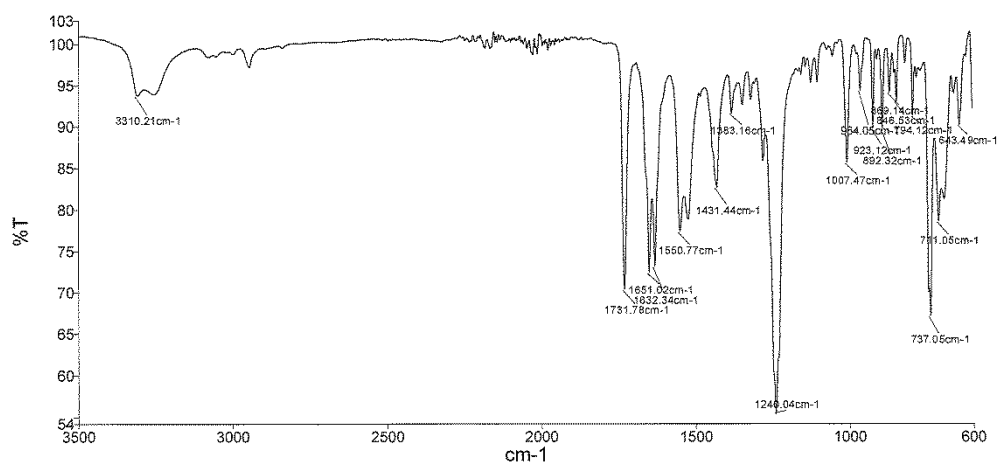
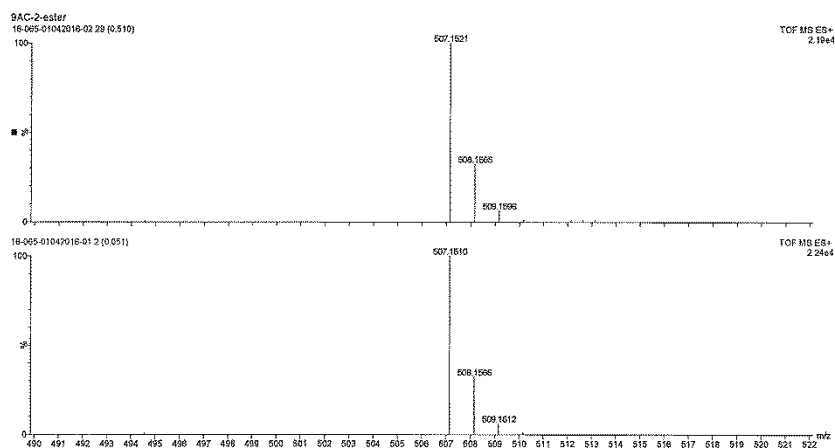


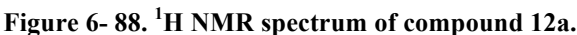
Figure 6- 85. FT-IR spectrum of compound 11a.



Accurate Mass Data

Observed Mass	Formula [M+Na] ⁺	Calculated mass	Difference (ppm)	iFIT (norm)
507.1510	C ₂₈ H ₂₄ N ₂ O ₆ Na	507.1532	-4.3	1.0
507.1521	C ₂₈ H ₂₄ N ₂ O ₆ Na	507.1532	-2.2	0.3

Figure 6- 86. Mass spectra of compound 11a.



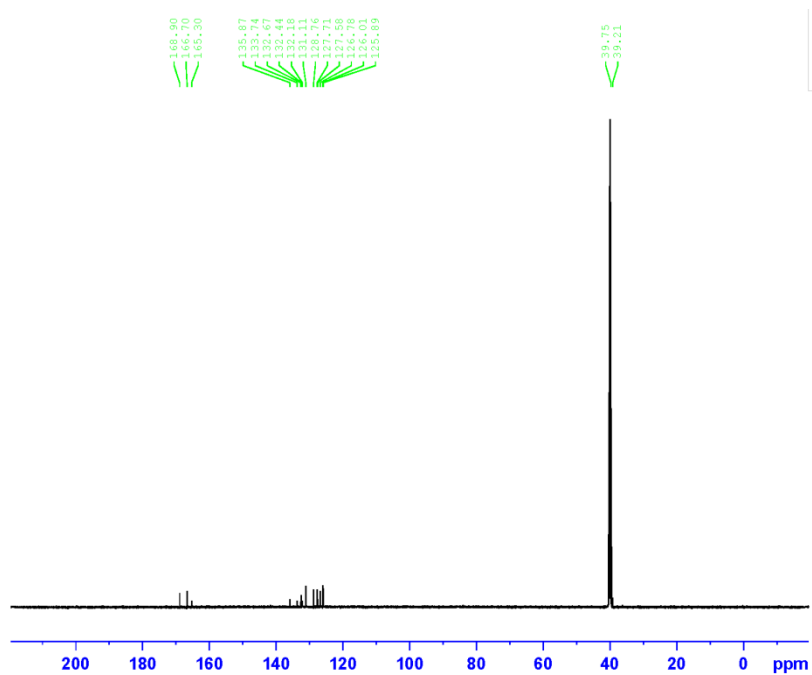


Figure 6- 89. ^{13}C NMR spectrum of compound 12a.

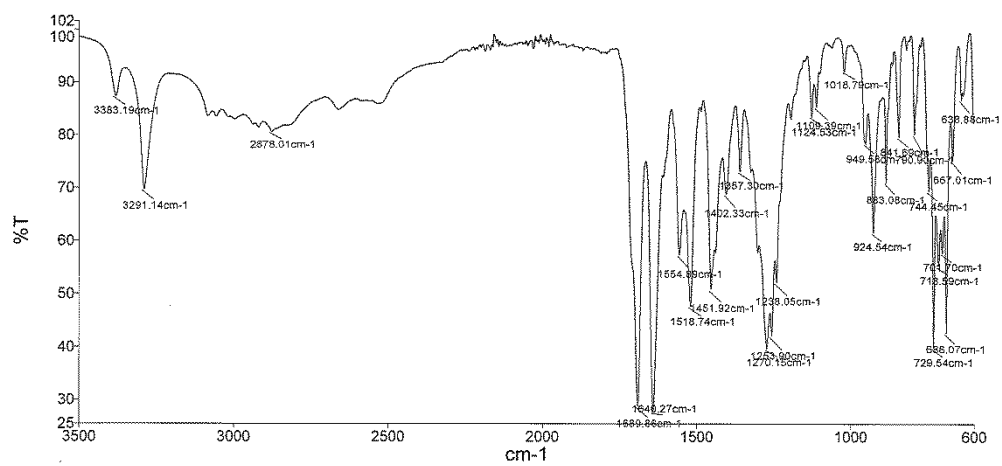
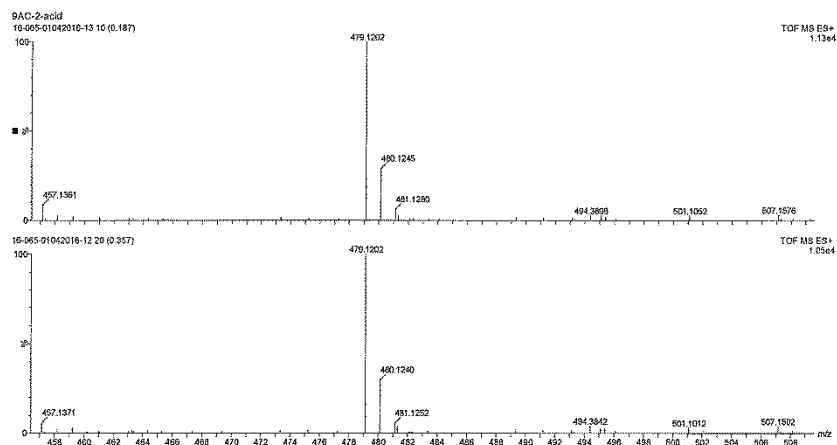


Figure 6- 90. FT-IR spectrum of compound 12a.



Accurate Mass Data

Observed Mass	Formula [M+Na] ⁺	Calculated mass	Difference (ppm)	iFIT (norm)
479.1202	C ₂₆ H ₂₀ N ₂ O ₆ Na	479.1219	-3.5	1.0
479.1202	C ₂₆ H ₂₀ N ₂ O ₆ Na	479.1219	-3.5	0.9

Figure 6- 91. Mass spectra of compound 12a.

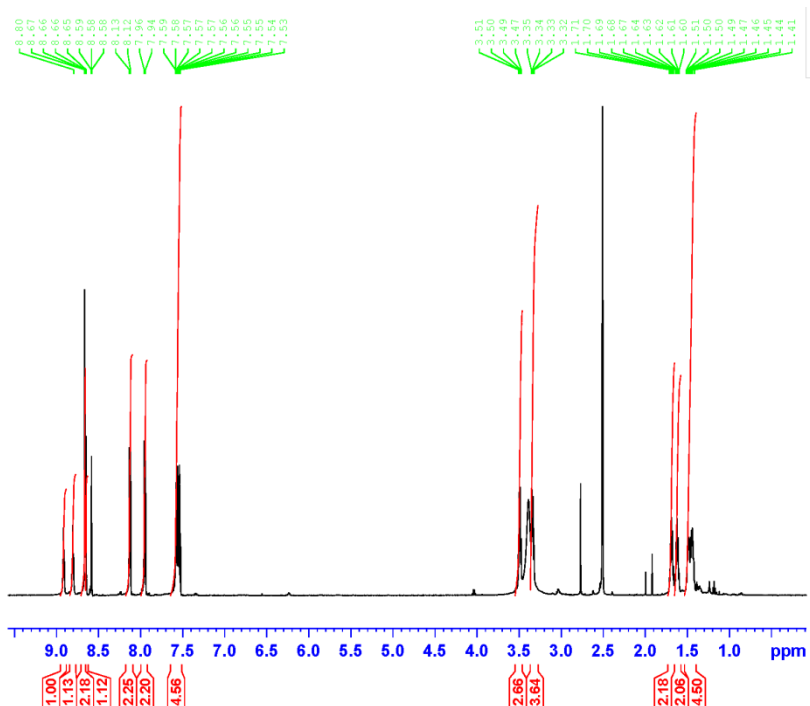


Figure 6- 92. ¹H NMR spectrum of compound 12b.

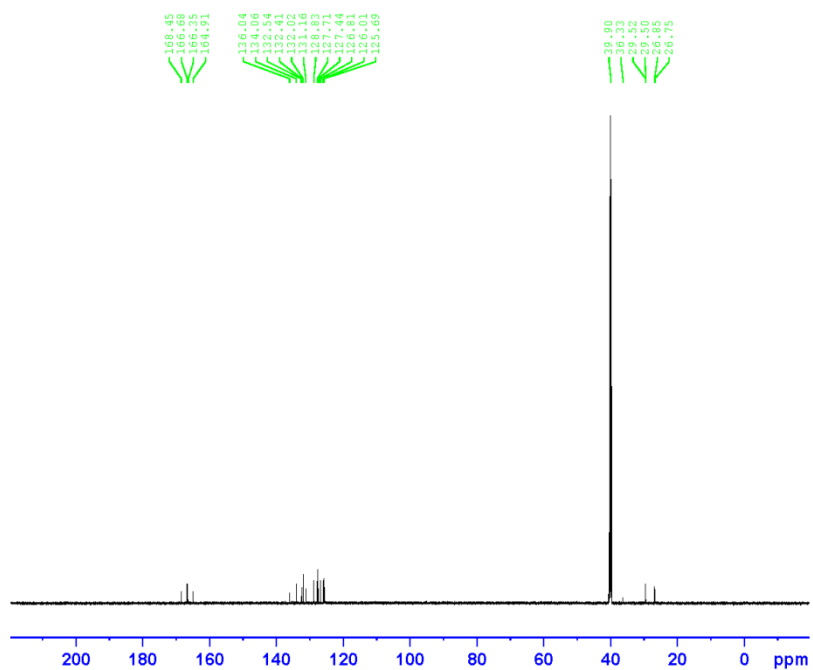
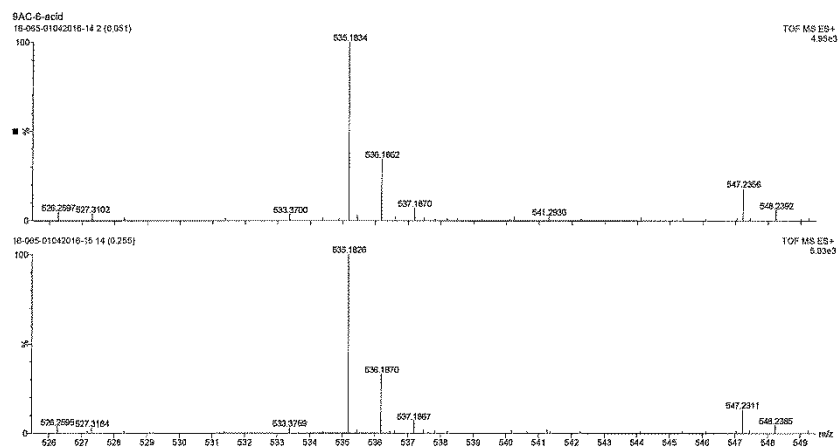


Figure 6- 93. ^{13}C NMR spectrum of compound 12b.



Accurate Mass Data

Observed Mass	Formula $[\text{M}+\text{Na}]^+$	Calculated mass	Difference (ppm)	iFit (norm)
535.1826	$\text{C}_{30}\text{H}_{28}\text{N}_2\text{O}_6\text{Na}$	535.1845	-3.6	2.6
535.1834	$\text{C}_{30}\text{H}_{28}\text{N}_2\text{O}_6\text{Na}$	535.1845	-2.1	1.5

Figure 6- 94. Mass spectra of compound 12b.

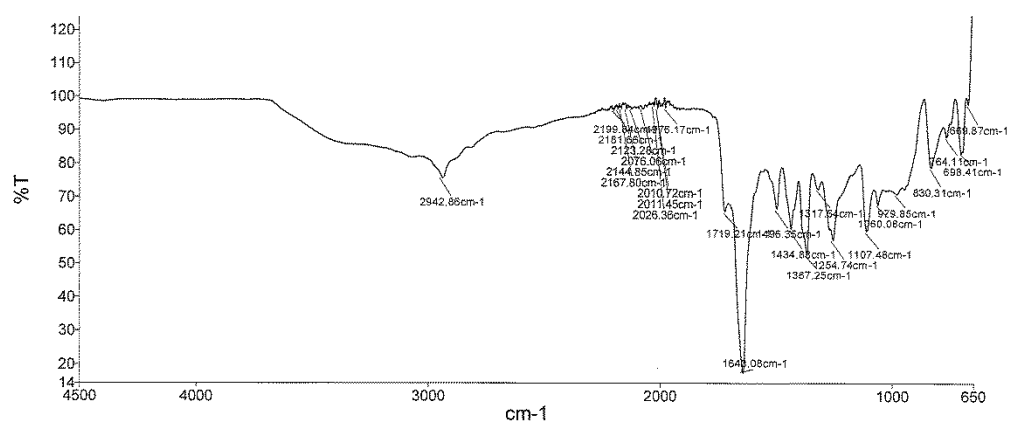


Figure 6- 95. FT-IR spectrum of compound 13a.